AUBURN UNIVERSITY
Samuel Ginn College of Engineering

Research Report

IMPACT OF IMPERFECTIONS, RESIDUAL STRESSES, ERECTION FIT-UP AND DISTORTION ON CURVED STEEL BRIDGE SERVICE LIFE

Submitted to

The Alabama Department of Transportation

Prepared by

Stephen T. Hammett
Sayed Mohamad Jalali Moghadam
James S. Davidson

September 2024

HIGHWAY RESEARCH CENTER
Harbert Engineering Center
Auburn, Alabama 36849

1. Report No.	2. Government Accession No.	3. Recipient Catalog No.
4 Title and Subtitle **IMPACT OF IMPERFECTIONS, RESIDUAL STRESSES, ERECTION FIT-UP AND DISTORTION ON CURVED STEEL BRIDGE SERVICE LIFE**		5 Report Date 6 Performing Organization Code
7. Author(s) Stephen T. Hammett, Sayed Mohamad Jalali Moghadam and James S. Davidson,		8 Performing Organization Report No.
9 Performing Organization Name and Address Highway Research Center Department of Civil Engineering 238 Harbert Engineering Center Auburn, AL 36849		10 Work Unit No. (TRAIS) 11 Contract or Grant No.
12 Sponsoring Agency Name and Address Alabama Department of Transportation 1409 Coliseum Boulevard Montgomery, Alabama 36130-3050		13 Type of Report and Period Covered 14 Sponsoring Agency Code

15 Supplementary Notes

16 Abstract

Curved steel girders experience large deflection and rotations during construction and service that can intensify the web breathing effect. In addition, the curvature-induced lateral forces in slender curved webs can lead to critical web boundary stresses that do not typically occur in straight bridges. These distortion mechanisms are amplified by millions of traffic load cycles over the life of the bridge, and therefore, the goals of this research were to investigate the web behavior of composite curved steel bridges and define design methodology that could be applied to the fatigue limit state. The web stress development mechanisms from construction to service were addressed through parametric finite element modeling of a horizontally curved composite bridge. Three regions of high bending, high shear, and high bend and shear locations were studied. Also, a novel LiDAR structural monitoring (LSM) method was investigated and used to survey horizontally curved steel girders during construction.

17 Key Words: curved steel bridge, distortion, fatigue, finite element, LiDAR, slender web, stress analysis, structural monitoring, web breathing		18 Distribution Statement No restrictions. This document is available to the public through the National Technical Information Service, Springfield, Virginia 22161	
19 Security Classification (of this report) Unclassified	20 Security Classification (of this page) Unclassified	21 No. of pages	22 Price

_____

Research Report No.

IMPACT OF IMPERFECTIONS, RESIDUAL STRESSES, ERECTION FIT-UP AND DISTORTION ON CURVED STEEL BRIDGE SERVICE LIFE

Submitted to

The Alabama Department of Transportation

Prepared by

Stephen T. Hammett
Sayed Mohamad Jalali Moghadam
James S. Davidson

September 2024

DISCLAIMERS

The contents of this report reflect the views of the authors who are responsible for the facts and accuracy of the data presented herein. The contents do not necessarily reflect the official views or policies of Alabama DOT, Auburn University, or the Highway Research Center. This report does not constitute a standard, specification, or regulation. Comments contained in this report related to specific testing equipment and materials should not be considered an endorsement of any commercial product or service; no such endorsement is intended or implied.

NOT INTENDED FOR CONSTRUCTION, BIDDING, OR PERMIT PURPOSES

Stephen T. Hammett, Sayed Mohamad Jalali Moghadam and James S. Davidson

ACKNOWLEDGEMENTS

This project was sponsored as Project 931-003 by the Alabama Department of Transportation. The original principal investigator was Dr. Justin Marshall, whose leadership in the early phases of the project is gratefully acknowledged. We also express our gratitude to ALDOT for the opportunity and for the guidance provided by Mr. Tim Colquett, Dr. Berhanu Woldemichael, and Mr. Robin Rhoden. We thank Mr. Keith Kelley at AECOM for his willingness to help and provide the necessary construction drawings, shop drawings, site pictures, and contacts as we worked our way through this project over several years. We are also grateful to McInnis Construction, LLC, Mr. Timothy McInnes, Mr. Ty Tyler, and Mr. Sammy Poynter for the time that they spent with us on conference calls and the site access provided for our field measurements. We also thank Mr. Wally Young at W&W AFCO Steel for promptly responding to our many emails, allowing us access to the girders during fabrication, and his willingness to position girders in the yard so that we could complete the LiDAR scans.

ABSTRACT

Modern steel bridge design is constantly evolving toward the use of slender elements due to the use of higher strength materials and improved fabrication and construction technologies. Design for strength and stability has been well defined through extensive research and testing; however, fatigue concerns have not been thoroughly investigated, especially for horizontally curved bridges. The out-of-plane displacements of slender webs result in secondary bending stresses at the web boundaries connections, i.e., flange and stiffeners. This "web breathing" phenomenon potentially leads to fatigue crack initiation at the web boundary connections and has been studied for straight girders. Curved steel girders experience large deflection and rotations during construction and service that can intensify the web breathing effect. In addition, the curvature-induced lateral forces pushing and pulling slender curved webs develop mechanisms that can lead to critical web boundary stresses that do not typically occur in straight bridges. These distortion mechanisms are amplified by millions of traffic load cycles over the life of the bridge, and therefore, the goals of this research were to investigate the web behavior of composite curved steel bridges and define design methodology that could be applied to the fatigue limit state. The web stress development mechanisms from erection to service were addressed through parametric finite element modeling of a horizontally curved composite bridge. Three regions of high bending, high shear, and high bend and shear locations were studied. Also, a novel LiDAR structural monitoring (LSM) method was investigated and used to survey horizontally curved steel girders in the fabrication yard and during construction of a large bridge (Ramp C) over I-565 in Madison, Alabama.

It was observed from the numerical studies that the slender web of the curved I-girder systems experiences significantly larger fatigue critical stress concentrations compared to the equivalent straight girders. In order to define a fatigue limit, parametric finite element modeling was done through the simulation of isolated curved web panels designed based on AASHTO limits. Two cases of pure bend and combined bend and shear loading configuration were analyzed. In the case of pure bend, a fatigue design equation was developed to limit the maximum in-plane bending stress critical for web breathing. In addition, it was concluded that AASHTO considerations related to the web-to-stiffener fatigue detail category control the web-to-flange fatigue cracking due to

web distortions for normal to moderately slender webs. In the case of bend and shear loading, a fatigue design limit was derived based on the in-plane bending stress. Also, it was observed that the share of the shear stress in combined loading significantly influences the curved web panel fatigue behavior. Fatigue breathing of curved web panels becomes almost identical to the flat web panels when the in-plane shear stress is equal to the bending stress.

At the time of writing this report, the bridge that was the subject of the field surveys was still under construction. Additionally, the low web slenderness ratio of the girders and close cross frame spacing would likely have resulted very limited observation of web breathing behavior. Nonetheless, the curved girders were scanned in the fabrication yard and in place after the cross frame bolts were tightened and temporary shoring was removed. A novel structural monitoring technique based on geometric data (point cloud data) obtained through the use of a conventional, terrestrial LiDAR scanner, was investigated for remote assessment of deformations and associated stresses. The LiDAR structural monitoring (LSM) method requires two LiDAR scans of the structural component being evaluated – one before and one after an applied load or an enforced displacement. The raw point data for each scan is transformed from a random collection of points into a regular, gridded representation of the scanned component. These discretized representations provide foundational geometry for the mathematical descriptions of the undeformed and deformed component that are needed to determine the change in surface strains that accompany the change in shape. Cross-section properties and constitutive relationships are used in combination with the change in surface strains to determine the change in the stress state at any point on the surface of or within the component. The proposed LSM method was evaluated through the several analytical and laboratory test problems. Additional field monitoring of the Ramp C bridge in Madison, Alabama, can be used in the future to further evaluate the derived methodology and assess the magnitude of distortion induced stresses that could evolve into fatigue concerns.

TABLE OF CONTENTS

LIST OF TABLES

LIST OF FIGURES

CHAPTER 1
INTRODUCTION

1.1 Background

Horizontally curved steel bridges provide economical design, long span, shallow depth, and aesthetic benefits. These structures are the dominant choice for highway overpass bridges and comprise significant share of U.S. steel bridges. Curvature affects both the flange and web behavior of I-girders. There is a reduced vertical (major axis) moment carrying capacity due to the addition of lateral flange bending moments caused by torsion. Also, the lateral forces that result from the non-alignment of internal forces push and pull the web panel in compression and tension regions, respectively, result in distortion of the web, especially for slender webs. In addition to web deformations due to pure in-plane bending, curved steel bridge girders experience large deformations during erection, construction, and service. The whole curved bridge system rotates upon receiving dead and live load that is transferred through cross-frames. The accumulated web distortions from construction to service affect the fatigue performance of curved bridge superstructures. However, these effects are typically neglected in defining fatigue design guidelines for curved bridges (Daniels and Herbin 1980; Nakai et. al 1990).

Large scale research programs were conducted from the 1970s through the 1990s to investigate the behavior of curved steel girders and develop design methodology and specification recommendations (Consortium of University Research Teams 1975; Zureick et al. 1994). Recently, numerous studies were carried out to further investigate the effect of curvature on the stability and strength of slender curved girders for more liberal design considerations (Sanchez

and White 2012; Issa-El-Khoury et al. 2014; Broujerdian et al. 2015; Frankl and Linzell 2017). Ultimately, three decades of research resulted in the integration of curvature-induced effects on strength into the AASHTO LRFD Bridge Design Specifications in 2005.

Although the stability and strength of curved steel girders have been comprehensively investigated, the fatigue design does not explicitly consider potential curvature effects. Even though they are relatively small in magnitude, the stresses that are induced by web distortion under millions of cycles of traffic loading, which are added to the normal flexure-induced stresses, can potentially result in fatigue cracking after decades of service. The likelihood of such problems will increase as higher strength steels result in the use of slenderer web panels. Therefore, the Alabama Department of Transportation (ALDOT) sponsored the project in which this report is based, "Impact of Imperfections, Residual Stresses, Erection Fit-up and Distortion on Curved Steel Bridge Service Life", to investigate whether the distortion that is inherent to curved steel bridges will eventually become a concern for current in-service structures and future designs.

1.2 Objectives

The overall objectives of the study were to characterize the mechanics associated with distortion induced stress concentrations in horizontally curved bridge girders that may lead to fatigue cracks and to develop recommendations for improving fatigue design methodology.

1.3 Scope and Methodology

This project (931-003) initiated on October 1st 2019 at Auburn University under the direction of Dr. Justin Marshall as principal investigator and Dr. James Davidson as co-PI. The performance period was planned as 21 months and scheduled to end in June 30th 2021. In general, Dr. Marshall's expertise was envisioned to apply to field testing tasks and Dr. Davidson's to theoretical and numerical tasks. Two PhD students supported the effort: Mehran Jalali (theory and modeling) and Steve Hammett (field testing).

At the time of proposal development, a curved bridge, referred to as the Town Madison Bridge, was being designed and planned for construction in Madison Alabama. As such, the scope of the project was planned as a strong integration between advanced simulation (nonlinear finite element analyses) and validation using field monitoring data. The background investigation tasks and finite element modeling tasks proceeded in good form, but the construction of the Town Madison Bridge encountered many delays. The first opportunity for construction site field measurements did not occur until August 2024. Other encountered challenges that significantly affected the execution methodology and timeline included COVID-19 setbacks and Dr. Marshall's resignation from Auburn to accept other employment. Also, the final design the Town Madison Bridge was extremely robust, with relatively stocky web panels, short spacing between cross-frames and stiffeners, no-load fit up and cut-curving of the flanges rather than heat curving. Therefore, it turned out that the Town Madison Bridge was far from ideal for this study. Nonetheless, the goals of the program were largely achieved through the diligence of the investigators, patience of the sponsors and stakeholders, and cooperation of those involved in the design, fabrication and construction of the Town Madison Bridge. The following outlines the scope as it was structured in the proposal:

Task 1 – Kickoff Meeting. Soon after notice to proceed, a meeting was held to inform all stakeholders of the project objectives, work plan and schedule. Other meetings with ALDOT bridge engineers and frequent interactions with contractor and local government representatives associated with the Town Madison Bridge also occurred throughout the project.

Task 2 – Literature Review. A thorough literature review was performed of all relevant published information. Due to Dr. Davidson's background on this topic, much of the strength and stability literature was familiar, but additional literature review related specifically to fatigue concerns, heat curving of steel girders and field measurement strategies was required.

Task 3 – Monitoring of Girder Fabrication and Erection. The primary focus of this task was to assess the impact of the imperfections and residual deformations that are induced in the steel curved girders due to fabrication and erection. The methodology proposed was the use of Lidar and drones. However, drones were not necessary due to ease of access of the superstructure sections involved in the study. This task required frequent coordination with the fabricators and erection/construction contractors. LiDAR scans of selected sections were taken in the fabrication yard and in the steel erected configurations, and the point-clouds and meshes of the girders at these stages of fabrication and erection were generated. Completion of the Town Madison Bridge construction is needed before the magnitudes of imperfections and distortion that develop in the webs can be evaluated.

Task 4 – Thermal Analyses of Heat Curving. This task was intended to assess the magnitude of residual stresses that develop due to the heat curving process. However, the girders of the Town Madison Bridge were cut-curved, rather than heat curved, and therefore the fabrication did not offer an opportunity to collect significant data. Nonetheless, LiDAR scans were taken at the

fabrication yard of the girders before transport and the literature background associated with heat curving as it relates to the fatigue concern was investigated.

Task 5 – Finite Element Modeling and Parametric Analyses. Detailed finite element models of full bridge superstructures at various stages of erection were developed in both GT STRUDL 2020 and ABAQUS. It was intended that data collected by the Town Madison Bridge monitoring tasks would be used to validate the finite element modelling approach, but construction delays resulted in disassociation between the two tasks, and therefore other literature data was used to verify the finite element modeling approaches. These models were used extensively to develop the field monitoring plan to and assess the implications of curvature-induced distortion on fatigue performance.

Task 6 – Live Load Field Test. The final experimental component of the research project was intended to be a live load test of one of the Town Madison Bridge ramp bridges using the ALDOT Load Truck. At the time of concluding the project and this report, nearly five years after project initiation, there were still several months before the bridge construction would be completed. Also, as briefly mentioned above, the robustness of the Town Madison Bridge, along with the measurement taken in the dead load configuration, imply that the distortion magnitudes that would be measured would not be significant. Nonetheless, the research team welcomes the opportunity to conduct the scan and analyses once the bridge is complete.

Task 7 – Final Report. This comprehensive final report was prepared and presentation will be made to the ALDOT stakeholders and the Research Advisory Committee.

1.4 Report Organization

Chapter 2 presents the mechanics of curved girders and defines how the applied vertical loads affect the resulting stress components. A brief background of specific curved girder stresses is given at the beginning, followed by a guide specification development review. Then, the stability of the flange and web of the curved I-girders is reviewed and the V-load method of analysis is explained. The various fatigue assessment methods, including nominal-stress and hot-spot stress approaches and the Linear Elastic Fracture Mechanics (LEFM) method, are discussed. The residual stress effect on the fatigue life of steel structures is presented. Chapter 2 also addresses fatigue associated with straight multi girders and slender girders. Distortion induced fatigue and web breathing are discussed, and fatigue studies specific to curved girders are reviewed. Current fatigue design limits related to each type of fatigue problem are presented at the end.

Chapter 3 presents the results of parametric finite element analyses of horizontally curved steel bridges. An advanced multi-level analysis technique was developed for the non-composite and composite simulation of curved bridges. Three web panel regions in terms of high bending, shear, and combined bending and shear were analyzed. The web stress development mechanism critical for the fatigue limit of the curved systems was explained and compared to the equivalent straight girders. Existing theoretical methods for straight and curved web panels are reviewed and the simplified methods and the governing nonlinear partial differential equations for the straight and curved web are discussed. The need for the proper method to study slender web behavior is illustrated through finite element analysis. A parametric finite element analysis of isolated curved web panels under pure bending is presented. Various models were simulated for the fatigue cracks occurring at the web-to-flange connection in the compression region. A post-processing code was developed and used to define the design equation for the fatigue limit state of slender curved web panels. Finally, Chapter 3 presents a parametric finite element analysis of isolated curved web

panels under combined loading. A modification was added to the post-processing code to investigate the shear and bend load effects. The parameter influences are discussed and a fatigue design limit is recommended for the combined loading condition.

Chapter 4 presents the LiDAR field monitoring of the Town Madison Bridge and the development of methodology for the evaluation of stress and strain in web panels using LiDAR scan data. It also presents a demonstration and validation of the approach using scans of controlled displacement of a buckled slender aluminum panel in shear and a slender steel plate in compression.

Chapter 5 summarizes the conclusions and recommendations of the study.

CHAPTER 2
LITERATURE AND MECHANICS OVERVIEW

2.1 Curved Girder Mechanics

2.1.1 Background

The state of stress in horizontally curved girders is more complex than straight girders due to the torsional loading induced by curvature (Culver and Nasir 1969). Normal stresses acting on the cross section include warping (non-uniform torsion), bending, distortional, and radial bending. Shear stresses are caused by bending, St. Venant torsion, and non-uniform torsion (Schuenzel 1982). Figure 2.1 shows the distribution of stresses on a cross-section. Several detailed curved girder mechanics literature summaries have been presented by others, such as Schuenzel (1982), Fiechtl et al. (1987), Ziemian (2010), and Moghadam et al. (2020).

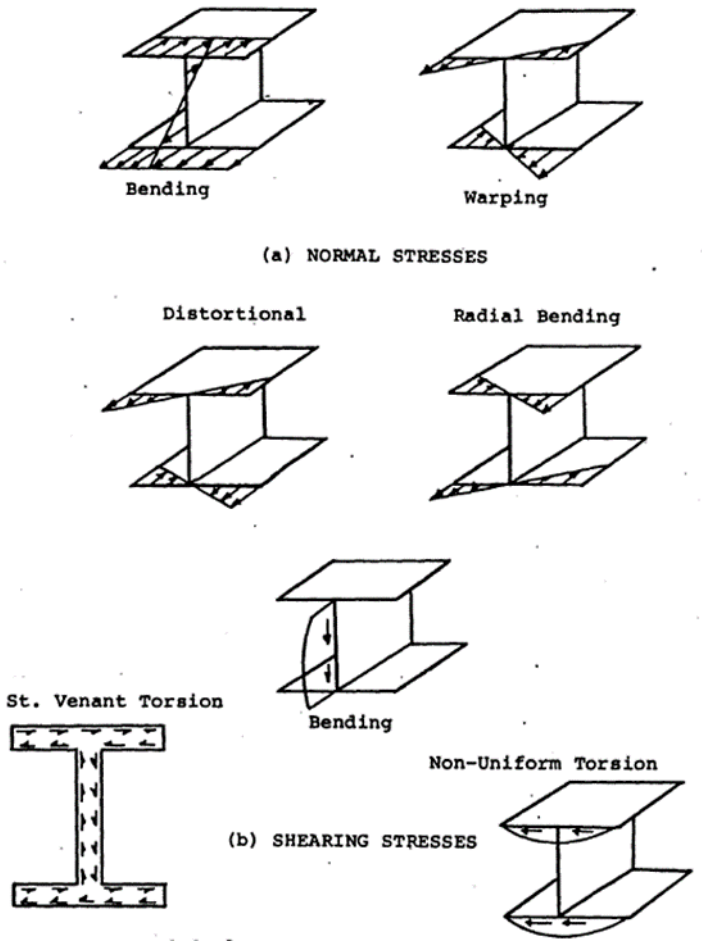

Figure 2.1: Curved Girder Stress Distributions (Schuenzel 1982)

2.1.2 Guide Specification Development

Research before the mid-1960s on the behavior of horizontally curved girders was limited to the theoretical work based on the linear elastic static behavior of curved elements, with the earliest work on curved beam theory attributed by St. Venant (1843) over 170 years ago (Ziemian 2010).

The initial step toward developing a guide specification for designing the curved bridges started by the Consortium of University Research Teams (CURT) project in 1969. The CURT project was run by the Federal Highway Administration (FHWA) as a financially granted research by 25 states. The CURT project aimed at a) reviewing published materials related to curved

bridges; b) running experimental and analytical analysis applying the knowledge of curved bridge design; c) investigating the other state corporation findings; d) developing the simple design and analysis methods; and e) verifying the recommended design and analysis methods with the acquired analytical and experimental data (Linzell et al. 2004).

Four Universities, namely: The University of Rhode Island, Syracuse University, the University of Pennsylvania, and Carnegie-Mellon University, participated in the CURT project. The University of Rhode Island conducted full-scale tests on two single scale curved boxed girders (Stegmann and Galambos 1976). A modified grid method of analysis, taking into consideration non-uniform torsion, was used to determine stresses (Schuenzel 1982). The University of Pennsylvania conducted small scale model tests using rolled beams (Stegmann and Galambos 1976). Non-uniform torsion was neglected while calculating stresses on the cross section (Schuenzel 1982). Hence, the method of analysis was not accurate. Syracuse University used a three-dimensional method of analysis of a scaled model of composite curved plate girder (Stegmann and Galambos 1976). The analysis assumed the effects of warping torsion and assumed that all members are straight and full composite action would be achieved. Charles Culver at Carnegie-Mellon investigated the limit states of horizontally curved girders (Schuenzel 1982). The investigation included studies of web shear, local and lateral buckling of compression flange, combined bending and shear failure, and web buckling. Carnegie-Mellon conducted an extensive testing program to test the strength of curved girders.

Based on the analytical and experimental studies carried out under CURT, a tentative design specification for horizontally curved girders (1975) was developed. This specification was based on allowable stress design considering only the elastic behavior (Schuenzel 1982). Later, Load Factor Design (LFD) criteria were added to the specifications through a research project

sponsored by the American Iron and Steel Institute (AISI) in the mid-1970s (Stegmann and Galambos 1976).

The above research done under CURT, along with some subsequent research, resulted in the development of AASHTO *Guide Specifications of Horizontally Curved Bridges* (AASHTO 1993). However, the *Guide Specifications* were disjointed and difficult to follow. There was a significant discontinuity in the compressive strength formulations for non-compact and compact sections (Davidson et al. 2000). Moreover, the value of strength calculated by strength predictor equations for curved sections did not approach that predicted by straight girder equations when the radius of curvature approached infinity (Davidson et al. 2000). For such reasons, among others, it was not adopted as an integral part of the AASHTO *Standard Specifications for Highway Bridges* (AASHTO 1992).

In 1992, the Federal Highway Administration (FHWA) started the Curved Steel Bridge Research Project (CSBRP) to understand the fundamental behavior of horizontally curved bridges that would lead to the development of LRFD specifications for curved bridge design (Ziemian 2010). A significant amount of research was undertaken to study the behavioral characteristics of curved girders. Strength predictor equations were developed involving a number of design issues like the curvature effect on the lateral buckling strength of curved girder over straight girders, strength reduction of web panels due to curvature under pure bending and combined bending and shear, inelastic behavior of horizontally curved girders, etc. (Davidson et al. 2000). The work of CSBRP was extended in 1999 through a project jointly sponsored by FHWA and the American Iron and Steel Institute (AISI) that used the nonlinear finite element analysis to expand the knowledge gained from experimental tests conducted under the CURT and CSBRP projects

(Ziemian 2010). This analytical work resulted in the unification of the design equations for straight and curved steel girders into the 2004 AASHTO *LRFD Bridge Design Specifications*.

2.2 Stability of Curved I-Girders

2.2.1 Flange Behavior

For straight I-shaped plate girders, the primary role of the web in the region of the high moment is to maintain relative distance between the flange plates. Therefore, the efficient design of plate girders requires the flanges to carry most of the moment, and the webs to be designed as slender as structurally possible. Thus, the nominal moment strength of straight, slender plate girders is controlled either by the limit state of yielding of the tension flange or buckling of the compression flange (Davidson et al. 1999). No inelastic behavior of webs is considered for design purposes.

However, for curved girders, the presence of curvature greatly complicates the behavior and design considerations. Curvature induces both warping torsion in the cross-section, and transverse displacement of the web (Davidson et al. 1999). To account for the effect of curvature on the flexure resistance contributed by the flanges, the normal stress acting on a flange is approximated as the linear addition of the bending normal stress and the normal stress resulting from the lateral bending of the flange, Figure 2.2. The sources of lateral bending stress are associated with either non-uniform torsion or from the lateral force acting on the girder (Ziemian 2010).

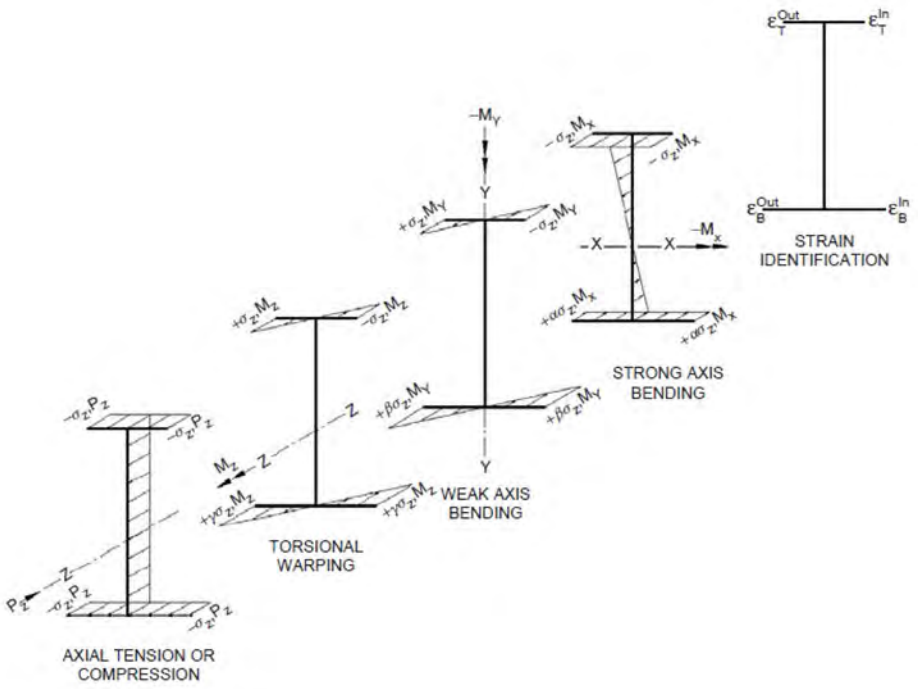

Figure 2.2: Components of longitudinal stress (Hartmann 2005)

In curved girders, as the curvature is increased, the membrane stress distribution becomes increasingly nonlinear through the depth of the section (Davidson et al. 1999). Because of this reduction of membrane stress along the web, the flanges carry a higher load. Thus, even without considering the warping stress acting due to curvature, the curved section would be unable to carry vertical moment as compared to the similar straight section before the yielding of the flanges initiates.

Culver and Nasir (1969) investigated the local buckling of curved girder flanges in both elastic and inelastic range to determine the governing differential equation. Shear stresses were neglected and the maximum bending and warping stresses were conservatively assumed to occur at the same point along the girder. The slenderness requirement generated from the characteristic equation is as follows (Culver and Nasir 1969):

$$\frac{b}{t} = \frac{kE}{12(1-\upsilon^2)F_y} \tag{2.1}$$

where b is width of the flange, t is thickness of flange, E is modulus of elasticity, F_y is yield stress, ν is the Poisson's ratio, and k is buckling coefficient.

For uniform stress (bending only), curvature had minimal effect on the value of k. For non-uniform stress, warping and bending, the value of k reduced a lot depending on the yielding of the flange, making the flanges more compact.

Davidson and Yoo (1996) showed that there is a reduction in elastic buckling strength of the curved compression flanges due to the warping stress gradient acting across the flanges. The primary factors that contributed to this reduction were stress ratio in the compression flange and the relative boundary condition provided by the web to the flanges. The effect of the curvature was given by:

$$(\sigma_{cr})_{cv} = (\sigma_{cr})_{st}\left[1.0643 - \frac{0.15 f_w}{0.35 f_b}\right] \tag{2.2}$$

where $(\sigma_{cr})_{cv}$ is critical stress for curved girder, $(\sigma_{cr})_{st}$ is critical stress for straight girder, f_w is warping stress, and f_b is bending stress.

One of the challenges of designing the curved girders was how to relate the combination of lateral bending stress and normal bending stress to flange bending resistance. Hall and Yoo (1998) proposed a unified approach, known as "1/3rd" rule, that applies to both tangent and curved I-girder bridges. The 1/3rd rule was first introduced into the 2004 AASHTO Load and Resistance Factor Design (LRFD) and is given by:

$$f_{bu} + \frac{1}{3} f_l \le \phi_f F_{nc} \tag{2.3}$$

Where f_{bu} is flange stress calculated without consideration of flange lateral bending, f_l is flange lateral bending stress, ϕ_f is resistance factor for flexural resistance, and F_{nc} is nominal flexural resistance of the flange.

2.2.2 Web Behavior

As mentioned in the previous section, curvature induces warping of the cross-section, and, more importantly, for the web consideration, transverse displacement of the web, which induces through the thickness stresses in the girder, decreasing the moment carrying capacity of the girder (Davidson et al. 1999). The curvature also causes nonlinear distribution of membrane stress, caused due to vertical bending, throughout the depth of the web. This distribution becomes increasingly nonlinear with the increase in curvature, which results in an increase in normal stress in the flanges, thus effectively reducing the moment carrying capacity of girders. Therefore, unlike straight girders, for curved girders along with flanges, webs also play an essential role in the design of curved girders in high moment regions.

2.3 V-Load Method

Horizontally curved bridges respond to loads differently than straight girders due to the torsional forces induced by the curvature. In 1963, Richardson (1963) published a structural report explaining a simplified approximate method for analyzing horizontally curved bridges. This method became to be known as the V-load method. In the V-load approach, the torque produced by curvature is represented as a self-equilibrating load acting at the girder diaphragms, and this load is known as V-load. Thus, a curved girder is modeled as a straight girder and analyzed twice, once for the load acting on the girder and second time for the self-equilibrating V-load acting on the girder. The results of both of the analyses are then added to obtain the demands on curved

girder due to the load acting on it. The mechanics involved in deriving the V-loads are mentioned in the proceeding sections.

Consider a horizontally curved bridge unit, as shown in Figure 2.3. As can be seen, the girders in the unit are spaced at distance *D*. The radius of curvature of the outer and inner girders are *R1* and *R2*, respectively. The diaphragms in the girder are spaced at distance *d*. The curvature of the unit is represented by θ. The arc length of the outer and inner girder is given as *L1* and *L2*.

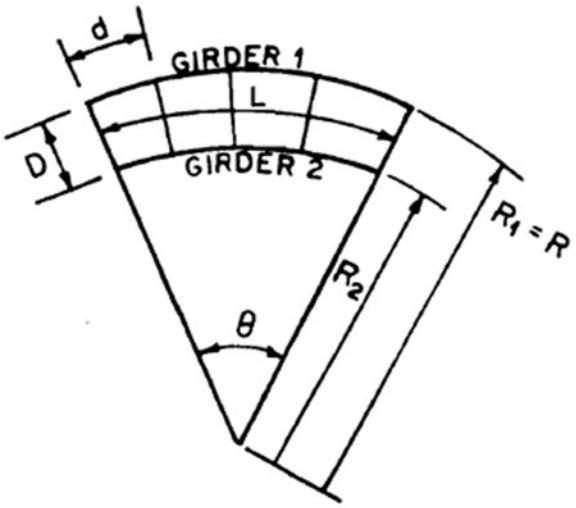

Figure 2.3: Two curved girder system (Fiechtl et al. 1987)

Bending moments due to vertical loads are resisted by the flanges and can be decomposed as longitudinal forces acting on the flanges. The longitudinal forces are represented by a force *M/h* on the flanges of the girder in equal and opposite directions, as shown in Figure 2.4. Here *h* is the distance between the flanges.

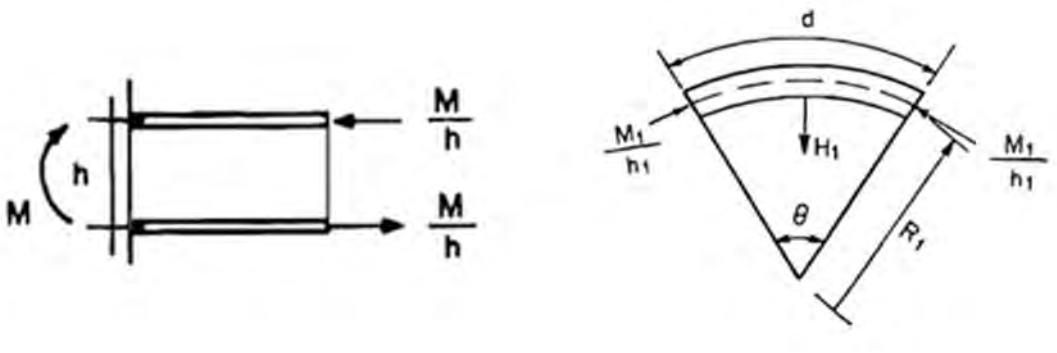

Figure 2.4: (left) Equivalent forces due to moments; (right) Resultant forces of top flange (Fiechtl et al. 1987)

As shown in Figure 2.4**,** due to the horizontal curvature, the longitudinal forces due to bending are not in equilibrium, and therefore it is not possible to calculate the demands on the girder due to static equilibrium. To maintain a radial equilibrium in the flange, a horizontal force (H_1) must be developed. This horizontal force develops along the diaphragm and is found by equilibrating along the radial line at the diaphragm location. The value of horizontal force acting for girder number one can be given as (Fiechtl et al. 1987):

$$H_1 = \frac{M_1 \theta}{h_1} \tag{2.4}$$

From geometry θ can be given as d/R, substituting the value of θ in equation 2.4 leads to:

$$H_1 = \frac{M_1 d_1}{h_1 R_1} \tag{2.5}$$

The same can be applied for girder 2. Vertical shear is required for the equilibrium of the diaphragm, as shown in Figure 2.5.

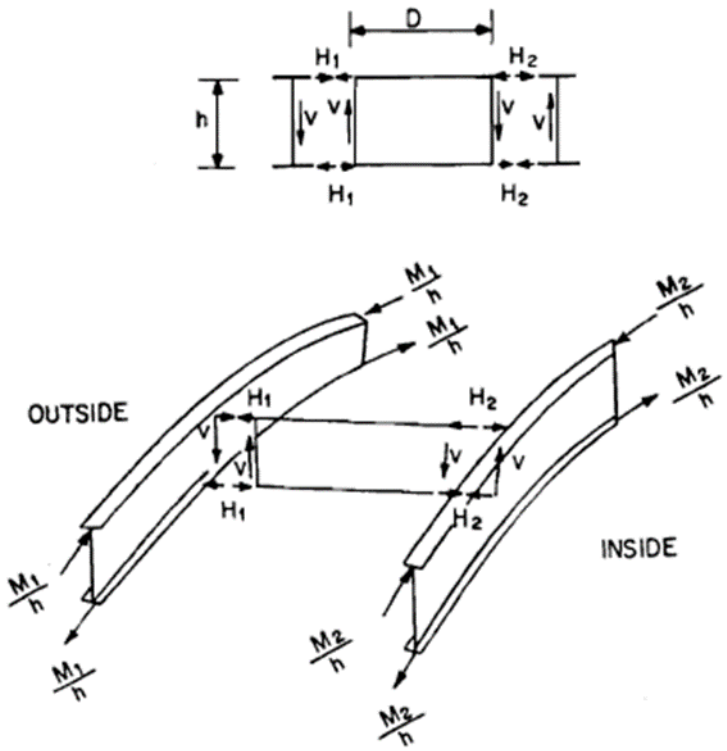

Figure 2.5: Forces acting at the diaphragm location (Fiechtl et al. 1987)

The vertical shear force acting along the girder can be calculated by taking a moment equilibrium along any end of the diaphragm, which can be given as:

$$V = (H_1 + H_2)\frac{h}{D} \tag{2.6}$$

By substituting the value of H_1 from equation 2.5 and H_2 from an equivalent term for H_2 into equation 2.6 leads to:

$$V = \frac{\frac{M_1 d_1}{R_1} + \frac{M_2 d_2}{R_2}}{D} \tag{2.7}$$

Considering $d_1/R_1 = d_2/R_2 = d/R$, the shear force is simplified as:

$$V = \frac{M_1 + M_2}{RD/d} \tag{2.8}$$

Figure 2.5 illustrates how these shear forces have opposite directions for each girder. The shear forces, so-called V-loads, are approximating the curvature effect on the bridge unit. It should be noted that they are self-equilibrating since they are not real loads acting on the bridge.

The total bending moments due to actual loads and forces developed by curved girder influence, V-loads, are denoted by M_1 and M_2 :

$$M_1 = M_{1p} + M_{1v} \tag{2.9}$$

$$M_2 = M_{2p} + M_{2v} \tag{2.10}$$

where subscript *P* and *V* represent the real loads and V-loads, respectively.

It was proven that the bending moment due to V-load was small as compared to moments due to primary load; therefore it was not included while calculating M_1 and M_2 (Fiechtl et al. 1987). Thus, substituting the values of *M* in equation 2.8, results in:

$$V = \frac{M_{1p} + M_{2p}}{RD/d} \tag{2.11}$$

A modified format of equation 2.11 that can be used for applying the V-loads on multi-girder bridges is given by;

$$V = \frac{\sum_{i=1}^{N_g} M_{pi}}{C(RD/d)} \tag{2.12}$$

where M_{pi} is primary girder moments, N_g is number of girders, and *C* is V-load coefficient, given by Table 2.1.

Table 2.1: V-Load coefficients (Fiechtl et al. 1987)

Number of girders, N_g	C
2	10000
3	10000
4	11111
5	12500
6	14000
7	15556
8	17143

2.4 Fatigue Assessment Methods

2.4.1 Introduction

Fatigue in metals is the initiation and growth of cracks under repetitive loading. This process can take place at stress levels that are substantially less than those associated with failure under static loading conditions (Fisher et al. 1998). The fatigue damage process physically takes place in three phases: the crack initiation stage, crack propagation, and fracture (failure) (ASCE 1982). The most common civil engineering structures that are most susceptible to fatigue are bridges, which is due to the repetitive loading acting upon them through vehicles passing over every day.

Fillet welded details have initial flaws such as partial penetration, porosity, undercut, etc. as shown in Figure 2.6. It has been proven that the fabrication flaws and stress-concentrations due to structural misalignment are the main causes of fatigue crack initiation (Berge and Myhre 1977; Fisher et al. 1998). The tensile stress component is the primary cause of crack propagation. Finally, the cracked section may fail due to reduced resistance under the cyclic load. There are various fatigue assessment methods for investigating the fatigue resistance and the remaining fatigue life of structures. This chapter presents standard fatigue assessment methods. In addition, the residual stress effect on fatigue behavior is explained briefly at the end.

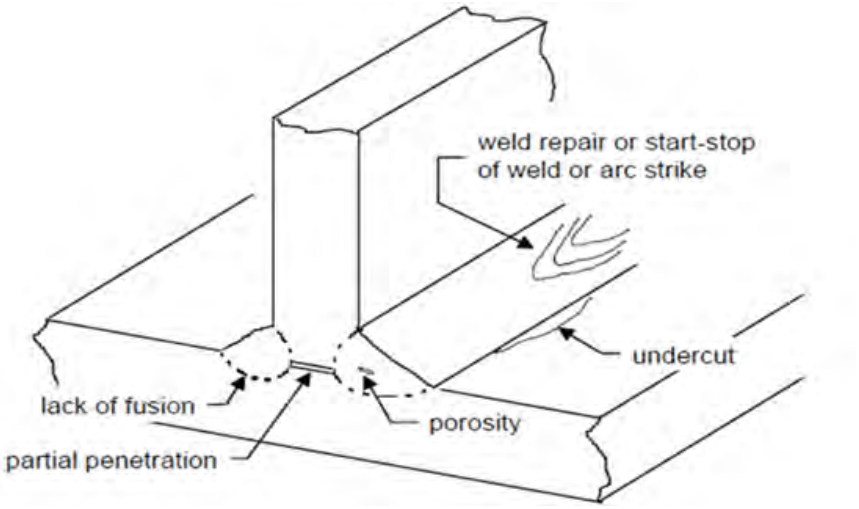

Figure 2.6: Flaws in a fillet-welded detail (Fisher et al. 1998)

2.4.2 Nominal Stress Method

S-N curves are the basis of fatigue assessment by the application of the nominal-stress method. The S-N curve represents the remaining fatigue life of detail under investigation versus stress range, Figure 2.7. The logarithmic scale is used for both axes. The S-N curves are provided in design codes based on fatigue test data under constant amplitude loading. It is assumed that the structural detail experiences the infinite fatigue life if the stress range is under the Constant

Amplitude Fatigue Limit (CAFL). The dashed lines in Figure 2.7 show the CAFL corresponding to each detail category.

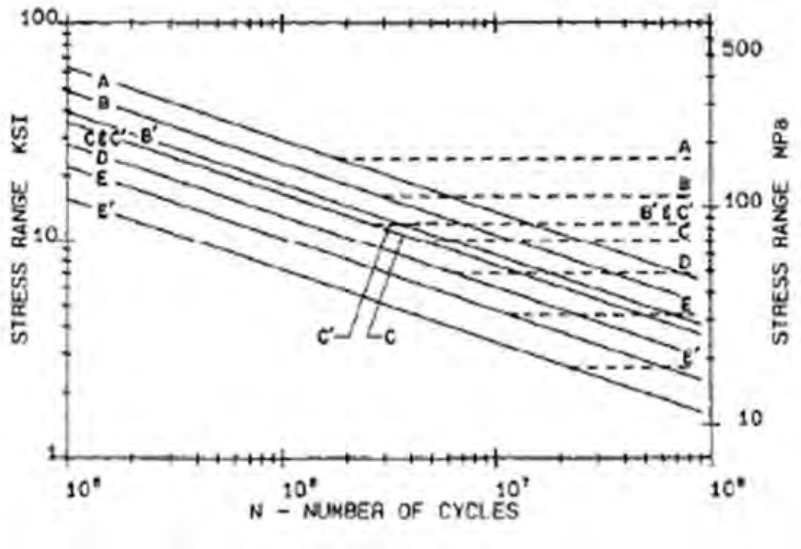

Figure 2.7: AASHTO S-N curve for different detail categories (Grubb et al. 2015)

The nominal-stress method is the most commonly used way to assess the fatigue life of steel structures. Stress range, the difference between the maximum and minimum stress, due to live load is calculated near the welded detail using simple analysis. The remaining fatigue life in terms of loading cycles is related to the calculated stress range by the following equations:

$$NS^m = A \tag{2.13}$$

$$\log N = -m \log S + \log A \tag{2.14}$$

where N is number of cycles, S is stress range, m is empirical material constants, and A is detail category constants. It should be noted that m is equal to the S-N curve slope, and A can be chosen by the corresponding detail category.

2.4.3 Hot-Spot Stress Method

The hot-spot stress method, also known as local-stress method, is similar to the nominal-stress fatigue assessment method in terms of comparing the stress ranges with the corresponding S-N curve. The stresses are calculated locally at the weld toe of the weldments. Stress concentration effects related to weld geometry are considered in the hot-spot method. The local-stress approach was initially developed for fatigue analysis of tubular joints of offshore structures (Marshall 2013). The hot-spot stress method is advantageous over the nominal-stress approach where the fatigue prone areas of a bridge structure with complex stress field, in-plane and out-of-plane stress combination, need to be investigated (Grubb et al. 2015).

There are two types of hot-spots related to weld geometry. As Figure 2.8 shows, Type “a” is located on the plate surface, and type “b” is located on the plate edge.

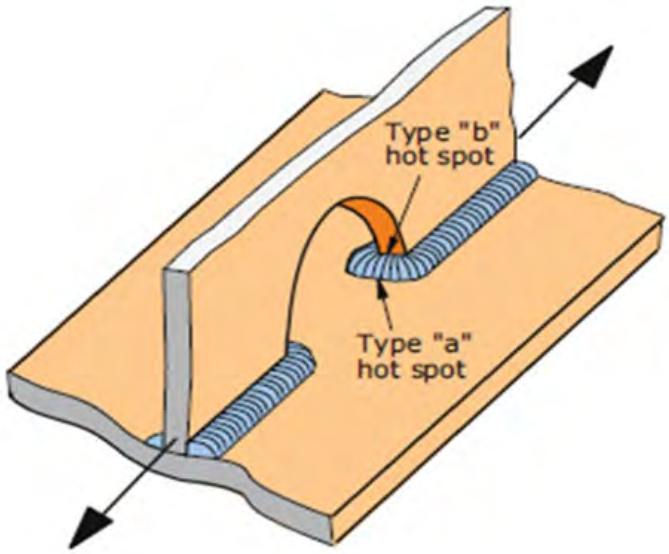

Figure 2.8: Types of hot-spots (Niemi et al. 2018)

The high stress gradient at hot-spots includes membrane stress, bending stress, and nonlinear stress peak due to weld notch. The nonlinear stress peak of the notch is not considered

in finding the hot-spot stress, and the S-N curves include the notch stress effect instead. Extrapolation techniques are used in order to separate the membrane and bending stresses from the notch stress. These methods are applicable to stresses defined by measurement or finite element analysis. The linearization methods also depend on types of hot-spots, type “a” or “b.”

Sensors or strain gages need to be installed at the reference points. The location of the reference points depends on the type of hot-spots. Type “b” hot-spot stress remains the same through the plate thickness, while type “a” hot-spot stress changes through the plate thickness. Figure 2.9 shows the stress distribution through the plate thickness for type “a” hot-spot. To calculate the type “a” hot-spot strain based on measured strain gages, equation 2.15 is used (Hobbacher 2016):

$$\varepsilon_{hs} = 1.68\varepsilon_A - 0.67\varepsilon_B \tag{2.15}$$

where ε_{hs} is hot-spot strain, ε_A is strain from the gage located at 0.9t, and ε_B is strain from the gage located at 1.4t.

The hot-spot stress can be defined by multiplying the elastic modulus of the welded plate, *E*, by the extrapolated hot-spot strain. In contrast to hot spot type “a”, stress distribution at the vicinity of weld toe related to type “b” hot spot is independent of plate thickness. Hence, extrapolation is done at three absolute distances from the weld toe. Type “b” hot-spot stress in terms of converted measured hot-spot strains into stresses is given by (Hobbacher 2016):

$$\sigma_{hs} = 3\sigma_{4mm} - 3\sigma_{8mm} + 3\sigma_{12mm} \tag{2.16}$$

where σ_{4mm}, σ_{8mm}, and σ_{12mm} are stresses corresponding to measured strains at 4, 8, and 12 millimeters from weld toe, respectively.

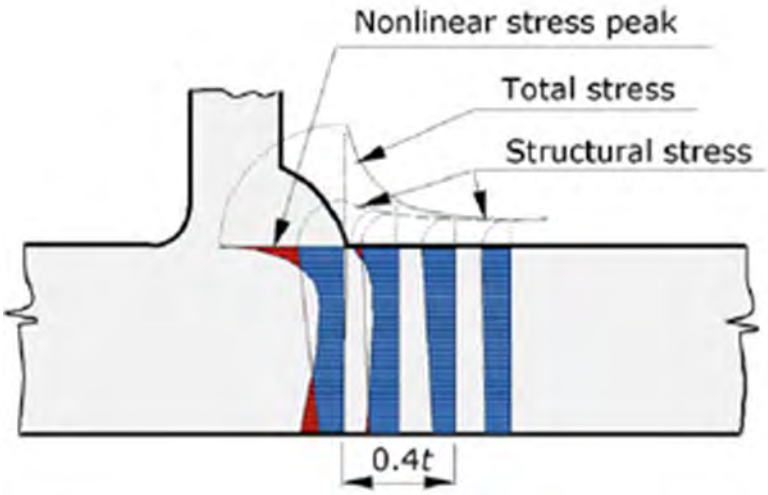

Figure 2.9: Stress distribution through the depth of the welded plate (Hobbacher 2016)

Hot-spot stresses can be determined by refined finite element analysis. However, the resulted hot-spot stresses are mesh dependent. Shell and solid elements are used for defining hot-spot stresses. The solid elements are more convenient in terms of modeling the weld geometry. Surface stress extrapolation is used for determining the hot-spot stresses at the weld toe. Reference points need to be defined to extrapolate the finite element stresses similar to the reference points in the measurement method. The reference point locations depends on the mesh density and type of hot-spot under investigation (Niemi et al. 2018). Figure 2.10 illustrates the reference point locations for fine and coarse mesh densities related to each kind of hot-spot “a” and ‘b”. The structural hot-spot stress can be calculated based on the following extrapolation equations (Hobbacher 2016).

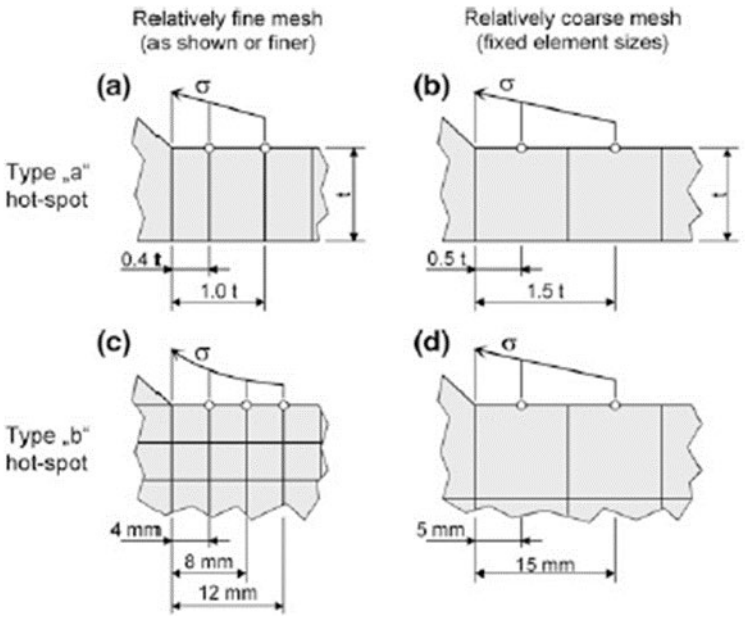

Figure 2.10: Reference point definition or surface stress extrapolation (Hobbacher 2016)

Type "a" hot spot:

Fine mesh including element sizes less than 0.4t with reference points located at 0.4t and 1.0t; the linear extrapolation is given by:

$$\sigma_{hs} = 1.67\sigma_{0.4t} - 0.67\sigma_{1.0t} \tag{2.17}$$

Fine mesh including element sizes less than 0.4t with reference points located at 0.4t, 0.9t, and 1.4t; the quadratic extrapolation is given by:

$$\sigma_{hs} = 2.52\sigma_{0.4t} - 2.24\sigma_{0.9t} + 0.72\sigma_{1.4t} \tag{2.18}$$

Coarse mesh including the higher-order elements having dimensions less than plate thickness, the extrapolation is as follows:

$$\sigma_{hs} = 1.50\sigma_{0.5t} - 0.5\sigma_{1.5t} \tag{2.19}$$

Type "b" hot spot:

Fine mesh including element sizes less than 4 millimeters with reference points located at 4, 8, and 12 millimeters, the extrapolation is given by:

$$\sigma_{hs} = 3\sigma_{4mm} - 3\sigma_{8mm} + 3\sigma_{12mm} \tag{2.20}$$

Coarse mesh including higher-order elements dimensioned less than 10 millimeters; the extrapolation is as follows:

$$\sigma_{hs} = 3\sigma_{5mm} - 0.53\sigma_{15mm} \tag{2.21}$$

2.4.4 Linear Elastic Fracture Mechanic Method (LEFM)

Fracture mechanics was first developed by Griffith (1921) to address the rupture of glass materials. The first structural engineering application of the method dates back to the 1940s for investigating the failure of ship hulls (Fisher et al. 1998). Linear Elastic Fracture Mechanics (LEFM) is a well-known method for predicting the fatigue crack growth in linear elastic materials with initial cracks. The length of these small cracks is between 0.05 millimeters and 1 millimeter (Martinsson 2002).

The stress intensity factor (SIF) defines the state of stress at the crack tip. There are analytical solutions to a limited number of crack configurations to find the stress intensity factor at the crack tip. In practical cases in which the analytical solution is not available the following expression can be used (Fisher et al. 1998):

$$K = WY\sigma\sqrt{\pi a} \tag{2.22}$$

where K is stress intensity factor, W is constant related to the plate and crack geometry, Y is constant related to crack tip stress field, and a is crack length.

Similar to S-N curves for the nominal-stress fatigue assessment approach, fatigue crack growth (*da/dN*) can be plotted against stress intensity range ($\Delta K = K_{max} - K_{min}$). As Figure 2.11 illustrates, three regions are corresponding to two asymptotes ΔK_{th} and K_C. The first region represents the threshold region in which crack propagation is negligibly slow. It is noteworthy that the ΔK_{th} does not represent the *da/dN* to be zero value, but it is corresponding to 4×10^{-10} m/cycle according to ASTM-E647 (Farahmand et al. 2012). The second region, Paris region, associated with the linear relationship between the crack growth rate and stress intensity range on a logarithmic scale. In the third region, crack growth occurs rapidly in order of 0.01 mm/cycle until reaching the critical value (Schijve 2001). K_C is defined by the stress intensity factor in which the materials fail. Different analytical approaches have been developed to determine the crack growth rate based on stress intensity ranges for the three regions of the crack propagation progress. Two methods are given in the following.

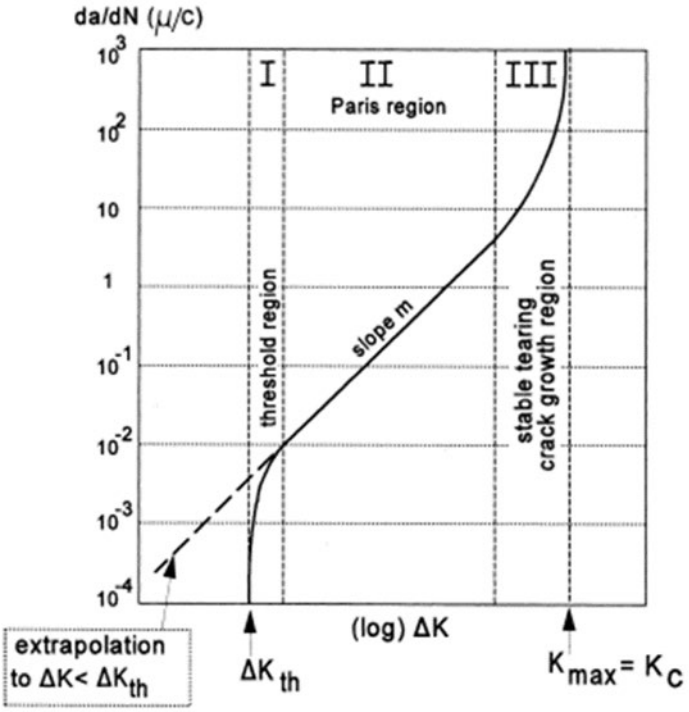

Figure 2.11: Crack growth phases corresponding to stress intensity range (Schijve 2001)

The most common expression to relate the da/dN and K was first developed by Paris (1961) and referred to as the Paris Law that is given as:

$$\frac{da}{dN} = C\Delta K^m \tag{2.23}$$

where the C and m constants can be found by experimental data. The m value ranges from 3 to 5, and C values are between 10^{-10} and 10^{-6} (Farahmand et al. 2012). The remaining fatigue life of the structure in terms of loading cycles can be determined by integrating the equation 2.23:

$$N = \frac{1}{C}\int_{a_i}^{a_f} \frac{1}{\Delta K^m} da \tag{2.24}$$

where a_i and a_f are initial and final crack lengths, respectively. As can be seen in Figure 2.11, the Paris Law is applicable to the second region where the variation of crack growth is linear with respect to stress intensity range. The asymptotic behavior of the first and third region are not included in the Paris expression. Forman et al. (1967) proposed the following expression that includes the crack propagation behavior in the third region:

$$\frac{da}{dN} = \frac{C\Delta K^m}{(1-R)(K_C - K_{\max})} \tag{2.25}$$

where R is the stress intensity ratio $\frac{K_{\min}}{K_{\max}}$.

2.4.5 Residual Stress Considerations

Residual stresses are unavoidable in built-up structural members that utilize welding as the connecting element of members. Hence, a brief review of residual stress patterns and how it is considered in fatigue analysis methods are given here. Generally, surface tensile residual stresses decrease fatigue performance by accelerating crack growth; however, compressive residual

stresses may have a positive effect due to reducing the fatigue crack tip stresses (Webster and Ezeilo 2001). The sources of residual stresses in horizontally curved steel girders are welding, flame-cutting, and heat curving. Differential shrinkage during welding and thermal cutting leads to tensile and compressive residual stresses in heated and unheated areas, respectively (Russo et al. 2016). The measured residual stresses for three different grades of steel are shown in the Figure 2.12. These stresses are related to residual stresses in the flanges of the welded plate girder parallel with the longitudinal axis of the beam. As can be seen in Figure 2.12, the highest magnitude of tensile residual stress occurs at the location of a web-to-flange fillet weld, and is equal to the yield stress.

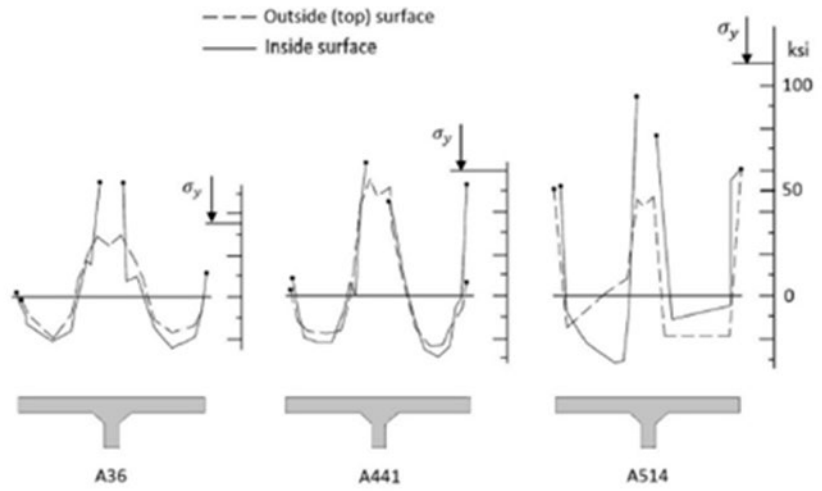

Figure 2.12: Measured residual stress patterns (Keating et al. 1990)

Numerous analytical models have been proposed to determine the residual stresses in welded structures (Barth and White 1998; Clarin 2004; Taras 2010; Kim 2010; Chacón et al. 2012). The two most commonly used residual stress models are based on The European Convention for Constructional Steelwork (ECCS 1976) and Culver and Nasir (Culver 1972). The ECCS model

approximates the residual stresses due to flame cutting and welding; the Culver and Nasir model considers the heat curving residual stress in addition to welding and cutting residual stresses.

The ECCS (1976) method considers the residual stress to be a constant tensile value equal to the plate yielding stress at the heat-affected zones due to flame cutting and welding. The other zones outside the tension zone are in compression and equilibrium with the resultant tensile forces. The tension block width at the flame-cut plate edge is given by:

$$C_f = \frac{1100\sqrt{t}}{F_y} \tag{2.26}$$

where t is plate thickness in millimeters, F_y is plate yield strength in MPa.

The tension width due to a single path of welding is as follows:

$$C_w = \frac{12000\, p\left(A_w\right)}{F_y\left(\sum t\right)} \tag{2.27}$$

where p is efficiency factor (0.9 for the submerged arc welding process), A_w is cross-sectional area of weld in (mm^2), F_y is plate yield strength (MPa), $\sum t$ is sum of the plate thicknesses meeting at the weld in mm.

The combining effect of flame cutting and welding is determined by:

$$C_{fw}^4 = C_f^4 + C_w^4 \tag{2.28}$$

Figure 2.13 illustrates the residual stress pattern calculated by the ECCS model for an I-shaped section. The governing factor in S-N nominal and local stress fatigue assessment methods is the stress range that remains unchanged by adding the residual stress to the minimum and maximum stresses. Hence, residual stresses are not modeled explicitly when the reference S-N approach is applied in fatigue analysis. The effect of residual stress is included in the detail

category fatigue resistance (Fisher et al. 1969). In another parametric study (Daniels and Batcheler 1979), the heat curving residual stress effect on fatigue strength of the curved steel girder was investigated. Two mechanisms were studied: mean stress effect and excessive web bowing under compressive residual stresses. It was concluded that "heat curving has no significant effect on the fatigue strength due to either mechanism." In addition, it was recommended that the entire stress range, including the compressive stress, should be considered if any stress reversal occurs. Residual stresses are effective if the LEFM fatigue assessment method is applied. Residual stresses increase the crack tip stress intensity factor and changes the stress intensity ratio, *R*.

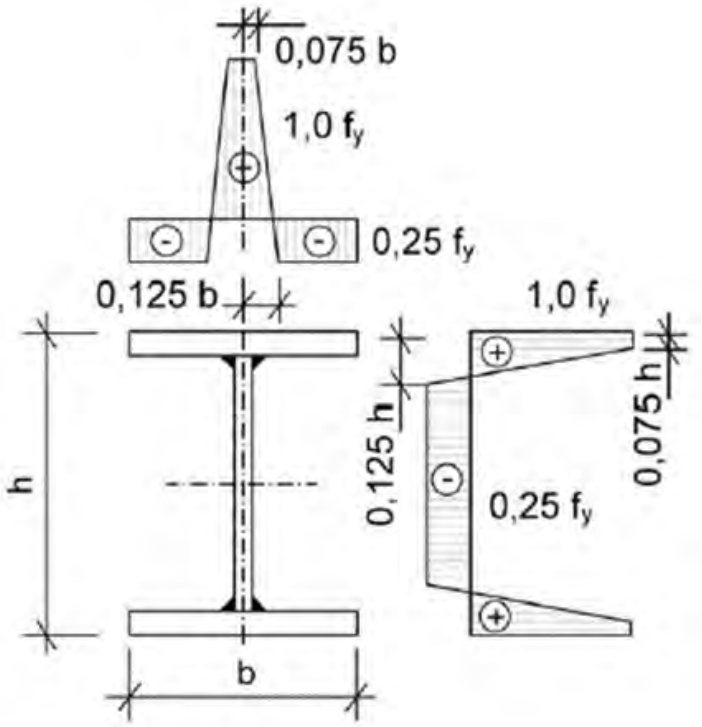

Figure 2.13: ECCS (1976) residual stress pattern distribution (Pasternak et al. 2015)

2.5 Fatigue Mechanisms in Steel Bridges

There are a variety of fatigue problems related to steel bridges. These issues can be categorized based on the critical region under investigation (web or flange), type of the bridge (straight or curved girders), type of loading in a single girder panel (shear or bending), and the mechanism in which fatigue cracks initiates. In this section, the two most common fatigue mechanisms are reviewed: distortion induced fatigue and web breathing in slender girder webs. Then experimental fatigue studies associated with curved girder systems are presented. Current design code limits addressing the reviewed fatigue mechanisms are lastly presented.

2.5.1 Distortion Induced Fatigue

Before the 1980s, it was common practice not to attach the transverse stiffeners and connection plates to the tension flange to prevent brittle fatigue in the welded flange region. However, another fatigue problem appeared in the web-gap region between the short cut transverse stiffener and tension flange. In multi-girder steel bridges, lateral deflection of adjacent girders leads to rotation of the connection plate and distortion of a relatively flexible web gap region. The out-of-plane distortion of the web generates large stress concentrations at the toe of the transverse stiffener and causes fatigue cracking. This phenomenon is referred to as distortion-induced fatigue and accounts for the majority of fatigue cracks in bridges across the United States (Fisher et al. 1998). Figure 2.14 illustrates the distortion-induced fatigue mechanism. There are several critical regions in the bridge where the distortion-induced fatigue is likely to occur. In a case study presented by Khalil et al. (1998), it was found that eight out of nine fatigue cracks occurred in the negative bending moment regions. In contrast, another research project suggested that differential deflections and out-of-plane bending moments are maximum in positive bending moment regions

(Roddis and Zhao 2001). Figures 2.15 and 2.16 show the distortion induced fatigue cracks in the lower and upper end of the connection plate, respectively.

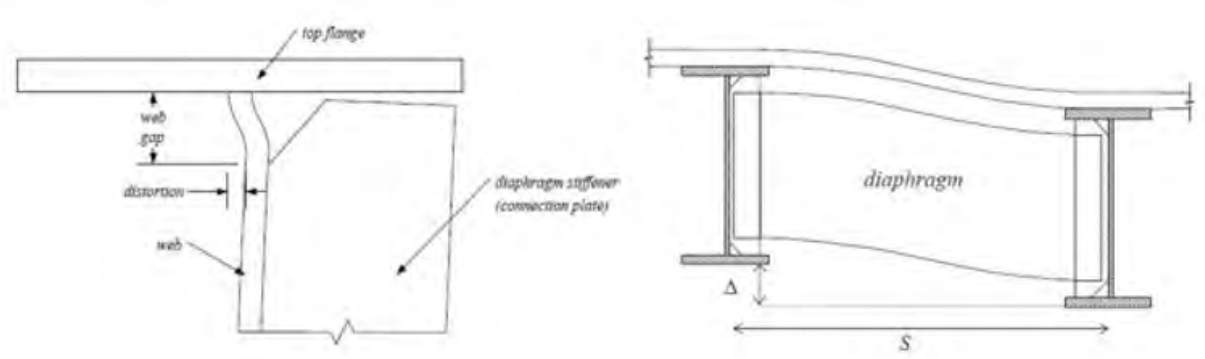

Figure 2.14: Distortion induced fatigue (Li and Schultz 2005)

Figure 2.15: Fatigue cracks at the lower end of the vertical connection plate (Bowman et al. 2012)

Figure 2.16: Fatigue cracks at the upper end of the connection plate (Bowman et al. 2012)

2.5.2 Web Breathing

When slender plate girders are designed to allow post-buckling resistance, large out-of-plane deformations can be induced under the in-plane loading. The repeated web buckling deformation known as “web breathing” leads to fatigue cracks under cyclic loading (Günther and Kuhlmann 2004). It should be noted that inevitable initial imperfections and residual stresses cause out-of-plane deformations under loads that are less than theoretical buckling loads (Crocetti 2003). Figure 2.17 illustrates the breathing mechanism in which buckling deformations lead to high secondary-bending stresses that causes fatigue cracks in the web.

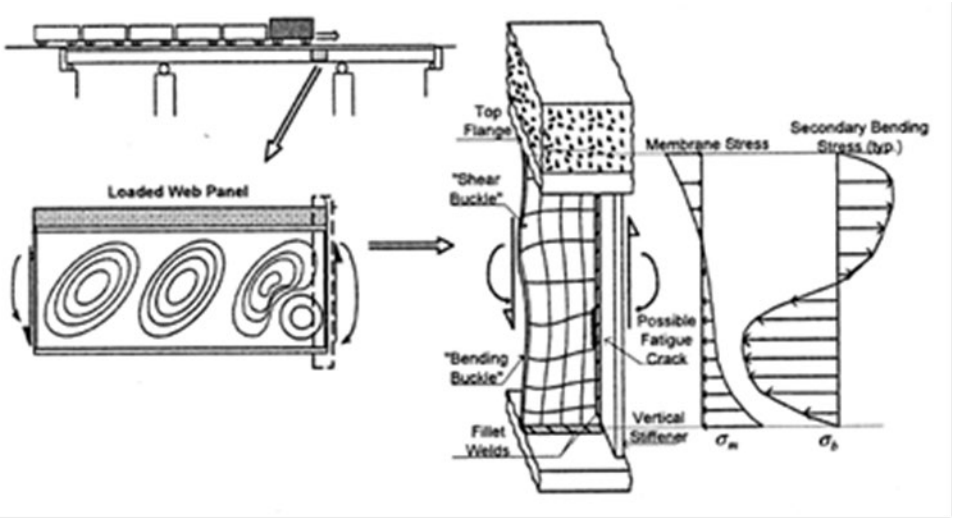

Figure 2.17: Web breathing effect for a slender composite bridge girder (Crocetti 2001)

Web breathing fatigue was investigated through analytical and numerical (FEM) studies to quantify the parameters affecting the web boundary stresses (Maeda and Okura 1982; Okura et al. 1993; Remadi et al. 1995; Davies and Roberts 1996; Duchene and Maquoi 1998; Spiegelhalder 2000). It was indicated that the main parameters that affect geometric stresses resulting from web breathing are panel aspect ratio and slenderness ratio, stiffness of boundary members, and shape and magnitude of initial out-of-plane deflections (geometric imperfections).

Various experimental tests on slender girders with web breathing indicated that the fatigue cracks could be classified based on the type of loading and place of origin (Yen and Mueller 1966; Toprac and Natarajan 1971; Spiegelhalder 2000; Crocetti 2001) as illustrated in Figure 2.18. The characteristics of each crack type are as follows:

- **Type 1** occurs at the toe of the weld connecting the compression flange to the web (Okura et al. 1993). Repeated out-of-plane deformations of web caused by secondary bending stresses (web breathing) under in-plane bending results in the fatigue crack initiation (Crocetti 2001). The initiated crack at the weld toe propagates with a relatively slow rate

at the web side of the girder under mixed modes 1 and 3 related to tension and tearing conditions, respectively (Roberts and Davies 2002).

- **Type 2** occurs at the weld toe on the web side of the transverse stiffener connection to the web (Crocetti 2001). Tensile membrane bending stresses below the neutral axis results in the propagation of the crack (under tension mode) into the tension flange and may lead to failure (Roberts and Davies 2002). It propagates at a faster rate compared to type 1 crack due to the fact that the tensile membrane stresses are more significant than the secondary bending stresses (Crocetti 2001).
- **Type 3** is observed at the weld toe connecting the web to the tension flange. Fillet weld discontinuities are the source of this crack. It is not associated with breathing.
- **Type 4** occurs when a panel is under shear loading, this type of crack happens at the corners weld toes where the diagonal tension field buckles are anchored (Okura et al. 1993). It propagates in the direction of weld toes and eventually through the web where high local shear deformations and plate bending stresses exist (Crocetti 2001). The breathing nature of the crack follows the crack type 1 propagation rate and mode combinations (Roberts and Davies 2002).
- **Type 5 and 6** cracks occur at the weld connecting the web to load-carrying transverse stiffener near the neutral axis of the girder (Roberts and Davies 2002). A part of the applied concentrated load is carried by the web region welded to the transverse stiffener that results in reduced web flexural stiffness and, consequently, large out-of-plane web deformations (Crocetti 2001). This mechanism causes fatigue crack propagation along the web to stiffener weld toe and through the web.

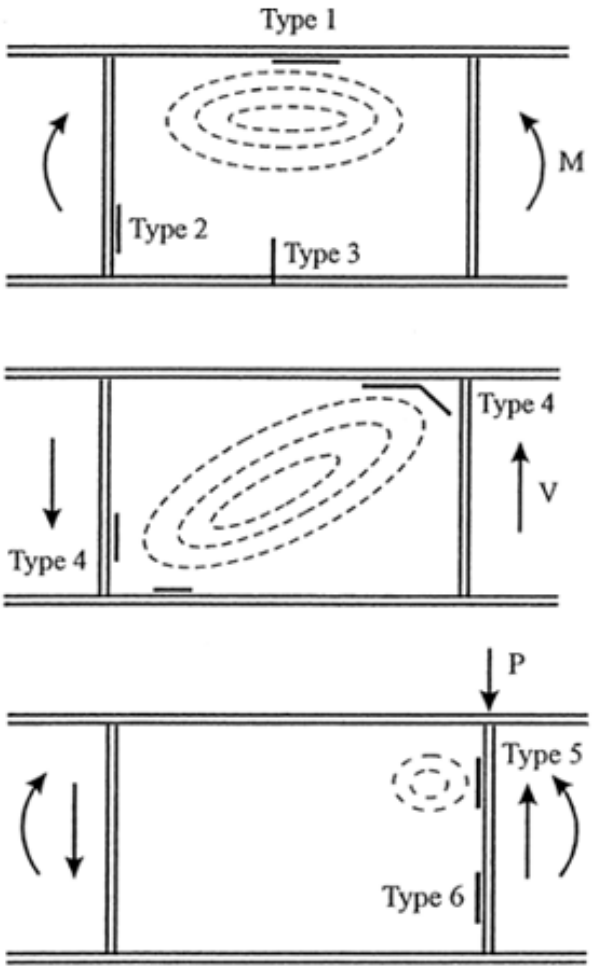

Figure 2.18: Fatigue cracks locations in slender webs corresponding to loading conditions (Roberts and Davies 2002)

2.5.3 Curved Girder Fatigue Research

Only a few studies have specifically focused on the fatigue behavior of curved steel girders; the most prominent are Daniels and Herbein (1980) at Lehigh University and Nakai et al. (1990) in Japan. In 1973, a multiphase project titled "Fatigue of Curved Steel Bridge Elements" was funded by the Federal Highway Administration (FHWA) to investigate the fatigue problems related to horizontally curved steel bridges. Both experimental approaches are discussed in the following, but the analytical methods are covered in subsequent sections of this report.

"Fatigue of Curved Steel Bridge Elements" project phases were: 1) analysis and design of curved I-girder and box girders; 2) special studies such as residual stress, heat curving, and diaphragm spacing; 3) fatigue test experiments; 4) investigation of ultimate strength of the test assemblies; and 5) final design recommendations considering the previous phases findings (Daniels and Herbein 1980).

Five weld detail categories were considered, and five twin-girder assemblies were fabricated to investigate each detail type fatigue behavior. As can be seen in Figure 2.19, the assemblies consisted of two girders connected by five X-type diaphragms with the 120 feet centerline radius of curvature for all of them. Two loading conditions with 2 million constant amplitude cycles were applied at the assemblies 1) loading at quarter points of each girder web and 2) loading at the middle space between the quarter points of the girders. Assemblies were monitored during loading cycles for two main fatigue cracking reasons: 1) primary cracking because of in-plane bending and torsion and 2) secondary fatigue cracks as the result of out-of-plane web plate bending. Geometric specifications associated with each assembly are given in the Table 2.2. Since the test setup was not designed specifically for slender-web curved girders, only two girders having web slenderness ratios of 192 and 186 were considered. Consequently, no fatigue cracking was observed at the web boundaries due to web out-of-plane displacements, referred to as the oil-canning effect at the time. It was concluded that the web-to-flange lateral deflections of the curved girders reduces the relative web boundaries stresses.

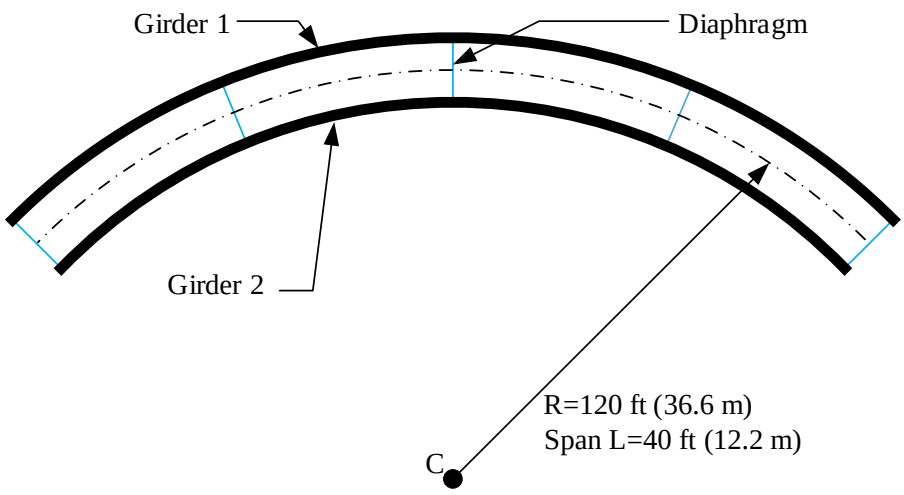

Figure 2.19: Girder assembly (plan view) of the Daniels and Herbein (1980) study

Table 2.2: Summary of cross section dimensions of the Daniels and Herbein (1980) study

Assembly	Girder	Flange Width (inch)	Flange Thickness (inch)	Web Depth (inch)	Web Thickness (inch)	Slenderness Ratio
1	1	12	1	54	3/8	144
	2	12	1	54	9/32	192
2	1	8	1/2	58	3/8	155
	2	10	3/4	58	5/16	186
3	1	8	1/2	58	3/8	155
	2	10	3/4	58	3/8	155
4	1	8	1/2	52	3/8	139
	2	12	1	52	3/8	139
5	1	8	1/2	52	3/8	139
	2	12	1	52	3/8	139

Nakai et al. (1990) conducted an experimental study to investigate the fatigue strength of fillet welds at the web boundaries of horizontally curved girders. Five single simply-supported

curved girders having web slenderness ratio of 144 were loaded under pure bending. The flange dimensions were different for each girder. The scaled testing girders had the length and radius of curvature of 11 ft (3.3 m) and 23 ft (7.0 m), respectively. Lateral restraints were enforced at the corners of the middle panel as illustrated in Figure 2.20. Fatigue cracks were observed under the load points due to stress concentrations, but no cracking occurred at the web panel boundaries.

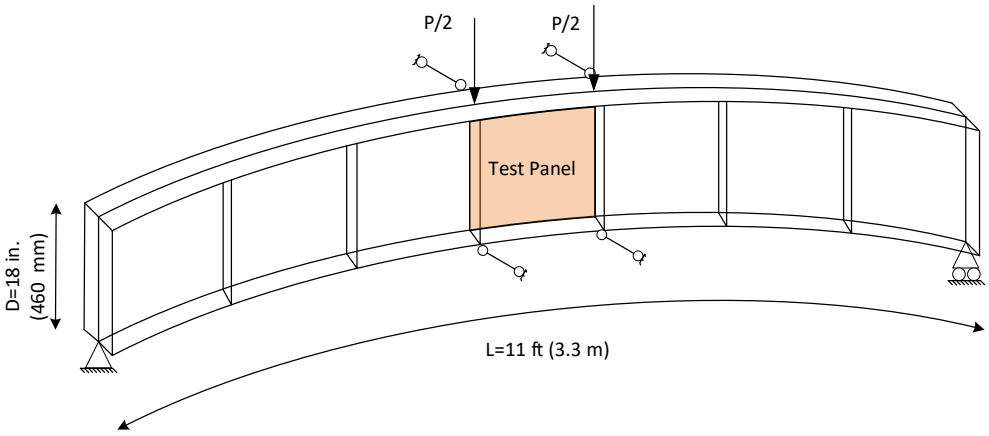

Figure 2.20: Test girder configuration of Nakai et al. (1990)

Further research on the fatigue performance of slender web curved girders is needed due to the limitations and drawbacks involved in the Lehigh and Nakai studies, which did not accurately replicate the stress and web breathing conditions of real multi-girder curved bridge systems. Only one radius of curvature was tested, and the behavior of the equivalent straight testing configuration and varying radii of curvature was not examined. Provided that the breathing effect occurs in highly slender web panels, the effect of curvature on the behavior of the test girders with slenderness close to 150 is controlled by the flanges rather than the web. Although the girder assemblies of Lehigh University research considers the effect of the diaphragm, the two-girder configuration is not sufficient to simulate the deflections and rotations that occur in real curved

bridges. In addition, the concrete deck role on the total rotations/deflections and stress distribution was neglected.

2.5.4 Current Design Limits

The AASHTO LRFD Bridge Design Specifications (2020) classifies fatigue analysis into two categories: load-induced and distortion-induced fatigue. Fatigue cracking at the web panel boundaries under cyclic loads is not explicitly addressed. Shear buckling at end panels is controlled at the strength limit state, and interior web panel shear force must be limited by equation 2.29 for fatigue:

$$V_u \leq V_{cr} \tag{2.29}$$

where V_u is shear in the web at the section under consideration due to the unfactored permanent load plus the factored fatigue load (kip), and V_{cr} is shear-buckling resistance. It is assumed that the member sustains infinite fatigue life related to elastic flexing of the web. The web bending stresses are also limited to the web bend-buckling resistance at the construction and strength limit states. In general, AASHTO (2020) preclude shear and bend buckling for flexural members at the construction and strength limit states, therefore the stress ranges at the web boundaries due to excessive web deformations are limited.

The distortion-induced fatigue section of the bridge specifications addresses web fatigue at the connection plate locations, where the differential deflection of the adjacent girders causes fatigue cracks at the web. As prior discussed, it was common practice through the 1980's to cut the end of the web stiffeners close to the flanges. Consequently, cracks occurred at the flexible web gap where the cross-frames and floor beams were attached. AASHTO (2020) now requires web stiffeners to be attached to the flanges at the diaphragms connection plates to minimize the potential for large stress concentrations and fatigue issues.

Eurocode 3: Part 2 (2006) considers a specific fatigue slenderness limit for webs of highway bridges:

$$\frac{b}{t} \le 30 + 4L \le 300 \tag{2.30}$$

where b is the web height and t is the web thickness, and L is the span length in meters and must be more than 20 meters. If the slenderness limit is not met by design, then the panel stresses are controlled by:

$$\sqrt{\left(\frac{\sigma_x}{k_\sigma \sigma_E}\right)^2 + \left(\frac{1.1\tau_x}{k_\tau \sigma_E}\right)^2} \le 1.1 \tag{2.31}$$

where σ_x and τ_x are normal and shear stresses, respectively, k_σ and k_τ are linear elastic buckling coefficients. $\sigma_E = 190000\left(\frac{t}{b_p}\right)^2$ where t is the web thickness and b_p is the smaller of the web panel side. It should be noted that the limitations of AASHTO and Eurocode specifications are derived for slender webs of straight girders, and none of them provide guidance specific to curved steel girders.

CHAPTER 3
EVALUATION OF FATIGUE ANALYSIS METHODS

3.1 Web Behavior of Curved Composite Steel Bridges

Curved steel girders experience large deflection and rotations during construction and service that can intensify the web breathing effect. In addition, the curvature-induced lateral forces pushing and pulling slender curved webs develop mechanisms that can lead to critical web boundary stresses that do not typically occur in straight bridges. This chapter defines the slender web behavior of composite curved steel bridges essential for the fatigue limit state. It focuses on capturing the distortion-induced web stresses from the construction stage through service using 3D finite element analyses. A novel technique was applied to simulate the non-composite and composite stages to quantify the continuous web stress development due to geometric nonlinearities. Three different web panels under high shear, high moment, and high shear-moment combination were studied. The stress ranges due to the AASHTO fatigue truck are presented for composite bridges with varying curvature radii. The mechanism involved in curved bridges is defined and the stress magnitudes are compared to that of equivalent straight bridges to understand the role of curvature in intensifying the critical fatigue stress ranges.

3.1.1 Modeling Methodology

3.1.1.1 Superstructure Configuration

The bridge superstructure used in the parametric studies, including the geometry and section properties, were taken from the National Cooperative Highway Research Program

(NCHRP) Project 12-52 (Kulicki et al. 2005). The NCHRP bridge analyses and configuration is included in the *Steel Bridge Design Handbook* by FHWA titled "Design Example 3: Three-Span Continuous Horizontally Curved Composite Steel I-Girder Bridge (Rivera and Chavel 2012)." The bridge cross-section is defined in Figure 3.1.

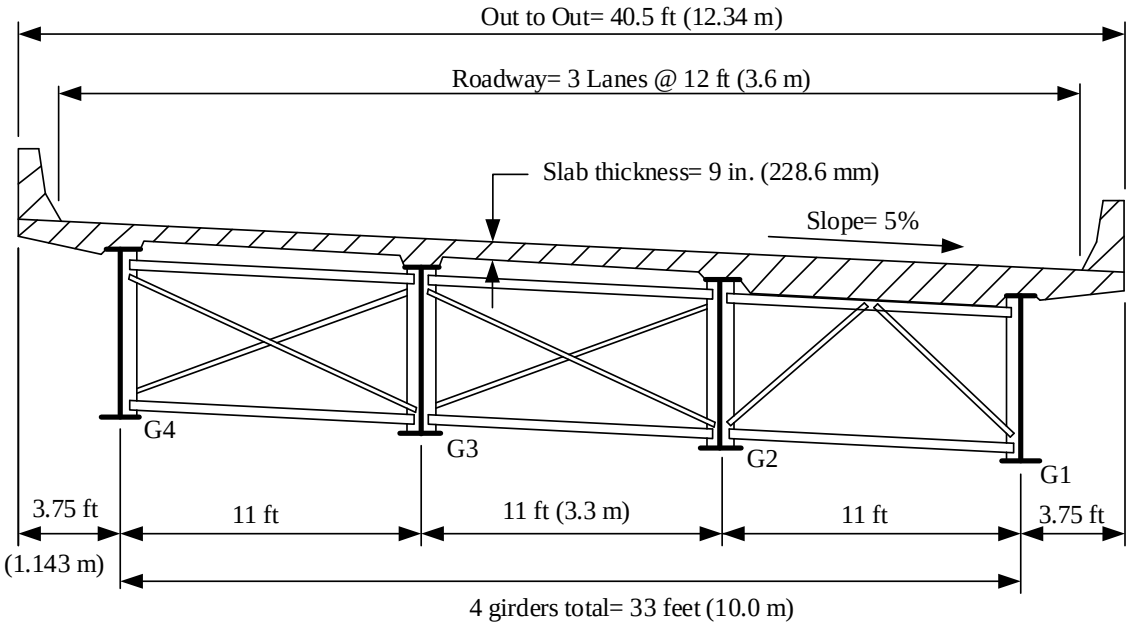

Figure 3.1: The NCHRP Project 12-52 bridge cross-section

The bridge has three spans of 160, 210 and 160 ft (48.8, 64.0, 48.8 m) and a radius of curvature of 700 ft (213.4 m) measured along the centerline of the bridge. There are four girders spaced at 11 ft (3.3 m) along the spans. The web height is 84 inches (2134 mm), and the web slenderness is 135 and 150 for the regions adjacent and far from the supports, respectively. There are no transverse stiffeners between the cross frames connection plates. The cross frame spacing is 20 ft (6.1 m), measured along the bridge centerline. The concrete deck has a structural thickness equal to 9 inches (228.6 mm). The elastic modulus for steel members and concrete deck are 29,000 ksi (200 Gpa) and 3,600 ksi (25 Gpa), respectively.

The goal of the full-bridge simulation is to define the stress formation in fatigue prone areas of the web boundaries. Hence, assumptions and changes to the original model were adopted for simplicity and comparison in the finite element modeling of the bridges:

- The slab deck slope was neglected.
- The web thickness along the spans was uniform.
- The top and bottom flange dimensions were taken as a constant value of 21 inches (533.4 mm) by 1.5 inches (38.1 mm) for width and thickness, respectively, for all girders and spans (flange section transitions were neglected).
- "X" cross-frame configuration was used for all of the intermediate and support locations.
- The focus of the present study is on the outer girder, girder number 4. Hence, the outer girder length was equal for all bridges with the varying radii of curvatures.

The live load effect was investigated on the composite steel and concrete deck bridge having initial web imperfections. It is common to assume buckling shape modes or sinusoidal functions for web distortions and scale them by the code limits. While this method is applicable for straight or non-slender curved girder assemblies, it ignores the construction effects on slender web configurations of curved systems. Consequently, the web geometry might not be simulated correctly at the live load stage. Curved steel girder webs experience considerable rotation and distortion during construction due to the steel and concrete dead loads. The initial web imperfection due to fabrication could be reduced by the application of high-performance steel and new fabrication technologies. However, the final slender curved web geometry could be highly rotated and distorted under live load and should not be neglected.

The present modeling procedure aims to consider all of the deflection amplifications effects due to web rotations and distortions during construction, as well as to examine the deformed web

behavior under the live load for fatigue investigation purposes. Hence, geometric nonlinear analysis was used in all steps (Davies and Roberts 1996; Issa-El-Khoury et al. 2014).

The finite element analysis studies were conducted using the commercial FEM software ABAQUS (2019). Figure 3.2 shows the global model and corresponding mesh density and element definition for the bridge assembly. The outer girder *G4* experiences larger deflections and web distortions due to higher major axis and lateral bending moment compared to the interior girders. Hence, girder *G4* was selected as the critical girder in the parametric studies. Higher resolution mesh and elements were used only for the *G4* to save computational cost. The green and red colors represent the shell and beam elements, respectively. All of the *G4* girder parts, including the web, cross frame connection stiffeners, and flanges, were shell elements. *G1*, *G2*, and *G3* girders were modeled with shell elements for the web, and beam elements for the connection stiffeners and flanges. Cross frame members were modeled with beam elements. The S4 shell element, a 4-node quadrilateral shell element, was used for the *G4* web, while the S4R shell element, a 4-node quadrilateral shell element with reduced integration, was used for the other three girders web and concrete deck. A coarse mesh was used for *G1*, *G2*, and *G3* because only their stiffness is essential to represent the response of the whole bridge assembly, and the *G4* behavior was the focus of the investigation. All the beam elements for the cross frames, connection stiffeners, and flanges were modeled with the B31 element, a 2-node beam element, as shown with red color in Figure 3.2. The shell element reference plane used for the concrete deck is located on top of the flange nodes, and the "OFFSET" command was applied to offset the distance between the centroid of the shell element surface and the reference plane.

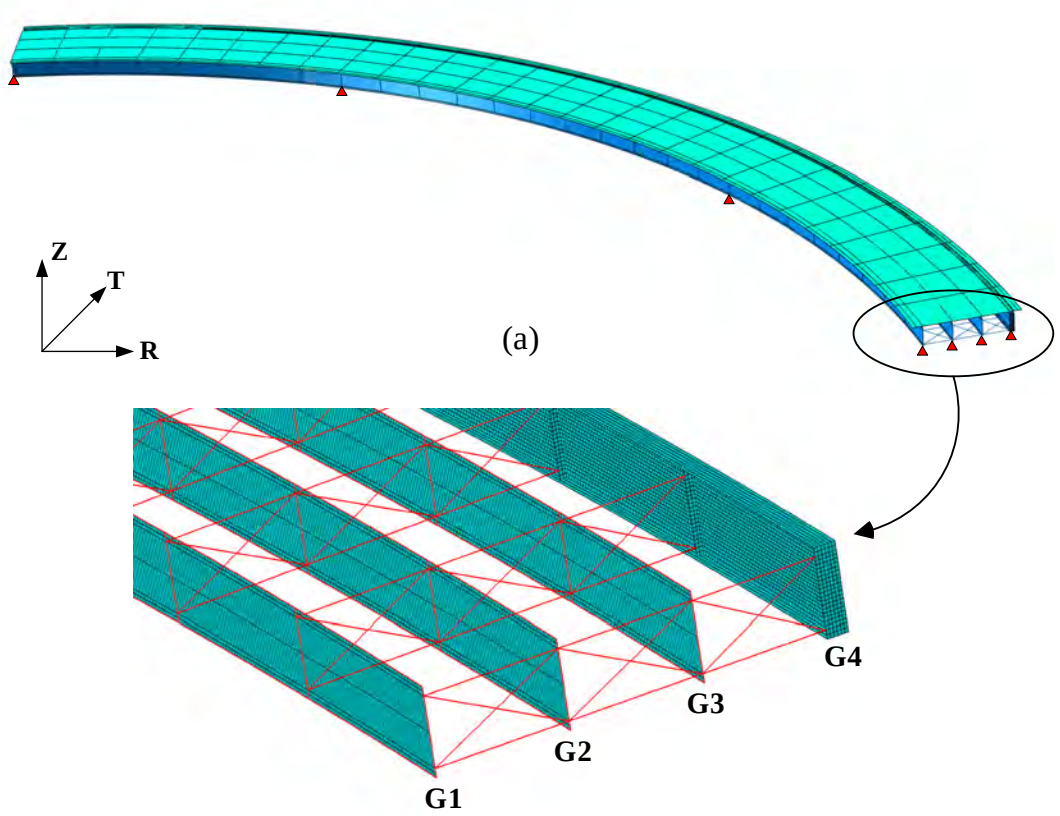

Figure 3.2: Bridge model (a) global assembly (b) girder numbering and mesh

3.1.1.2 Non-composite and Composite Modeling

A two-level multi-step analysis modeling technique (referred to as analysis 1 and analysis 2) was implemented to simulate the non-composite and composite action during the construction and live load phases, respectively. This method updates the constraints between the girders flange nodes degree of freedom (dofs) and shared bridge deck nodes dofs to add and remove the concrete deck stiffness incorporation through steps.

In analysis 1, the deck shell elements were tied to the girder's top flange nodes. The deck shell elements stiffness was set to a negligible value, $E_{concrete}/1000$, thus only having enough rigidity to carry the concrete weight without excessive deflection. The steel and concrete weights

were applied as gravity loads. Analysis 1 resulted in compatibility between the deformed deck geometry and the girder assembly deformations under the total dead load in the construction step. Basically, the output deck mesh resembles the stay-in-place forms used to support the wet concrete weight.

In analysis 2, two bridge decks were introduced in the assembly to simulate the non-composite step and composite step. As Figure 3.3 illustrates, the green deck, referred to as the null-slab, has perfect geometry compatible with undeformed girders assembly. The null-slab stiffness is a negligible magnitude so that it provides enough rigidity to transfer the weight of the concrete to the girders without excessive deflection. The imported deformed mesh from analysis 1 is shown by the red color in Figure 3.3 with compatible geometry along with the deformed girders assembly at the end of the non-composite construction step. Realistic concrete deck stiffness was assigned to the imported mesh that transfers the fatigue truck load to the girders assembly in the composite step.

A linear "multi-point constraint" relationship between the shared nodes of girders top flange, null-slab, and concrete-deck was defined by applying the ABAQUS "equation" command:

$$\sum_{i=1}^{6}\left\{\left(dofs\right)^{i}_{Flange}-\left(dofs\right)^{i}_{null-slab}-\left(dofs\right)^{i}_{cnct.-Deck}\right\}=0 \tag{3.1}$$

where dof^{i} represents the i^{th} translation or rotation of the corresponding node.

Figure 3.3 illustrates the boundary conditions of the null-slab and concrete deck that simulates the non-composite and composite action through the application of equation 3.1. At the beginning of step 1, all of the concrete-deck nodes are fixed, and the null-slab nodes are free. This condition sets the $(dof)^{i}_{cnct.-Deck}$ term in equation 3.1 equal to zero; therefore the top flange nodes only have negligible null-slab stiffness in the non-composite step. At the end of step 1, after all of the deflection and rotations under total dead load take place, the null-slab, concrete-deck, and top

flange nodes are in the same position. At the beginning of step 2, the composite step, the null-slab nodes boundary conditions are assigned to be fixed at their current position, and the concrete-deck nodes are released. Consequently, the top flange nodes get the concrete-deck stiffness incorporation in the composite step when the fatigue truck is applied. In fact, all the translational and rotational dofs of the flange nodes and concrete deck are tied together at this stage to simulate the full composite action. The same position of the concrete-deck and top flange nodes at the end the composite step is also shown in Figure 3.3. Geometric nonlinearities were included in both analyses 1 and 2.

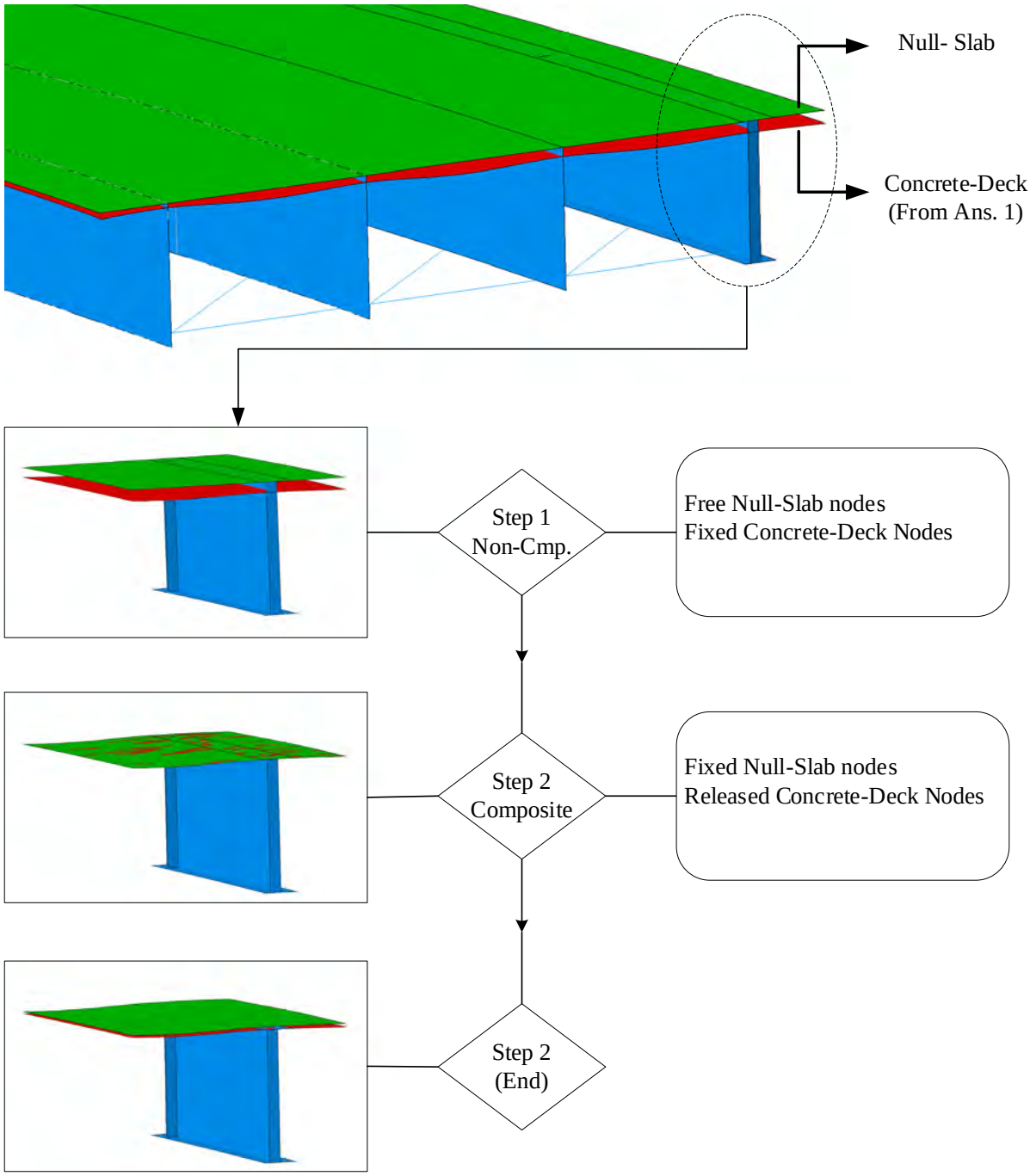

Figure 3.3: Analysis 2 bridge assembly, deformed configurations, and boundary conditions through steps

3.1.1.3 Validation

The NCHRP Project 12-52 (Kulicki et al. 2005) bridge superstructure calculations were based on a three-dimensional finite element program specific to the design of horizontally curved steel bridges. Some benchmark positions were used for comparison purposes between the reported values and those resulting from the present ABAQUS simulations. All of the flanges, stiffeners and cross-frames were modeled using beam elements in the validation simulation to consider the flange section transitions. Two locations along the exterior girder were considered: A) middle of span 1, and B) interior support (Figure 3.4). The top and bottom flange lateral bending moments under the steel dead load are given in Table 3.1. All the simulated values are within 10% of the reported values, which is reasonable given that the values reported in NCHRP Project 12-52 are whole numbers. Furthermore, the use of the ABAQUS software for steel bridge research and the approach used herein have been used and validated by many other researchers, for example for strength (Phoawanich 2001; Hartmann 2005; Jung and White 2006; Subramanian and White 2017) and stability (Issa-El-Khoury et al. 2014, 2016).

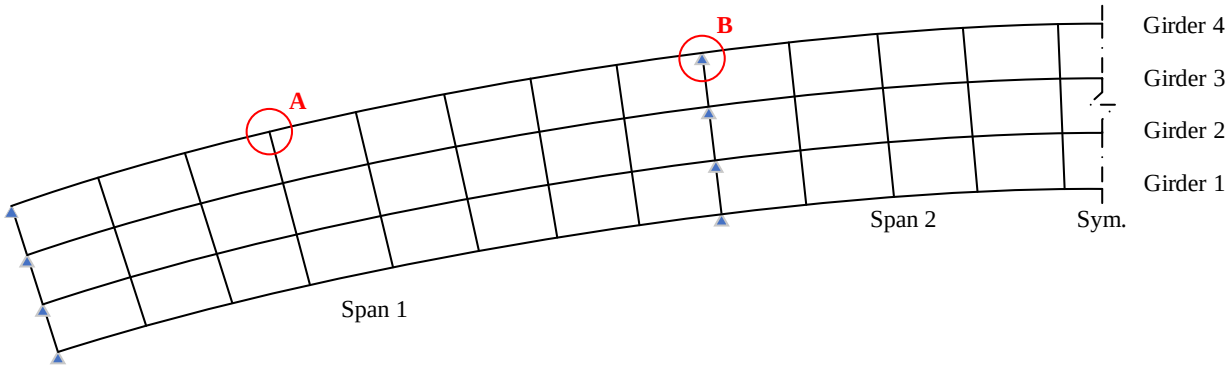

Figure 3.4: Selected locations for validation comparison: A) Mid-span 1; B) Interior support

Table 3.1: Girder 4 flange lateral bending moment under steel dead load

	Reported (kip-ft)	Simulated (kip-ft)
Interior support	8	8.50
	-7	-7.74
Mid-span 1	-4	-4.43
	4	4.41

3.1.2 Fatigue Analysis

3.1.2.1 Web Panel Regions

Three fatigue-prone regions at the web panel boundaries were considered: (1) web-to-bottom flange connection located at mid-span 2, and web-to-bearing stiffener connection located at the (3) interior and (2) exterior support. Figure 3.5 illustrates the global position of panels and the critical web boundary region within each panel. Maximum vertical bending and lateral bending occur at the mid panel of span 2, between the interior supports, panel 1. The bottom flange undergoes larger rotation than the top flange, which is restrained by the concrete deck. Web normal stress range in the transverse direction, normal to the bottom flange, was investigated for panel 1. Panels adjacent to the exterior and interior supports, panel 2 and panel 3, are related to the dominantly shear and combined shear and moment loading conditions, respectively. Web normal stress ranges in the longitudinal direction, normal to the bearing stiffeners, at the web-to-bearing stiffener connection of these panels, were analyzed. It should be noted that curvature may affect the fatigue performance of the web panel boundaries detail category. However, it was assumed

that the curvature influence on fatigue resistance is minimal (Daniels and Herbein 1980), and the same welding condition is used for all cases.

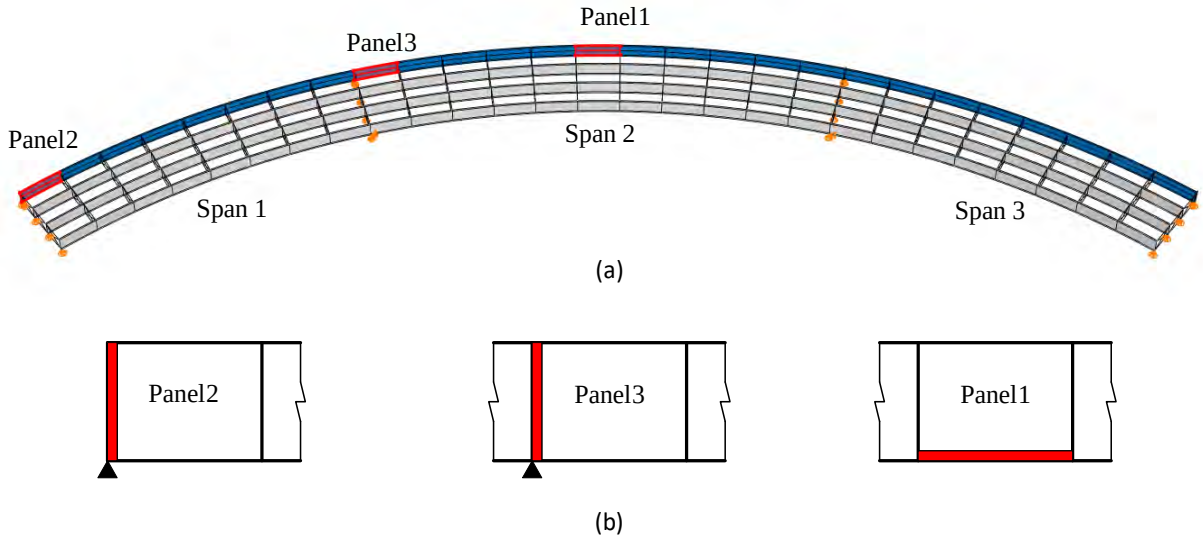

Figure 3.5: Fatigue details categories (a) global panel position (b) critical panel region

Various radii of curvature was considered for the parametric bridge models to study the curvature effect on stress range development in critical panels. In practical bridge design considerations, curvature radius of 300 ft to 500 ft represents the extreme conditions and radius of 700 ft to 1200 ft is the moderate curvature. The curvature has diminishing effects for radius of over 1500 ft. Two web slenderness D/t_w values of 150 and 300, were selected to compare the secondary bending stresses due to the geometric nonlinearities in slender webs. In addition, web panel aspect ratio d_0/D was changed from 3 to 1.5 for the panels close to supports. All parameters used in the simulations are given in Table 3.2.

Table 3.2: Variables used in the parametric studies

	Web slenderness	Panel aspect ratio	Radius of curvature
Panel Position	D/t_w	d_0/D	R ft (m)
Bending, P1	150, 300	3	300 (91.4), 400 (121.9), 550 (167.6), 700 (213.4), 1000 (304.8), 1500 (457.2), ∞
Shear, P2	150, 300	1.5, 3	300 (91.4) ,400 (121.9), 550 (167.6), 700 (213.4), 1000 (304.8), 1500 (457.2), ∞
Bend/shear, P3	150, 300	1.5, 3	300 (91.4), 400 (121.9), 550 (167.6), 700 (213.4), 1000 (304.8), 1500 (457.2), ∞

The nominal stress range method was applied to evaluate and compare the stress ranges resulting from the AASHTO fatigue truck loading. It should be noted that there is high uncertainty in the fatigue loading of real-life bridges. The AASHTO fatigue truck loading was used in the present study because it is recommended by AASHTO LRFD (2020) bridge design specifications. The web normal stress perpendicular to the weld direction, web boundary members, was considered for each fatigue detail category. Various loading positions were considered depending on the fatigue details under investigation.

3.1.2.2 Fatigue Truck Loading Scheme

As Figure 3.6 illustrates, the fatigue truck was positioned at the mid-span and end-span to produce the maximum positive and negative bending effect on panel 1, respectively. The total stress range was calculated by summing up the tensile and compressive stress ranges. The compressive stress ranges were taken into account only if the total stress, due to dead load and fatigue truck load, were in tension.

The fatigue truck was located close to the support to induce the maximum shear effect for the web-to-bearing stiffener connection. The rear fatigue truck axle was not located on top of the support to prevent stress concentration at the top of the bearing stiffener. The fatigue truck location for the interior and exterior support is shown in Figure 3.7. Only the tensile stress range was considered for the web-to-bearing stiffener connection.

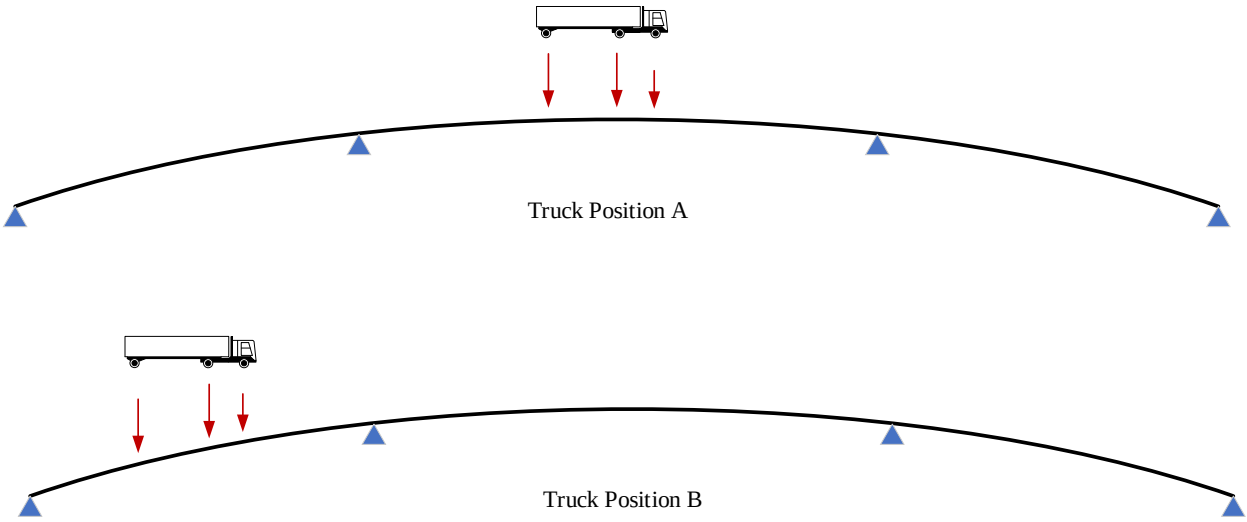

Figure 3.6: Schematic loading positions for web-to-bottom flange connection of panel 1

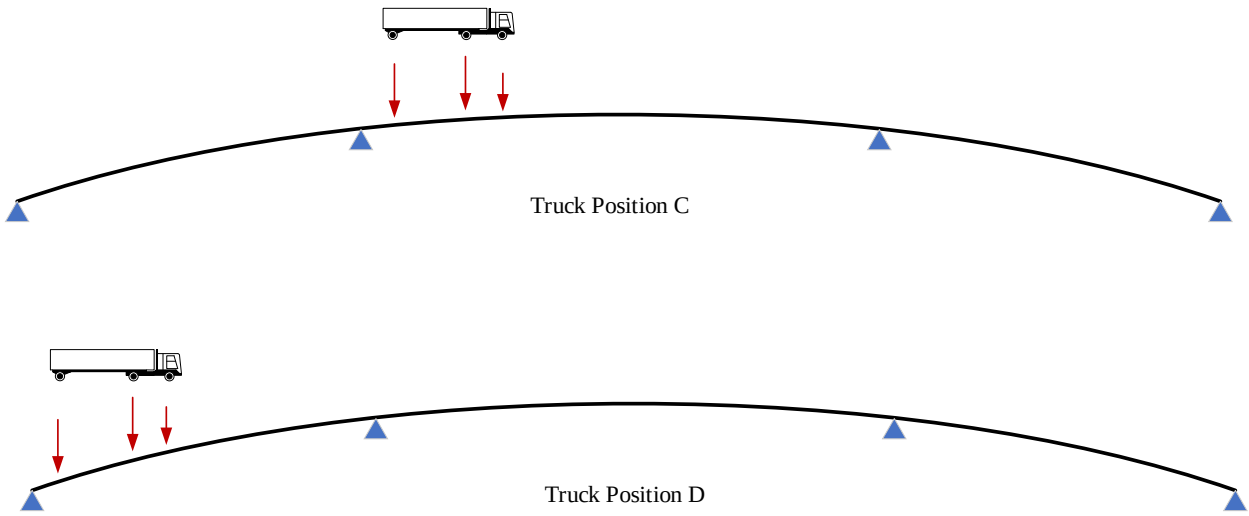

Figure 3.7: Loading positions for the web-to-bearing stiffener connection, position C) interior support panel 3, position D) exterior support panel 2

3.1.2.3 Sensitivity Analysis (Mesh Density)

Günther and Kuhlmann (2004) used 4-noded shell elements with a side length of approximately 4 inches (100 mm) to evaluate secondary bending stresses at the boundaries of slender straight web panels. The mesh density was reported to be sufficiently accurate for taking into account the geometric deformations; however, the shell element nodal stresses could not be directly used due to the high stress gradient close to the web boundaries of test panels. Web stresses close to the edges were four times larger than those recorded 4 inches away. Hence, nodal forces and moments were used to calculate the stresses normal to the web boundaries welding. Crocetti (2001) simulated the breathing web test panels with 8-node shell elements of 3 by 3 square inch size having four and three integration points in the plane and through the thickness of shell elements. The web surface stresses normal to the weld were read at the integration points located at 0.63 inches (16 mm) from the weld toe to be consistent with the strain gauges positions.

A sensitivity analysis was done to understand the stress gradient at web boundaries of the full-bridge model. The aim was to evaluate the mesh refinement effect on the stress range

calculation resulting from the AASHTO fatigue truck. ABAQUS provides a sub-modeling capability that enables analyzing a region of the global model in a subsequent analysis having finer mesh. The nodal translational and rotational dofs derived from the global model were applied as the external boundary conditions. The web-to-bottom flange connection located at panel 1 of the bridge having the radius of curvature and slenderness equal to 400 ft (121.9 m) and 300, respectively, was selected for the stress gradient check. The global assembly and submodel are shown in Figure 3.8. The sub-model has the 4-noded shell elements, finely meshed with one-inch dimension for sides. The global model mesh has the 4-noded shell elements of a 4-inch side dimension. In both the global and sub-model, the web normal stresses in transverse direction due to the total dead load and fatigue truck located at position A and the corresponding stress ranges are plotted in Figure 3.9. The stresses are outputted from the centroid of web shell element surfaces adjacent to the bottom flange. The sub-model includes the full panel width, but the results from the elements located at one-tenth of each end are neglected due to stress concentration at the sub-model boundaries.

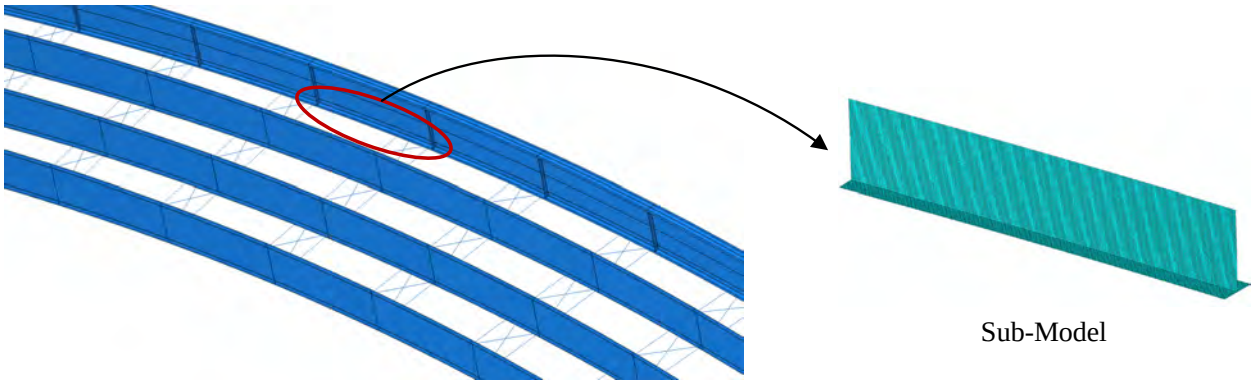

Figure 3.8: Global assembly and sub-model

As Figure 3.9 shows, the maximum stress range associated with the sub-model refined mesh is 20% larger than the global model, and the accumulated stress under dead load and fatigue truck is 2 ksi (14 MPa) larger for the submodel. It should be noted that 20% stress range gradient

moving from 4 inch to 1 inch away from the web boundary is significantly smaller than the 400% stress gradient of the test girders (Günther and Kuhlmann 2004) for the same locations. In addition, the focus of the study is to investigate the curvature effect on intensifying the stress range compared to the equivalent straight girders, and the absolute stress range values are not the primary target. Consequently, it was decided that the global model stress output at the centroid of the shell-elements of the web boundary should be selected for all parametric simulations.

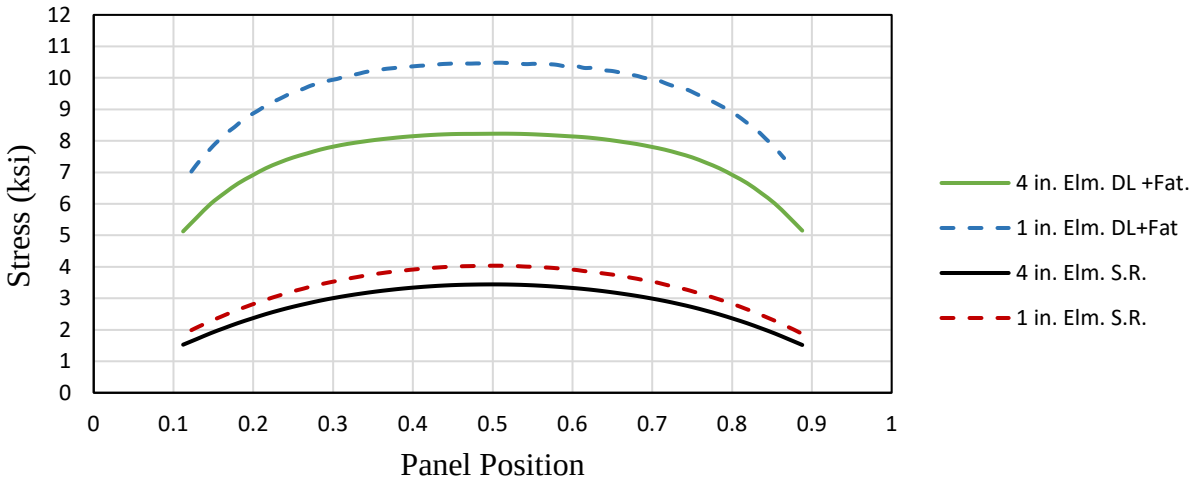

Figure 3.9: Element size effect on transverse web stress

3.1.3 Results and Discussion

3.1.3.1 Web-to-Bottom Flange Fatigue Detail, Panel 1

The vertical web normal stress at the web-to-bottom flange connection of panel 1, shown in Figure 3.5, is discussed in this section. The fatigue truck positions *A* and *B* (Figure 3.6) are chosen to examine the stress ranges due to the corresponding maximum positive and negative bending moment effects. Figure 3.10 shows the vertical web normal stress range distribution corresponding to the highly curved and slender bridge having a radius of curvature of 400 ft (121.9 m) and slenderness of 300. High stress concentration occurs at the web elements adjacent to the

bottom flange. It should be noted that the high stress range located at the left corner is parallel to the web-to-stiffener connection weld and does not correspond to fatigue cracking.

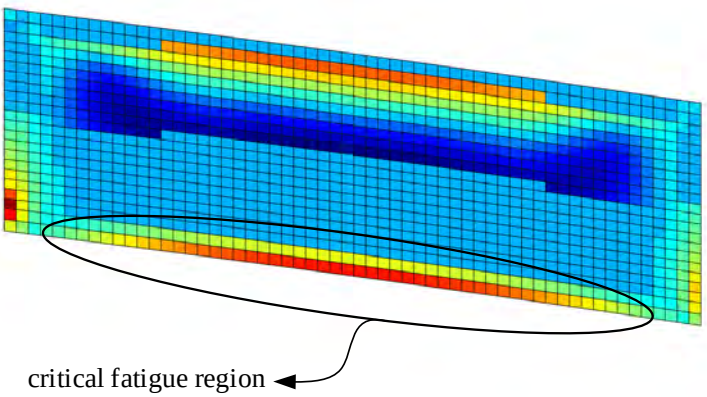

Figure 3.10: Web normal stress range in the transverse direction, *R* = 400 ft (121.9 m), D/t_w = 300

Web normal stresses in the vertical direction due to dead load and dead load plus fatigue truck at positions *A* and *B* are plotted in Figure 3.11. The positive truck loading induces tensile stress ranges that are 200% larger than the negative fatigue truck compressive stress ranges.

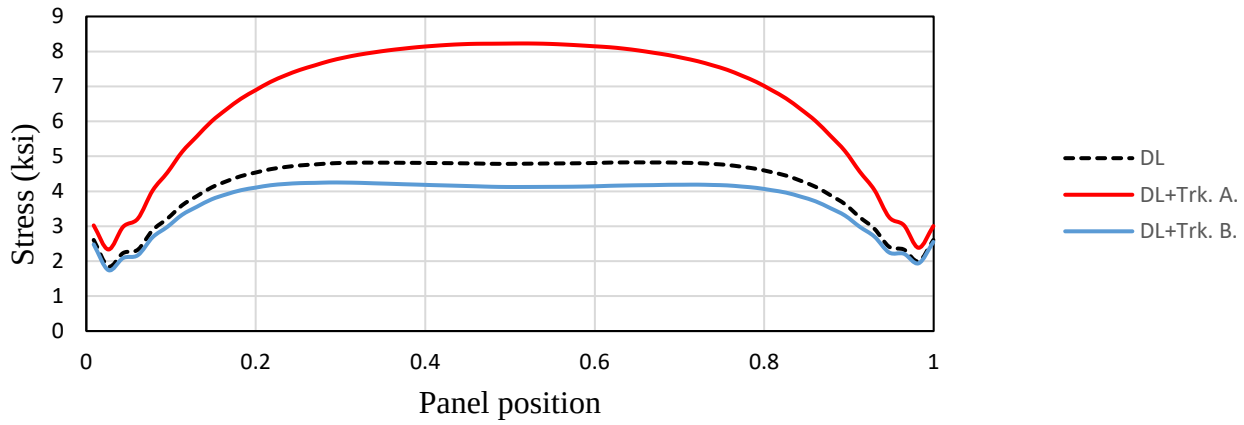

Figure 3.11: Web normal stress in the transverse direction at the web-to-bottom flange, *R* = 400 ft (121.9 m), D/t_w = 300

The total stress range for two groups of bridges with the varying radius of curvature having non-slender and slender web, D/t_w = 150 and D/t_w = 300, is given in Figures 3.12 and 3.13, respectively. The compressive stress range is considered only if the entire state of stress, dead load plus fatigue, is in tension. The fatigue strength limit for crack occurrence due to web stresses normal to the boundary elements was recorded as the 16 ksi (110 MPa) in straight girder test panels having breathing webs (Crocetti 2001; Günther and Kuhlmann 2004). Although this study aims to capture the rate at which the stress range is intensified by the curvature-induced mechanisms, the fatigue strength limit (half of the constant amplitude fatigue limit) is plotted as a dashed line for the matter of comparison between different fatigue detail categories.

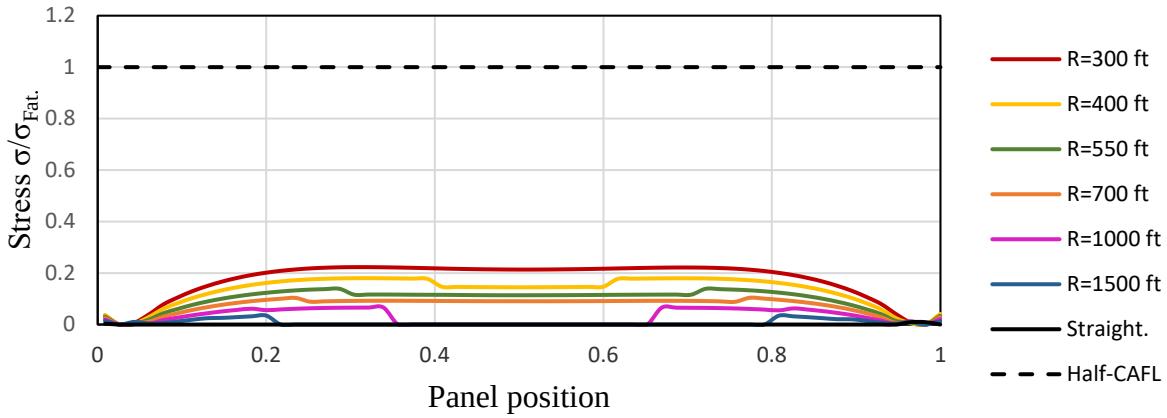

Figure 3.12: The radius of curvature effect on web normal stress in the transverse direction at the web-to-bottom flange connection of Panel 1, D/t_w = 150

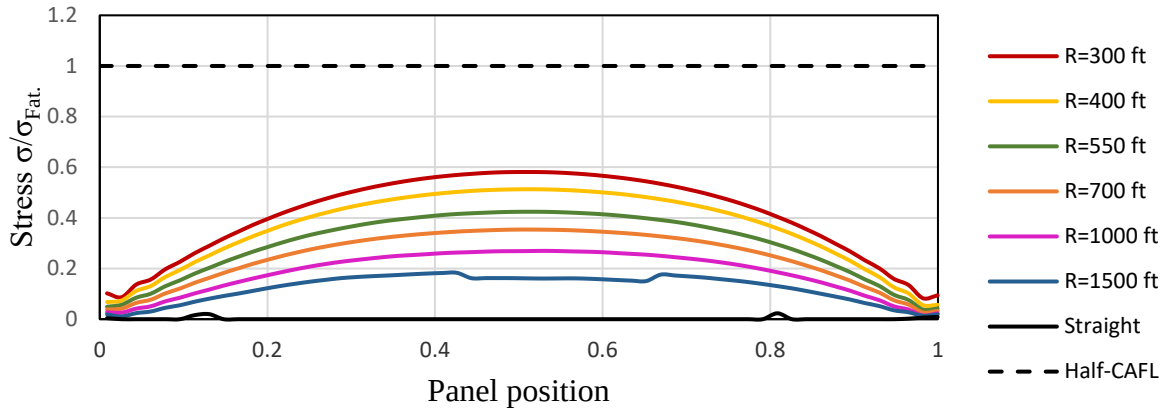

Figure 3.13: The radius of curvature effect on web normal stress in the transverse direction at the web-to-bottom flange connection of Panel 1, D/t_w = 300

As Figure 3.13 demonstrates, the peak stress range for the curved girder bridges greatly increases with increasing curvature compared to straight bridge, especially for the slender web. The web deformations under the total dead load for the highly curved bridge having a radius of 400 ft (121.9 m) and the straight bridge are shown in Figure 3.14. The curved panel web experiences large rotation and web distortion compared to the straight equivalent web. The applied fatigue truck load leads to higher transverse web stresses in curved webs because of two simultaneous actions: 1) the truck load forms a deflection-amplification effect with the web distortions and relative rotation of the top and bottom of the curved web, while the equivalent straight girder remains mainly flat, and only the top compressive part of the web distorts; and 2) the vertical fatigue loads transform into lateral forces that further intensifies the web deformations and transverse web stresses. In other words, the primary axis bending moment stabilizes the distortion of the bottom web of the straight girder, while it amplifies the web out-of-flatness and membrane stresses of the same region due to the lateral bending effect for the curved girders. The concrete deck composite action that has been neglected in analytical and experimental studies also plays an essential role in large web stress concentrations at the bottom flange connection. The

concrete slab provides continuous lateral support for the top flange and removes the lateral bending effect on the top of the web. It also shifts the neutral axis up, which makes secondary bending stresses resulting from transformed shear forces, from main axis bending moment, at the bottom flange locations more severe than the top flange.

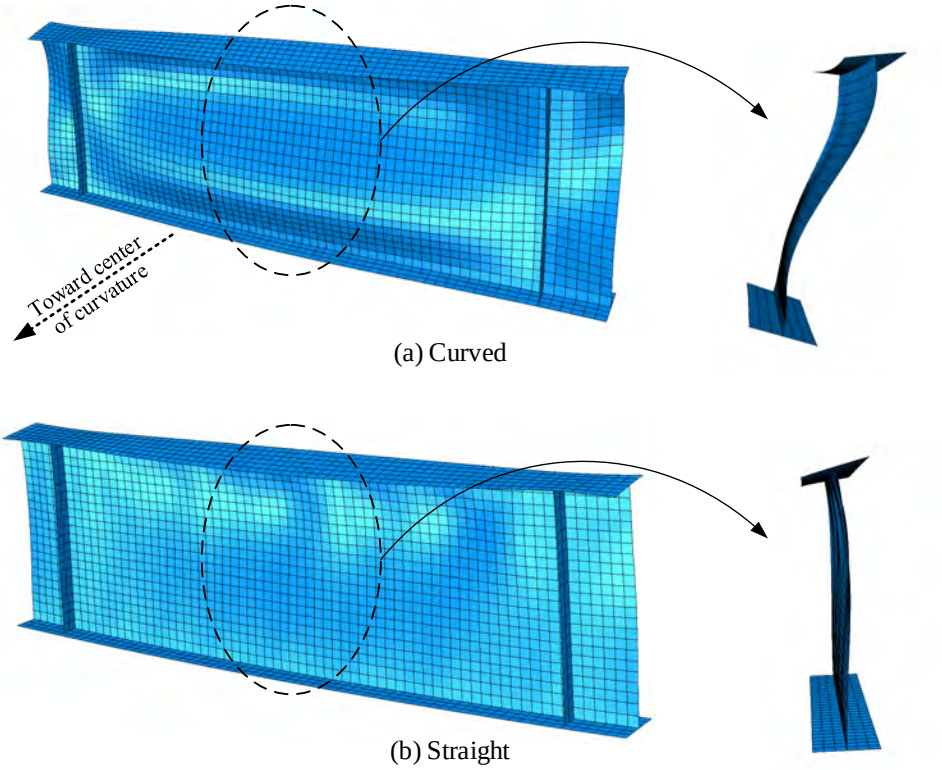

(a) Curved

(b) Straight

Figure 3.14: Web panel 1 deformations (magnified) and cross sections, D/t_w = 300

3.1.3.2 Web-to-Bearing Stiffener of Exterior Support Fatigue Detail, Panel 2

This section investigates the web-to-bearing stiffener connection of dominantly shear-loaded panel. Panel 2 is located at the end span of the exterior girder (Figure 3.5) and is loaded by the truck position *D* (Figure 3.7). The web normal stress component in the tangential direction was considered for stress range calculations because the web stress perpendicular to the weld direction of the web-to-bearing stiffener is associated with fatigue cracking. As Figure 3.15 shows, diagonal

web out-of-plane distortion forms toward the corners of the slender web panel. High stress range concentrations occur at the bearing stiffener, where the distortions are anchored.

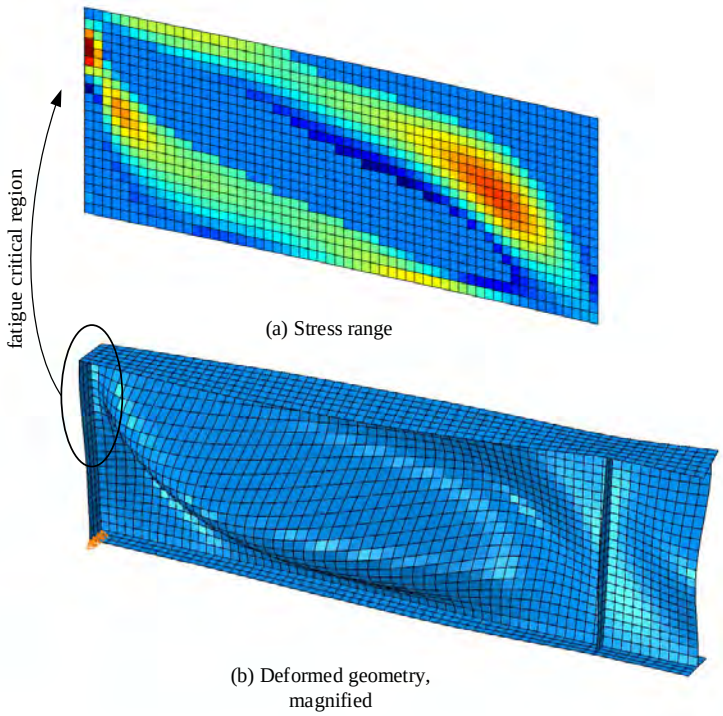

Figure 3.15: Web normal stress range in the longitudinal direction and the corresponding deformed geometry, R = 300 ft (91.4 m), D/t_w = 300

Figure 3.16 depicts the web normal stress in the longitudinal direction due to dead load, dead load plus fatigue truck, and the corresponding stress range for a bridge having a radius of curvature and web slenderness of 300 ft (91.4 m) and 300, respectively. It should be noted that fatigue truck loading intensifies the compression and tension stresses due to dead load and no stress reversal occurs. The maximum stress range occurs at approximately one-fifth (0.2) of the web depth from the top.

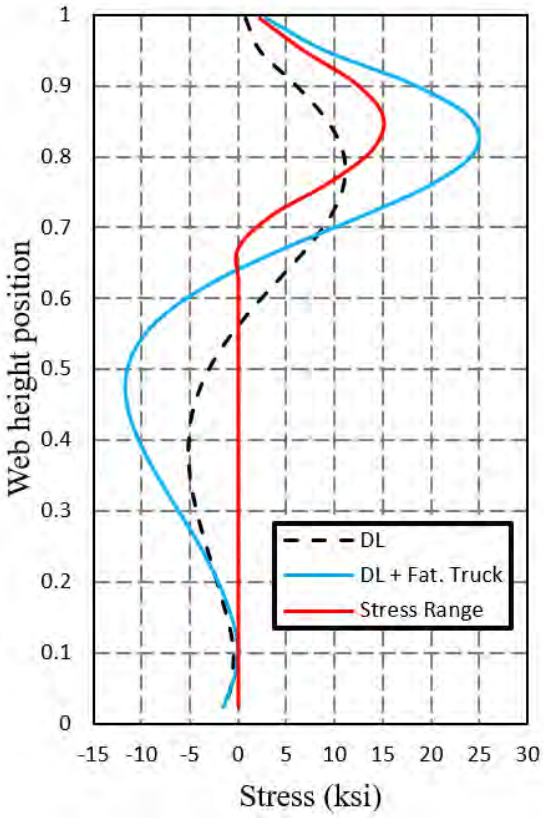

Figure 3.16: Web normal stress in the longitudinal direction at the web-to-bearing stiffener location, R = 300 ft (91.4 m), D/t_w = 300

The curvature effect on web breathing stresses at the bearing stiffener location was studied for two classes of bridges having web slenderness ratios of 150 and 300. For the bridges with slenderness of 150, the load effects are less than the shear buckling capacity, and web breathing effects are minimal for all the bridges (Figure 3.17). On the other hand, for the slender group (D/t_w = 300), the curvature effect on increasing the stress range is noticeable. For the panel with an aspect ratio equal to 3, the maximum stress range for the bridge with a radius of 300 ft (91.4 m) is approximately 1.4 times larger than the straight girder. However, the curvature effect on intensifying the stress ranges is more influential for the highly curved bridges, i.e., R = 400 ft (121.9 m) and 300 ft (91.4 m). There is a small difference (2%) in the peak stress range between the bridge with the curvature radius of 1500 ft (457.2 m) and the straight bridge.

Another group of parametric bridges having a panel aspect ratio of 1.5 was simulated to study the change in the stress range magnitudes and web distortion patterns due to panel dimensions. As Figure 3.18 shows, curvature increased the maximum stress range by approximately 70% over the straight versus 400 ft (121.9 m) radii of curvature bridge. Curvature generally increased the tangential stress ranges in both panel aspect ratio cases. However, smaller stress range peaks occurred for the bridges having an aspect ratio of 1.5 due to limited web out-of-flatness distortion.

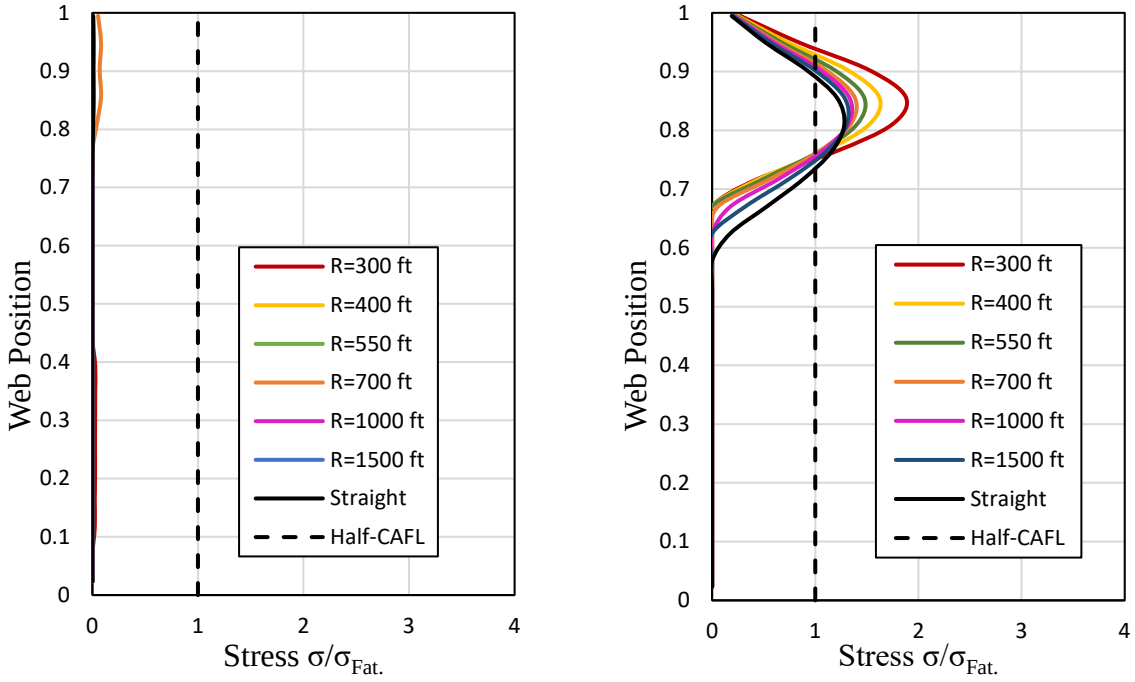

Figure 3.17: The radius of curvature effect on web normal stress in the tangential direction of Panel 2, (left) D/t_w = 150 and (right) D/t_w = 300, d_0/D = 3

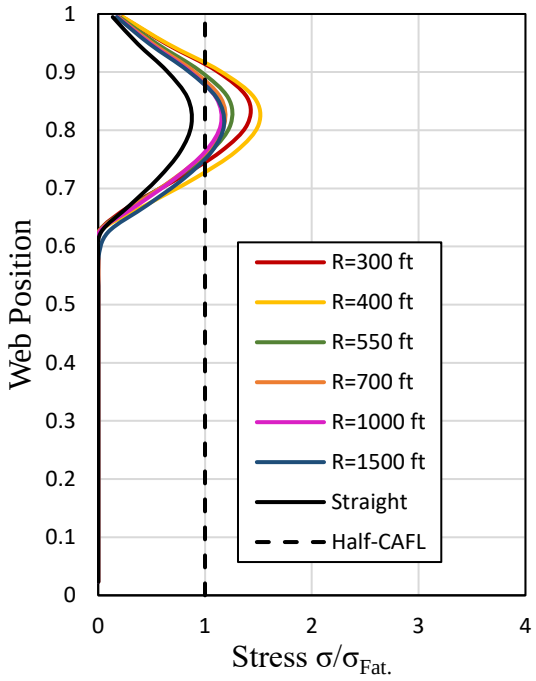

Figure 3.18: Radius of curvature effect on web normal stress in the tangential direction of Panel 2, D/t_w = 300, d_o/D = 1.5

The panel aspect ratio effect on web deformation patterns for the straight and highly curved bridge is given in Figure 3.19. Both the curved and straight panels experience web bulging out in the diagonal direction toward the panel corners. The rotated web out-of-plane deformation appears at the top corner close to the bearing stiffener. It diminishes at about one-third of the panel length from the diaphragm connection plate for the panels with an aspect ratio of 3. For panels with aspect ratio of 1.5, the web deformation patterns are similar to those with an aspect ratio of 3 but are anchored at the web panel corners. The web of the straight girder does not experience significant out-of-plane deformations.

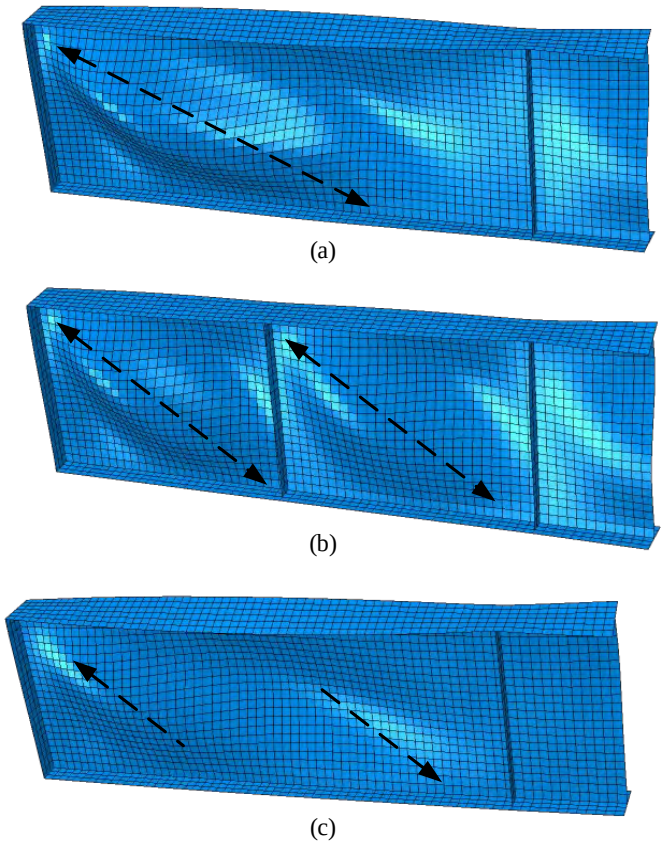

Figure 3.19: Web deformations (magnified) for end panel 2 D/t_w = 300: (a) curved bridge d_o/D = 3, (b) curved bridge d_o/D = 1.5, and (c) straight bridge d_o/D = 3

3.1.3.3 Web-to-Bearing Stiffener of Interior Support Fatigue Detail, Panel 3

The web-to-bearing stiffener of the panel experiencing high shear and moment is discussed. Panel 3, located at the mid support of the exterior girder (Figure 3.5), was loaded by fatigue truck position *C* to maximize the force and deformation effects (Figure 3.7). The web normal stress range in the tangential direction and the corresponding deformed geometry for a highly curved and slender web bridge are given in Figure 3.20. Diagonal web bulging out deformations occur toward panel corners similar to end panel 2; however, the distortion is more severe and the lower part of web close to the support is highly deformed.

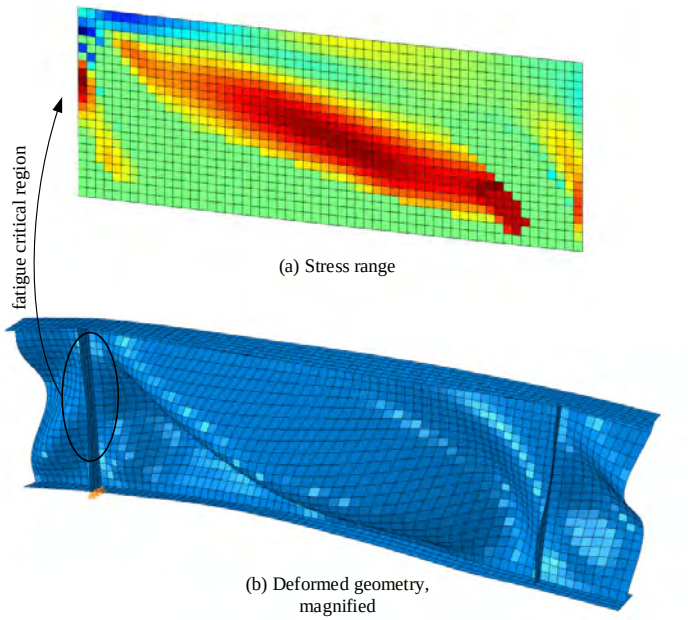

Figure 3.20: Web normal stress range in the longitudinal direction and the corresponding deformed geometry, R = 400 ft (121.9 m), D/t_w = 300

The radius of curvature influence on web normal stress ranges were studied for non-slender and slender web bridges having panel aspect ratio of 3 (Figure 3.21). The breathing effect in the non-slender group is not significant, but the slender group experience critical stress ranges. Curvature shifts the location of the maximum stress range peak along the web height for all curved bridges compared to the straight girder. However, there is an inconsistent trend at which curvature changes the stress range magnitudes. The largest stress ranges occurred for bridges having radii of curvature of 700, 1000, and 1500 ft (213.4 m, 304.8 m, 457.2 m), while the straight and highly curved bridges, radius of curvature equal to 300, 400, and 550 ft (91.4 m, 121.9 m, 167.6 m), had the smallest stress range peak. The discrepancy in curvature effect on stress range development could be the result of inconsistent web distortion shapes under the construction load. A combination of high shear and moment concentration at the interior bearing stiffener along with a large aspect ratio of 3 resulted in a complex web out-of-plane distortion patterns. The web panel

aspect ratio was reduced to 1.5 to maintain a similar web distortion pattern at the end of the dead load step for all bridge simulations. As Figure 3.22 shows, stress ranges for all parametric bridges having panel aspect ratios of 1.5 follow the same pattern and experience approximately the same stress range peak value. The curvature actually decreased the maximum stress ranges compared to the straight girder.

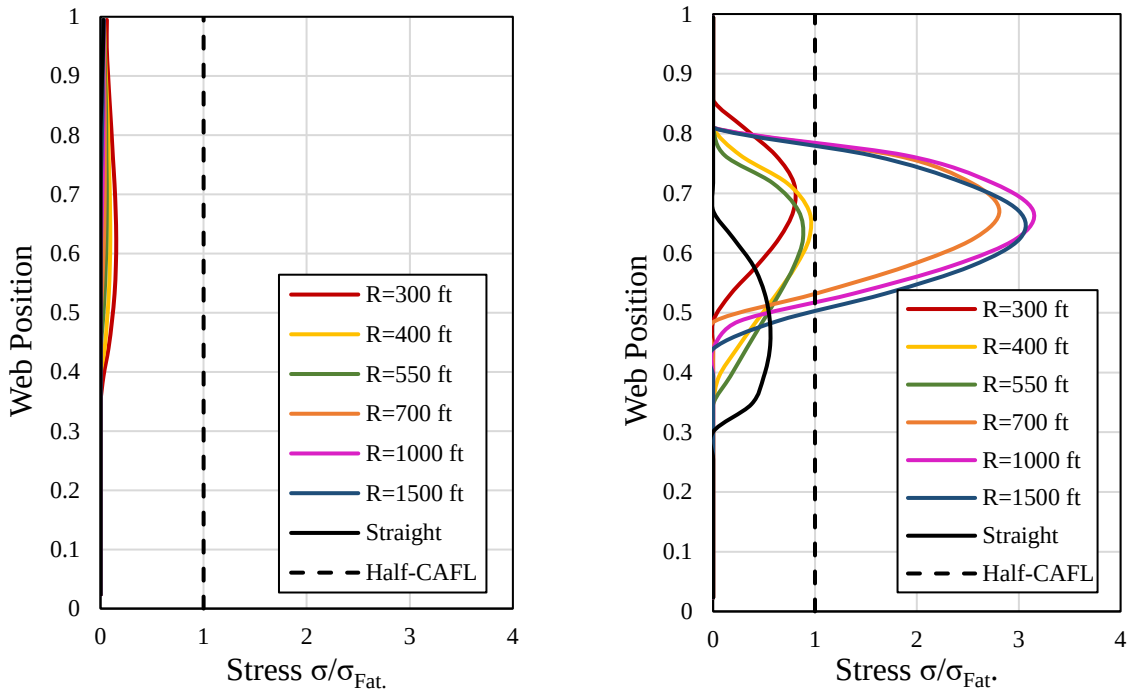

Figure 3.21: Radius of curvature effect on web normal stress in the tangential direction of Panel 3, (left) D/t_w = 150 and (right) D/t_w = 300, d_o/D = 3

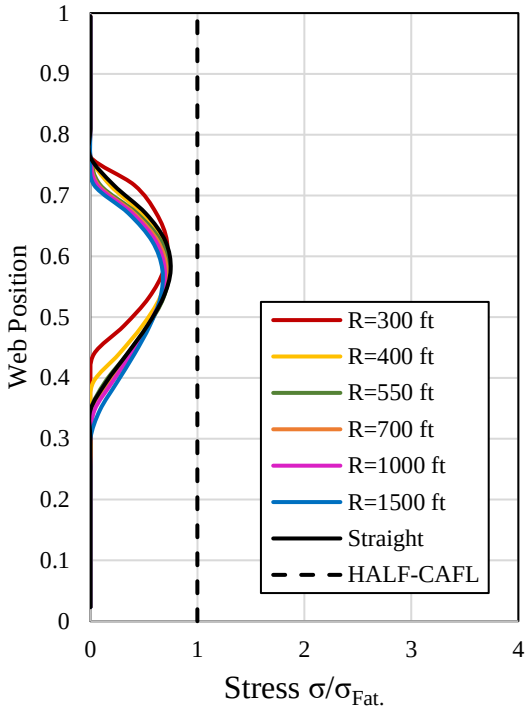

Figure 3.22: Radius of curvature effect on web normal stress in the tangential direction of Panel 3, D/t_w = 300, d_o/D = 1.5

3.1.4 Conclusions

A parametric study was done through refined 3-D FEM analyses to investigate the curvature effect on critical stress ranges at the web boundaries of full-bridge models. A compatibility technique was applied to capture the continuous stress and displacement development from the construction through service. Three different fatigue-prone regions related to high bending, high shear, and combined shear and moment were considered.

For the high bending region, the curved bridge web panels experienced high lateral moments and rotations due to dead load. Consequently, vertical web stress ranges at the web-to-bottom flange connection of curved bridges were higher than the equivalent straight girders under the effect of fatigue loading. It was concluded that if the curved bridges with slender web are

designed based on the straight girder considerations, these amplified stress ranges could potentially lead to fatigue crack initiation.

For the high shear region, the curved bridges with slender webs experienced the same stress development as the straight girders. Panels with smaller aspect ratios experienced considerably smaller stress range magnitudes for both the curved and straight girders. However, curvature increased the stress range peaks, for both panel aspect ratios of 1.5 and 3, compared to the equivalent straight girders.

For the combination of high shear and moment, a meaningful trend in curvature effect on the stress range could not be observed for the web panels with an aspect ratio of 3. The analysis for the web panel aspect ratio of 1.5 showed that curvature has a diminishing effect on stress ranges compared to the straight girders.

These simulation results need to be verified through experimental testing explicitly designed for fatigue evaluation of the slender curved assemblies. This study aimed to provide insight into the effect of curvature on the fatigue performance of curved bridges, which is currently not explicitly considered. It is also recommended to study the longitudinal web stiffener effect on stress concentrations as a future study.

3.2 Evaluation of Analytical Methods

3.2.1 Introduction

Theoretical studies associated with curved webs under bending can be divided into two categories. First, very limited research investigated the curvature effect at web panel boundaries that is critical for the fatigue limit state. The simplified methods, based on beam theory, are not capable of properly modeling the actual behavior of curved girders with slender webs. Second, more accurate analytical models that are based on plate theory were conducted to establish the ultimate web stress and lateral displacements corresponding to strength and stability limit state, respectively. This chapter reviews the analytical approaches related to the breathing of straight girders and stability and strength of curved web panels, and evaluates the applicability of an analytical method particular to the fatigue of curved web panels proposed by Japanese researchers.

3.2.2 Flat Web Panel Methods

Web breathing of slender web panels under different load conditions was illustrated in previous sections. The bending load condition is explained in detail here. When a plate girder is loaded by repeated bending, three types of fatigue cracks appear at the web panel boundary elements, i.e., flanges, and stiffeners, as shown in Figure 3.23. Crack type 2 and 3 results from in-plane membrane and bending stress, respectively. Initial imperfections and high load levels cause the compression region to bulge out of the plane and forms crack type 1 at the web-to-compression flange location. Crack type 1 is caused by large web surface stress normal to flange, denoted by $\sigma_{\perp}$, consisting of web membrane stress in the transverse direction and out-of-plane bending stress. For pure bend loading, detailed measurements of test girders (Kuhlmann and Günther 1999) showed that the secondary bending stress σ_b is much larger than the membrane stress in the transverse direction and is almost equal to the $\sigma_{\perp}$.

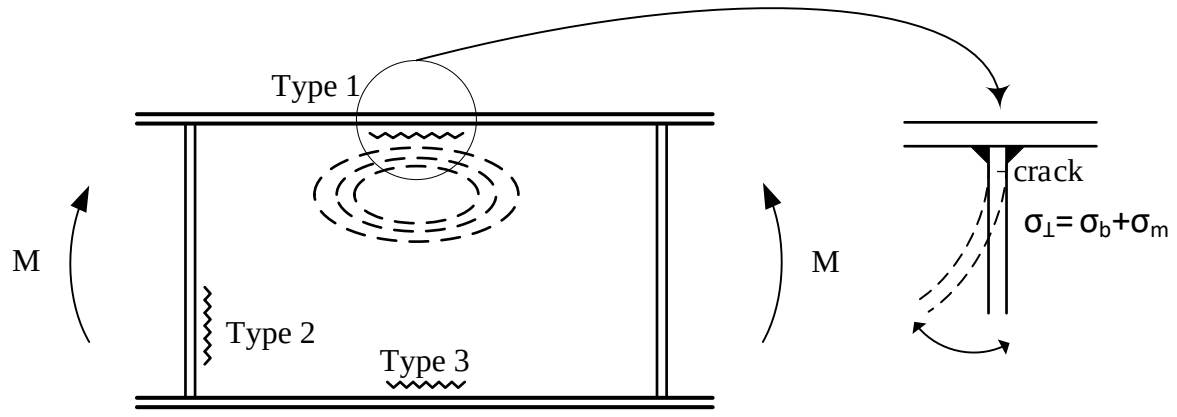

Figure 3.23: Web breathing under pure bending

Web breathing is a complex problem that corresponds to the post-buckling state and requires advanced solutions to define the nonlinear web response and secondary bending stresses. Marguerre (1938) developed the governing differential equation (G.D.E) for a plate with initial deformation:

$$D_p \nabla^4 w = \left[\frac{\partial^2 \Phi}{\partial y^2} \frac{\partial^2 (w + w_0)}{\partial x^2} + \frac{\partial^2 \Phi}{\partial x^2} \frac{\partial^2 (w + w_0)}{\partial y^2} - 2 \frac{\partial^2 \Phi}{\partial x \partial y} \frac{\partial^2 (w + w_0)}{\partial x \partial y} \right] \tag{3.2}$$

$$\nabla^4 \Phi = \left[\left(\frac{\partial (w + w_0)^2}{\partial x \partial y} \right) - \frac{\partial^2 (w + w_0)}{\partial x^2} \frac{\partial^2 (w + w_0)}{\partial y^2} - \left(\frac{\partial^2 w_0}{\partial x \partial y} \right)^2 + \frac{\partial^2 w_0}{\partial x^2} \frac{\partial^2 w_0}{\partial y^2} \right] \tag{3.3}$$

where $D_p = \frac{Et^3}{12(1-\nu^2)}$ is the plate bending stiffness, E is the elastic modulus, t is the plate thickness, v is the Poisson's ratio, ∇ is the Del operator, w is the plate deflection function, w_0 is the initial deformation, Φ is the Airy stress function.

Equations 3.2 and 3.3 represent a coupled nonlinear biharmonic differential equation without closed-form solutions, and numerical methods such as Galerkin approximate the solution

space. The secondary bending stresses at the web panel boundaries can be found in terms of the plate deflection function *w*. Analytical approaches, including the simplified methods and efforts to solve the Marguerre equation for defining the secondary bending stresses at the web panel boundaries, are discussed in the following.

Muller and Yen (1966, 1968) applied a semi-empirical method to define the web panel secondary stresses by fitting a fourth-order polynomial to the measured web lateral deformations. The stiffener and flange rigidities were considered through compatibility equations in terms of web deflections. Other tests by Patterson et al. (1970) verified their proposed approach, and the following web slenderness requirements for fatigue limit were reflected in the AASHTO specifications (1989):

$$\beta \le \frac{3047}{\sqrt{F_y}} \text{, for girders without longitudinal stiffener} \tag{3.4}$$

$$\beta \le \frac{6094}{\sqrt{F_y}} \text{, for girders with longitudinal stiffener} \tag{3.5}$$

where β is the web thickness to web height ratio, and F_y is the yield stress in MPa.

Maeda and Okura (1982) attempted to solve the Marguerre equations by utilizing the Galerkin method for the web panel shown in Figure 3.24. The assumed initial deformation and plate deflection response were given by:

$$w_0(x,y) = e_0 \sin\frac{\pi x}{a}\sin\frac{n\pi y}{b} \tag{3.6}$$

$$w(x,y) = \sin\frac{\pi x}{a}\left(e_1 \sin\frac{\pi y}{b} + e_2 \sin\frac{2\pi y}{b}\right) \tag{3.7}$$

where w_0 is the initial deformation, w is the deflection function, and $e_{i's}$ are the coefficients. Given that the Sine function cannot model the tangency condition at the fixed horizontal edges, the

Galerkin method could not be applied entirely. Consequently, the analytical model only served as a mathematical formulation, and the coefficients were found by finite element analysis. The solution resulted in two dependent expressions that define the displacement at point *B (a/2,b/4)* and secondary bending stress at point *A (a/2,0)*. Based on experimental results (Maeda et al. 1976) and regardless of the analytical approach, it was proposed that crack Type 1 due to web breathing does not occur if crack Type 2 is prevented.

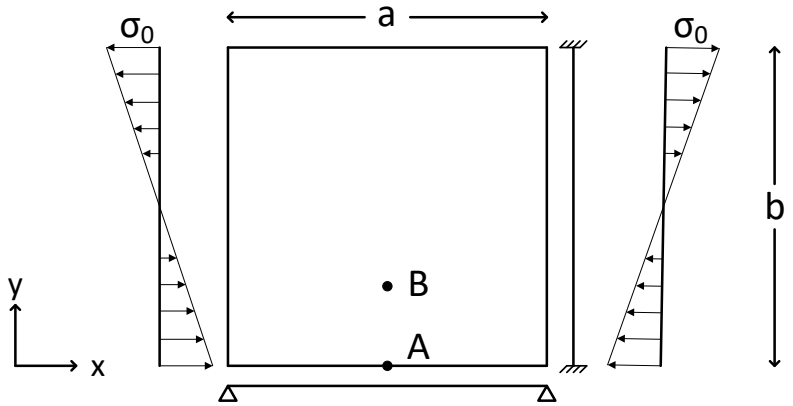

Figure 3.24: Maeda et al. (1976) plate loading and boundary condition

Dubas (1992) modeled the compressive region of the web panel by the simple framework made of cross beams in the two directions. The same limit as Maeda and Okura (1982) was concluded. Remadi et al. (1995) further improved the analytical model of Maeda and Okura (1984) by considering larger aspect ratios, additional deflection function coefficients, and a higher number of half-waves. The following limit for prevention of crack Type 1 based on parametric FEM analysis was proposed (Aribert et al. 1996):

$$\max \sigma_0 \le \min \left\{ \frac{71}{1-ST} \left(\frac{N}{mm^2} \right), \sigma_{cr,F-S} \right\} \tag{3.8}$$

where σ_0 is the in-plane stress, *ST* is the stress ratio, and $\sigma_{cr\text{-}F\text{-}S}$ is the linear elastic buckling stress of the plate with fixed and simply supported longitudinal and vertical edges, respectively.

Spiegelhalder (2000) solved the Marguerre equation for web plates under bending with all edges fixed and considered the flange stiffness in terms of additional Airy stress functions. A parametric FEM model calibrated with the test data was used for developing a design limit instead of the pure analytical solution of the Marguerre equation, due to the extreme computational cost of the mathematical formulation,

$$\max \sigma_0 \le \min \left\{ \frac{\Delta \sigma_c^{Type2}}{1-ST}, 2\sigma_{cr} \right\} \tag{3.9}$$

where $\Delta \sigma_c^{Type2}$ is the fatigue strength of crack type 2, σ_{cr} is linear elastic buckling of the plate with all edges simply supported.

3.2.3 Curved Web Panel Methods

The elastic behavior of curved web panels has been studied extensively through purely theoretical analysis and numerical methods (Culver et al. 1972; Daniels et al. 1979*a*; Davidson et al. 1999*a*). The main focus of the works was to assist in understanding the geometric nonlinear effects and developing web bending stresses limits in terms of moment reduction factors with respect to straight web panels. In addition, setting a limit on web out-of-plane displacement was investigated for stability concerns. Featured analytical research resulted in defining design guideline limits or highlighting important characteristics of curved web panels behavior are presented in the following.

Dabrowski (1968) developed the nonlinear G.D.E of curved web panels under pure bending based on shell theory that assisted in the fundamental understanding of curved web panels behavior:

$$D_p \nabla^4 w = t\sigma_y^0 \left(\frac{1}{R} + \frac{\partial^2 w}{\partial y^2} \right) + \frac{t}{R} \frac{\partial^2 \Phi}{\partial x^2} + \frac{\partial^2 \Phi}{\partial x^2} \frac{\partial^2 w}{\partial y^2} - 2 \frac{\partial^2 \Phi}{\partial x \partial y} \frac{\partial^2 w}{\partial x \partial y} + \frac{\partial^2 \Phi}{\partial y^2} \frac{\partial^2 w}{\partial x^2} \tag{3.10}$$

$$\frac{1}{Et} \nabla^4 \Phi = -\frac{1}{R} \frac{\partial^2 w}{\partial x^2} + \left(\frac{\partial w^2}{\partial x \partial y} \right)^2 - \frac{\partial^2 w}{\partial x^2} \frac{\partial^2 w}{\partial y^2} \tag{3.11}$$

where $D_p = \frac{Et^3}{12(1-\nu^2)}$ is the plate bending stiffness, σ_y^0 is the maximum normal stress in the *y* direction, and *R* is the panel radius of curvature. The solution of the Dabrowski equations revealed that web membrane stress distribution deviates from linear beam theory at high loads (Wachowiak 1967). Washizu (1975) derived another form of nonlinear curved web panel G.D.E. for additional loading conditions based on the total potential energy.

Culver et al. (1972) investigated the maximum web bending stress by dividing the web panel into cylindrical strips supported elastically, i.e, spring foundation. The stiffness of each strip was calculated by considering unit vertical strips between the neutral axis and the compression flange. The final stress state solution was found by applying the total potential energy. A web-slenderness limit was developed in the form of:

$$\frac{D}{t_w} \leq \frac{36500}{\sqrt{F_y}} \left[1 - 8.6 \frac{a}{R} + 34 \left(\frac{a}{R} \right)^2 \right] \tag{3.12}$$

where *D* is the web height, t_w is web thickness, *a* is panel length, and F_y is the yield stress in psi.

An extended version of the approach improved the cylindrical strips stiffness calculation by considering the whole web panel portion instead of discrete vertical strips (Culver et. al 1973). The following web-slenderness limit for curved girders was developed.

$$\frac{D}{t_w} \leq \frac{46000}{\sqrt{f_b}} \left[1 - 2.9 \sqrt{\frac{a}{R}} + 2.2 \frac{a}{R} \right] \tag{3.13}$$

where f_b is the flange bending stress in psi.

The only research related to curved girder fatigue investigations in the U.S. took place at Lehigh University. Two twin-girder assemblies, I-shaped and box, were analyzed only experimentally (Daniels et al. 1979a). The test assemblies were designed based on the early works on the straight girder fatigue requirements (Mueller and Yen 1968). It was concluded that the Culver et al. equations were too conservative, and the following slenderness requirements were proposed:

$$\frac{D}{t_w} \le \frac{36500}{\sqrt{F_y}}\left[1-4\frac{a}{R}\right] \le 192 \tag{3.14}$$

$$\frac{D}{t_w} \le \frac{23000}{\sqrt{f_b}}\left[1-4\frac{a}{R}\right] \le 170 \tag{3.15}$$

It should be noticed that no effort was done to measure or calculate the secondary bending stress intensities.

Another research on fatigue testing of the horizontally curved girder was conducted in Japan (Nakai et al. 1990). A simplified method to approximate the maximum out-of-plane bending stress was developed and used for designing the scaled I-girder test setup. The curved web panel was idealized as a vertical strip with unit width, as illustrated in Figure 3.25. The equivalent radial loading from in-plane bending was applied to the fixed-end strip beam model. The formula for maximum out-of-plane bending stress and displacements of the vertical strip was obtained by application of the beam theory:

$$\sigma_{b-\max} = \frac{1-\nu^2}{10}\sigma_0\left(\frac{a}{R}\right)\left(\frac{h_w}{a}\right)\left(\frac{h_w}{t_w}\right) \tag{3.16}$$

$$\delta_{w-\max} = \frac{\sqrt{5}(1-\nu^2)}{1250E}\left(\frac{a}{R}\right)\left(\frac{h_w}{a}\right)\left(\frac{h_w}{t_w}\right)^2 \sigma_{In-\max} h_w \tag{3.17}$$

where $\sigma_{b\text{-}max}$ is the maximum out-of-plane bending stress, σ_0 is the maximum in-plane stress, a is the panel width, v is Poisson's ratio, t_w is web thickness, h_w is web height, $\delta_{w-\max}$ is the maximum lateral displacement, E is the elastic modulus, and R is the radius of curvature. Although equations 3.16 and 3.17 were verified by the finite displacement method, only a web panel aspect ratio of 0.7 was considered in both the experiments and analyses. In other words, equations 3.16 and 3.17 do not include the two-way action of the web panel. The applicability of equation 3.16 is subsequently presented in the results and discussion section.

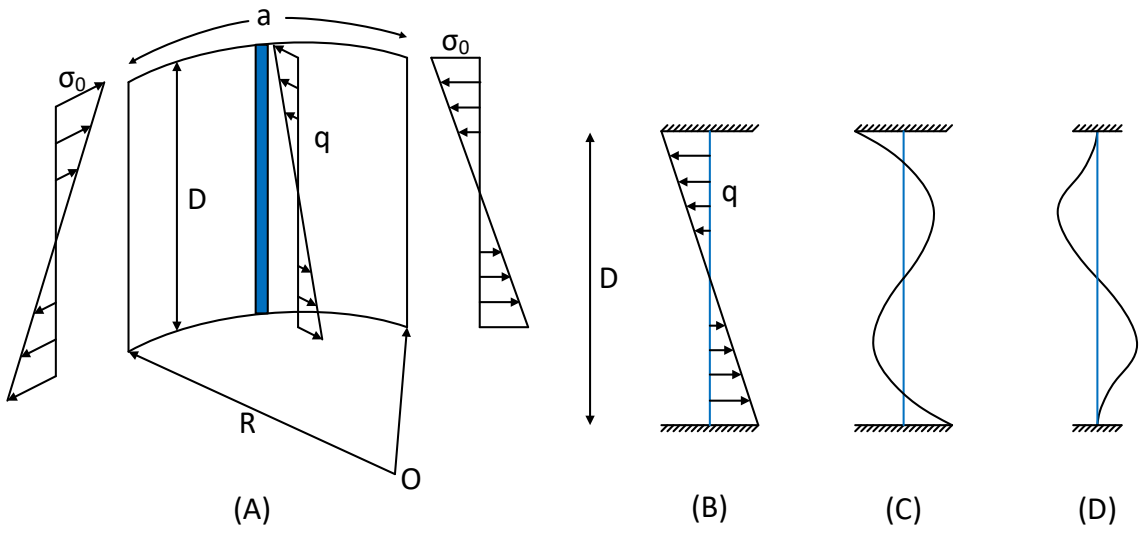

Figure 3.25: Nakai et al. (1990) analytical model (A) loading condition, (B) lateral load on the vertical strip beam, (C) stress distribution of the vertical strip, and (D) displacement distribution

Davidson et al. (1999*a*) developed a theoretical model referred to as the "lateral pressure analogy" to calculate the curved web panel bending stress and lateral displacement based on linear plate theory. The equivalent lateral load resulting from in-plane bending was applied to a flat panel with the same dimensions, as shown in Figure 3.26. The curved web panel behavior is similar to the flat plate under hydrostatic pressure with the G.D.E (Timoshenko and Woinowsky 1959):

$$\frac{\partial^4 w}{\partial x^4} + 2\frac{\partial w^4}{\partial x^4 \partial y^4} + \frac{\partial^4 w}{\partial y^4} = \frac{q}{D} = \frac{q_{0x}}{bD} \tag{3.18}$$

where w is the plate deflection function, b is the web height in compression, q_0 is the lateral pressure due to in-plane loading $q_0 = \frac{\sigma_0 t}{R}$, σ_0 is the in-plane bending stress at the web-flange juncture.

The maximum web lateral displacement and bending stress were calculated based on the simply and fixed support condition for the top of the web (web-to-flange connection), respectively:

$$\delta_{\max} = \frac{\alpha h_c^4 \sigma_0 (1-\nu^2)}{Et^2 R} \tag{3.19}$$

$$M_{b\theta} = \frac{\lambda h_c^2 t \sigma_0}{R} \tag{3.20}$$

where α and λ are coefficients dependent on panel aspect ratio and the location of the displacement and bending, respectively, h_c is the web in compression. The coefficients were found using parametric FEM analyses.

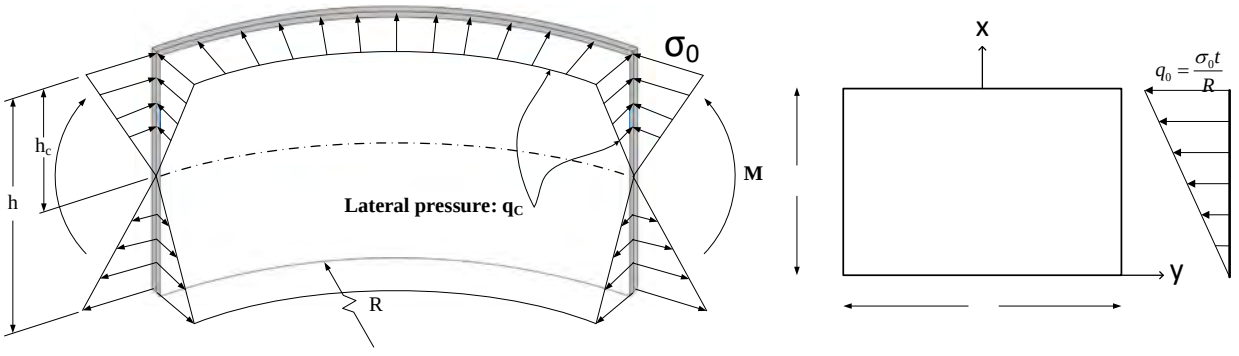

Figure 3.26: Davidson et al. (1999a) lateral pressure analogy model

3.2.4 Maximum In-plane Stress Calculation

Calculation of the secondary bending stresses σ_b requires complex methods and cannot be defined by an ordinary equilibrium of applied loads. Hence, it is not practical to establish design guides directly based on limiting the secondary bending stress ranges to the web breathing fatigue strength:

$$\Delta\sigma_b \leq \Delta\sigma_C \tag{3.21}$$

where $\Delta\sigma_b$ is the secondary bending stress range, $\Delta\sigma_c$ is the fatigue strength. A more appropriate method, developed by Maeda and Okura (1983), is to limit in-plane loads that prevent high out-of-plane bending stresses that can cause fatigue cracking. Figure 3.27 represents a typical nonlinear relationship between the applied in-plane stresses and out-of-plane bending stresses for flat plates. The secondary bending stress increases more rapidly at higher levels of applied loads. Consequently, the smaller in-plane stress amplitude $\Delta\sigma_0$ of load condition 2 results in the same $\Delta\sigma_b$ of load condition 1.

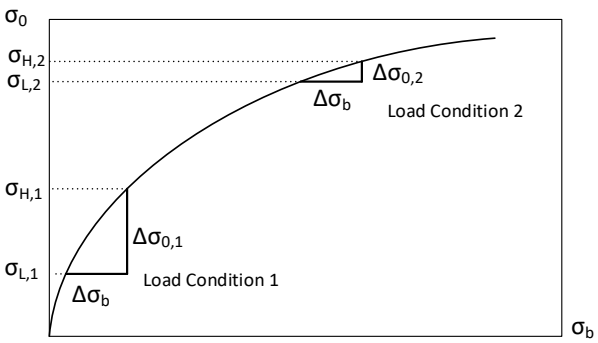

Figure 3.27: Normal stress σ_0 vs. secondary bending stress σ_b

The relationship between in-plane stress and stress range can be given by:

$$ST = \frac{\sigma_L}{\sigma_H} \tag{3.22}$$

$$\Delta\sigma_0 = \sigma_H(1 - ST) \tag{3.23}$$

where *ST* is in-plane stress ratio, $\Delta\sigma_0$ is the in-plane stress range, σ_L and σ_H is the minimum and maximum in-plane stress, respectively. Figure 3.28 illustrates the Maeda and Okura (1983) approach for a stress ratio of 0.5. A slope triangle with a fixed base equal to $\Delta\sigma_C$ is moved along the curve. The triangle with the solid lines shows the governing loading condition in which by applying the in-plane stress range $\Delta\sigma_0 = 0.5\sigma_H$ the amplitude of the secondary bending stress is equal to the fatigue strength $\Delta\sigma_c$. Consequently, the maximum in-plane bending stress can be defined in such a way that the secondary bending stress range does not lead to fatigue cracking.

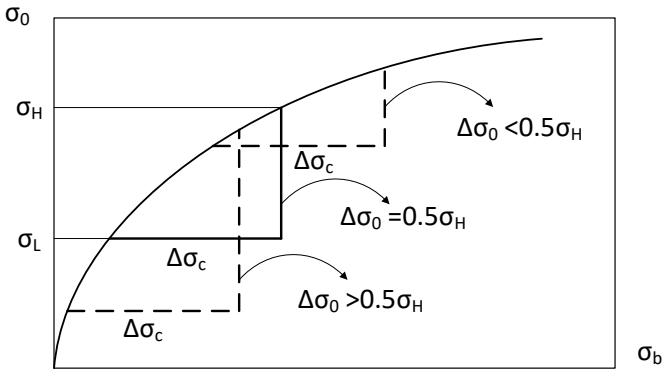

Figure 3.28: Maeda and Okura (1983) approach for finding the maximum σ_0

3.2.5 Finite Element Analysis and Comparison

The accuracy and applicability of equation 3.16 proposed by Nakai et al. (1990) was evaluated by the FEM analysis through an example. ABAQUS (2019) FEM package was used to simulate the curved web panel. 4-noded Shell elements, S4 elements, with full integration in the plane of the element, and 5 integration through the thickness was considered. The fine mesh was constructed by 100*100 elements through the depth and length of the web panel to properly capture the secondary bending stresses at the top and bottom of the web, as shown in Figure 3.29. Bending stress in the plane of the web was modeled by the equivalent nodal forces in the tangential direction

of the cylindrical coordinate system. The web panel dimensions and loading magnitudes are given in Table 3.3.

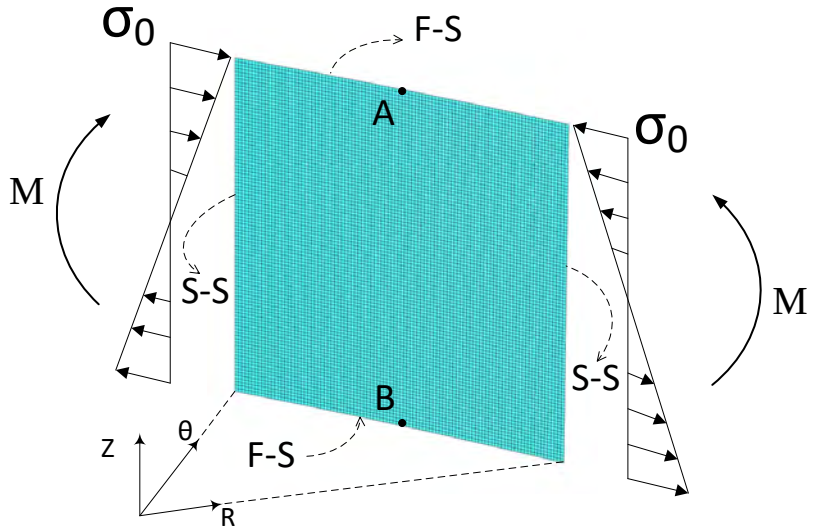

Figure 3.29: Load and boundary condition

Table 3.3: Web panel dimensions and loading condition

t_w (in)	D (in)	a (in)	R (ft)	$(\sigma_0)_{max}$ (ksi)	$(\sigma_0)_{min}$ (ksi)	$\Delta\sigma_0$ (ksi)	Elastic Modulus (ksi)	Slenderness ratio
0.334	100	100	100	36	24	12	29000	250

The maximum and minimum in-plane stresses were selected so that the resultant in-plane stress range, $\Delta\sigma_0$ is equal to the fatigue strength of crack type 2, $\Delta\sigma_c^{Type2}$. The secondary bending stress range, $\Delta\sigma_b$, was calculated based on the analytical equation (Nakai et al. 1990), linear, and nonlinear FEM simulation. The corresponding results are presented in Table 3.4.

Table 3.4: Secondary bending stress range comparison

	$\Delta\sigma_b$ (ksi)	$\Delta\sigma_b$ (ksi)
	Point A,B	Point C,D
Nakai equation	13.62	---
Linear FEM	13.68	---
Nonlinear FEM	15.13	24.32

The Nakai et al. equation accurately calculates the mid-panel linear response, and the nonlinear response can be approximated by applying proper amplification factors. The web normal stress in the transverse direction for the linear and nonlinear FEM analyses is shown in Figure 3.30 for further explanation. The maximum web deformation and secondary bending stress occur at the mid-panel and points *A/B*, respectively. The deformation pattern is the same for the both minimum and maximum in-plane bending stresses, $(\sigma_0)_{min}$ and $(\sigma_0)_{max}$. However, the nonlinear displacement response experiences a jump of buckling shape mode-1 to mode-3 in the compression region as the in-plane bending stress increases, shown by points *C* and *D* in Figure 3.30. Fuji and Ohmura (1985) first observed this phenomenon by solving the nonlinear G.D.E. of curved web panels under bending. The maximum secondary bending stress range increased to almost double the linear analysis, 24.3 ksi compared to 13.6 ksi. This phenomenon has significant effect on fatigue behavior of slender curved web panels but was ignored by simplified methods such as Nakai et al. (1990).

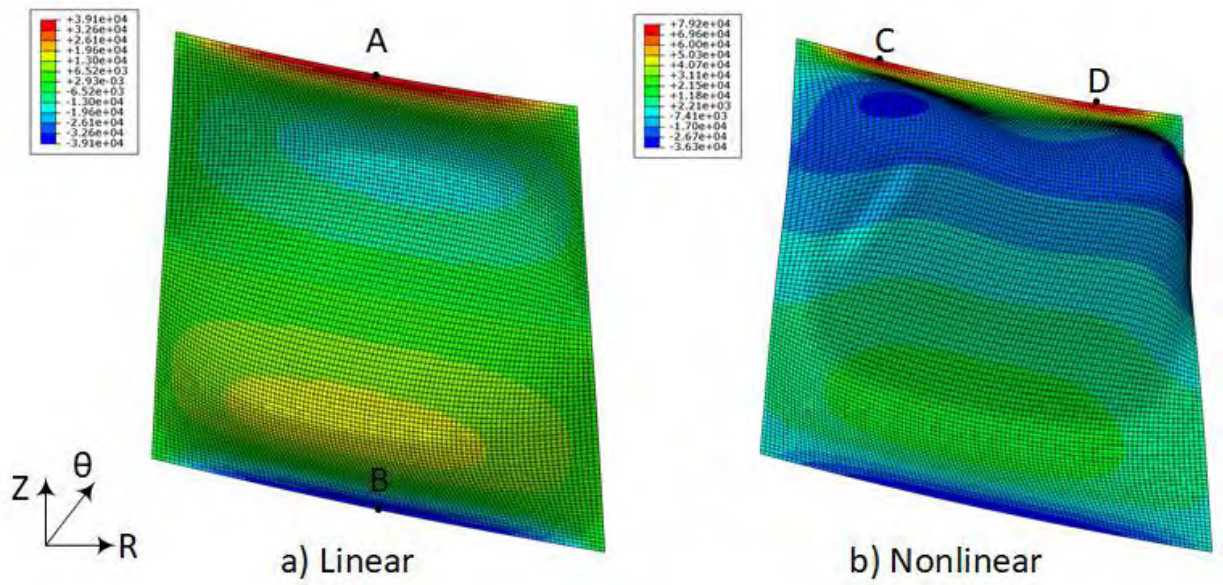

Figure 3.30: Web normal stress in transverse direction under maximum in-plane bending $(\sigma_0)_{max}$, (a) linear analysis and (b) geometric nonlinear analysis (magnified deformation)

3.2.6 Conclusions

Analytical methods for modeling the secondary bending stresses for flat web panels, web breathing, and stability methods of curved web panels were reviewed. The most accurate theoretical response of slender webs are defined by developing the solution of nonlinear governing differential equations based on plate and shell theory. However, the sophisticated mathematical solution procedures makes them less practical compared to simplified methods. It was shown that fatigue behavior of slender curved web panels requires nonlinear geometric models that take into account the 2-way action of shells and could not be fully recognized by the simplified methods based on beam theory.

3.3 Curved Web Panel under Pure Bending

3.3.1 Introduction

The compression region of isolated curved web panel under pure bending is investigated in this section. As explained in the previous section, the cyclic web out-of-plane deformation of the compression region causes fatigue cracks in the web-to-flange connection area (Figure 3.31). Parametric finite element analysis analyses were conducted to define maximum in-plane stress bending stress that can be applied to slender curved web panels without web breathing fatigue cracks.

In the positive bending region of composite steel bridges, the bottom flange under tension is affected by the cross-frame movements and the rotation of the tensile flange as explained in the prior sections. The global bridge mechanism is required to accurately study the web-to-tension flange connection. However, the compression flange is restrained by the concrete deck of the composite bridge that results in fixed web rotation and minimal effects of cross-frame movements at the top flange. Hence, the web region under compression was investigated through isolated web panel simulations.

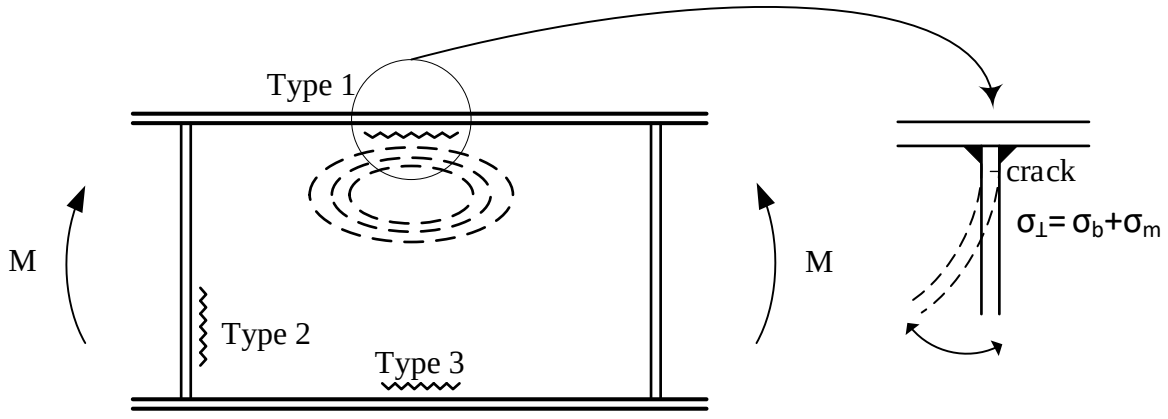

Figure 3.31: Slender web panel fatigue crack categories under bending

3.3.2 FEM Model Specification

Parametric models of the curved web panels were analyzed by ABAQUS (2019) FEM software. The fine mesh, 1-inch by 1-inch square elements, was constructed of the S4 shell elements, having 6 DOF's per node with five integration points through the thickness. Geometrically nonlinear analysis type was chosen to take into account the secondary bending effects. The base model under pure bending moment and the resultant in-plane stress distribution are given in Figure 3.32. The in-plane bending stress was applied as the equivalent nodal forces in the tangential direction of the cylindrical coordinate system established in the ABAQUS. Shell element stress output at the surface of the elements represented the secondary bending stress. The modulus of elasticity and the yield stress are 29000 ksi and 50 ksi, respectively. The minimum web thickness currently allowed by AASHTO (2020) is 0.3125 inch. Hence, the web height of 100 inches was chosen so that the slenderness of 300 is within the design limits.

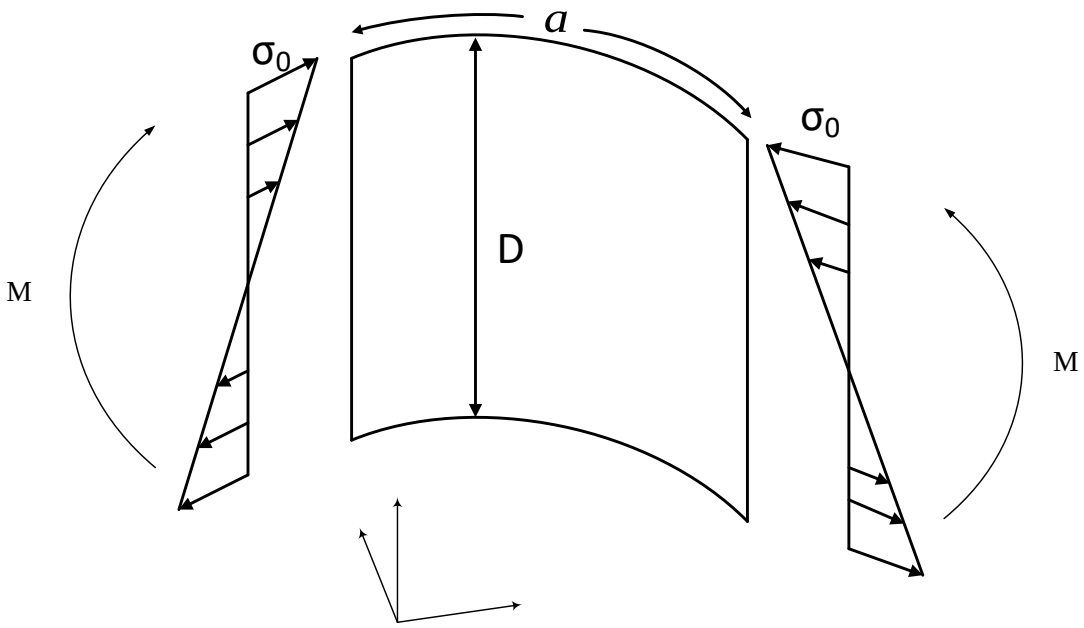

Figure 3.32: Base FEM model loading configuration

A schematic demonstrating the boundary conditions of the FEM model is depicted in Figure 3.33. The translation of the bottom two corners is restrained about vertical, *Z* direction, and the bottom mid-panel node is fixed in the tangential direction. All of the radial translations of the web panel edges are restrained. The rotational degrees of freedom of the top and bottom edges are fixed about the tangential direction to simulate the flange effects.

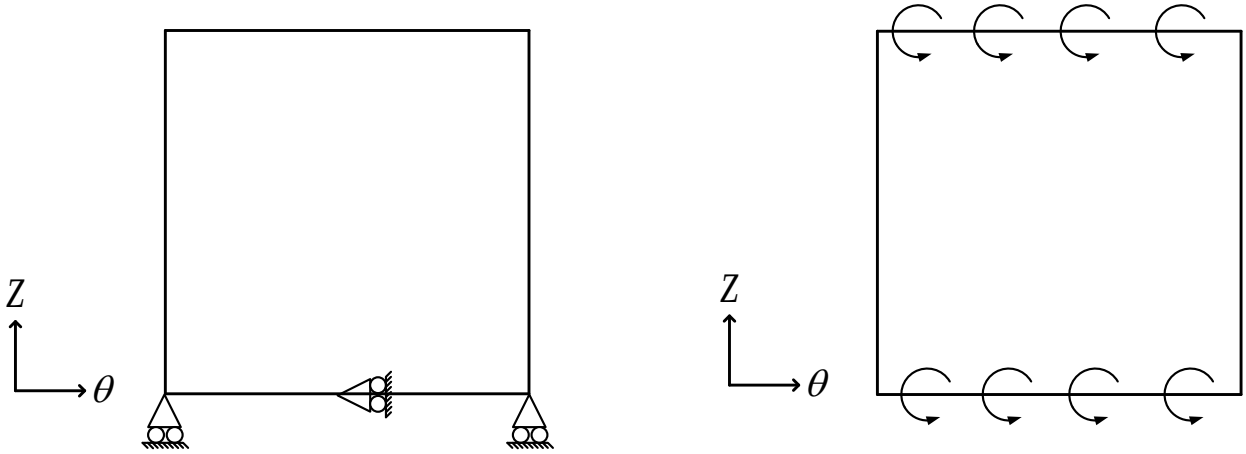

Figure 3.33: Base FEM model boundary conditions

The variable parameters in the study include the radius of curvature, web panel slenderness, and web panel aspect ratio. The range of the variable parameters is as follows:

- Panel aspect ratio: 1,2,3
- Radius of curvature: 300, 500, 700, flat (ft)
- Web panel slenderness: 150, 200, 250, 300
- Stress ratio: 0, 0.2, 0.5

The stress ratio represents the relationship between high and low cyclic in-plane stresses as shown in Figure 3.34. The stress ratio and stress range relationship will be discussed later.

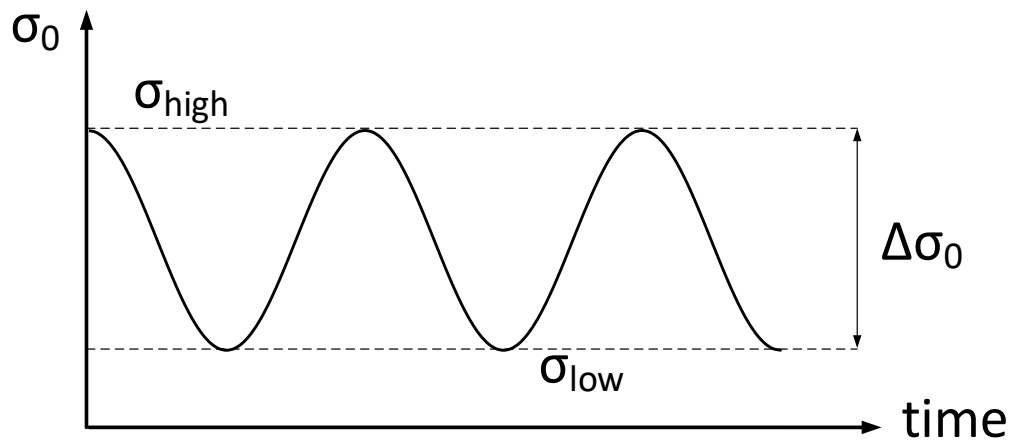

Figure 3.34: In-plane cyclic stress

The initial imperfection of the web panel W_0 was considered to follow a half-Sine function pattern, as shown in Figure 3.35.

$$w_0(x,y) = e_0 \sin\frac{\pi x}{a}\sin\frac{n\pi y}{b} \tag{3.24}$$

The maximum value of the W_0, e_0, is scaled to the web panel fabrication tolerance given by the bridge welding code (AWS 2010):

$$e_0 \le \frac{D}{t} \tag{3.25}$$

where D is the web height. Considering the web height of 100 inches results in the e_0 = 0.67 inch. The web panels of curved girders experience cross-section rotations, and flange rotations. As explained in the introduction, these geometric imperfections have negligible effects for the web-to-compression flange region. Therefore, only web panel out-of-plane imperfections were considered. MATLAB (2020) code was programmed to impose the initial imperfection and generate a FEM mesh of the curved web panel. The imperfect mesh was inputted in the ABAQUS to run the analysis.

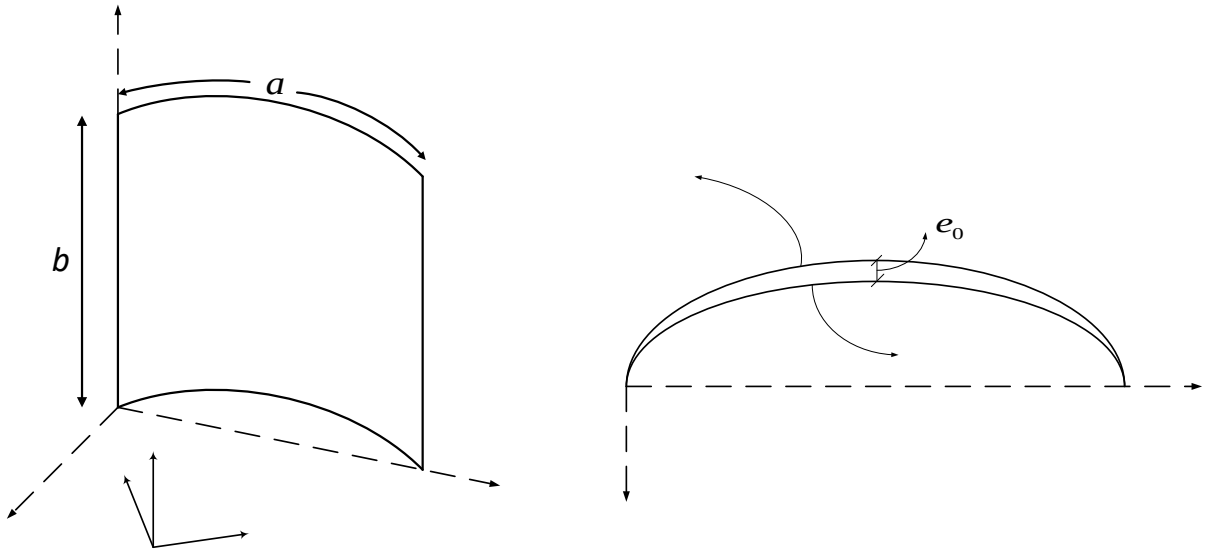

Figure 3.35: Curved web panel and initial imperfection definition

Three variations of the initial imperfection pattern were used for the three groups of the parametric models with a panel aspect ratio of one to three. Figure 3.36 illustrates the imperfection pattern corresponding to the web panel aspect ratios.

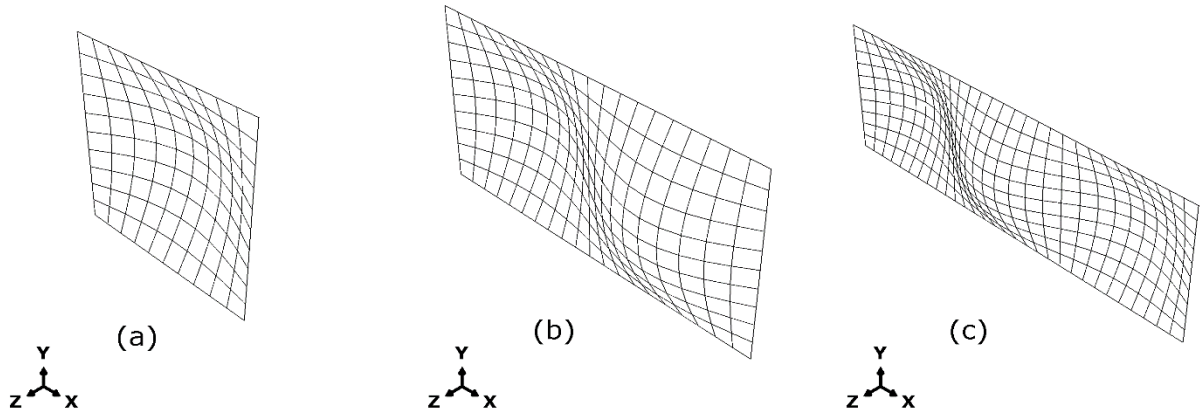

Figure 3.36: Imperfection patterns, (a) panel aspect ratio = 1, (b) panel aspect ratio = 2, and (c) panel aspect ratio = 3

3.3.3 Selection of In-plane Bending Stress

The in-plane bending stress, σ_0, was chosen based on the linear elastic buckling load of the parametric models and the resultant secondary bending stress. In the more slender web panels, the in-plane stress was decreased accordingly. Table 3.5 presents the magnitudes of in-plane bending stress and the critical buckling load corresponding to the web panel slenderness ratios. The buckling load was calculated by the Euler buckling formula (Ziemian 2010):

$$\sigma_{cr} = k_{\sigma}\sigma_e \tag{3.26}$$

$$\sigma_e = \frac{\pi^2 E}{12(1-\nu^2)}\beta^2 \tag{3.27}$$

where σ_{cr} is the web panel critical buckling stress, σ_e is the Euler's buckling stress, k_σ is the coefficient of the buckling stress under bending, E is elastic modulus, ν is the Poisson's ratio, β is the slenderness ratio. The k_σ is equal to 39.6 for the flat web panel under pure bending with the simply-supported at loaded edges, and fixed-supported at the unloaded edges. The in-plane bending stress, σ_0 was applied in 200 fixed increment steps to obtain a smooth in-plane stress versus corresponding secondary bending stress curve.

Table 3.5: In-plane bending stress and critical buckling stress of the parametric models

Slenderness β	**In-plane bending stress σ_0 (ksi)**	**Elastic buckling stress σ_{cr} (ksi)**
150	50	46
200	35	26
250	25	16.5
300	18	12

3.3.4 Fatigue Assessment Method

The applicability of the hot-spot stress and nominal-stress method for fatigue assessment is discussed and compared. In the hot-spot method, the secondary bending stress at the web top, i.e., flange, needs to be extrapolated based on at least 2 points in the vicinity of the web top. The extrapolation is required to exclude the weld notch effect. The location of the extrapolation points depends on the web thickness, as shown in Figure 3.37. The reference point positions would change for varied web thickness, slenderness, of the parametric models.

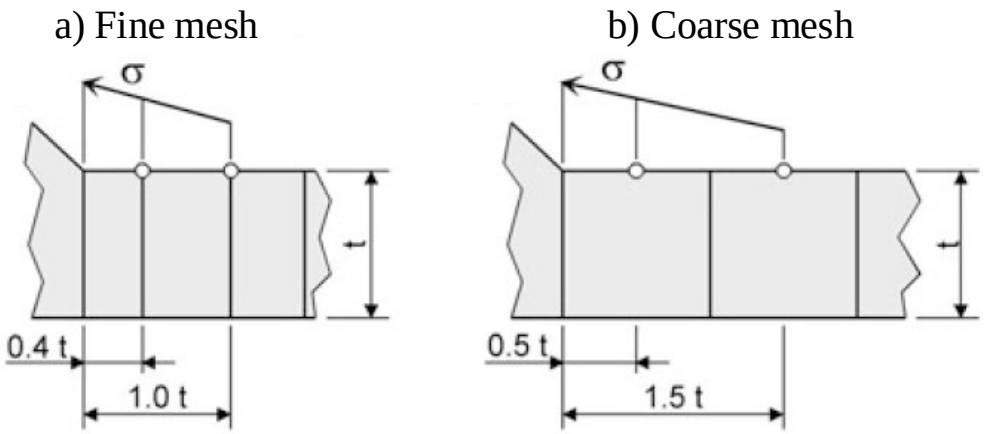

Figure 3.37: Hot-spot method reference point locations (Hobbacher 2016)

In addition to the extra computational cost, a reliable conclusion based on the slenderness effect could not be obtained due to the different hot-spot reference points in the parametric models. Therefore the nominal-stress method was applied in this study, and the constant amplitude fatigue threshold, CAFL, of 16 ksi corresponding to the web breathing experimental study (Kuhlmann and Spiegelhalder 1999) was considered. High stress gradients and concentrations were recorded at the cracked regions of the breathing test girders (Figure 3.38). A proper selection of FEM mesh in terms of mesh size, element type, and integration point is required to capture the accurate secondary bending stress. The validity of the FEM method is discussed in the next section.

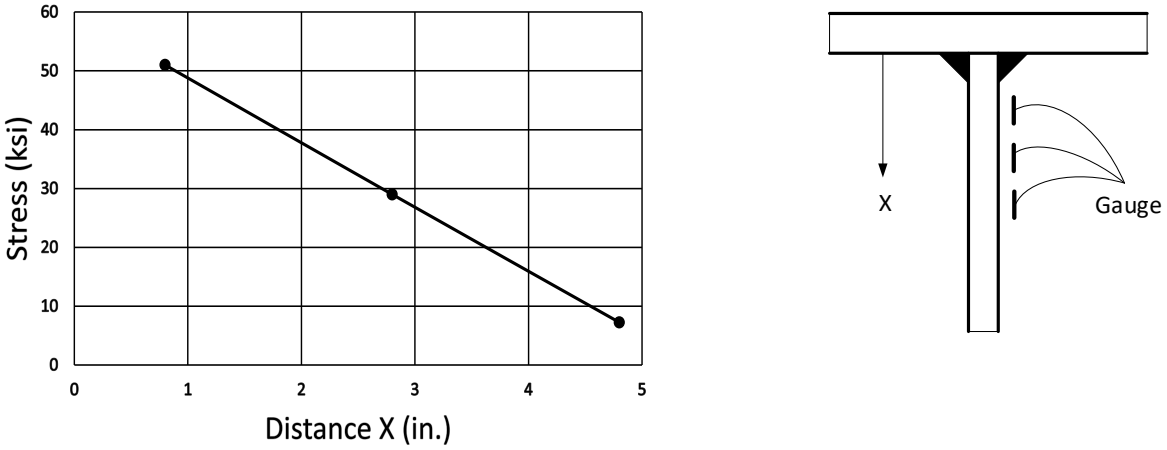

Figure 3.38: Secondary bending stresses measured on a test girder (Spiegelhalder 2000)

3.3.5 Secondary Bending Stress Calculation Validation

Proper calculation method of the secondary bending stresses is crucial to investigate the crack prone regions in the parametric studies. The experimental study by Kuhlmann and Spiegelhalder (1999) was selected for the secondary bending stress calculation validation due to availability of the test data and also the study output was used in developing the Eurocode (2006) web breathing limit. Four simply supported girders with slender webs were loaded under the concentrated load to examine the web breathing cracks. Non-prismatic flange cross-sections were considered in the way that the web panels located at the mid-span experience the uniform bending and shear as shown in the Figure 3.39.

The test girders dimensions and properties used for validation are given in the Table 3.6. In order to impose the initial geometric imperfections of web panels into analysis, the following two step procedure was implemented. First, a linear buckling analysis was conducted to extract the buckling shape modes, and the magnitude of the deformations were scaled to fit the average measured initial imperfection of the test girder. Second, the scaled buckling shape modes were used as the initial geometry to run a geometrically nonlinear analysis. The ABAQUS (2019) S4

shell elements, having 6 DOF's per node with 5 integration point through the thickness, were used to model the web, transverse stiffeners, and flanges. As Figure 3.40 shows, a fine mesh, 1 inch by 1 inch square, was used for modeling the web region to capture the high stress concentration at the cracked area. Shell element stress output in vertical direction, normal to the flange, located at the surface of the element was used to define the secondary bending stress at the web-to-flange connection.

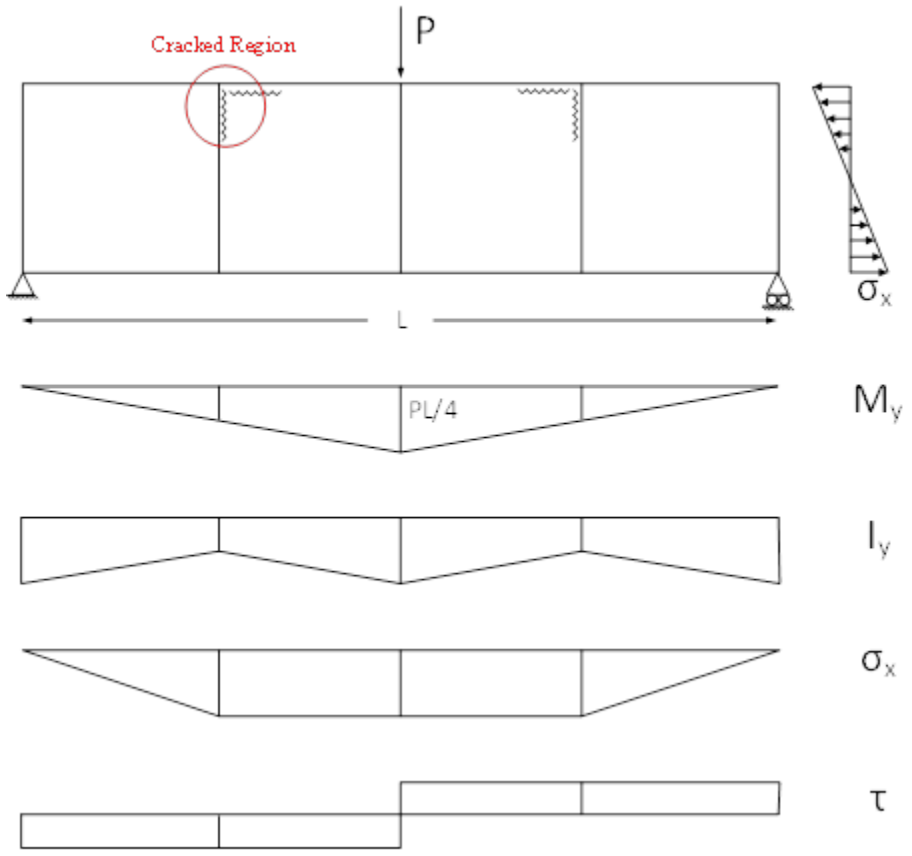

Figure 3.39: Loading, bending, and shear stress diagram of (Kuhlmann and Spiegelhalder 1999) study

Table 3.6: Test girder dimensions and properties

Web slenderness	Web height (inch)	Panel aspect ratio	Elastic modulus (ksi)	Flange Thickness (inch)
250	59	1	$30.5*10^3$	0.6

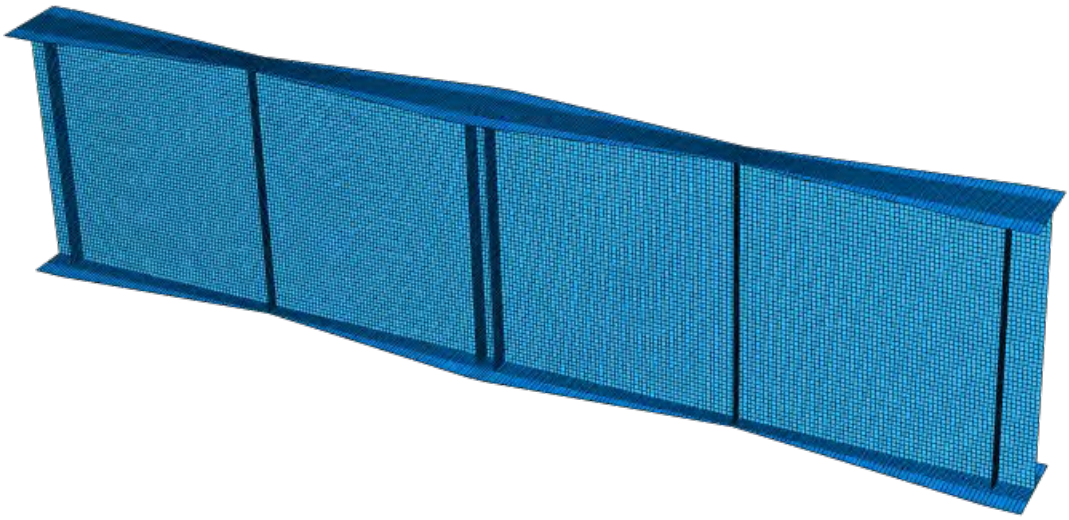

Figure 3.40: ABAQUS test girder model

The simulated and measured web secondary bending stress at the cracked region of the test girders are given in Table 3.7. The critical element outputs of the simulated girders are shown in the Figure 3.41, the flange elements are hidden for better illustration. Excellent agreement (3.5% error) between the measured and simulated web stresses was obtained due to the fine mesh and full integration of shell elements.

Table 3.7: Simulated and measured secondary bending stresses of the Kuhlmann and Spiegelhalder (1999) study

Simulated (ksi)	Measured (ksi)	Error
41.9	43.5	3.5 %

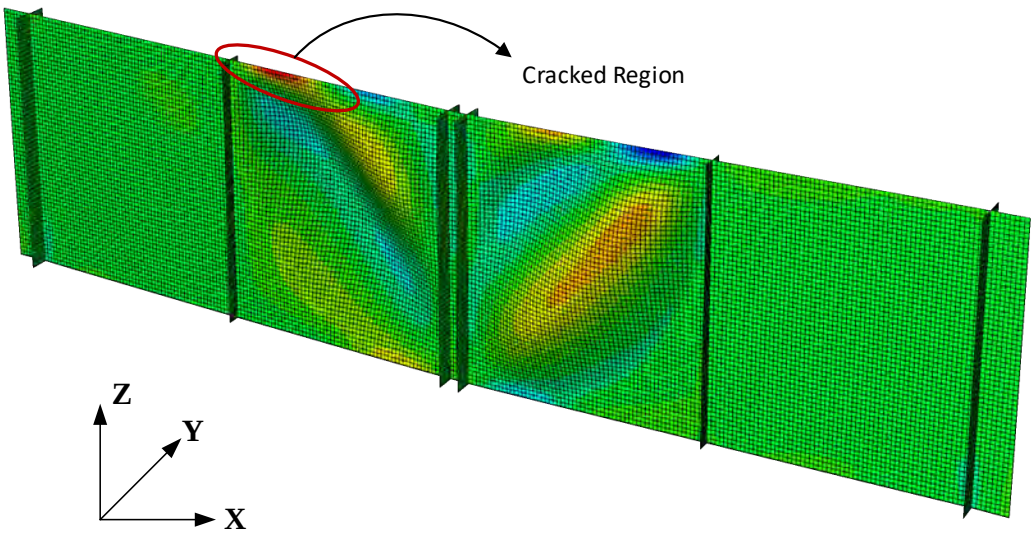

Figure 3.41: Vertical stress distribution and corresponding critical elements

3.3.6 Maximum In-plane Stress Determination

The method developed by Maeda and Okura (1983) was applied to determine the maximum allowable in-plane stress so that the resultant secondary bending stress range does not lead to fatigue cracking. The approach was explained in prior sections and therefore is discussed only briefly here. The relationship between in-plane stress and stress range can be given by:

$$ST = \frac{\sigma_L}{\sigma_H} \tag{3.28}$$

$$\Delta\sigma_0 = \sigma_H (1 - ST) \tag{3.29}$$

where ST is in-plane stress ratio, $\Delta\sigma_0$ is the in-plane stress range, σ_L and σ_H is the minimum and maximum in-plane stress, respectively. A slope triangle with a fixed base equal to the secondary bending stress range fatigue resistance, $\Delta\sigma_c$, is moved along the in-plane versus secondary bending stress curve until the predefined stress ratio is met. Figure 3.42 illustrates the method for the preset stress ratio of 0.5, and the triangle with a solid line defines the maximum in-plane stress denoted by σ_H.

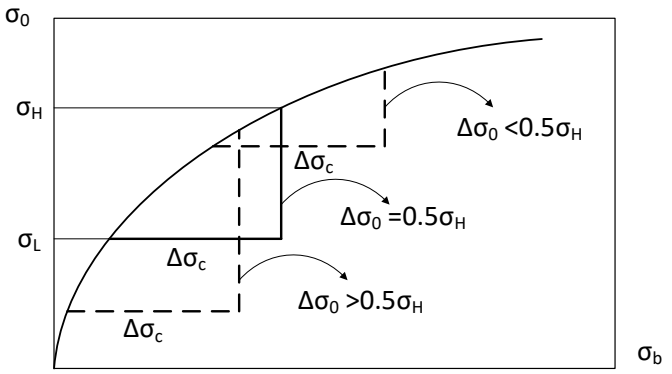

Figure 3.42: Maeda and Okura (1983) approach for finding the maximum σ_0

A search module was programmed in MATLAB (2020) to implement the procedure. Figure 3.43 explains the different steps from simulation to post-processing. First, the parametric models were simulated and analyzed by incremental geometric nonlinear analysis through ABAQUS (2019) FEM software. The in-plane and secondary bending stress were accessible in terms of the load step time and shell elements stress output, respectively. The in-plane and secondary bending stress were outputted for all the elements located at the top of the curved panel representing the web-to-compression flange connection. The secondary bending stresses were outputted at both sides of the shell elements surfaces. All the data related to the in-plane stress versus secondary bending stress curves for each element were inputted in the search module developed in MATLAB (2020). The search module loops over all the elements and the related stress curves and finds the corresponding maximum in-plane stress based on the Maeda and Okura (1983) approach.

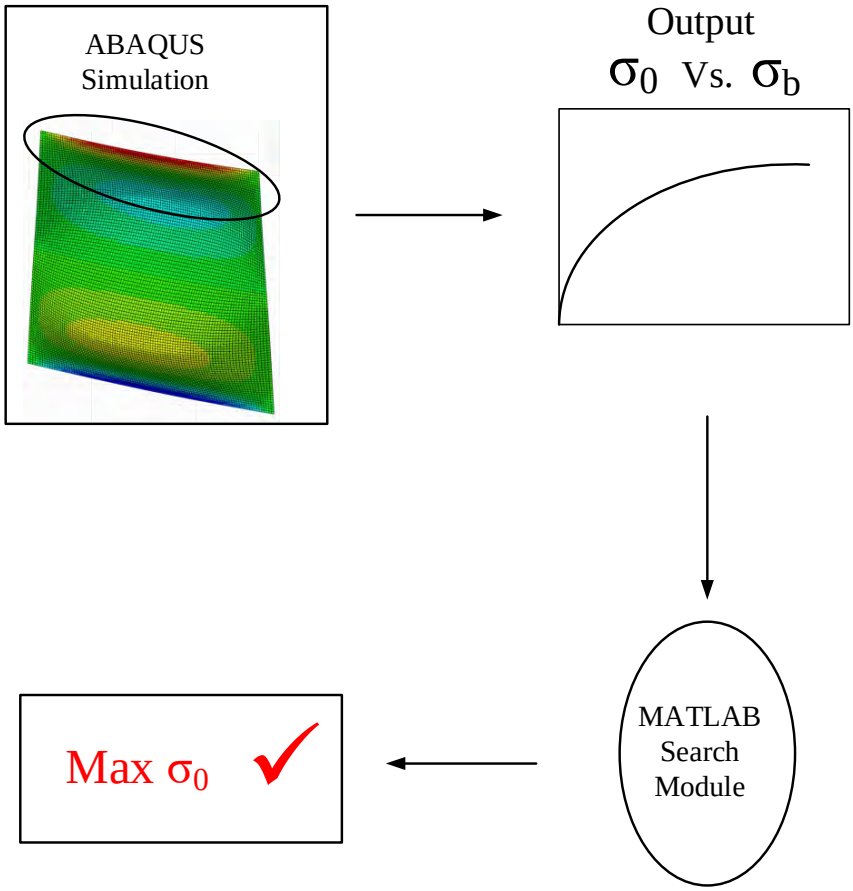

Figure 3.43: Finding maximum in-plane stress flow chart

3.3.7 Result and Discussion

The location of the critical elements for fatigue cracking depends on the web panel slenderness, aspect ratio, and stress ratio and can occur anywhere along the top of the web panel. In addition, since the focus of the study was to determine the web breathing of the curved web panels and to examine the parameters on the maximum in-plane stress to prevent fatigue cracking, the results based on the maximum in-plane stress are discussed in the following. Supporting data, including the absolute values of the maximum in-plane stresses, are provided in Jalali (2022).

3.3.7.1 Curvature Effect

Figure 3.44 shows the radius of curvature effect on the maximum in-plane stress that can be applied to the web panels without fatigue cracking at the compressive region. The in-plane stresses of the curved web panels were normalized to the corresponding flat web panel stress. As the curvature increases, the maximum allowable in-plane stress decreases due to the amplified web lateral distortions. In other words, smaller in-plane bending moment causes fatigue cracks in curved web panels compared to the equivalent flat web panels. The curvature influence on in-plane bending stress reduction gets smaller as the web panel slenderness increases. This behavior is analogous to the initial imperfection effect on the ultimate load bearing of the flat plates, if the curvature is considered as an additional imperfection. The initial imperfection effect is more significant for stocky plates, and the influence vanishes for plates with high slenderness.

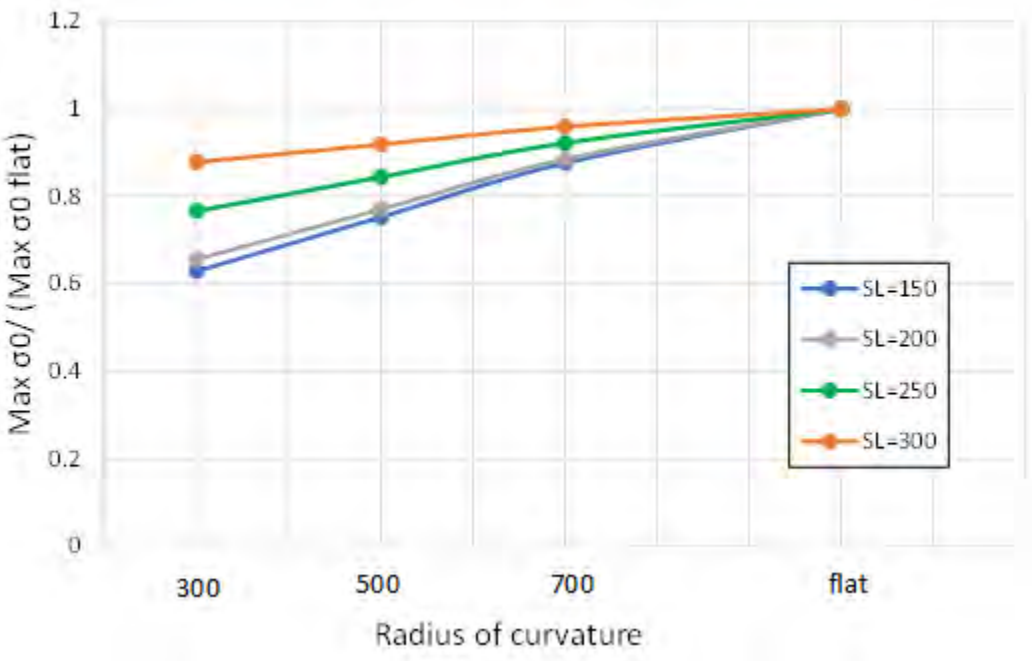

Figure 3.44: Maximum in-plane stress critical for web breathing, panel aspect ratio = 1, stress ratio = 0

3.3.7.2 Stress Ratio Effect

The in-plane stress ratio was investigated on the web breathing of the curved panels. Three stress ratios, represented by equation 3.28, were considered to examine the most critical in-plane stress combination. Maximum in-plane stress for the curved web panel of a radius of 300 feet was plotted against the slenderness for the three web panel aspect ratios of 1 to 3, given in Figures 3.45 through 3.47. The maximum in-plane stresses were normalized by the maximum in-plane stress of slenderness equal to 150. For all cases, the controlling stress ratio was equal to zero, where the smallest values for maximum in-plane stress were obtained. The influence of stress ratio was higher on the web panels with a smaller slenderness ratio, i.e., 150, and as the slenderness increases, the effect became less prominent.

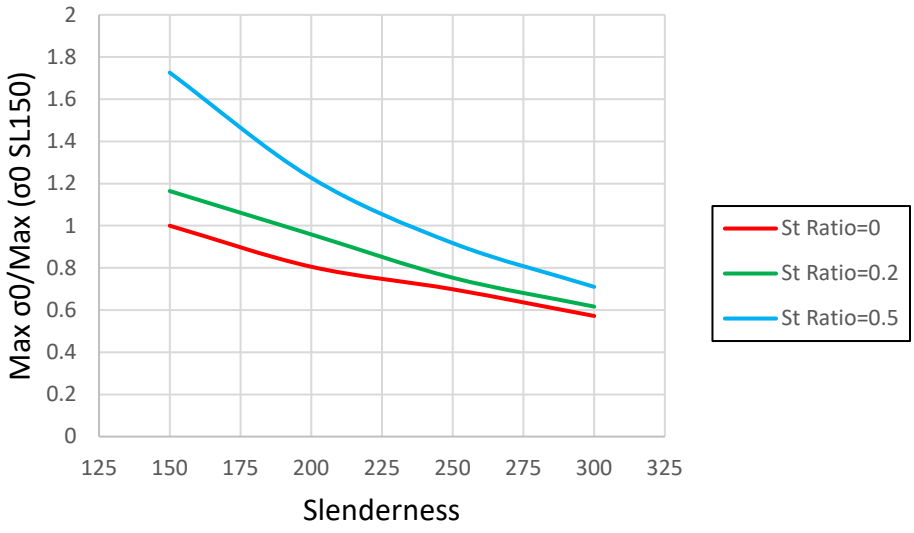

Figure 3.45: Stress ratio effect on the maximum in-plane stress, radius of curvature = 300 ft, panel aspect ratio = 1

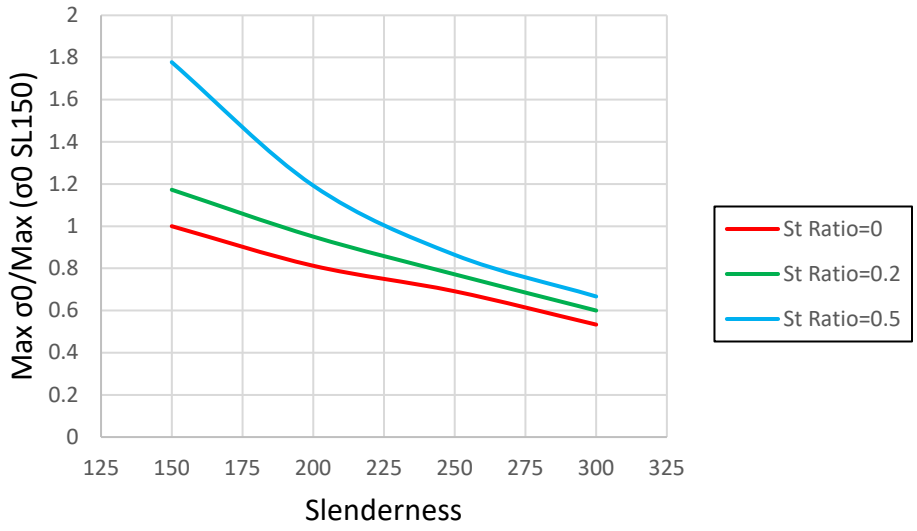

Figure 3.46: Stress ratio effect on the maximum in-plane stress, radius of curvature = 300 ft, panel aspect ratio = 2

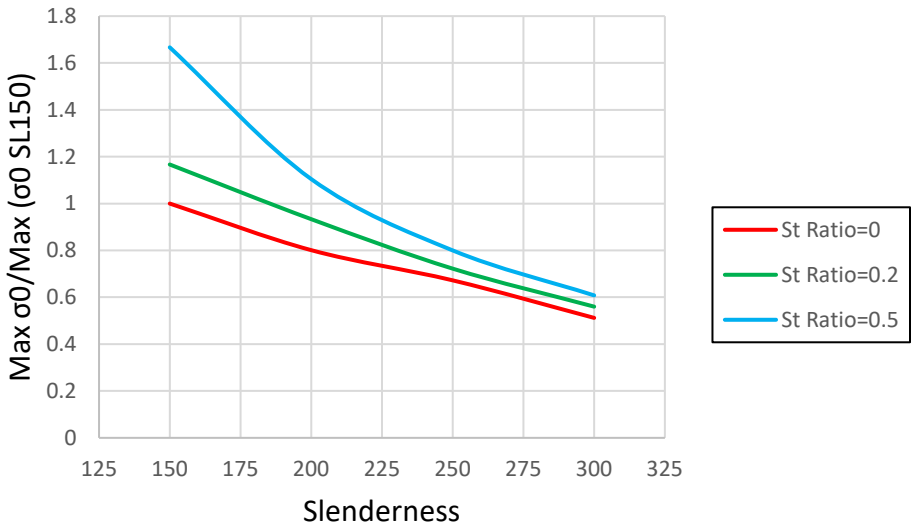

Figure 3.47: Stress ratio effect on the maximum in-plane stress, radius of curvature = 300 ft, panel aspect ratio = 3

3.3.7.3 Fatigue Design Limit Development

It is desired to define a fatigue limit in terms of in-plane bending stresses that allows the safe design of curved web panels without fatigue cracking due to web breathing. The following equation was developed based on the parametric finite element simulations:

$$\max \sigma_0 \leq \begin{cases} \dfrac{\Delta\sigma_c^{Type\,2}}{1-ST} \\ 1.5\sigma_{cr} \end{cases} \tag{3.30}$$

where *max* σ_0 is the maximum in-plane bending stress, $\Delta\sigma_c^{Type\,2}$ is the fatigue resistance of crack type 2, *ST* is the stress ratio, and σ_{cr} is the linear elastic bend buckling stress of flat web.

The tensile component of the in-plane bending stress causes fatigue crack type 2 at the bottom of the web-to-transverse stiffener. Hence, the controlling equation to prevent fatigue cracking at web-to-flange connection must be bounded by both tensile and compressive stresses. The top term of the derived equation limits the in-plane bending stress range to the fatigue crack type 2 strength, and the bottom term controls the maximum in-plane bending stress in the compressive region of the web.

AASHTO (2020) defines the web-to-stiffener fatigue (crack type 2) detail category as C' with fatigue resistance, constant amplitude fatigue threshold, equal to 12 ksi. The maximum in-plane stresses calculated by the simulations were normalized to the fatigue crack type 2 resistance (12 ksi) to explain the developed equation (Figure 3.48). The curves located on the top of the dashed lined correspond to the models that the crack type 2 governs the design. As can be seen, fatigue crack type 2 controls the design for the web slenderness ratios up to almost 250. The bottom term of the derived equation controls the design for high slenderness ratios, i.e., 275. This means that fatigue cracks at the web-to-bottom stiffener occur before fatigue cracks at the web-to-flange connections for the models having slenderness up to 250. Consequently, a selection of the models

that web breathing governs, the curves located below the dashed line, was made to define the bottom term of equation 3.30. The maximum allowable in-plane stress were averaged and normalized to linear elastic bend buckling stress of the equivalent flat web panel.

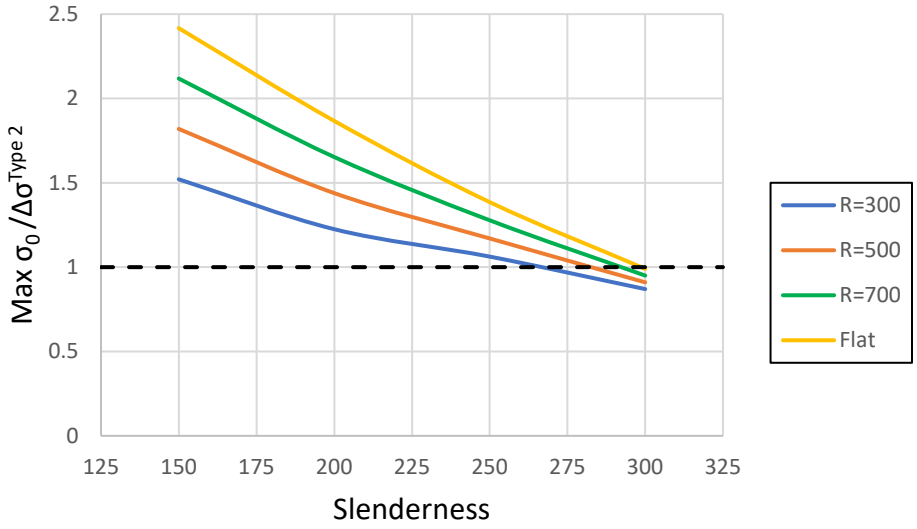

Figure 3.48: In-plane stress versus slenderness, web panel aspect ratio = 1, stress ratio = 0

It should be noted that AASHTO (2020) requires a longitudinal web stiffener for web slenderness of over 150. The present study shows that there is no concern for the web breathing fatigue cracking in the compression web area for the slenderness of up to 250 as long as the fatigue crack at the web-to-stiffener is checked.

The recommended equation was derived based on curved web panels with a neutral axis located in the middle of the web height. The composite action of the horizontally curved steel bridges shifts up the neutral axis. A smaller area of the composite web is in compression compared to the non-composite webs. Hence the proposed equation is applicable to the composite girders and results in a conservative limit.

3.3.8 Conclusions

Web breathing of the curved web panels was studied through parametric finite element analysis. The effects of the radius of curvature, web slenderness, stress ratio, and panel aspect ratio were discussed. It was observed that increasing curvature decreases the in-plane bending stress critical for web breathing. However, the difference is more significant for the less slender webs. A fatigue design limit equation was proposed that is applicable to both the curved and straight girders within the AASHTO (2020) limits. In addition, it was observed that the fatigue crack at the web-to-stiffener controls the web breathing for the web slenderness up to 250.

3.4 Curved Web panel Under Combined Loading

3.4.1 Introduction

This section investigates the combined effects of bending and shear stress on the fatigue behavior of curved web panels. When a slender web is loaded under bending and shear, fatigue cracks appear at the web-to-flange and web-to-stiffener connection due to cyclic web deformations. Figure 3.49 shows the fatigue cracks of a straight girder test (Kuhlmann and Spiegelhalder 1999) under combined loading condition.

Figure 3.49: Fatigue cracks under combined loading test (Kuhlmann and Spiegelhalder 1999)

3.4.2 Methodology

3.4.2.1 FEM Model Specification

ABAQUS (2019) FEM software was used to run the parametric simulation of the curved web panels. The fine mesh, 1-inch by 1-inch square elements, was constructed of the S4 shell elements, having 6 DOF's per node with five integration points through the thickness. The loading scheme is illustrated in Figure 3.50. The bending stress was applied as equivalent nodal forces on the vertical edges as explained in the previous chapter. The shear force was applied by a constant state of shear stress with shear stresses on all four edges. The shear stresses were also modeled by constant nodal forces. The direction of the shear forces on the horizontal edges, representing flanges, were applied in the tangential direction of the cylindrical coordinate. The shell element normal vectors were defined in the cylindrical coordinate system, so the longitudinal shell element stress outputs were normal to the vertical, representing the stiffener, edges.

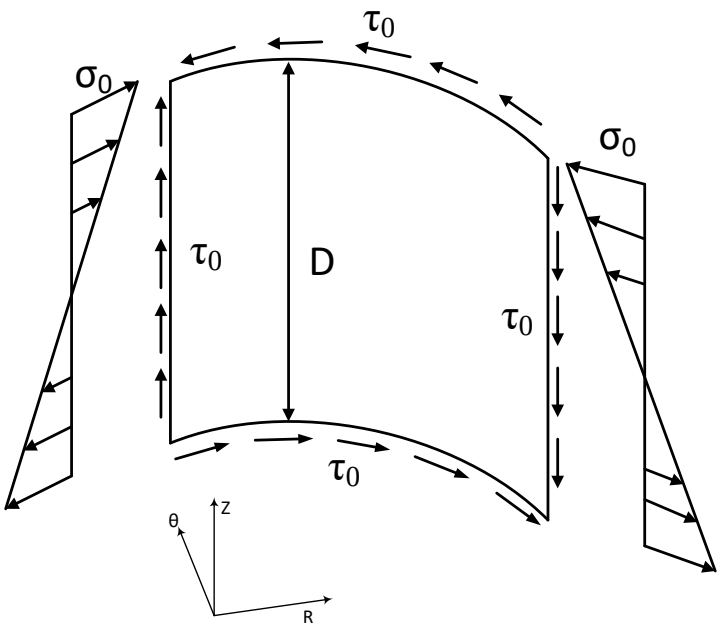

Figure 3.50: Base FEM model loading

The web height, *D*, is equal to 100 inches, and the panel length was changed according to the panel aspect ratio of the models. The modulus of elasticity and the yield stress are 29000 ksi and 50 ksi, respectively.

The boundary conditions were imposed based on the Broujerdian et al. (2015) study and illustrated in Figure 3.51. The radial translation of all edges is restrained. The rotation of vertical and horizontal edges is fixed against the tangential and vertical direction, respectively.

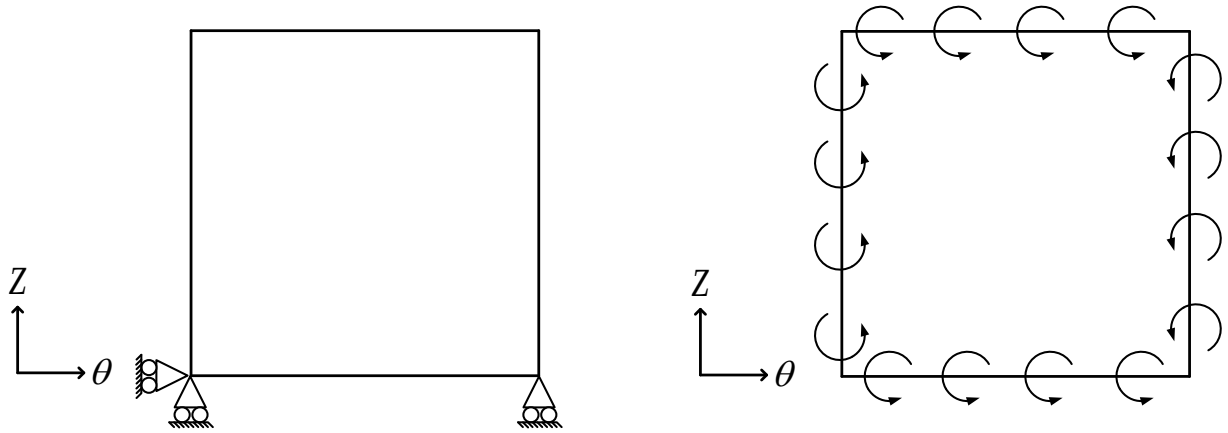

Figure 3.51: FEM model boundary conditions

The range of parameters that were investigated in the study are as follows:

- Panel aspect ratio: 1, 1.5, 2
- Radius of curvature: 300, 500, 700, flat (ft)
- Web panel slenderness: 100, 125, 150, 200
- Load combinations: $\tau_0=\sigma_0$ and $\tau_0=0.5\sigma_0$
- Stress ratio = 0, 0.2, 0.5

The maximum panel aspect ratio was selected as 2 because the web panel shear buckling stress decreases dramatically for the web panel aspect ratio of 1 and slenderness over 150. The maximum web slenderness allowed by AASHTO (2020) is 300, and longitudinal stiffeners are required for slenderness over 150. Three slenderness below 150 and one slenderness over 150 were considered to examine the need for a longitudinal stiffener. In the case of bending beams, the normal stresses are usually a multiple of shear stresses. Two combinations were selected to investigate the superimposed bending and shear stress on the fatigue performance of the curved web panels.

The initial imperfection of the web panel w_0 was considered to follow a half-Sine function pattern, as shown in Figure 3.52:

$$w_0(x,y) = e_0 \sin\frac{\pi x}{a}\sin\frac{n\pi y}{b} \tag{3.31}$$

The maximum value of the W_0, e_0 , was scaled to the web panel fabrication tolerance given by the bridge welding code (AWS 2010) :

$$e_0 \le \frac{D}{t} \tag{3.32}$$

where D is the web height. Considering the web height of 100 inches results in the e_0 =0.67 inch. A MATLAB (2020) code was programmed to impose the initial imperfection and generate a FEM mesh of the curved web panel. The imperfect mesh was entered in ABAQUS.

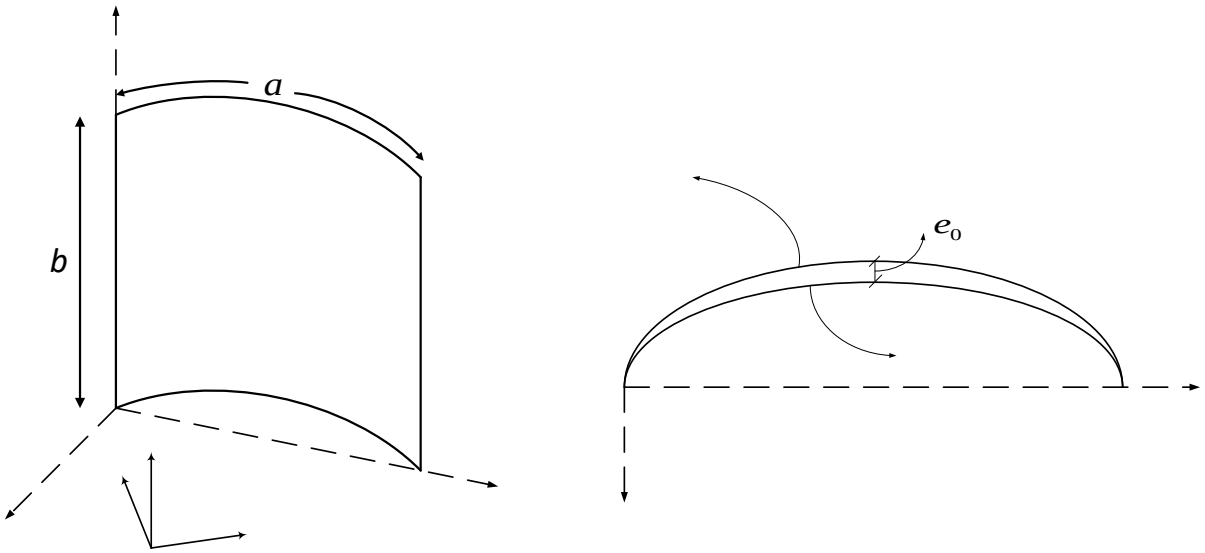

Figure 3.52: Curved web panel and initial imperfection definition

3.4.2.2 Selection of In-plane Stresses

The in-plane bending and shear stresses, σ_0 and τ_0 , were chosen based on the linear elastic buckling load of the parametric models and the resultant secondary bending stresses at the top and

vertical edges representing the flange and stiffener, respectively. The buckling load was calculated using the Euler buckling formula (Ziemian 2010):

$$\sigma_{cr} = k_{\sigma}\sigma_{e} \tag{3.33}$$

$$\tau_{cr} = k_{\tau}\sigma_{e} \tag{3.34}$$

$$\sigma_{e} = \frac{\pi^2 E}{12(1-\nu^2)}\beta^2 \tag{3.35}$$

$$k_{\tau} = \begin{cases} 5.6 + \dfrac{8.98}{\alpha^2}, \alpha \le 1 \\ 8.98 + \dfrac{5.6}{\alpha^2}, \alpha \ge 1 \end{cases} \tag{3.36}$$

where σ_{cr} is the web panel critical bend buckling stress, τ_{cr} is the shear buckling stress, σ_e is the Euler's buckling stress, k_σ is the coefficient of the bend buckling stress, k_τ is the coefficient of the shear buckling, E is elastic modulus, ν is the Poisson's ratio, β is the slenderness ratio, α is the web panel aspect ratio.

The in-plane stress is given in Table 3.8; the same in-plane stress was used for both load combinations. The ratio of bending stress to shear stress remained constant for both stress combinations, $\tau_0 = \sigma_0$ and $\tau_0 = 0.5\sigma_0$, throughout the single analysis. The geometrically nonlinear elastic analysis was applied in fixed 100 steps.

Table 3.8: In-plane bending stress and critical buckling stress of the parametric models

Slenderness β	In-plane bending stress σ_0 (ksi)	Bend buckling stress σ_{cr} (ksi)	Shear buckling stress τ_{cr} (ksi)
100	45	62	24.5
125	35	40	15.7
150	25	27	10.9
200	20	15	6.1

3.4.2.3 Fatigue Assessment Method and Validation

The nominal-stress method was applied to the parametric simulation results, as explained in the previous sections, to define the maximum in-plane stress with no risk of web breathing. The critical web stresses at the top of the web panel, representing the flange, and the vertical edge of the web panel, representing the stiffener, were compared to the fatigue resistance related to web breathing. The constant amplitude fatigue threshold, CAFL, of 16 ksi corresponding to the web breathing experimental study (Kuhlmann and Spiegelhalder 1999) was considered.

Shell element stress output was used to determine the critical web stresses. Consequently, a proper selection of FEM mesh in terms of mesh size, element type, and integration point was required to capture accurate results. The experimental study by Kuhlmann and Spiegelhalder (1999) was selected for the web stress calculation validation due to the availability of the test data. In addition, the study output was used in developing the Eurocode (2006) web breathing limit.

The test girders specification used for the validation study are given in Table 3.9 and Figure 3.53. In order to impose the initial geometric imperfections of web panels into analysis, the following two-step procedure was implemented. First, a linear buckling analysis was conducted to extract the buckling shape modes. The magnitude of the deformations was scaled to fit the

average measured initial imperfection of the test girder. Second, the scaled buckling shape modes were used as the initial geometry to run a geometrically nonlinear analysis. The ABAQUS (2019) S4 shell elements, having 6 DOF's per node with five integration points through the thickness, was used to model the web, transverse stiffeners, and flanges. Figure 3.54 shows that a fine mesh, 1 inch by 1 inch square, was used to model the web region to capture the high stress concentration at the cracked area.

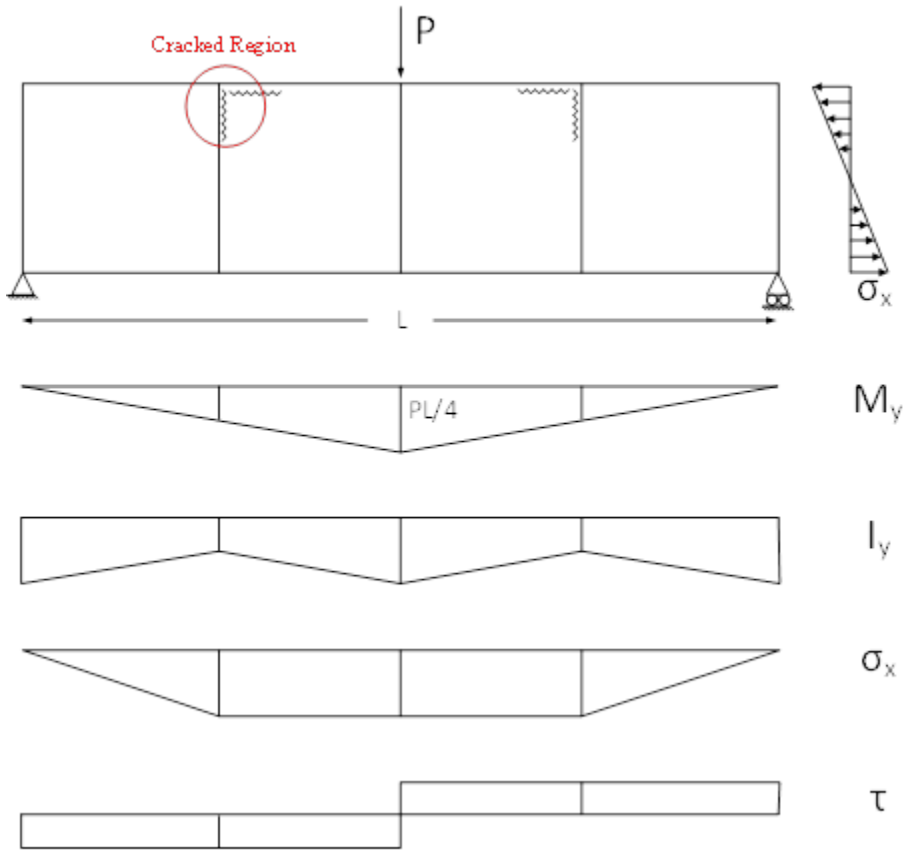

Figure 3.53: Loading, bending, and shear stress diagram of the Kuhlmann and Spiegelhalder (1999) study

Table 3.9: Test girder specification

Web slenderness	Web height (inch)	Panel aspect ratio	Elastic modulus (ksi)	Flange Thickness (inch)
250	59	1	$30.5*10^3$	0.6

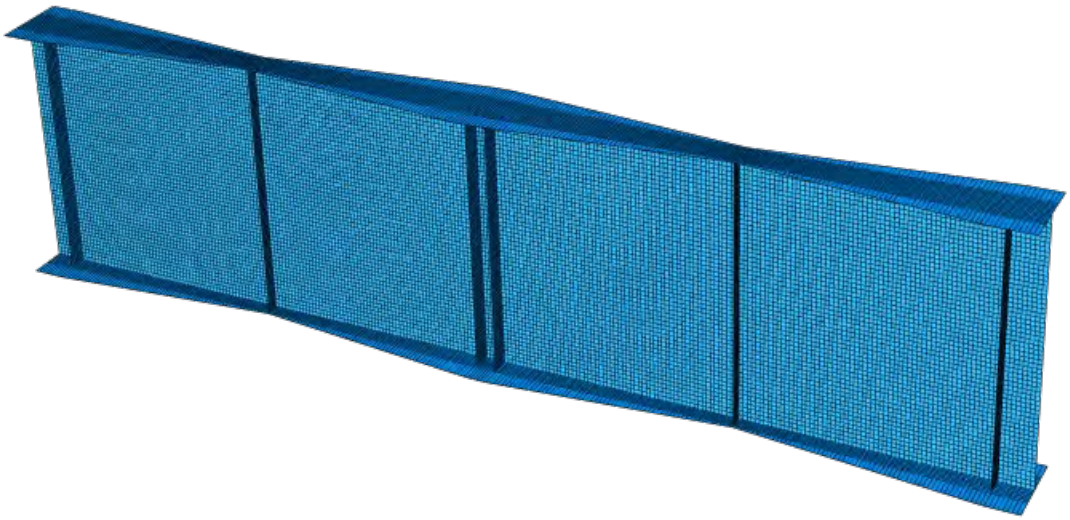

Figure 3.54: Abaqus test girder model

The simulated and measured web secondary bending stress at the cracked region of the test girders are given in Table 3.10. The critical element outputs of the simulated girders are shown in Figure 3.55, the flange elements are hidden for better illustration. Shell element stress output in the vertical and longitudinal direction was used for the web-to-flange and web-to-stiffener regions, respectively. There was an excellent agreement between the measured and simulated web stresses, within 3.5% error, for both regions due to the fine mesh and full integration of shell elements.

Table 3.10: Simulated and measured secondary bending stresses of the Kuhlmann and Spiegelhalder (1999) study

Case	Simulated (ksi)	Measured (ksi)	Error
Web-to-flange	41.9	43.5	3.5%
Web-to-stiffener	43.1	44.6	3.3%

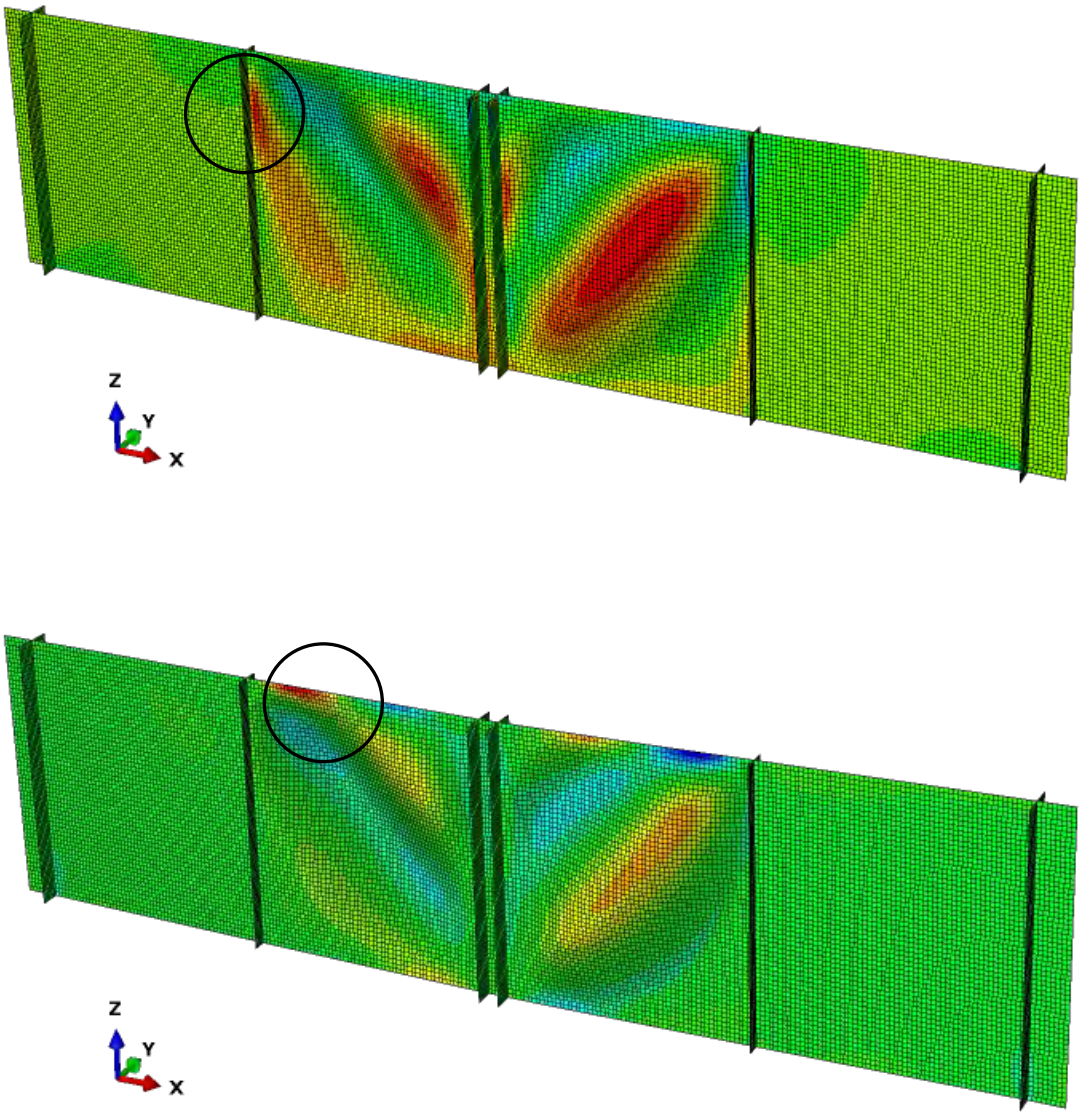

Figure 3.55: Critical elements at the cracked locations, (top) longitudinal stress distribution (bottom) vertical stress distribution

3.4.2.4 Maximum In-plane Stress Determination

The same approach considered in section 3.3 was applied to find the maximum in-plane stress to prevent web breathing cracks. An extension was added to the search module program in MATLAB (2020) to consider the vertical edge stress, representing the web-to-stiffener location,

in addition to the top web panel edge stress. The procedure is explained in Figure 3.56. The in-plane and secondary bending stress were outputted for the elements located at the top and vertical edge of the curved panel. Vertical and longitudinal shell element stress were considered for the flange and stiffener elements, respectively. The in-plane stress versus secondary bending stress curves were generated at both sides of the shell element surfaces. The search module in MATLAB (2020) program investigates the curves and outputs maximum in-plane stress based on the Maeda and Okura (1983) approach.

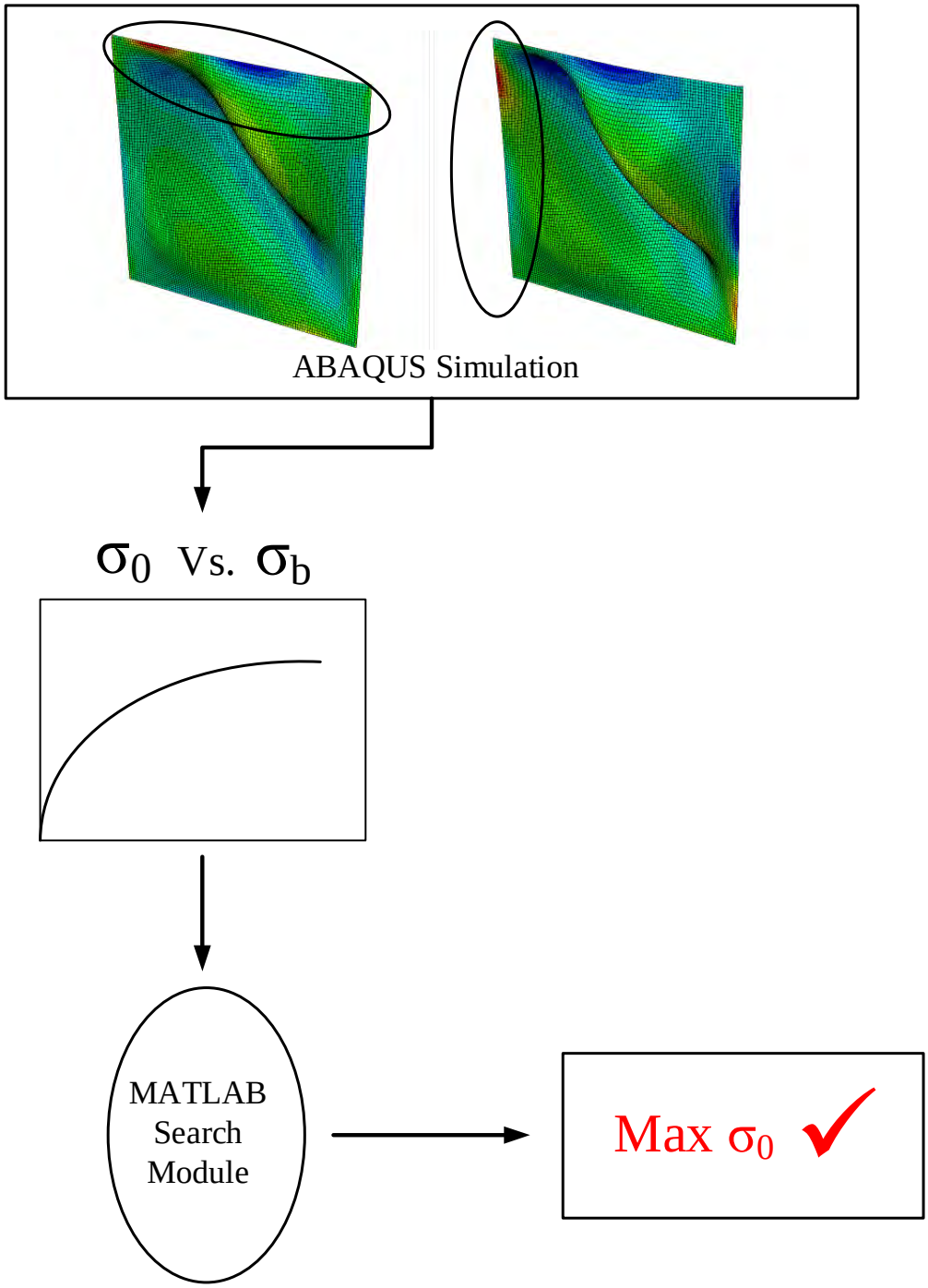

Figure 3.56: Finding maximum in-plane stress procedure

3.4.3 Result and Discussion

The result of analyzing the 288 cases of the parametric simulations is discussed in this section. The data were normalized accordingly for a better illustration of each section. The complete raw data are given in Jalali (2022).

3.4.3.1 Combined Loading Effect

Figure 3.57 shows the web deformations corresponding to the pure in-plane bending and combined bending and shear loading configuration. The in-plane shear stress had a dominant effect in changing the web deformations into the diagonal shear buckling pattern. The shear buckling stress was reached earlier than the bend buckling stress in both combined loading configurations $\tau_0=\sigma_0$ and $\tau_0=0.5\sigma_0$. The elastic shear buckling stress to bend buckling stress ratio for different panel aspect ratios was calculated based on equations 3.33 and 3.34 and is presented in Figure 3.58. The buckling stress ratios are independent of the web slenderness and apply to all slenderness ranges of the parametric models. The penetrating buckling shape modes under pure in-plane bending stress did not occur in the models under the combined action of bending and shear stress. This phenomenon resulted in a more stable web deformation. As a result, secondary bending stresses due to web out-of-plane distortions occurred at both the flange and stiffener.

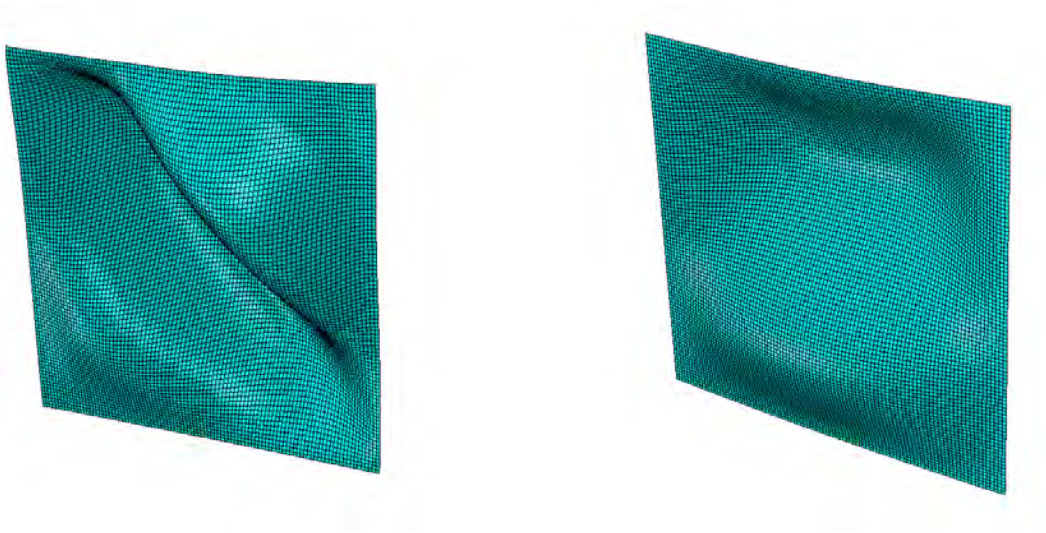

Figure 3.57: Web deformations for curved web panel (R = 300 ft, β = 200), (left) combined bend and shear loading: $\tau_0 = \sigma_0$ =20 ksi, (right) pure bending: loading σ_0 = 20 ksi

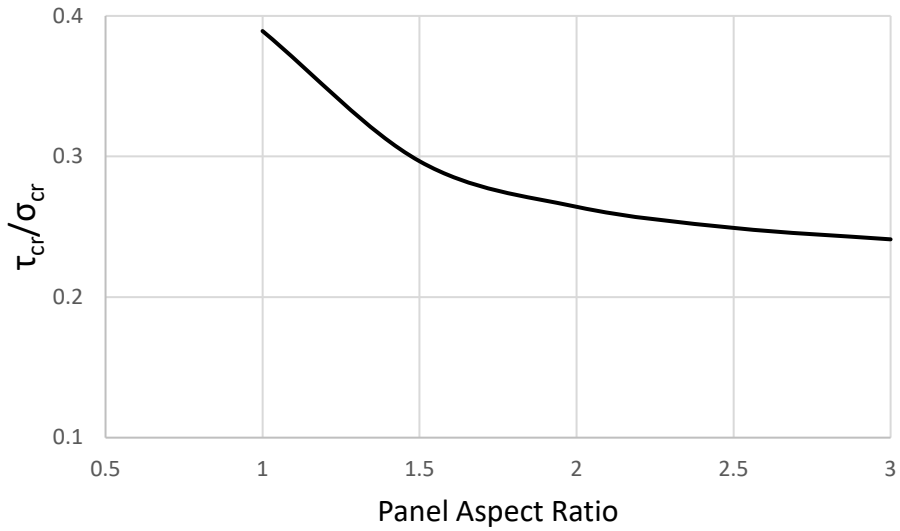

Figure 3.58: Shear to bend buckling stress ratio

3.4.3.2 Radius of Curvature Effect

Three radii of curvature representing the highly curved 300 ft, and moderately curved, 500 ft and 700 ft, bridges were analyzed and compared to the equivalent flat web panel. Figures 3.59 and 3.60 show the radius of curvature effect on maximum in-plane stress critical for web breathing considering the two load combinations τ_0=0.5σ_0 , and τ_0=σ_0 , respectively. The in-plane stresses of

the curved web panels were normalized to the corresponding flat web panel stress. The curvature effect on the maximum in-plane stress critical for web breathing depends on web panel slenderness and the combination of in-plane stresses. As the curvature increases, the maximum allowable in-plane stress decreases due to the amplified web lateral distortions, as given in Figure 3.59. The curvature influence on in-plane bending stress reduction gets smaller as the web panel slenderness increases.

The shear stress share of the combined loading significantly affects the curved web panel behavior. In the $\tau_0=\sigma_0$ case, the curvature effect in decreasing the maximum in-plane stress got smaller compared to the $\tau_0=0.5\sigma_0$ stress configuration, given in Figure 3.60. This can be explained by considering the shear buckling capacity compared to the bend buckling capacity (Figure 3.58). For each load increment of the $\tau_0=\sigma_0$ case, the shear buckling stress reaches 2.5 times faster than the bend buckling stress, and the resultant secondary bending stresses at the web panel are heavily affected by the shear stress. For the high web panel slenderness ratio β = 200, where the curvature effect decreases under in-plane bending stress, and the shear stress dominates the combined loading, the curved and flat web panels performed almost identically in terms of web breathing.

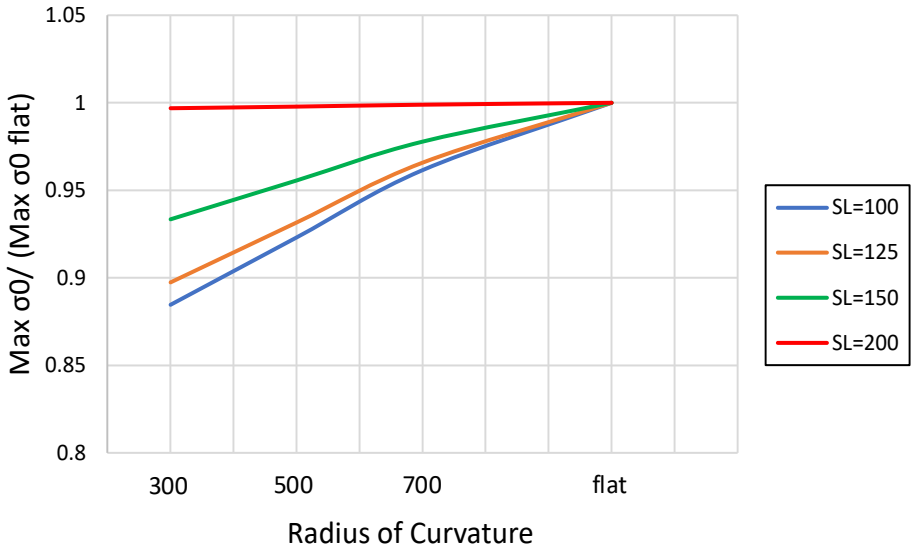

Figure 3.59: Maximum in-plane stress critical for web breathing versus radius of curvature, $\tau_0 = 0.5\sigma_0$, panel aspect ratio = 1

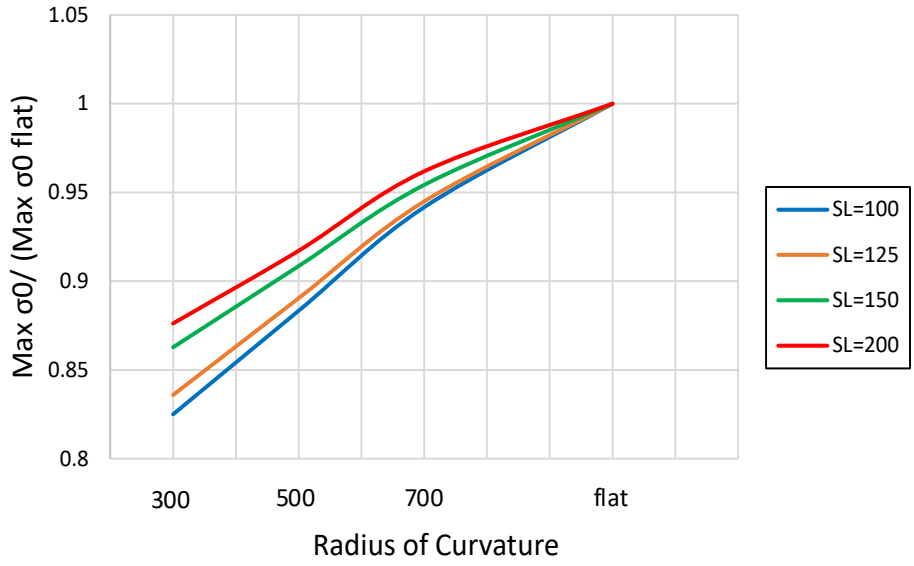

Figure 3.60: Maximum in-plane stress critical for web breathing versus radius of curvature, $\tau_0 = \sigma_0$, panel aspect ratio = 1

3.4.3.3 In-plane Stress Ratio Effect

The bending to shear stress ratio of the combined loadings τ_0=0.5σ_0 and τ_0=σ_0 remained constant during the ABAQUS simulations to generate in-plane stress versus secondary bending

stress curves. However, three stress ratios of 0, 0.2, 0.5 (defined by equation 7.5: $ST = \frac{\sigma_L}{\sigma_H}$) representing the relationship between high and low cyclic stresses were considered in the MATLAB search module. Maximum in-plane stress for the curved web panel of a radius of 300 feet was plotted against the slenderness for the three web panel aspect ratios of 1 to 2, given in Figures 3.61 through 3.63. The maximum in-plane stresses were normalized by the maximum in-plane stress of slenderness equal to 100. The τ_0=0.5σ_0 load combination was used for all graphs. For all cases, the controlling stress ratio was equal to zero, where the smallest values for maximum in-plane stress were obtained. The influence of stress ratio was higher on the web panels with a smaller slenderness ratio, i.e., 100, and as the slenderness increased, the effect became less prominent.

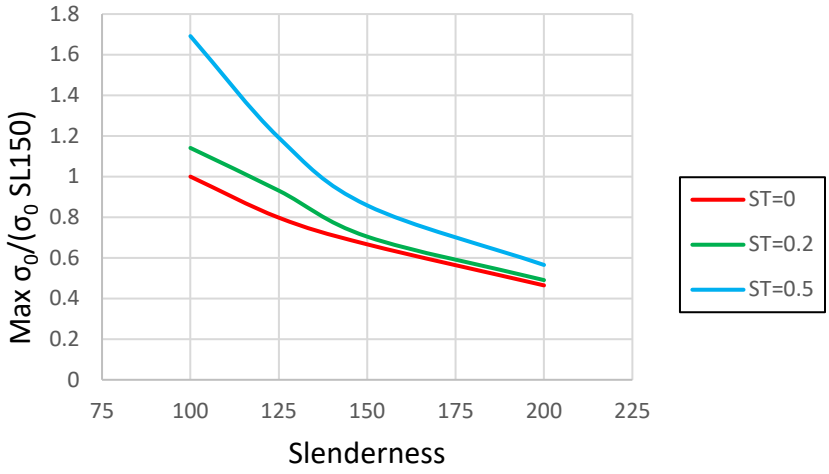

Figure 3.61: Stress ratio effect on the maximum in-plane stress, radius of curvature = 300 ft, τ_0 = 0.5σ_0 , panel aspect ratio = 1

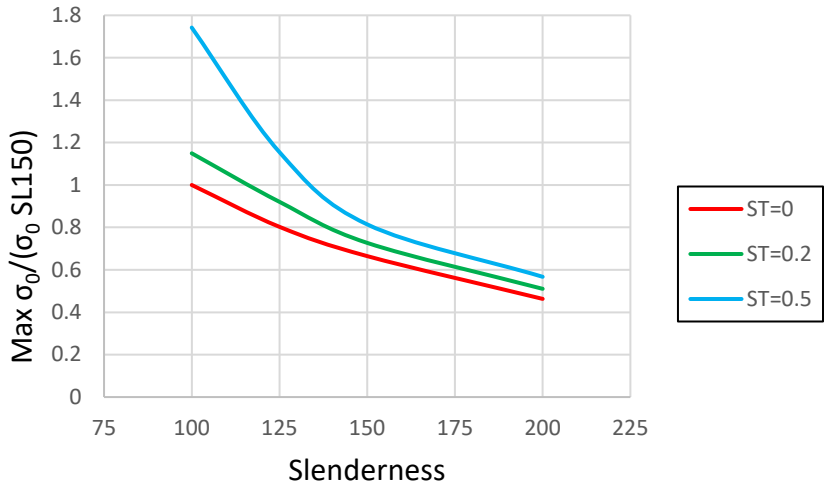

Figure 3.62: Stress ratio effect on the maximum in-plane stress, radius of curvature = 300 ft, $\tau_0 = 0.5\sigma_0$, panel aspect ratio = 1.5

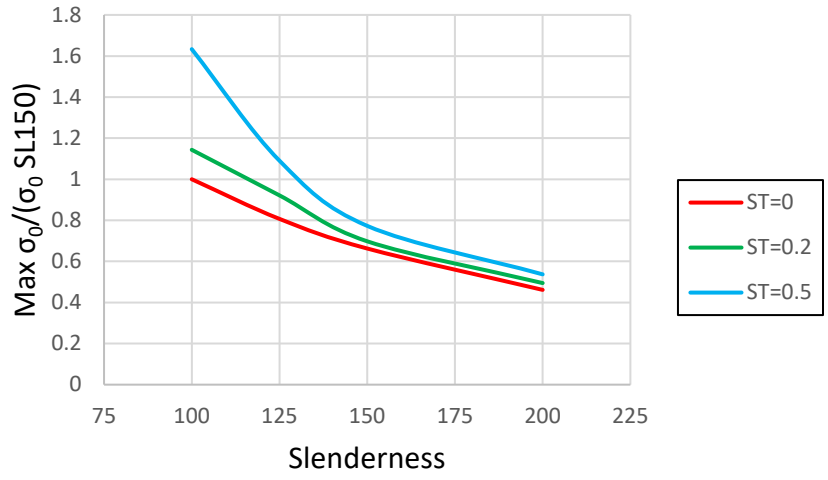

Figure 3.63: Stress ratio effect on the maximum in-plane stress, radius of curvature = 300 ft, $\tau_0 = 0.5\sigma_0$, panel aspect ratio = 2

3.4.3.4 Design Limit Development

In order to define a design limit for controlling the web breathing of curved web panels under combined loading, the effect of the fatigue crack at the web-to-stiffener, crack type 2, is discussed first. The maximum in-plane stresses calculated by the simulations were normalized to fatigue crack type 2 resistance (12 ksi). Figures 3.64 and 3.65 illustrate the in-plane stress versus

slenderness for two load combinations $\tau_0=0.5\sigma_0$ and $\tau_0=\sigma_0$, respectively. Both graphs were plotted based on the critical stress ratio, *ST=0,* and the web panel aspect ratio of 1. Figure 3.16 shows that fatigue crack type 2 governs the maximum in-plane bending stress corresponding to web breathing for web slenderness up to 175. On the other hand, fatigue crack type 2 has a controlling effect only for the slenderness of almost 100 for the group with the $\tau_0=\sigma_0$ load combination.

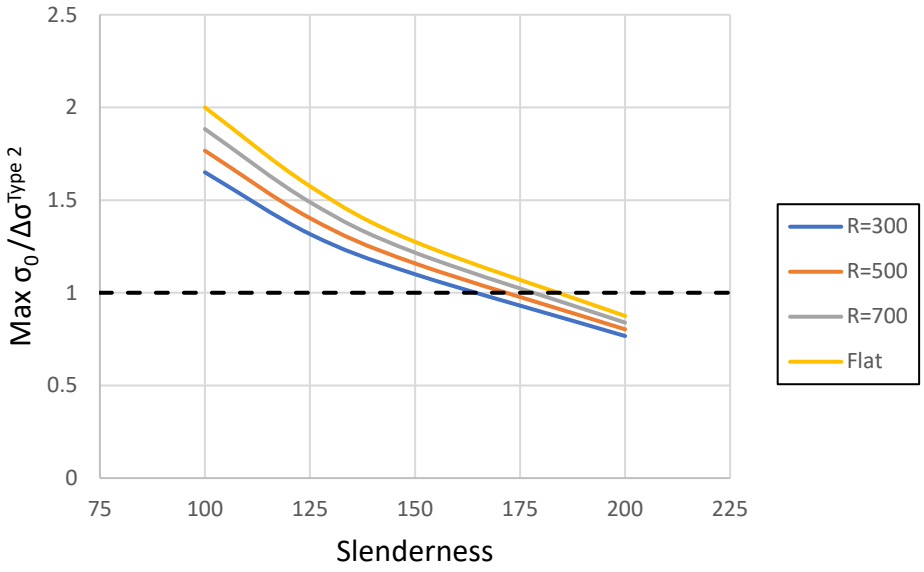

Figure 3.64: Maximum in-plane stress versus slenderness, $\tau_0 = 0.5\sigma_0$

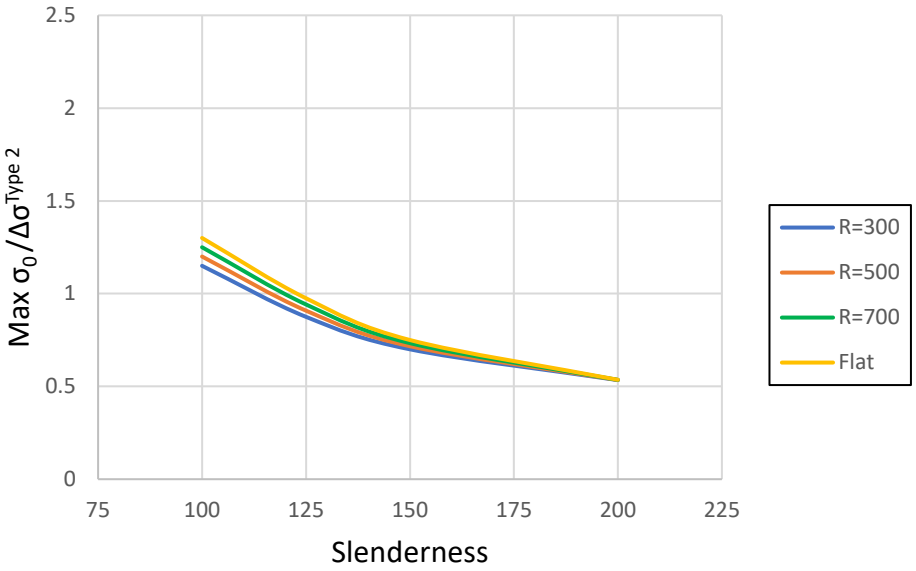

Figure 3.65: Maximum in-plane stress versus slenderness, $\tau_0=\sigma_0$

The other important factor to consider for developing a design limit for the combined loading case is the curvature effect on intensifying web breathing stress compared to the straight web panels. As explained in prior sections, the curvature effect became negligible in the case of $\tau_0=\sigma_0$ load combination due to the dominant shear effects. Consequently, it is recommended that in the case of load combinations where the share of shear stress is high, such as $\tau_0=\sigma_0$ the fatigue design limit of curved web panels, be on the basis of the flat panel shear design.

The following equation was derived based on the parametric finite element simulations of load combinations $\tau_0=0.5\sigma_0$ to limit the in-plane bending stress to prevent web breathing:

$$\max \sigma_0 \leq \begin{cases} \dfrac{\Delta\sigma_c^{Type2}}{1-ST} \\ 0.7\sigma_{cr} \end{cases} \tag{3.37}$$

where $max\ \sigma_0$ is the maximum in-plane bending stress, $\Delta\sigma_c^{Type2}$ is the fatigue resistance of crack type 2, ST is the stress ratio, and σ_{cr} is the linear elastic bend buckling stress of a flat web. The bottom term was calculated based on the curves located at the bottom of the dashed line of Figure

3.64. These models are controlled by the web breathing crack. The corresponding maximum in-plane stress were averaged and normalized to the bend buckling stress of the equivalent flat web panel.

Equation 3.37 applies to curved and flat web panels without longitudinal stiffeners with a slenderness ratio of up to 200. The equation was derived based on the isolated web panels with the neutral axis in the mid-height of the web panel. It is applicable to the negative bending region of the composite curved girders. In addition, the result is conservative for the positive bending area where the composite action of the bridge decreases the compressive area of the web by shifting up the neutral axis.

AASHTO (2020) limits the shear force of the interior web panels, regardless of the shear and bend load combination, by the following equation:

$$V_u \leq V_{cr} \tag{3.38}$$

where V_u is shear in the web at the section under consideration due to the unfactored permanent load plus the factored fatigue load (kip), and V_{cr} is shear-buckling resistance. The web bending stresses are also limited to the web bend-buckling resistance at the construction and strength limit states.

A direct comparison between the developed equation and the AASHTO (2020) requirement could not be made due to the nature of the parametric study. However, the applicability of the AASHTO limit for both the curve and straight girders was approved in the case of high shear stress in the combined loading case.

It should be noted that the shear stress due to the concentrated force applied on the stiffener causes fatigue cracking under the concentrated force along the transverse stiffener in both compression and tension regions. This type of combined loading configuration resembles the

interior web panels that are directly on the interior supports of the bridge. Web distortions are heavily affected by dead loads during the construction phase and affect fatigue behavior during the service phase. This effect was investigated qualitatively in section 3.1, in which the global behavior of the bridge was addressed through a full superstructure simulation.

3.4.4 Conclusions

Web breathing of the curved web panels under combined bending and shear stress was studied through parametric finite element analysis. The influence load combinations, $\tau_0=\sigma_0$ and $\tau_0=0.5\sigma_0$, radius of curvature, web panel slenderness ratio, and stress ratio were investigated. It was observed that shear stress significantly affects the fatigue performance of curved web panels. In the case of high web panel slenderness ratio, i.e. $\beta=200$, and high shear portion of combined loading, i.e. $\tau_0=\sigma_0$, web breathing critical stresses become identical for curved and straight web panels. The critical stress ratio, $ST=\frac{\sigma_L}{\sigma_H}$, for all curved web panel under combined loading is equal to zero. The controlling effect of web-to-stiffener fatigue detail dissipates as the shear stress share of combined loading increases.

A fatigue design limit equation was developed in terms of limiting the bending stress that is applicable to both the curved and straight girders. In addition, it was concluded that the current AASHTO (2020) limit for web panels under combined shear and bend loading is satisfactory for both curved and straight web panels.

CHAPTER 4
EVALUATION OF STRESS AND STRAIN IN WEB PANELS USING LIDAR SCAN DATA

4.1 Background and Literature Review

Assessing structural behavior with conventional field monitoring techniques is a challenging task that can be time consuming and expensive. This is especially true when the structure being investigated is a highway bridge where access issues can make it difficult and dangerous for personnel to install and maintain conventional monitoring components, such as strain gauges, that must be physically attached to the structure. The field monitoring portion of this project presented this difficulty in the large horizontally curved steel girder bridge (Ramp C) over I-565 in Madison, Alabama that was a focal point of the research. The 650 ft bridge, consisting of three continuous spans over six lanes of interstate traffic, presented instrumentation challenges because of its size, its proximity to traffic, and the number of strain gauges needed to capture relevant data. Additionally, the relatively low web slenderness ratio of the girders would likely severely limit the web breathing behavior that was a focus of the study. Because of the challenges and the likelihood that the desired behavior would not be observed, a novel structural monitoring technique based on geometric data (point cloud data, scan data) obtained through the use of a conventional, terrestrial LiDAR scanner, was pursued.

The LiDAR structural monitoring (LSM) method explored here requires two LiDAR scans of the structural component being evaluated – one before and one after an applied load or an enforced displacement. The raw point data for each scan is transformed from a random collection of points into a regular, gridded representation of the scanned component. These discretized representations provide the foundational geometry for the mathematical descriptions of the

undeformed and deformed component that are needed to determine the change in surface strains that accompany the change in shape. Cross-section properties and constitutive relationships are used in combination with the change in surface strains to determine the change in the state of stress at any point on the surface of or within the component. The proposed LSM method is evaluated through the use of three analytical problems, two laboratory test problems, and field monitoring of the Ramp C bridge in Madison, Alabama.

4.1.1 Conventional, Contact-Required Field Monitoring Techniques

Conventional, contact-required field monitoring techniques are commonplace in contemporary structural engineering research for numerous reasons. Resistance strain gauges, for example, were invented in 1938 (Wikipedia, 2024) and have benefited from over 80 years of use and refinement that have made it one of the most important tools available to the researcher. Other instruments such as accelerometers, inclinometers, and load cells have been similarly developed such that the capabilities and limitations are also well understood by the research community. The widespread availability, level of technological development, and familiarity of these devices make them an obvious choice for most of the field monitoring performed today.

Despite the advantages of conventional, contact-required devices, there are disadvantages that should be considered prior to their selection for a project. Strain gauges, for example, are capable of taking measurements only at discrete points. Each installation requires the removal of protective coatings such as paint or hot-dip galvanizing so that the gauge is bonded directly to the metal surface. Once installed, each gauge is susceptible to damage and must be protected for the duration of the research project. Additionally, structures such as highway bridges often present challenging access conditions that can be both difficult and dangerous. For small projects, these

problems may be mere inconveniences. For larger projects and projects that require numerous measurements, these problems can be very time consuming and very expensive. Several field monitoring methods, developed at least in part to overcome these difficulties, are discussed in the following sections.

4.1.2 Digital Image Correlation

The Correlated Solutions, Inc. website, accessed on May 10, 2024 at www.correlatedsolutions.com, provides the following description of digital image correlation (DIC):

> *Digital image correlation (often referred to as "DIC") is an easy-to-use, non-contact optical method which measures deformation on the surface of an object. This method tracks the displacements in the speckle pattern in small neighborhoods called subsets … during deformation. Digital image correlation has repeatedly proven to be accurate when compared to LVDTs, strain gauges, and valid FEA models for many years. It is now the industry-leading optical measurement method around the world …*

The use of the term "non-contact" in the above description is true from the perspective that no gauges or instruments are physically attached to the object while surface deformations are monitored. It is misleading, however, since it can be assumed to imply that the object does not have to be contacted during the use of this method. In reality, the object to be monitored must be contacted prior to taking measurements, usually several times, to paint, apply the speckled pattern,

and to perform the initial calibration procedure. Therefore, while DIC does eliminate contact during testing, contact is still required during the preparation phase of this method. The removal of this contact requirement through the use of the LSM method would be a significant improvement over current DIC methodology.

4.1.3 LiDAR Point Cloud Data-Based Method

A novel method was presented by Jo et al. (2020) in which a LiDAR point cloud data-based method was used to evaluate the strain on a curved steel plate subjected to lateral pressure. From the abstract to this paper, this research is summarized as follows:

> *This study demonstrates a strain evaluation method using a LiDAR system in order to analyze the behavior of steel structures. To evaluate the strains of structures from the initial and deformed shape, a combination of distributed 3D point cloud data and finite element methods (FEM) was used. The distributed 3D point cloud data were reconstructed into a 3D mesh model, and strains were calculated using the FEM. By using the proposed method, the strain could be calculated at any point on a structure for SHM and safety assessment during construction.*

Explaining further, the presented method requires two LiDAR scans of the same component -- one before and one after the change in shape. A quadrilateral mesh is constructed for both the initial shape and the deformed shape. The nodes for both meshes have the same x and y coordinates, but with different z coordinates that fully define the change in shape. A finite element model of the mesh for the initial shape is constructed within a commercially available

finite element analysis program and the nodal displacements representing the change in shape are modeled as enforced displacements. The quality of the results obtained from this method are a function of point cloud quality, mesh density, and the capabilities of the element chosen for analysis. When fully developed, it is believed that the current LSM research (being conducted as part of this ALDOT sponsored project) will simplify the extraction of strain data from scanned components since the use of finite element software will be eliminated.

4.1.4 Vision-Based Measurements

The research by Ghyabi et al. (2023) is comprised of two full-scale tests of a vision-based measurement system that includes a results comparison with conventional measurement techniques. From the abstract, this research is summarized as follows:

> *This paper presents a case study on the use of vision-based methods for bridge load testing and provides a comparison of a digital image correlation (DIC) approach with a phase-based optical flow method. Two sets of field experiments were performed on bridges in the state of Delaware. The results show that vision-based methods can provide comparable results to conventional sensor installations, given sufficient consideration of the unique technical demands of these methods, as well as operational logistics. In most cases, the DIC and phase-based methods provided comparable results, though the DIC system yielded generally better accuracy, owing to a combination of algorithmic differences and additional signal postprocessing.*

The results of this study demonstrated the potential of the phase-based optical flow method for capturing structural displacements such as the maximum midspan displacement of a girder. However, there was no attempt in this study to track the small, localized displacements necessary for the evaluation of strain conditions. As a result, there appears to be no significant overlap in their vision-based research and the current LSM research.

4.1.5 Problem Statement

Chapter 4 thus far has shown that traditional structural monitoring includes the use of strain gauges, displacement gauges, tilt meters, and accelerometers, and that each of these devices must be physically attached to the structure to capture the desired data. It has also been shown that digital image correlation (DIC), an optical method that is often thought of as a noncontact approach, requires the structure to be accessed for the application of the speckled pattern needed to track surface displacements -- a nontrivial operation that limits the use of this technique (Sabato et al. 2023). The disadvantages of these methods have been discussed, so despite the effectiveness and widespread use of these contact-required methods, there remains a need for a truly noncontact structural monitoring system with accuracy and resolution comparable to the existing techniques mentioned above.

4.1.6 Scope

This research evaluates the use of a conventional, terrestrial LiDAR scanner to capture the change in shape of a structural component resulting from an applied load or an enforced displacement. This change in shape will be used to determine the accompanying change in strain anywhere on the surface of the component that is located within the scanned area. Cross-sectional properties and constitutive relationships will then be used to determine the state of stress at any point of the surface of or within the component that corresponds to this change in strain.

4.1.7 Objectives

The overall objectives represented by this chapter are to develop a noncontact, LiDAR based structural monitoring (LSM) method with measurement accuracy and resolution similar to or better than existing methods, but with improved speed, safety, and economy, and apply the technique to assessing the deformation associated with fatigue concerns in curved steel superstructure bridges. The advantages of the proposed LSM method include speed, economy, contact avoidance (no damage to structural component), and safety (personnel do not have to access the structure). The disadvantages of the proposed LSM method include the requirement to have a direct line of sight to the structural component and only static conditions can be evaluated (because of currently available scan speeds).

4.2 Town Madison Bridge Overview

The Alabama Department of Transportation (ALDOT) provided the Auburn University research team with a horizontally curved steel girder bridge to study for this project. The selected

bridge was the Ramp C overpass to be constructed as part of a new interchange on I-565 in the City of Madison, Alabama between Wall-Triana Road and Zierdt Road. When the research project began, the Ramp C bridge had already been designed by engineering consultant AECOM, but bids for construction had not yet been received. The horizontally curved portion of the Ramp C bridge, taken from the General Plan sheet in the construction drawings, is shown in Figure 4.1.

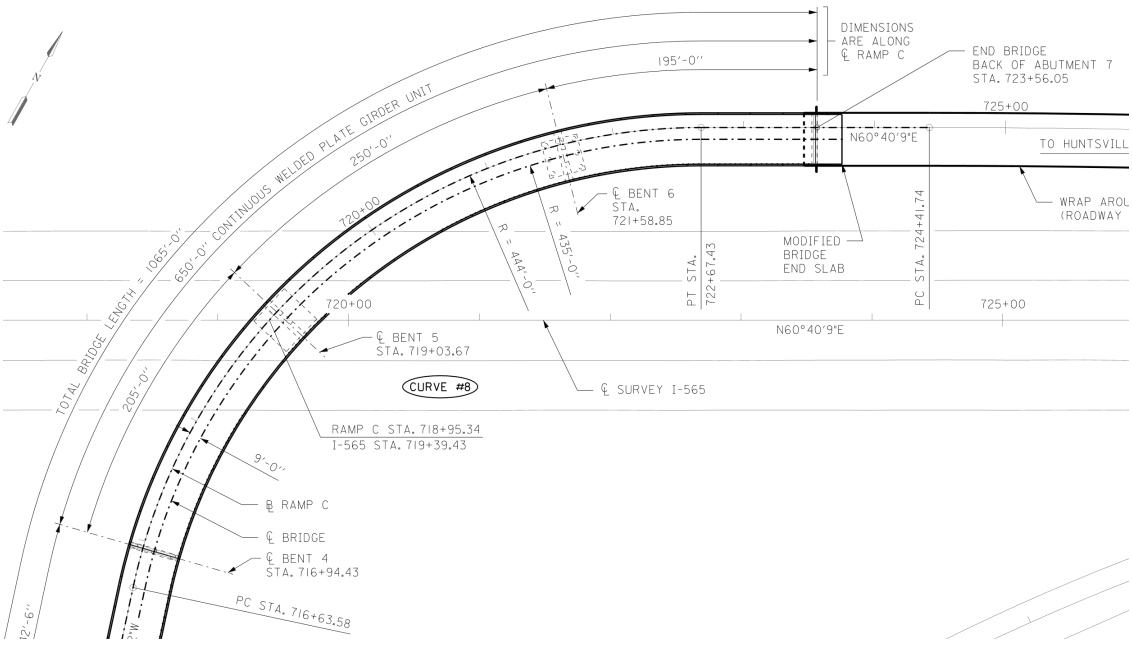

Figure 4.1: Horizontally curved portion of the Ramp C Bridge, Madison, Alabama

The horizontally curved portion of the Ramp C bridge is comprised of five steel girders over three spans (Spans 4, 5, and 6 in the contract documents) with a centerline radius of 435 feet. The curved steel girders begin at Bent No. 4, where they are simply supported, and are continuous over Bent No. 5 and Bent No. 6 before extending to Abutment No. 7 at the end of the bridge where they are simply supported. The dimensions of the flanges vary along the length of each girder, but the web is the same throughout the bridge, measuring 96 inches tall and 0.75 inches thick. The girders are spaced 8 feet, 9 inches center-to-center and the radially oriented crossframes are spaced at approximately 15 feet center-to-center. The web dimensions provide a web slenderness ratio of

128 and the spacing of the crossframes provides a web panel aspect ratio of approximately 1.9. Figures 4.2 through 4.4 show the framing plan for Span 4, Span 5, and Span 6, respectively. Figure 4.5 shows a typical section of the horizontally curved portion of the Ramp C bridge.

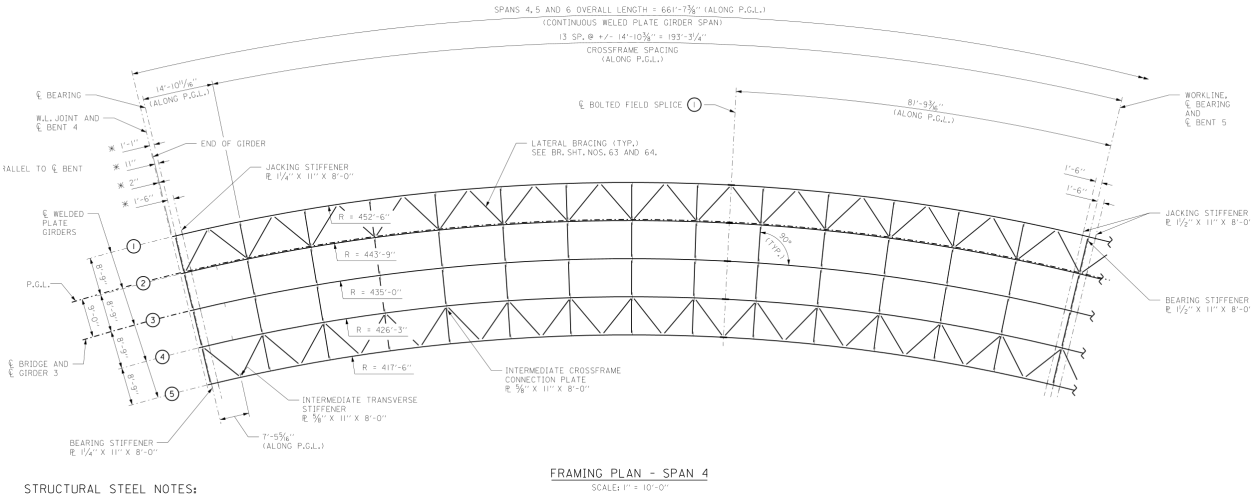

Figure 4.2: Span 4 framing plan

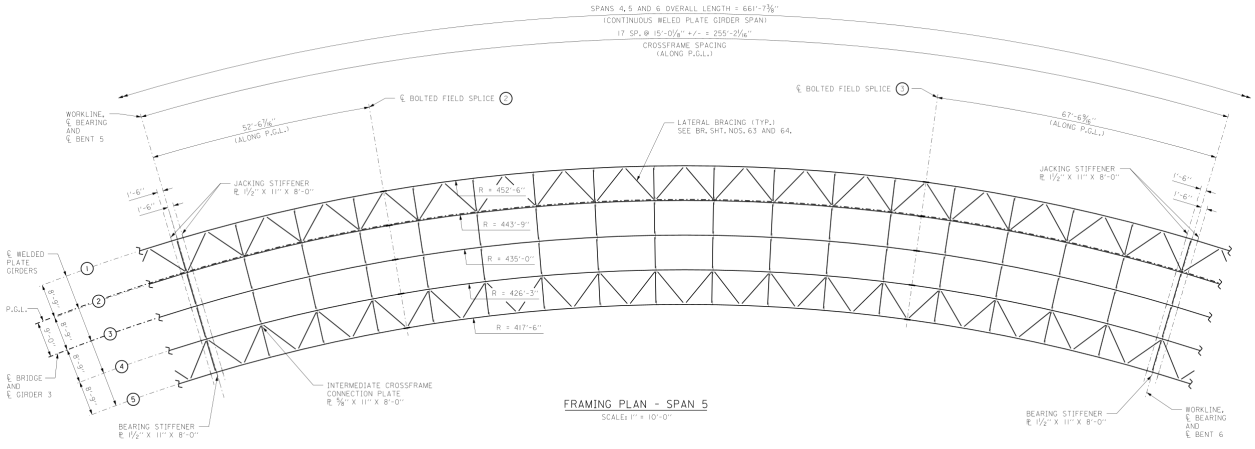

Figure 4.3: Span 5 framing plan

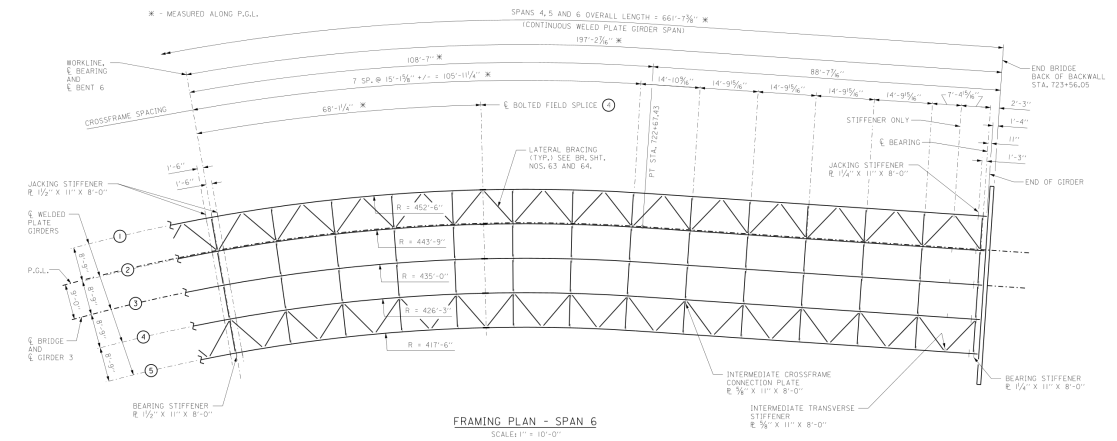

Figure 4.4: Span 6 framing plan

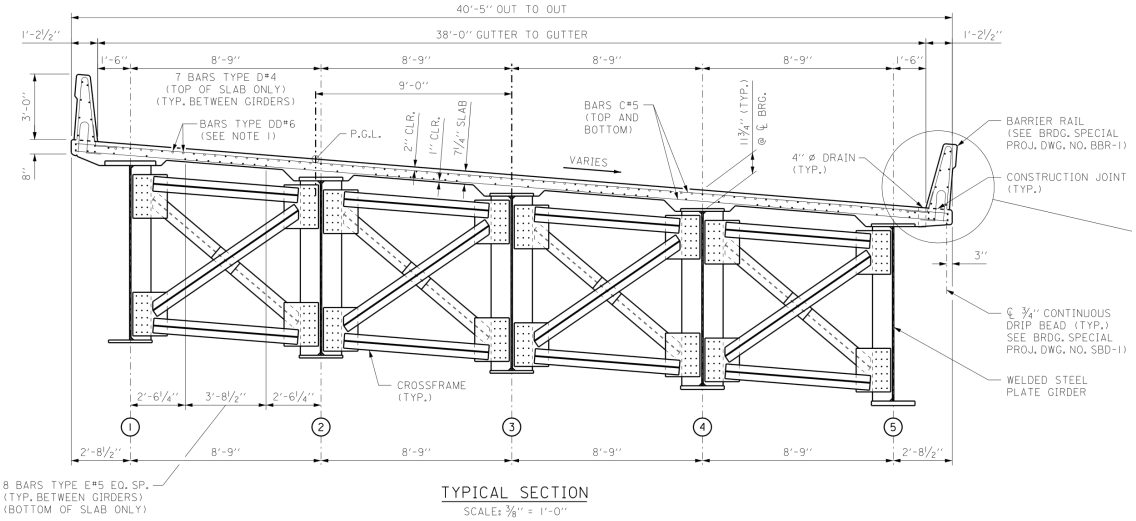

Figure 4.5: Typical section

4.3 Monitoring of Girder Fabrication and Erection

Field monitoring of the Ramp C bridge was required to empirically corroborate the theoretical and numerical analyses that were performed during the initial, preconstruction phase of the research. The field monitoring plan that was eventually implemented was largely based on the results of the numerous finite element models developed, refined, and studied over the long first phase of this project. One of the first models developed used the GT STRUDL 2020 finite

element program. This model of the complete superstructure used beam elements for all flanges, stiffeners, and crossframes, and shell elements (GTSTRUDL element SBHQ6) for the webs and the deck. In spite of the somewhat simplistic approach, at least for research purposes, the model was very large and consisted of 63,448 elements and 11,042 members for a total of 386,088 degrees of freedom. The AASHTO fatigue truck presented additional modeling complications because of the number of individual load cases that were evaluated to closely approximate this moving load. For example, a single pass of the AASHTO fatigue truck across the bridge, modeled using GT STRUDL's Moving Load generator, created 657 individual load cases with each of these load cases requiring the solution of a unique stiffness analysis. Understanding that multiple passes of the AASHTO fatigue truck would be required to fully define the structural response envelope, it was apparent that the thousands of corresponding individual load cases would make this approach computationally overwhelming. As a result, the full array of moving load cases was only used to identify primary areas of interest. Load cases causing a desirable or useful structural response remained active loads in the model while all other loads were inactivated. The paring of thousands of individual load cases down to a very small number that were relevant to the research allowed progress at a good pace while maintaining high standards.

Figure 4.6 shows an overall model of the Ramp C superstructure that includes only components modeled as frame members (flanges, stiffeners, and crossframes). All 2D finite elements (webs and deck) have been removed from this figure for clarity.

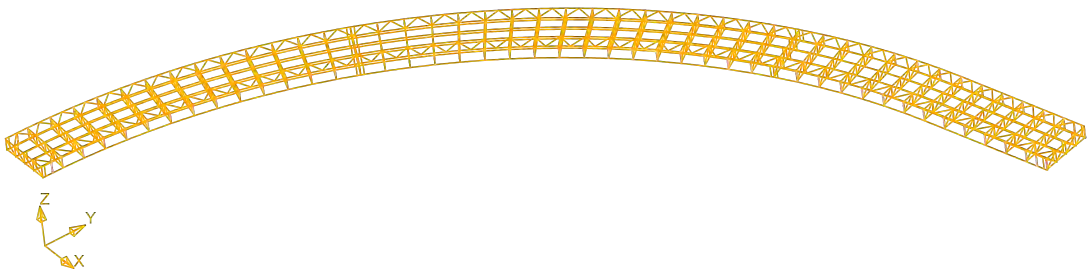

Figure 4.6: Overall view of Ramp C superstructure showing only members

Figure 4.7 shows a large portion of the GT STRUDL Ramp C bridge model near the beginning of the horizontally curved portion of the bridge. Approximately 90 feet of Span No. 4 is shown. The end of the bridge (left) is radially oriented near the centerline of Bent No. 4. Barrier rails were not included in this model and no attempt was made to capture the multiple stiffness conditions that would occur during the various stages of construction, such as deck placement where composite behavior was gradually created over the five separate deck pours indicated in the bridge plans.

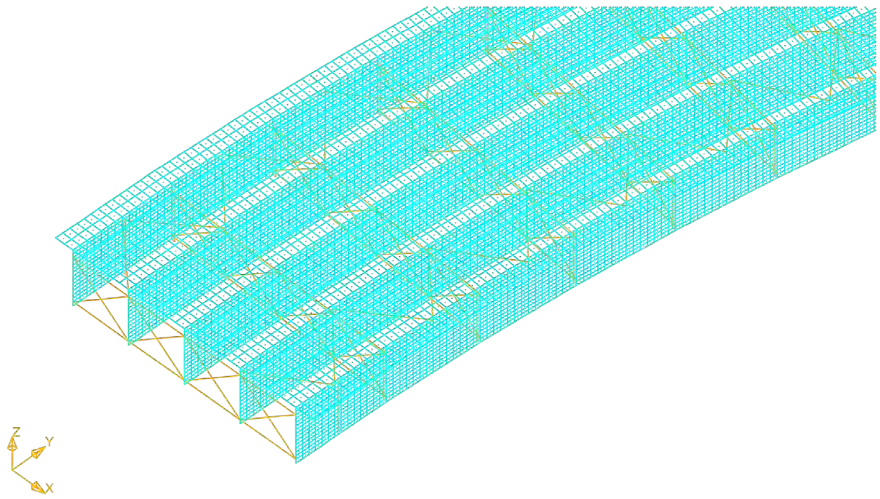

Figure 4.7: Ramp C superstructure near bent No. 4 showing members and elements

The work in this initial phase indicated that the web panels most susceptible to fatigue problems associated with web breathing were located in four specific areas along Girder No. 1, the outermost girder on the bridge. These four areas are shown in Figure 4.8. The web panel in Area

1 is subjected to high shear and low positive moment. The web panels in Areas 2 and 3 are subjected to moderate shear and high positive moment. The web panel in Area 4 is subjected to high shear and high negative moment. LSP 1 and LSP 2 indicate the locations of the LiDAR scanner for the collection of point cloud data that will be used to keep track of the change in shape of the superstructure that occurs between the erected condition (steel only), the completed condition (self-weight only), and the fatigue truck condition (completed structure with fatigue truck placed as required on the deck).

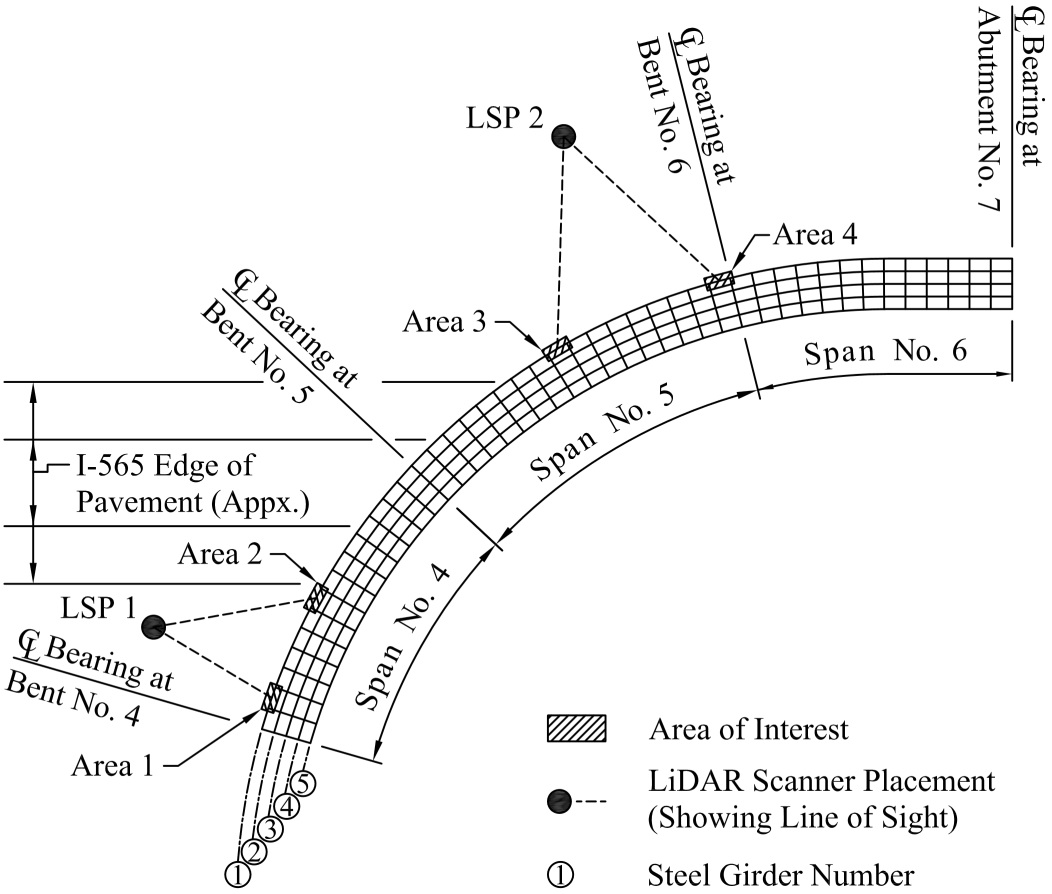

Figure 4.8: Areas of interest

This initial modeling was the result of a collaborative effort between Mr. Stephen Hammett, currently a PhD candidate, and Dr. Mehran Jalali, as part of his dissertation research. Dr. Jalali used these initial results as a starting point for his deeper investigation into the potential

fatigue problems associated with web breathing in horizontally curved steel plate girder bridges, which involved ABAQUS finite element models developed to investigate the effects of radius of curvature, web slenderness, initial imperfection, and fatigue detail category, while also accounting for the impact of staged construction. Figure 4.9 shows a typical model employed in his research. The red and green colors represent the shell and beam elements, respectively. All of the G4 girder parts, including the web, connection plates, and flanges, are shell elements. G1, G2, and G3 girders are modeled with shell elements for web and beam elements for connection plates and flanges. All cross frames are made of beam elements. S4 shell element, a 4-node quadrilateral shell element, is used for the G4 web, while the S4R shell element, a 4-node quadrilateral shell element with reduced integration, is used for the other three girder webs and concrete deck. All of the beam elements for the cross frames, connection plates, flanges are modeled with the B31 element, a 2-node beam element, as shown with red color in Figure 4.9. All rotational and translational degrees of freedom of the concrete deck are tied to the corresponding rotational and translational degrees of freedom of the girders top flange to simulate the concrete deck full composite action.

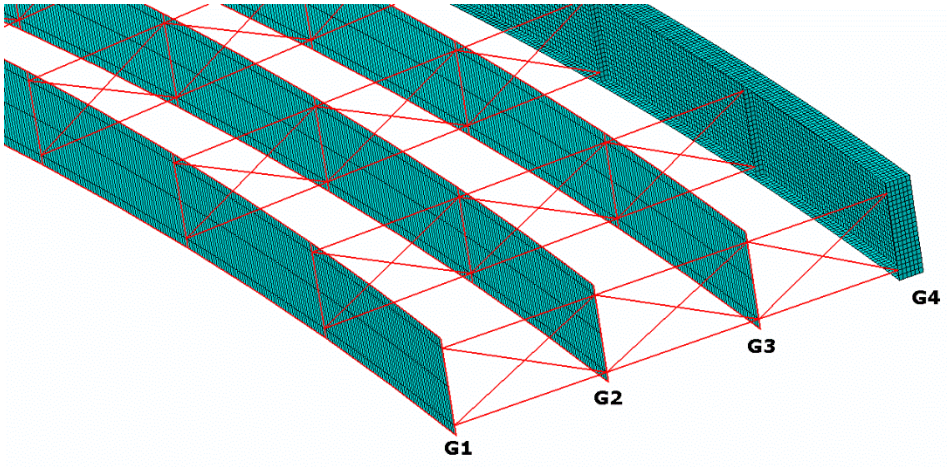

Figure 4.9: ABAQUS finite element model in showing crossframes and mesh

Figure 4.10 shows an overall view of the ABAQUS model with the boundary conditions shown at the left and right supports. The translation of the girders bottom nodes in the vertical and

radial direction was restrained at the right end. All three translation degrees of freedom of the girders bottom nodes were restrained at the left end. The AASHTO (2017) fatigue truck with the 1.15 impact factor was used for loading. The individual wheel loads are shown as red arrows and are positioned for the fatigue evaluation of the center web panel on the outside girder. The truck was positioned transversely at 2 feet distance from the outer curb to induce the maximum effect on the exterior girder. The truck was positioned longitudinally in the middle of the span to induce the maximum bending effect when the middle panel was under investigation. The fatigue truck was positioned close to support such that the rear axle (the heaviest) is in the middle of the second panel near the supports for investigating the maximum shear effect. It should be recognized that the stress values discussed in this context are equivalent to stress ranges used for fatigue analysis because the truck passage over the single-span bridge does not create negative stresses. In other words, zero values (the minimum stress) is subtracted from the positive stress (tensile) values at the detail under investigation.

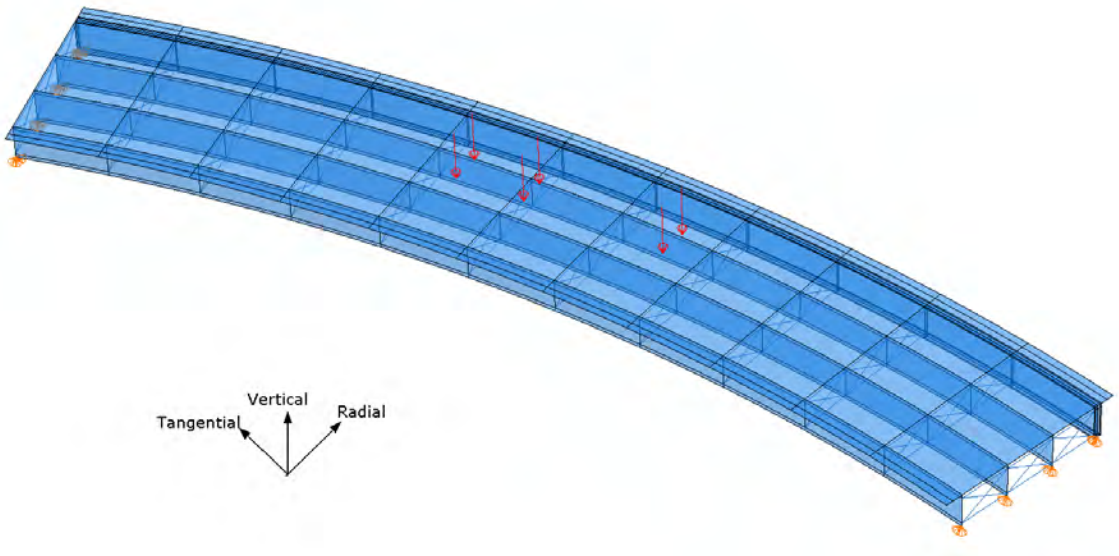

Figure 4.10: Overall view of finite element model in ABAQUS

Sine functions were used to define the geometry of the initially deformed (imperfect) web. The direction of the web bulging out/in is determined based on previous analyses and buckling shape modes of the curved web panels. Figure 4.11 shows the initial web deformation geometry. These shape modes are scaled based on the Bridge Welding Code (AWS 2010).

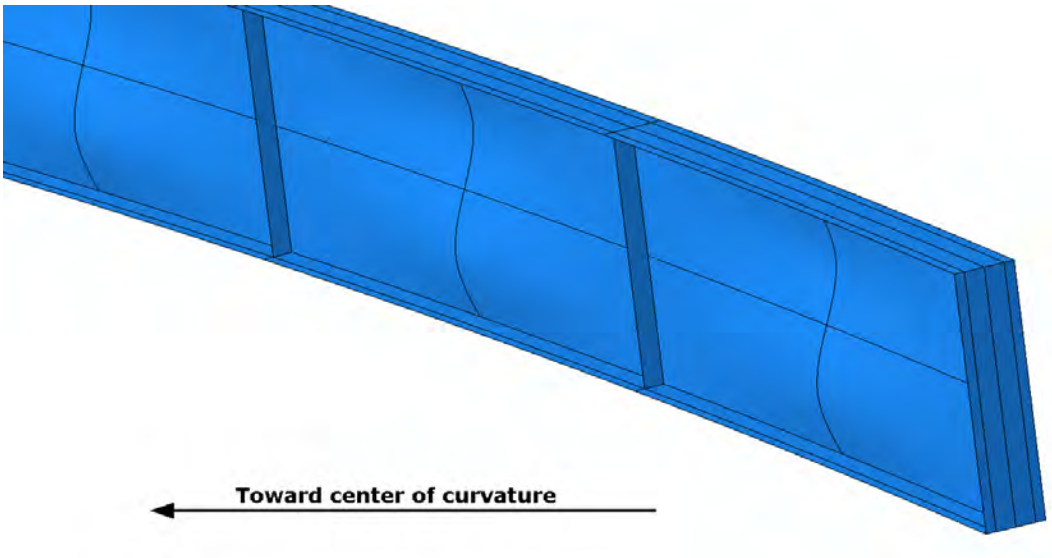

Figure 4.11: Web imperfection initial geometry

A bridge having a radius of 400 feet, slenderness of 300, considering the initial web imperfection for the outer girder (G4), was simulated to evaluate the web imperfection effect. It was observed that imposing an initial web out-of-flatness changed both the web vertical stress intensities and distributions. As shown in Figure 4.12, the highest web vertical stress concentrations close to the bottom flange did not occur at the panel MC, as expected. The vertical stress at elements adjacent to the bottom flange are plotted for each panel in Figures 4.13 through 4.15. The solid and dashed lines represent the curved girder stresses of the perfect and imperfect web, respectively. It is observed that the middle panel MC maximum stresses are decreased upon imposing the web distortion. Side panels MR and ML have the same maximum stress, but the

distribution has changed. The form of the initial imperfections may be the reason for these stress reductions and pattern differences.

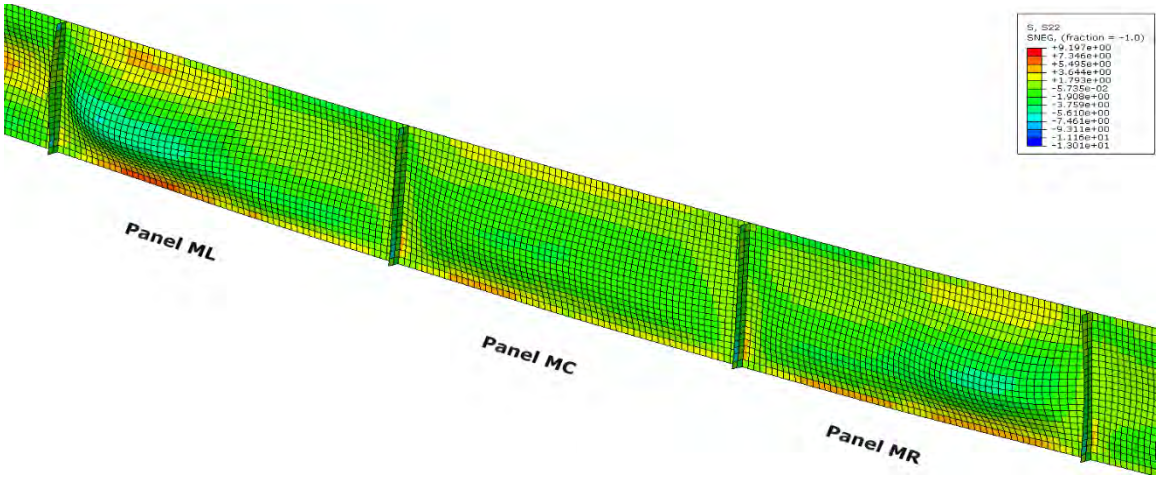

Figure 4.12: G4 web vertical stress (S22) for web imperfection, R=400 ft, SL=300

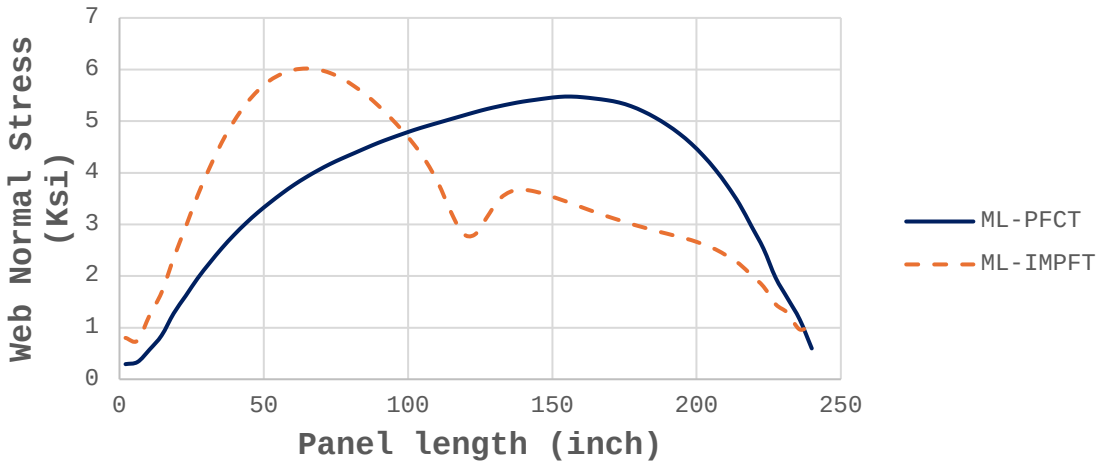

Figure 4.13: Web ML normal stress (S22), perfect, imperfect, R=400 ft, SL=300

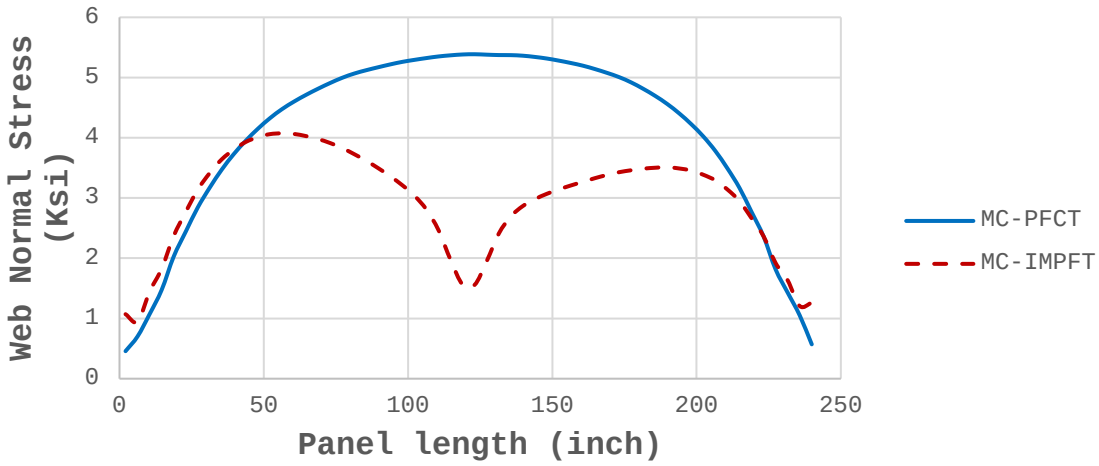

Figure 4.14: Web MC normal stress (S22), perfect, imperfect, R=400 ft, SL=300

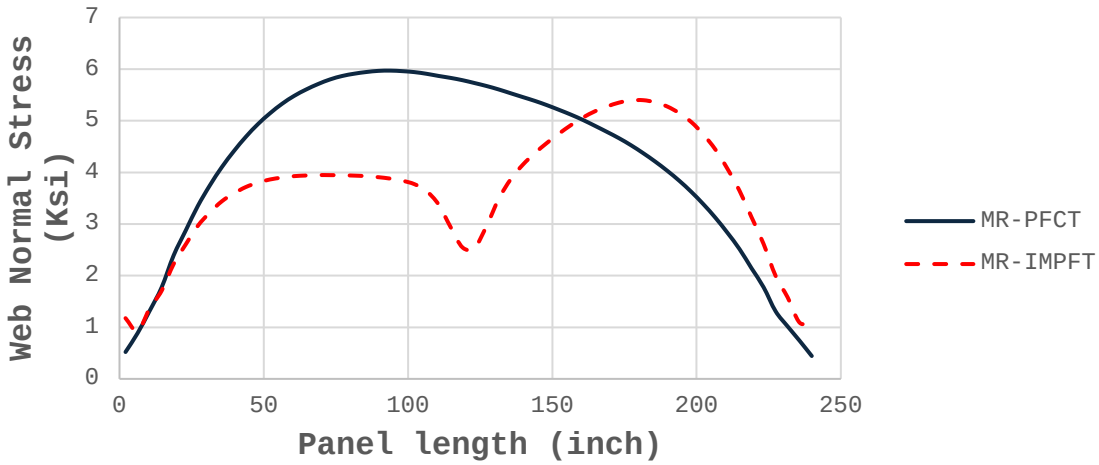

Figure 4.15: Web MR normal stress (S22), perfect, imperfect, R=400ft, SL=300

Similar investigations into the effects of web slenderness and radius of curvature were also performed. The results of all the theoretical and numerical studies were used to develop a field monitoring plan for the areas of interest shown in Figure 4.8. Figures 4.16 through 4.19 show the field monitoring plans for Areas 1, 2, 3, and 4, respectively.

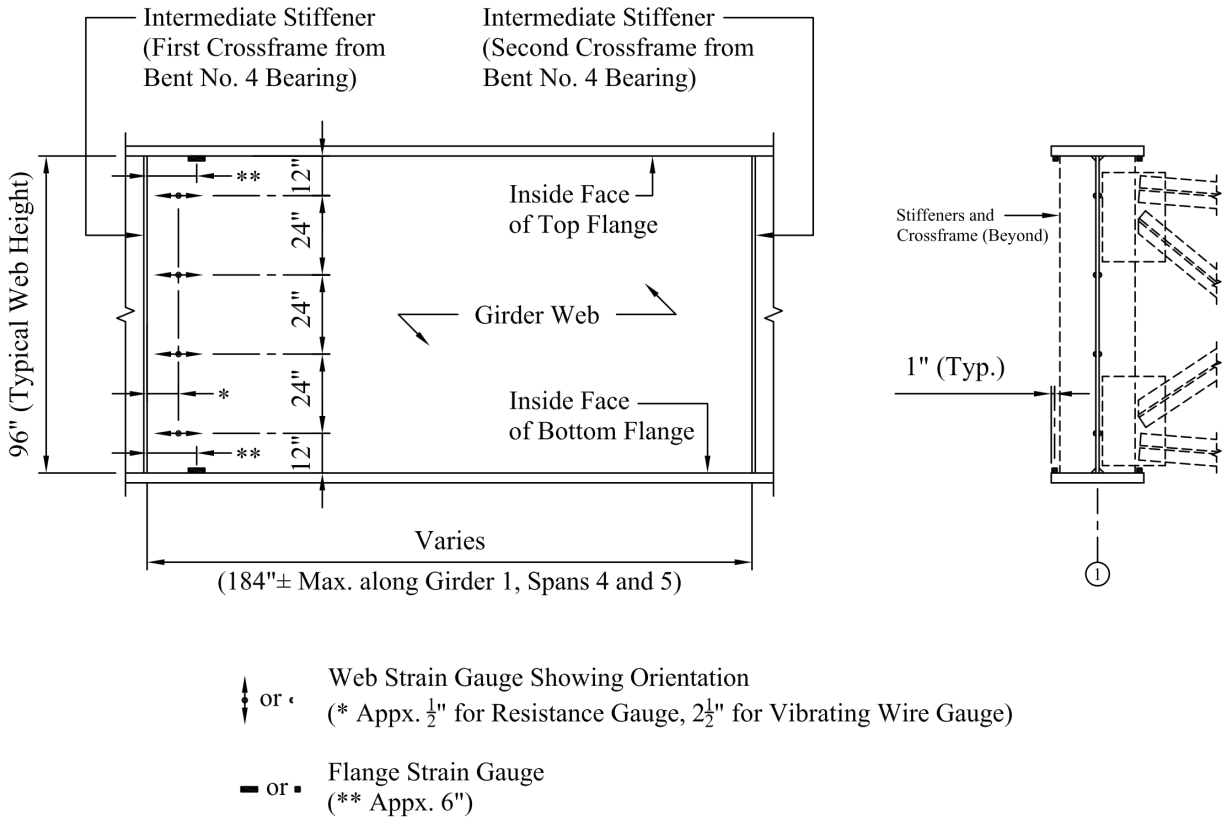

Figure 4.16: Strain gauges for Area 1 (high shear, low positive moment, 12 gauges)

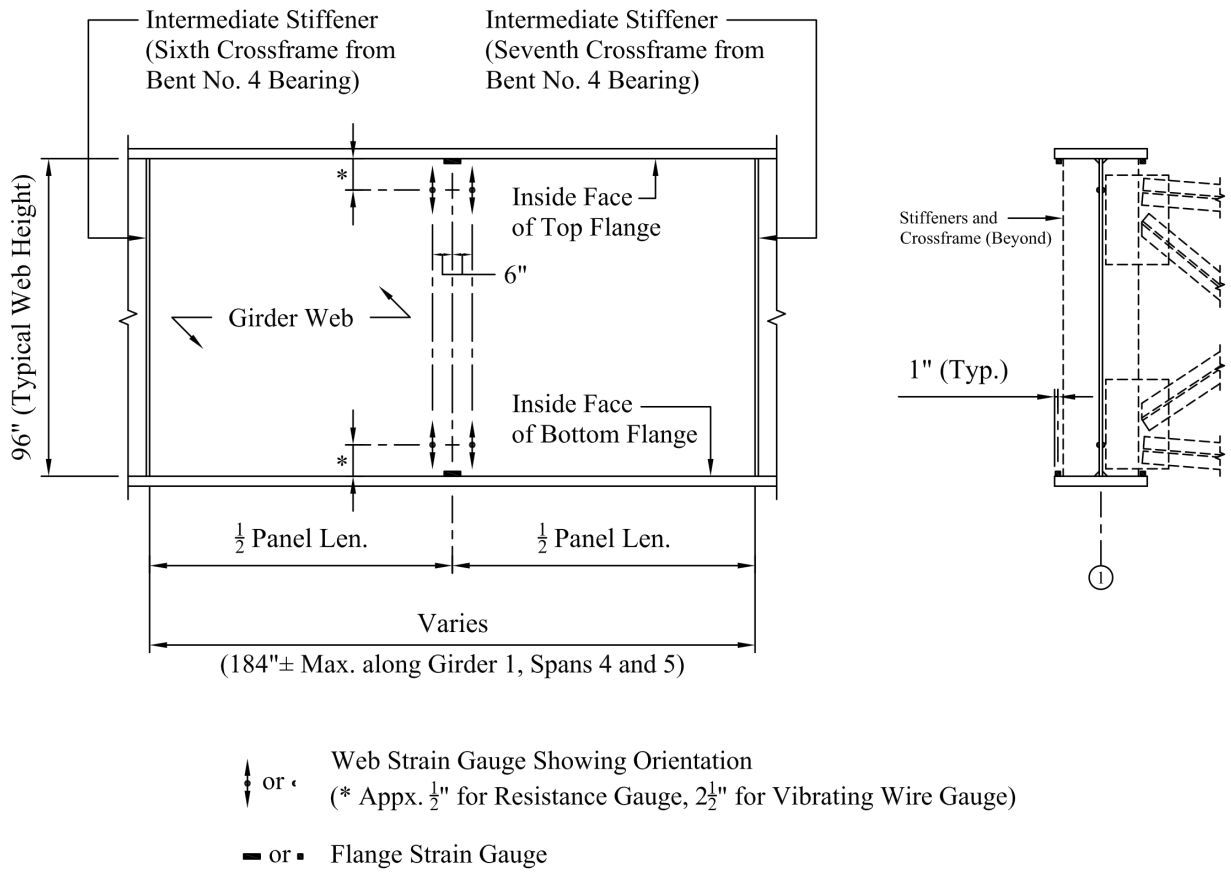

Figure 4.17: Strain gauges for Area 2 (low shear, high positive moment, 12 gauges)

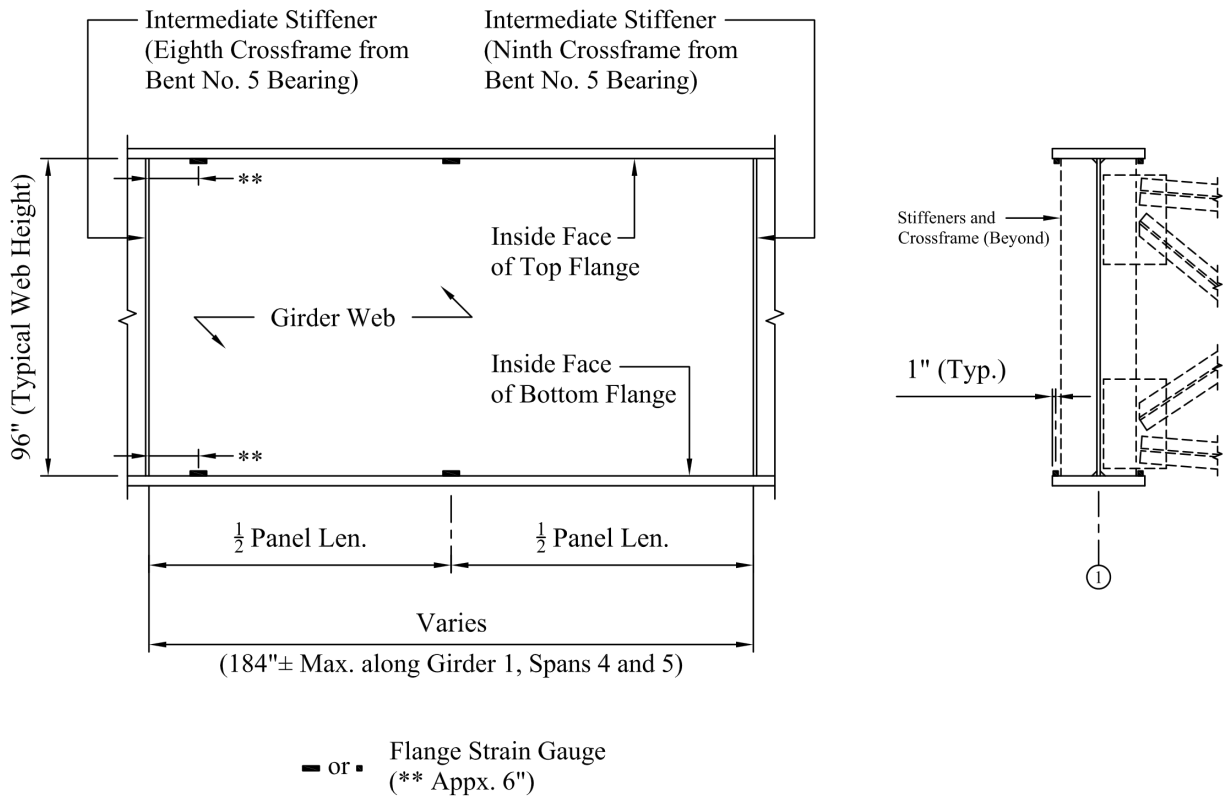

Figure 4.18: Strain gauges for Area 3 (low shear, high positive moment, 8 gauges)

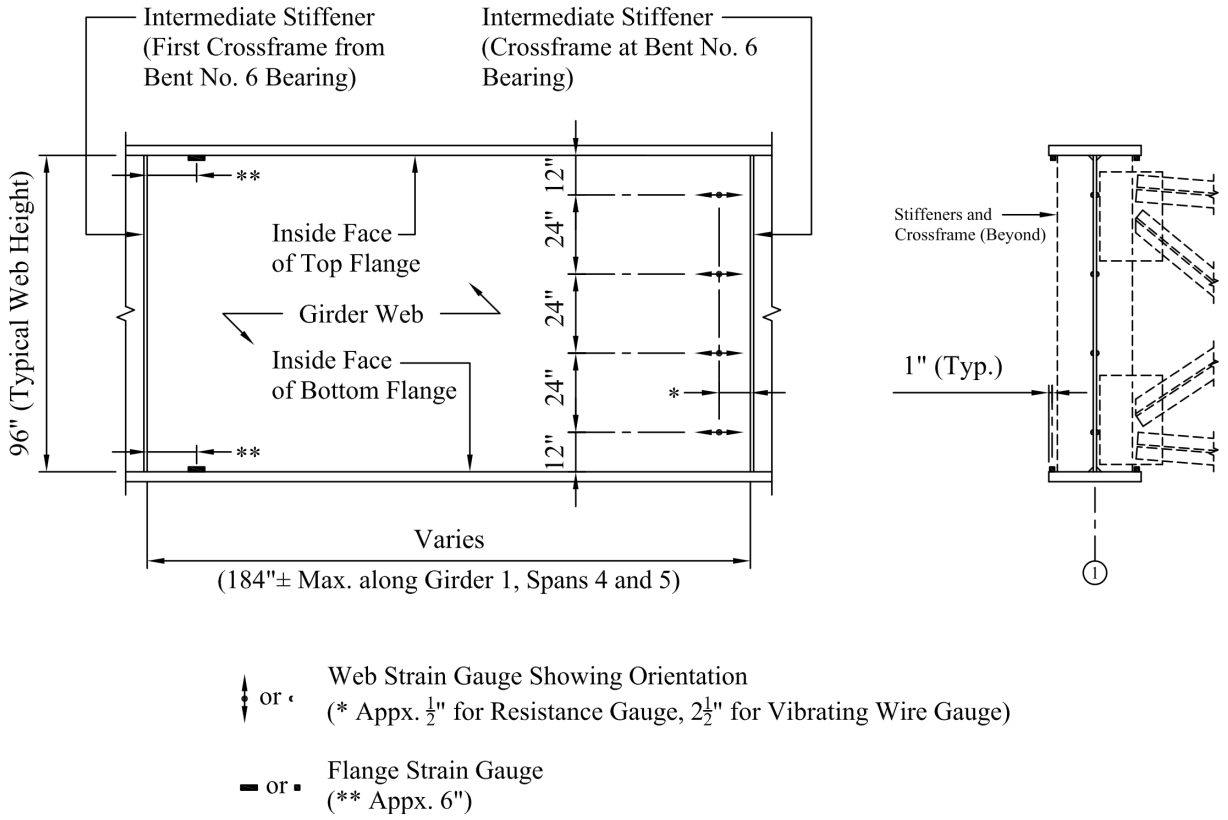

Figure 4.19: Strain gauges for Area 4 (high shear, high negative moment, 12 gauges)

The ABAQUS parametric studies accounted for the wide variations in radius of curvature, web slenderness, and initial imperfections that are currently permitted by governing design specifications. The proposed strain gauge layouts for Areas 1, 2, 3, and 4 shown above were based on the results of these studies and were strategically placed to capture strain data that would corroborate the findings from the initial, analytical portion of this research project. However, the Ramp C bridge that was planned for the field monitoring had a web slenderness ratio of 128, which is typical for steel plate girder bridges designed and constructed in Alabama, but it is well below the slenderness ratio where significant web breathing behavior would be observed and that would potentially lead to related fatigue problems. Because of the likelihood that web breathing behavior would not be observed, the decision was made to pursue a novel structural monitoring technique based on geometric data (point cloud data, scan data) obtained through the use of a conventional,

terrestrial LiDAR scanner rather than using the conventional field measurement plan. The acquisition of LiDAR scan data, the estimation of structural response, and the evaluation of the results from the proposed method are discussed in the sections that follow.

4.4 LiDAR Scan Data: Acquisition of Structural Component Geometry

LiDAR, an acronym for light detection and ranging, is a method for determining range (distance to an object) by targeting a surface or an object with a laser and measuring the time for the reflected light to return to the receiver. This technology has found applications in many areas such as surveying, archeology, geology, seismology, military, spaceflight, and atmospheric physics (Wikipedia, 2024). For the LiDAR structural monitoring (LSM) method being developed in this research project, the Leica RTC360 laser scanner is used for the collection of all point cloud data. This scanner is a conventional, terrestrial scanner that is generally operated from the top of a tripod. Figures 4.20 and 4.21 show the Leica RTC360 scanner collecting point cloud data on one of the outer loop bridges over I-85 just outside of Montgomery.

Figure 4.20: Leica RTC360 LiDAR scanner setup at outer loop

Figure 4.21: Leica RTC360 LiDAR scanner setup at outer loop

The geometric data captured by LiDAR scanners provides a discretized representation of the scanned component. These data points tend to be randomly located and, as a result, are difficult to use for stress analysis purposes while in this condition. Further, the accuracy and resolution of

these data points is a function of multiple physical parameters such as distance to the scanner, angle of incidence, weather, and albedo (color, reflectivity of the component). Because of these inherent complexities, post processing is required to transform the raw scan data so that the component geometry is accurately represented and is mathematically meaningful and suitable for stress analysis. The elimination of errant data points, often referred to as noise, is largely accomplished through the use of standard features included in the Leica programs Cyclone Register 360 and Cyclone 3DR, both of which are compatible with the Leica Cyclone RTC 360 scanner being used for this research. Figure 4.22 shows an overall view of the point cloud resulting from the scan taken between the girders. The dark line through the middle of the web represents a section (a plane) through the scan data. Figure 4.23 shows a contour map of the web panel at the end of the exterior girder that was generated in Leica Cyclone 3DR from the point cloud data. Figure 4.24 shows a view of the first web panel on the exterior girder along the section line visible in Figure 4.22. The view is from the first interior stiffener and is looking back along the section line through the web toward the bearing stiffener. The out-of-plane deformations in the web can be clearly seen and are consistent with the contours shown in Figure 4.23.

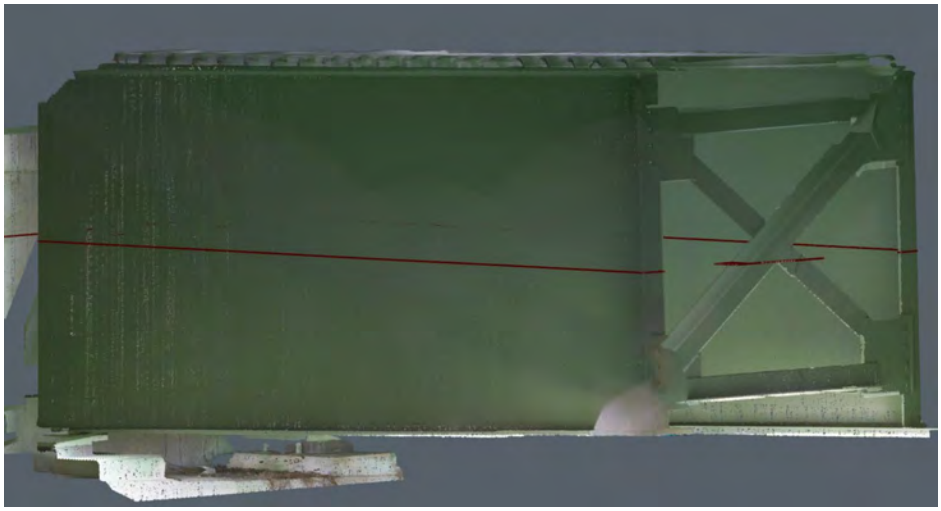

Figure 4.22: Point cloud data

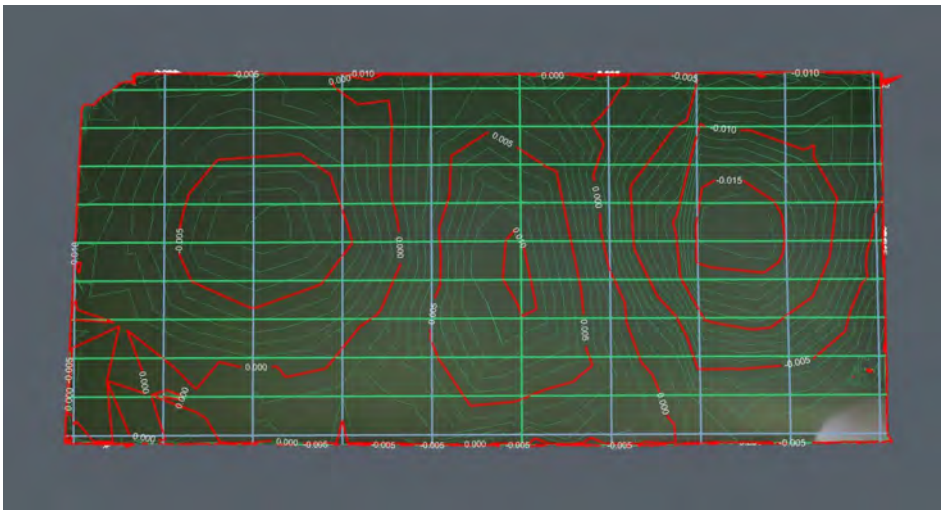

Figure 4.23: Contour map of web panel

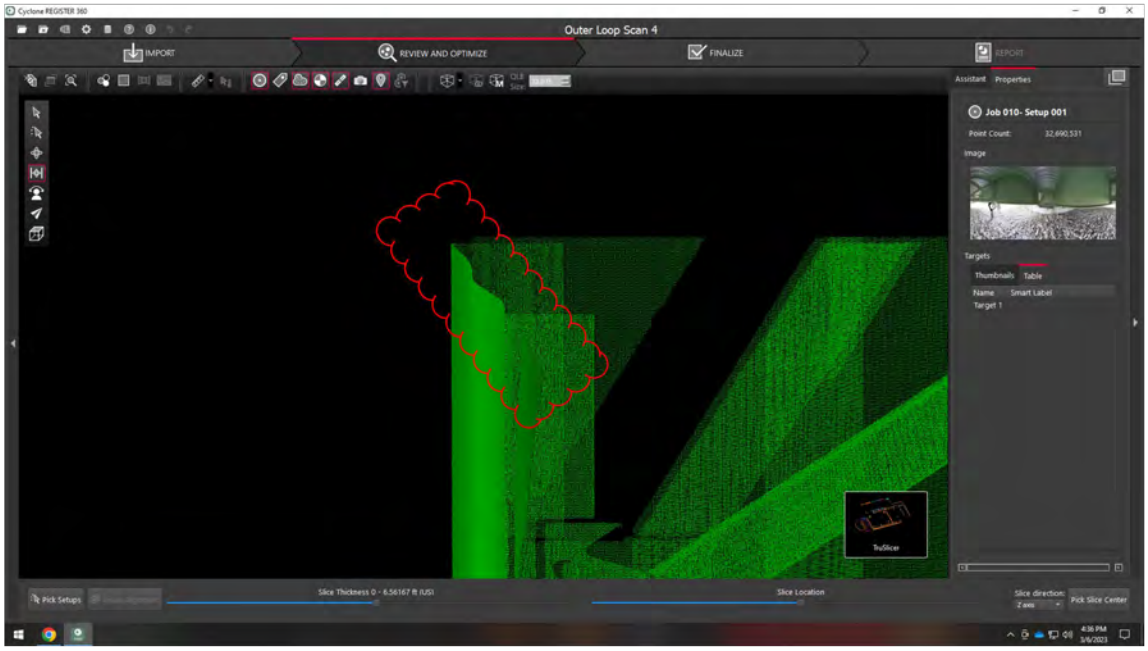

Figure 4.24: View along section showing web deformations

Figure 4.25 shows the LiDAR scanner setup for a scan of the Ramp C web panels on Girder No. 1 at Bent No. 6. The middle stiffener is the bearing stiffener at Bent No. 6 and the stiffeners on either side are jacking stiffeners. This picture of the unpainted girder was taken on September 18, 2023, in the yard of the W&W AFCO Steel fabrication plant in Montgomery.

Figure 4.25: Scanner setup for Girder No. 1, web panels at Bent No. 6

Figure 4.26 shows the LiDAR scanner setup for a scan of the Ramp C web panels on Girder No. 1. The view shown is of the interior of the girder. The left end is near the location of the field splice of Span No. 6. The web panel of interest is slightly right of the visible left end at what will be the maximum positive moment region. This picture of the painted girder was taken on February 6, 2024, in the yard of the W&W AFCO Steel fabrication plant in Montgomery. Obtaining scans of both the unpainted and painted girders was important to the research in order to account for the potential influence of surface condition on scan accuracy.

Figure 4.26: Scanner setup for Girder No. 1, positive moment web panels

Figure 4.27 shows the LiDAR scanner setup on the construction site of the Ramp C bridge. Girder No. 1 is the outside girder and is the girder nearest the scanner in the picture. Abutment No. 7, at the end of the bridge, is shown in the left, center portion of the picture and Bent No. 6 can be seen on the right side. The web panels on either side of Bent No. 6 and the web panel just to the left of the field splice in Span No. 7 are being scanned at the erection phase of construction to provide a link between the fabricated condition and the completed condition. This scan can provide a valuable benchmark as the structural condition from fabrication, to erection, to the completed bridge loaded with the ALDOT load truck is tracked.

Figure 4.27: Scanner setup for Girder No. 1, erection condition

As briefly discussed above, the accuracy of the data in a point cloud is a function of many factors such as distance to the scanner, angle of incidence, weather, and albedo (color, reflectivity of the component). Because of these multiple factors, the accuracy of each point in a cloud, which may contain millions of individual, unique points, can vary depending on the conditions present at the instant a data point is captured. Each scan taken by the Leica RTC360 is a full dome scan that takes almost 2 minutes to complete on the high-density setting. The ambient lighting conditions can change for outdoor scans when clouds move overhead or trucks pass by, creating a situation where the conditions for data collection are inconsistent. The angle of incidence for each point in a cloud can also vary significantly unless the scanned object is very small or the distance between the object and the scanner is relatively large. Additionally, the albedo of an object can vary within the scanned area because of changing surface conditions. For example, the sheen of a painted surface can easily vary over small areas depending on the skill of the painter and the conditions

during painting operations. As a result, it is not possible to provide a single number to describe the accuracy of LiDAR point cloud data. The Leica RTC360 user manual provides basic accuracy data for several isolated conditions, but the expected accuracy for any point will always be the combined result of the unique conditions present at the time each point is captured during the scan.

There are two types of accuracy that are generally important when attempting to assess the quality of a LiDAR scan. Absolute accuracy refers to how near the scanned point data is to their actual positions in the real world. In general, absolute accuracy is not an important component of this research. Relative accuracy refers to how accurately the points in a cloud are positioned relative to each other. It is a measure of how closely the geometric data from a LiDAR scan represents the scanned object. Relative accuracy is an extremely important component of this research since the shape of the component, both before and after scans, is being used to determine the corresponding change in surface strains.

A phenomenon referred to as noise is always present in LiDAR scan data, at least to some extent. Noise can refer to points that were captured in a scan but are not useful or needed as part of the final geometric product. Noise can also refer to points that are obviously not accurately located. These points can be the result of dusty conditions at a construction site or movement of the scanner (or scanned object), among many other causes. The Leica software packages include at least three ways to remove noise from point cloud data. The statistical outlier removal (SOR) method is a data cleaning feature that removes points that are farther away from their neighbors compared to the average for the point cloud. The radial outlier removal (ROR) method is a data cleaning feature that removes points that have few neighbors within the sphere around them. There is also a manual noise removal method that allows for the deletion of erroneous data that remains after the use of the automated noise removal tools. Noise removal, or cleaning, of the scanned

data captured for this research is performed manually. Local variations in the scanned date are addressed in a process discussed in the following section.

After the noise reduction step, the remaining data points, believed to be sufficiently representative of the component, are transformed onto an xy grid that is constructed using an averaging technique referred to as kriging (or Kriging) that will assign a z coordinate to each intersection of an x and y gridline (Matheron 1963, Wackernagel 2003, Wikipedia 2024). The z coordinate in this research is taken as the average of the z coordinates of all of the points located near the xy intersection, but no farther than halfway to the adjacent gridlines in both the x and y directions. The kriging step provides a convenient, regular geometric arrangement of the point data that represents the scanned component while also serving as a smoothing operation that should reduce the potential for erroneous data to influence the results. This refined 3D geometry is the foundational information that will be used to determine the displacement, slope, and curvature at any point on the surface of the deformed component.

4.5 Stress Analysis: Estimation of Structural Response

The estimation of structural response using LiDAR scan data begins with a simplified approach employed as a first step to test the potential for this novel method of structural assessment. It is beneficial to recall that this research project is focused largely on the potential fatigue problems in the webs of horizontally curved steel plate girders. The fatigue cracks associated with this behavior tend to be related to the repeated bending of the web panels. Since bending and curvature are related by the simple equation $M = \phi EI$, it seemed natural to start the research by attempting to extract the curvature of the surface of the scanned component. In rudimentary mechanics of materials, the curvature of a beam is generally determined by taking the

second derivative of the displacement function that describes the shape of the beam. Because the approach provides discrete point data only, a displacement function that represents the deformed shape of the web is not available. A displacement function that passes through the grid points while simultaneously exhibiting realistic beam behavior must therefore be derived, preferably as a polynomial, so that the curvature can be readily determined.

Two methods of extracting a displacement function for the web along a gridline were tried before a suitable solution was discovered. The idea was to start with what was believed to be the simplest solution and then progress to more complex solutions only as needed. The first attempt was to use a conventional polynomial regression equation in which a curve is fit to an entire set of data points. This approach was easily accomplished in Microsoft Excel, and the effectiveness of the solution was quickly checked. The conventional regression equations provided a good approximation of the displacement and curvature functions near the start of the beam but were found to be significantly in error at all remote points. In Figure 4.28, the black curve represents the shape of a beam element that spans between 0 and 39 inches along the horizontal axis. The beam is fixed at both ends and is in a slightly buckled configuration. The red curve represents the 6^{th} degree regression equation. The blue and green curves overlay one another and represent the 4^{th} and 5^{th} degree regression equations, respectively. All three conventional regression equations provide what appear to be reasonable approximations between about 0 and 7 inches, but diverge at points farther along the beam. This behavior prompted the change from conventional regression equations to moving regression equations.

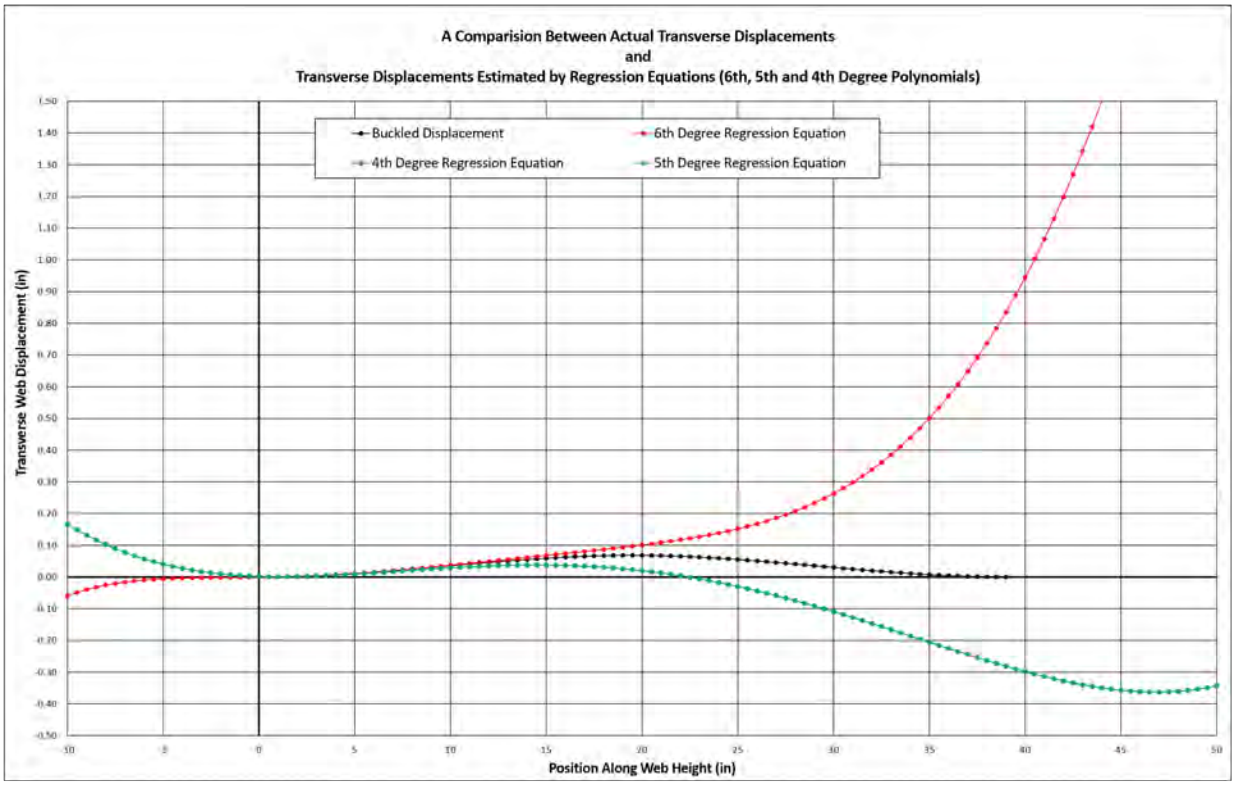

Figure 4.28: Graph showing fit comparison for regression analysis

It was hoped that the use of moving regression equations would provide a more suitable solution for finding the displacement functions through a set of known points. In contrast to conventional regression equations, that attempt to fit a single polynomial to an entire dataset, moving regression equations attempt to fit a single polynomial only to the points in the immediate vicinity of the area of interest. The new displacement function is not a single function, but rather a series of unique polynomials that each do a reasonable job of approximating the displacement and curvature at the point of interest. The moving regression approach was a clear improvement over conventional polynomial regression equations since it avoided the divergence problem at distant points, but the lack of continuity between the individual functions was an obvious indication that improvements could be made. The actual beam would be a sufficiently smooth curve that was both continuous and differentiable along its entire length. The eventual solution

was found in the splines that were originally used in the aircraft and shipbuilding industries to fit complex curves between the key points in a wing or hull design (Wikipedia 2024).

The use of the cubic spline not only provides continuity for the displacement function, but for the first and second derivatives as well through all of the points along the beam under investigation. Individual data points on the refined grid behave as boundary conditions, so a discontinuity exists for the third derivative of the displacement function as expected. Additionally, the potential energy of the deflected beam is minimized (Ahlberg et al. 1967), indicating that provided solution should match observed behavior exactly.

Once a continuous and differentiable displacement function has been found, the stress and strain at any point along a gridline can be easily determined. For one-dimensional elements, the second derivative of the displacement function provides the curvature, ϕ at the point of interest. The curvature is then used to find the moment, M through the basic mechanics of materials relationship $M=\phi EI$. The stress and strain are then found using the relationships $\sigma = \frac{Mc}{I}$ and $\sigma = \frac{\varepsilon}{E}$. A similar approach is used for two-dimensional elements. The curvature for each orthogonal direction, ϕ_x and ϕ_y, is found which leads directly to the calculation of M_x, M_y, σ_x, σ_y, ε_x, and ε_y. The resultant bending moment, M_R and its orientation can be found from vector mechanics. This of course leads directly to the calculation of $\sigma_R = \frac{M_R c}{I}$ and $\varepsilon_R = \frac{\sigma_R}{E}$, the corresponding resultant stress and strain. The calculation of stress and strain based only on curvature is admittedly a simplification of actual web panel behavior. However, it is the bending action occurring near the boundary elements of web panels that is the primary cause for the formation of fatigue cracks. As a result, this simplified approach provides a very good method for identifying potential problem areas on existing steel girders using the point cloud data from two scans and without ever having

to access the structure. It is believed that this will be a powerful tool that can be used by ALDOT to assess structural behavior safely, conveniently, and economically.

The proof-of-concept approach from the above section was a simple, first step to show that basic stress and strain information could be gleaned from the LiDAR scan data of a deformed component. Now that this has been shown at a rudimentary level, a continuum mechanics approach will be developed to show that at any point within the scanned area, the stress and strain can be determined once the necessary LiDAR scan data is acquired and the cross-section properties are known.

Using cubic splines to define the displacement functions, the shape of the web panel can be completely defined along the gridlines in both orthogonal directions. With the three-dimensional coordinates of all points along each gridline known, a section through the web panel can now be taken at any orientation. Each intersection of this new section, or plane, and one of the orthogonal displacement functions provides the three-dimensional coordinates of a point on the surface of the web panel that is located on this new section. The set of all such points provides a discretized representation of the web panel along the section. The application of cubic splines to this new set of points can be used to derive the corresponding displacement functions. With this approach, it is possible to completely define the surface geometry at any point and along any line across the surface of the scanned component.

With the surface geometry of the scanned component completely defined, it is now possible to learn much more about the structural condition of the scanned component. This deeper investigation will start with the strain of a line element (Green strain) which will be used to determine surface strain. Using the before and after LiDAR scans of a deformed component, the components of the Green strain will be used to determine the various stresses and strains that result

from the change in shape. Based on the geometry of a line segment in an undeformed and deformed body (see Figure 2.18 in *Advanced Mechanics of Materials*, Sixth Edition), Boresi and Schmidt derive the following components of the Green strain:

$$\varepsilon_{xx} = \frac{\partial u}{\partial x} + \frac{1}{2}\left[\left(\frac{\partial u}{\partial x}\right)^2 + \left(\frac{\partial v}{\partial x}\right)^2 + \left(\frac{\partial w}{\partial x}\right)^2\right] \tag{4.1}$$

$$\varepsilon_{yy} = \frac{\partial v}{\partial y} + \frac{1}{2}\left[\left(\frac{\partial u}{\partial y}\right)^2 + \left(\frac{\partial v}{\partial y}\right)^2 + \left(\frac{\partial w}{\partial y}\right)^2\right] \tag{4.2}$$

$$\varepsilon_{zz} = \frac{\partial w}{\partial z} + \frac{1}{2}\left[\left(\frac{\partial u}{\partial z}\right)^2 + \left(\frac{\partial v}{\partial z}\right)^2 + \left(\frac{\partial w}{\partial z}\right)^2\right] \tag{4.3}$$

$$\varepsilon_{xy} = \varepsilon_{yx} = \frac{1}{2}\left[\frac{\partial v}{\partial x} + \frac{\partial u}{\partial y} + \frac{\partial u}{\partial x}\frac{\partial u}{\partial y} + \frac{\partial v}{\partial x}\frac{\partial v}{\partial y} + \frac{\partial w}{\partial x}\frac{\partial w}{\partial y}\right] \tag{4.4}$$

$$\varepsilon_{xz} = \varepsilon_{zx} = \frac{1}{2}\left[\frac{\partial w}{\partial x} + \frac{\partial u}{\partial z} + \frac{\partial u}{\partial x}\frac{\partial u}{\partial z} + \frac{\partial v}{\partial x}\frac{\partial v}{\partial z} + \frac{\partial w}{\partial x}\frac{\partial w}{\partial z}\right] \tag{4.5}$$

$$\varepsilon_{yz} = \varepsilon_{zy} = \frac{1}{2}\left[\frac{\partial w}{\partial y} + \frac{\partial v}{\partial z} + \frac{\partial u}{\partial y}\frac{\partial u}{\partial z} + \frac{\partial v}{\partial y}\frac{\partial v}{\partial z} + \frac{\partial w}{\partial y}\frac{\partial w}{\partial z}\right] \tag{4.6}$$

These strain components can be used in combination with the appropriate constitutive relationships and section geometry to determine the state of stress at any point within the scanned area of the structural component. In addition to the Green strain components discussed above, it will be shown that multiple types of strain information can also be gleaned from the change in geometry of the scanned component. These different types include engineering strain, logarithmic (true) strain, and Almansi strain.

4.6 Evaluation of Results for Proposed LiDAR Structural Monitoring (LSM) Method

The primary goal in developing the LiDAR structural monitoring (LSM) method is to provide engineers and researchers with an entirely non-contact structural monitoring technique with accuracy and resolution similar to or better than existing methods, but with improved speed, safety, and economy. The foundational work needed to achieve this goal has been completed and

is described in the preceding sections of this chapter. It is believed that sound engineering principles have been appropriately applied to this problem and that the associated mathematical challenges have been adequately addressed. Despite the confidence in the tasks completed to this point, the proposed LSM method must be rigorously tested to show that this novel procedure will work as intended. The evaluation of LSM results is being carried out through three analytical test problems and two physical tests performed at the Advanced Structural Engineering Laboratory (ASEL) on the Auburn University campus. The LSM method can also be used on Ramp C in Madison, Alabama to assess the behavior of the web panel in Area 4 (see Figure 4.8) from fabrication, to erection, to bridge completion and loaded with the ALDOT Load Truck configured to LC-3 (to closely approximate the AASHTO fatigue truck) after the bridge construction is complete.

The LSM method developed through this research will be evaluated first by comparing the results to problems with both theoretical and finite element solutions. Three problems of increasing complexity will be used in this portion of the evaluation. The first and simplest analytical problem is a cantilevered beam. The idealized cantilevered beam will have a concentrated load at the free end and conventional mechanics of materials methods will provide the theoretical solutions to the problem. Points located at regular intervals along the displacement curve of the idealized beam will be used as refined grid points. A cubic spline approach will be used to fit a series of piecewise polynomials through these grid points. The first and second derivatives of these polynomials will be derived and compared to those from the theoretical solution. The moment, stress, and strain along the length of the beam determined by the LSM method will be compared to the theoretical solution.

4.6.1 Cubic Spline Analytical Demonstrations

The cantilever beam example consists of a 48-inch beam with a concentrated load of 40,000 lbs acting transversely on the free end as shown in Figure 4.29. The theoretical displacement along the length of the beam was calculated using the well-known displacement formula, $v = \frac{Px^2}{6EI} \cdot (x - 3L)$. Twenty-five displacements were calculated at 2-inch intervals along the length of the beam providing 25 sets of xy-coordinates to be used as the geometric basis for the cubic spline that will be used to estimate the structural response of the beam. The theoretical slope and curvature at each point was calculated as the first derivative, $v = \frac{P}{2EI} \cdot \left(x^2 - 2Lx\right)$, and second derivative, $v'' = \frac{P}{EI} \cdot (x - L)$, respectively, of the above formula. The cubic spline, which consists of a series of piecewise third-degree polynomials between each of the 25 sets of coordinates, was calculated in Excel. The displacement, slope, and curvature of the beam were calculated using the cubic splines developed from the coordinates of the theoretical displacements. A comparison was made between the theoretical results and the results based on the cubic spline displacement curve. The cubic spline provided excellent results that can be seen in the graph in Figure 4.30. Additionally, the Tables 4.1 and 4.2 demonstrate that the cubic spline results for slope and curvature are equally accurate.

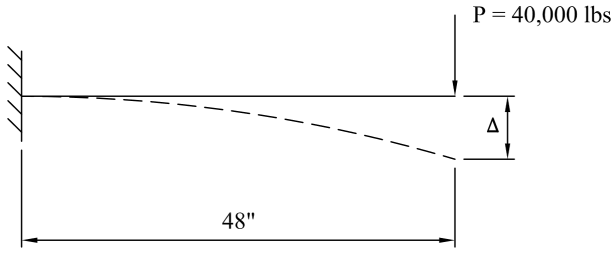

Figure 4.29: Cantilever beam example

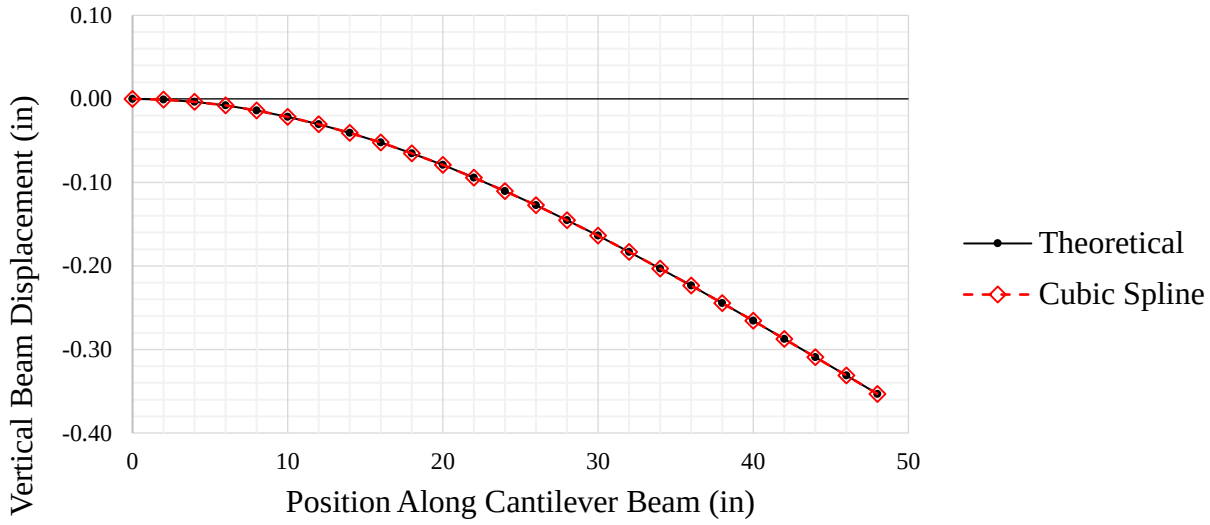

Figure 4.30: Comparison of theoretical and cubic spline displacements

Table 4.1: Comparison of theoretical and cubic spline slopes

Slope Comparison (Theoretical versus Cubic Spline)			
X	**Theoretical**	**Cubic Spline**	**Difference**
0	0.00000	0.00000	0.00000
2	-0.00090	-0.00090	0.00000
4	-0.00176	-0.00176	0.00000
6	-0.00259	-0.00259	0.00000
8	-0.00337	-0.00337	0.00000
10	-0.00412	-0.00411	0.00000
12	-0.00483	-0.00483	0.00000
14	-0.00550	-0.00550	0.00000
16	-0.00613	-0.00613	0.00000
18	-0.00672	-0.00672	0.00000
20	-0.00728	-0.00728	0.00000
22	-0.00780	-0.00780	0.00000
24	-0.00828	-0.00827	0.00000
26	-0.00872	-0.00872	0.00000

28	-0.00912	-0.00912	0.00000
30	-0.00948	-0.00948	0.00000
32	-0.00981	-0.00981	0.00000
34	-0.01010	-0.01010	0.00000
36	-0.01034	-0.01035	0.00000
38	-0.01056	-0.01055	0.00000
40	-0.01073	-0.01073	0.00000
42	-0.01086	-0.01087	0.00000
44	-0.01096	-0.01096	0.00000
46	-0.01102	-0.01101	0.00000
48	-0.01103	-0.01103	0.00000

Table 4.2: Comparison of theoretical and cubic spline curvatures

Curvature Comparison (Theoretical versus Cubic Spline)			
X	**Theoretical (1/in)**	**Cubic Spline (1/in)**	**Difference**
0	-0.00046	-0.00046	0.00000
2	-0.00044	-0.00044	0.00000
4	-0.00042	-0.00042	0.00000
6	-0.00040	-0.00041	0.00001
8	-0.00038	-0.00038	-0.00001
10	-0.00036	-0.00037	0.00000
12	-0.00034	-0.00035	0.00001
14	-0.00033	-0.00032	-0.00001
16	-0.00031	-0.00031	0.00000
18	-0.00029	-0.00029	0.00000
20	-0.00027	-0.00027	0.00001
22	-0.00025	-0.00024	-0.00001
24	-0.00023	-0.00024	0.00001
26	-0.00021	-0.00021	0.00000
28	-0.00019	-0.00018	-0.00001
30	-0.00017	-0.00018	0.00001

32	-0.00015	-0.00015	0.00000
34	-0.00013	-0.00014	0.00000
36	-0.00011	-0.00012	0.00000
38	-0.00010	-0.00009	-0.00001
40	-0.00008	-0.00008	0.00001
42	-0.00006	-0.00006	0.00000
44	-0.00004	-0.00004	0.00000
46	-0.00002	-0.00002	0.00000
48	0.00000	0.00000	0.00000

Two additional demonstrations paired with finite element are planned as part of Steve Hammett's dissertation research. The first (second analytic problem) is a fixed-fixed supported beam subjected to both bending and axial compression. The beam will be subjected to a uniformly distributed load and an axial force. The beam will be modeled with 3D elements so that a unique displaced shape will be created on each side of the component. The nodes of the elements on each side of the model will be used as refined grid points. A cubic spline approach will be used to fit a series of piecewise polynomials through the grid points on each side of the model so that two unique displacement functions are created. The change in length between grid points that occurs as the model moves from the undeformed to the deformed condition will be used to derive the strain that exists on both sides of the beam. This strain information will permit the calculation of the moment and axial forces that exist at any point along the modeled component. The moment, axial force, stress, and strain along the length of the beam determined by the LSM method will be compared to the finite element solution.

The third analytic problem will be a rectangular plate subjected to a uniformly distributed pressure. The rectangular plate will be fixed supported on all edges and be subjected to a transverse, uniformly distributed pressure. 2D elements will be used for the finite element

comparison while theoretical solutions will be taken from the *Theory of Shells and Plates*, Second Edition by Timoshenko and Woinowsky-Krieger. Consistent with the approach used for the first two analytical problems, the finite element nodes will be used as refined grid points that will serve as the foundational geometric data for the cubic splines that are the basis for the displacement functions. The change in shape of the plate determined by comparing the undeformed and deformed conditions will provide the strain data necessary for the comparison to the numerical model and the theoretical solution.

4.6.2 Validation Tests Performed at ASEL

Two physical validation tests were performed at the AU Advanced Structural Engineering Laboratory (ASEL). The first test consisted of the shear buckling of a thin aluminum plate. The plate was 0.02 inches thick and is made from 2024 T3 aluminum. The clear span of the web panel is 22.5 inches x 10.5 inches for an aspect ratio is approximately 2.1. The plate was fixed supported within a frame on four sides. The left end of the frame was fixed supported and the remaining three sides of the frame were free to translate in the plane of the frame. A vertical displacement was enforced at the right end of the frame inducing a shear buckling response in the aluminum plate. A sketch of this test is shown in Figure 4.31. The test was carried out as indicated in the sketch except that digital image correlation (DIC) was used instead of strain gauges to monitor structural response, and the plate was only 0.02 inches thick instead of the 0.04 inch thickness indicated. The aluminum plate was scanned before and after buckling to allow for the determination of the change in stress between the undeformed and deformed conditions. The LSM results will be compared against the results from digital image correlation (DIC) monitoring that

will be performed concurrently. Figure 4.32 shows the undeformed plate (top) and deformed plate (bottom).

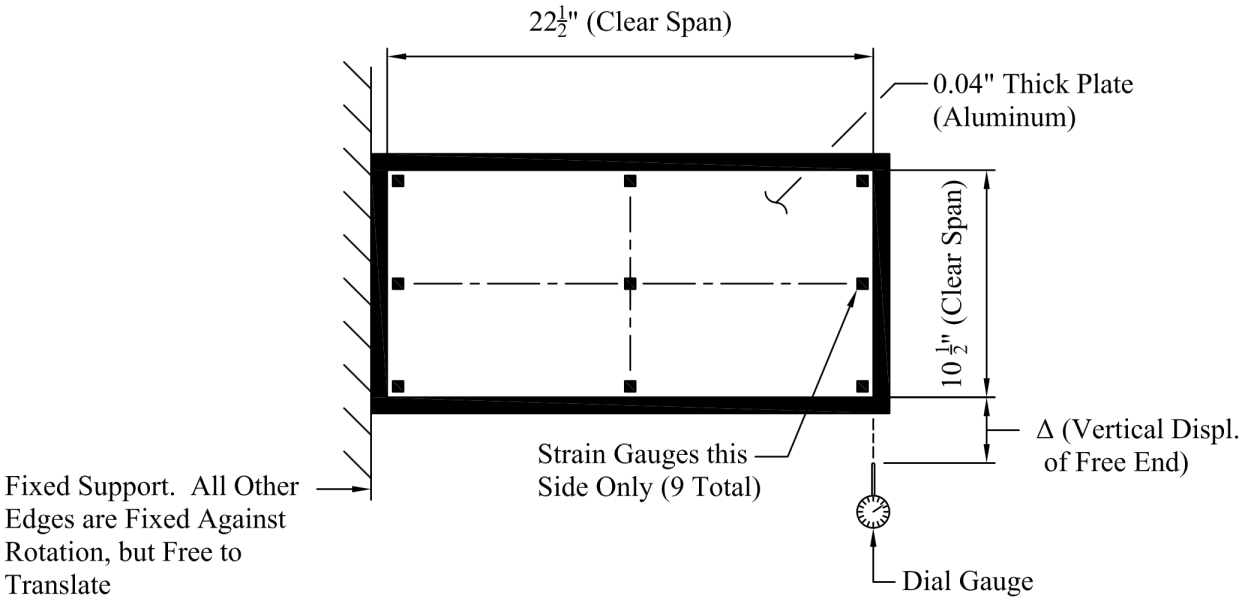

Elevation View of Thin Plate
Scale: 1½"=1'-0"

Buckling Test of Thin Plate:

1. Install resistance strain gauges as shown above.

3. Install dial gauge to capture vertical displacement at free end of plate.

3. Perform a LiDAR scan on undeformed plate.

4. Enforce vertical displacement, Δ at free end of plate until buckled condition is clearly visible. A vertical displacement of approximately 0.25 inches anticipated.

5. Perform a LiDAR scan of buckled plate.

6. Total time needed to perform both LiDAR scans should no more than one hour.

7. Testing apparatus and plate to be tested are already located at ASEL and are ready for testing pending installation of strain gauges.

Figure 4.31: Sketch of shear buckling test for thin plate

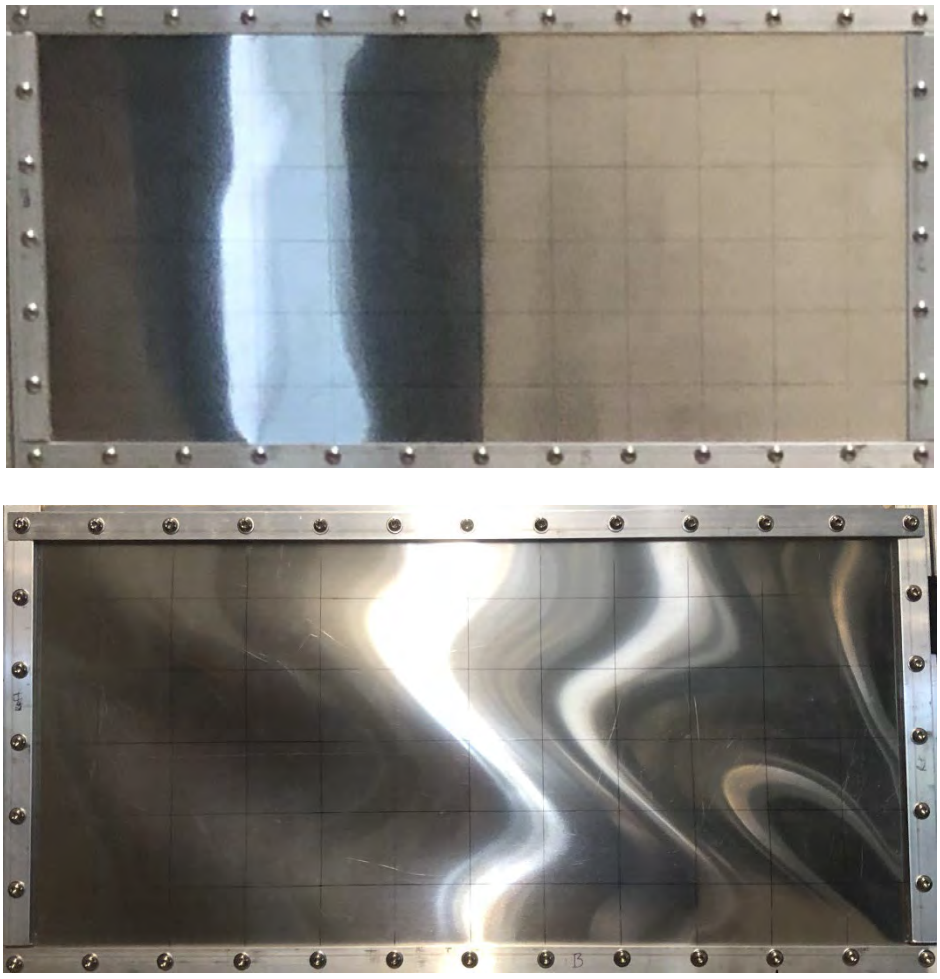

Figure 4.32: Undeformed plate (top) and deformed plate (bottom)

The second test performed at ASEL consists of buckling a plate column in a universal testing machine. The plate measures 0.5 inches thick by 4 inches wide and spans 39 inches between the grips in the machine. Each end of the plate is fixed supported in the grips. A sketch of this test is shown in Figure 4.33. The plate was scanned before and after buckling to allow for the determination of the change in stress between the undeformed and deformed conditions. The LSM results will be compared against the strain gauge results that were captured simultaneously. Figure 4.34 is a picture of the buckling test. Strain gauges at the top, middle, and bottom can be seen. The dial gauge that can be seen on the right side of the plate captured lateral deflections at midpoint of the plate during the test.

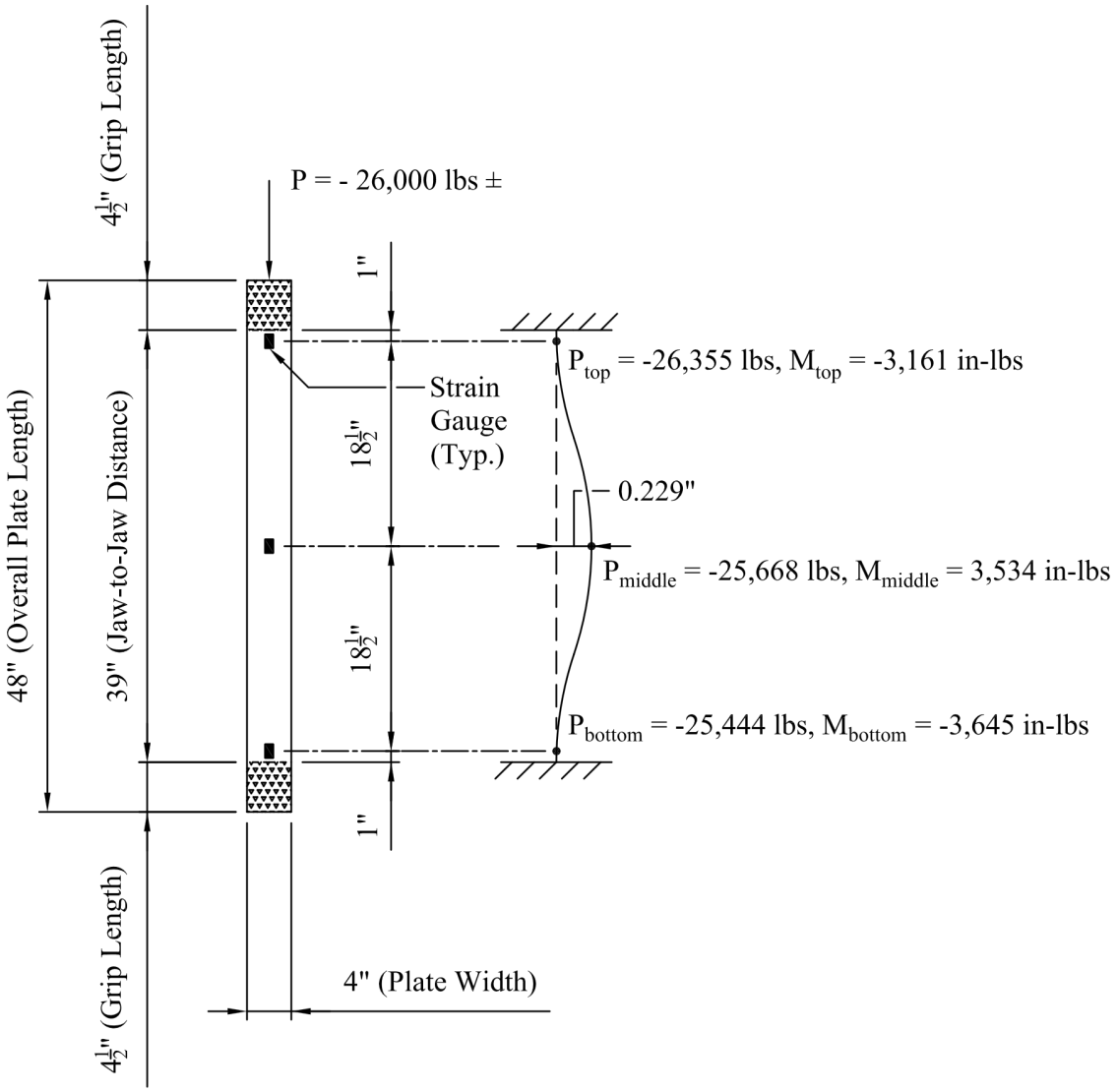

Figure 4.33: Sketch of buckling test for 0.5 inch thick plate

Figure 4.34: Picture of 0.5 inch thick plate during buckling test

The plate buckling example consists of a steel plate column that is buckled by compression in a universal testing machine. The plate has a cross section that is 0.5 inches thick and 4 inches wide. The plate has a clear scan of 39 inches between the grips of the universal testing machine and is fixed supported at each end. The plate column buckled at approximately 26,000 lbs and assumed the displaced shape that is included in the sketch in Figure 4.33

The test was performed on August 9, 2024 at ASEL and a LiDAR scan captured the displaced shape of the buckled plate column. The raw scan data was registered in the Leica Cyclone Register 360 program and then exported in the LAS file format for post-processing in the Leica Cyclone 3DR program. Cyclone 3DR was used to remove all the unnecessary point data captured in the scan and to create a CSV file containing the three-dimensional point data to be used for estimating the structural response. The CVS file was imported into Excel where the process of kriging and fitting of the cubic spline occurred. Figure 4.35 shows a graph of the raw scan data as well as graph of the data after going through the kriging process. The roughness of the raw scan data can be seen, especially when compared to the data after the kriging process. An overlay of these graphs, shown on the right, confirms that the data refined by the kriging process simply smooths the raw data while accurately capturing the structural deformations. A cubic spline was fit to the data following the kriging process and the curvature at the middle of the plate was determined to be 0.00283 1/in. The curvature of the plate based on the strain gauge date was determined to be 0.00296 1/in. The ratio of the curvatures (strain gauges/splines) was determined to be 1.046, indicating that the bending stress determined by the two methods differed by less than 5 percent. The bending stress determined by the strain gauges was 21,437 psi compared to that determined using splines was 20,518 psi.

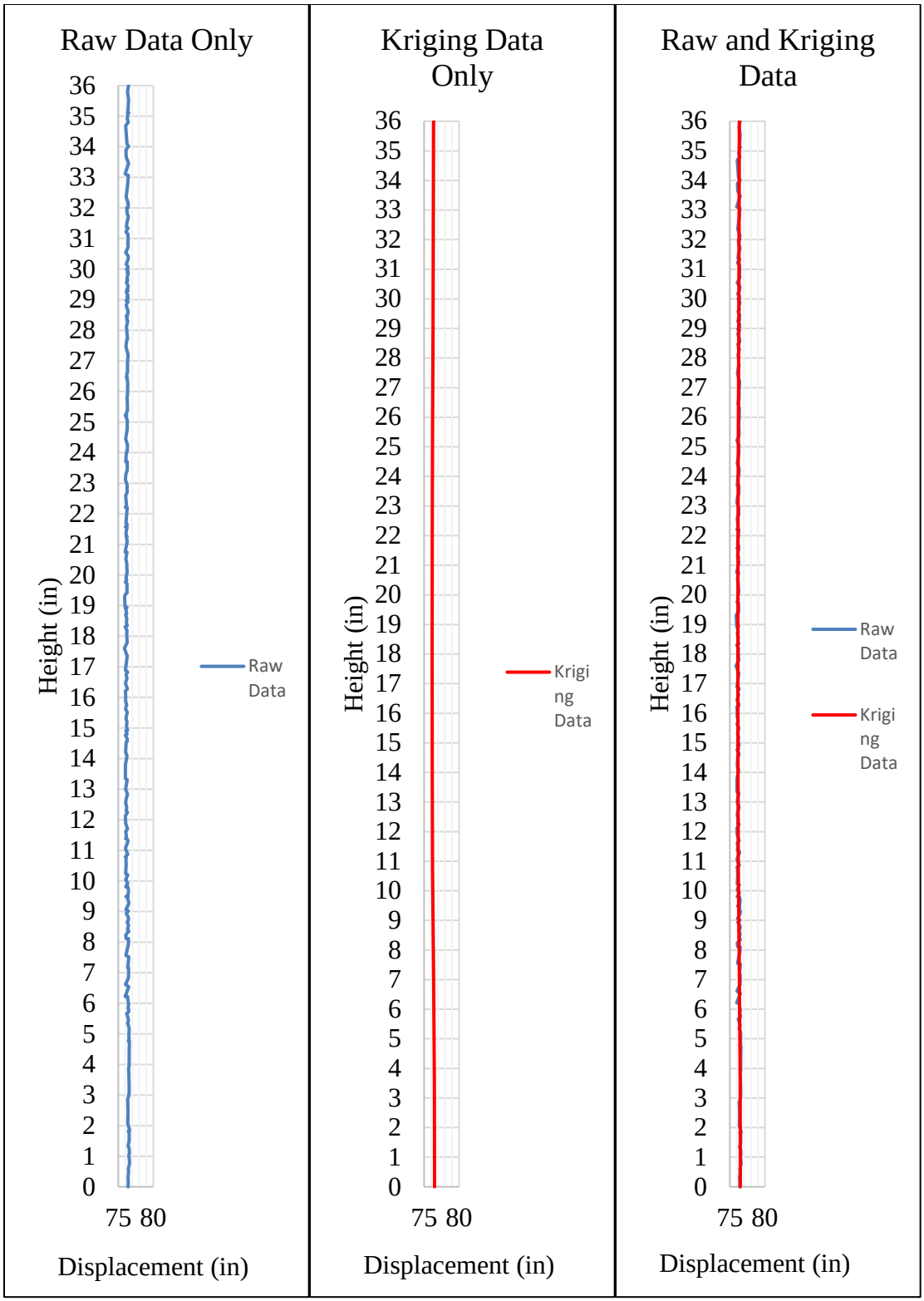

Figure 4.35: Graph comparing the raw data with the data refined by kriging

4.6.3 Ramp C Bridge Scan

The fabrication and erection phases of the Ramp C bridge horizontally curved steel plate girders are complete and LiDAR scans of the areas of interest (Area 4, Figure 4.9) were performed as indicated in Figure 4.26 and Figure 4.27. The Ramp C bridge is currently being prepared for concrete deck placement, but at the time of writing this report, the completion of the bridge is still several months away. Once the bridge is completed and just prior to being opened to traffic, the ALDOT load truck can be used to take scans under traffic loading and complete the evaluation of the LSM method.

The erection of the superstructure for the Ramp C bridge in Madison, Alabama was completed on Monday, August 5, 2024. On Tuesday, August 6, 2024, multiple LiDAR scans of the superstructure were taken. Consistent with the analytical work performed as part of the initial phase of this research project, the scanner was positioned as close as possible to Girder No. 1 in the vicinity of Bent No. 6. Figure 4.36 shows the primary scanner placement where capturing the best scan data was anticipated. Several additional scans were taken of Girder No. 1, but the scanner was never more than about 100 feet from Bent No. 6.

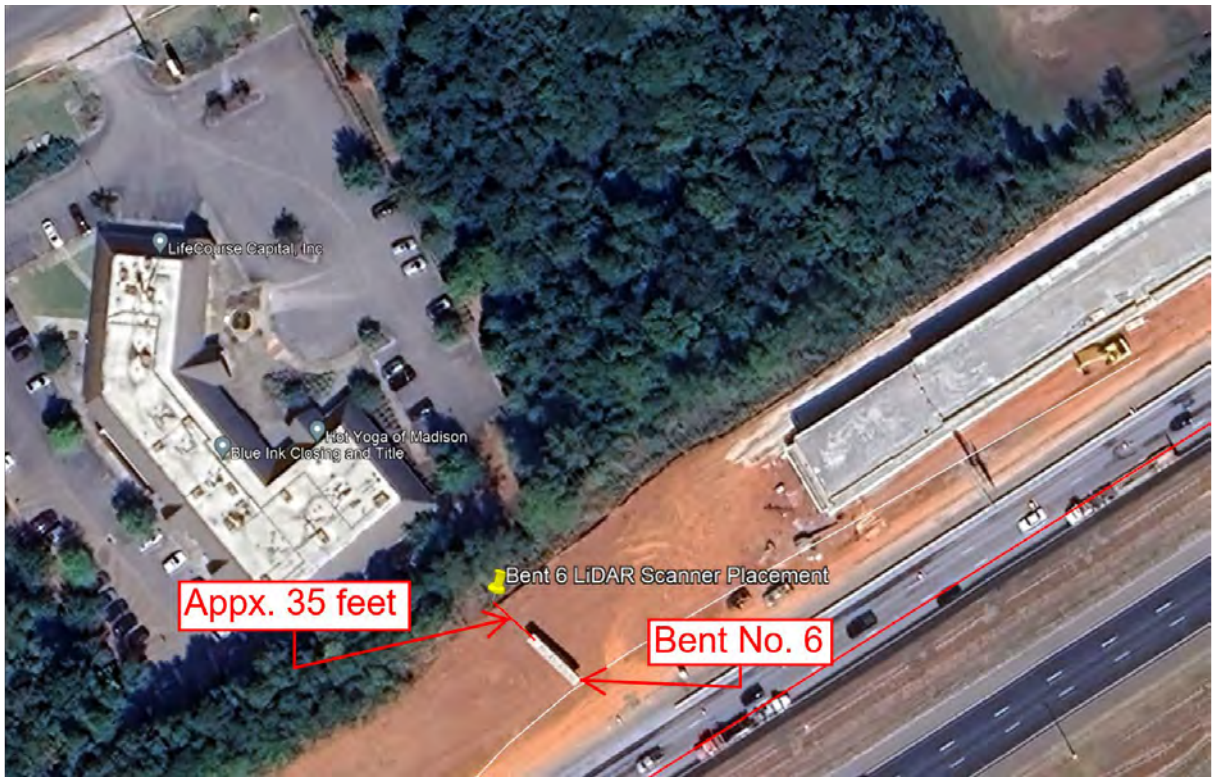

Figure 4.36: Scanner placement at the Ramp C Bridge

Figure 4.37 shows a screen shot of the point cloud taken from within the Cyclone 3DR program. Bent No. 6 is in the middle of the picture with abutment No. 7 in the background near the left of the image.

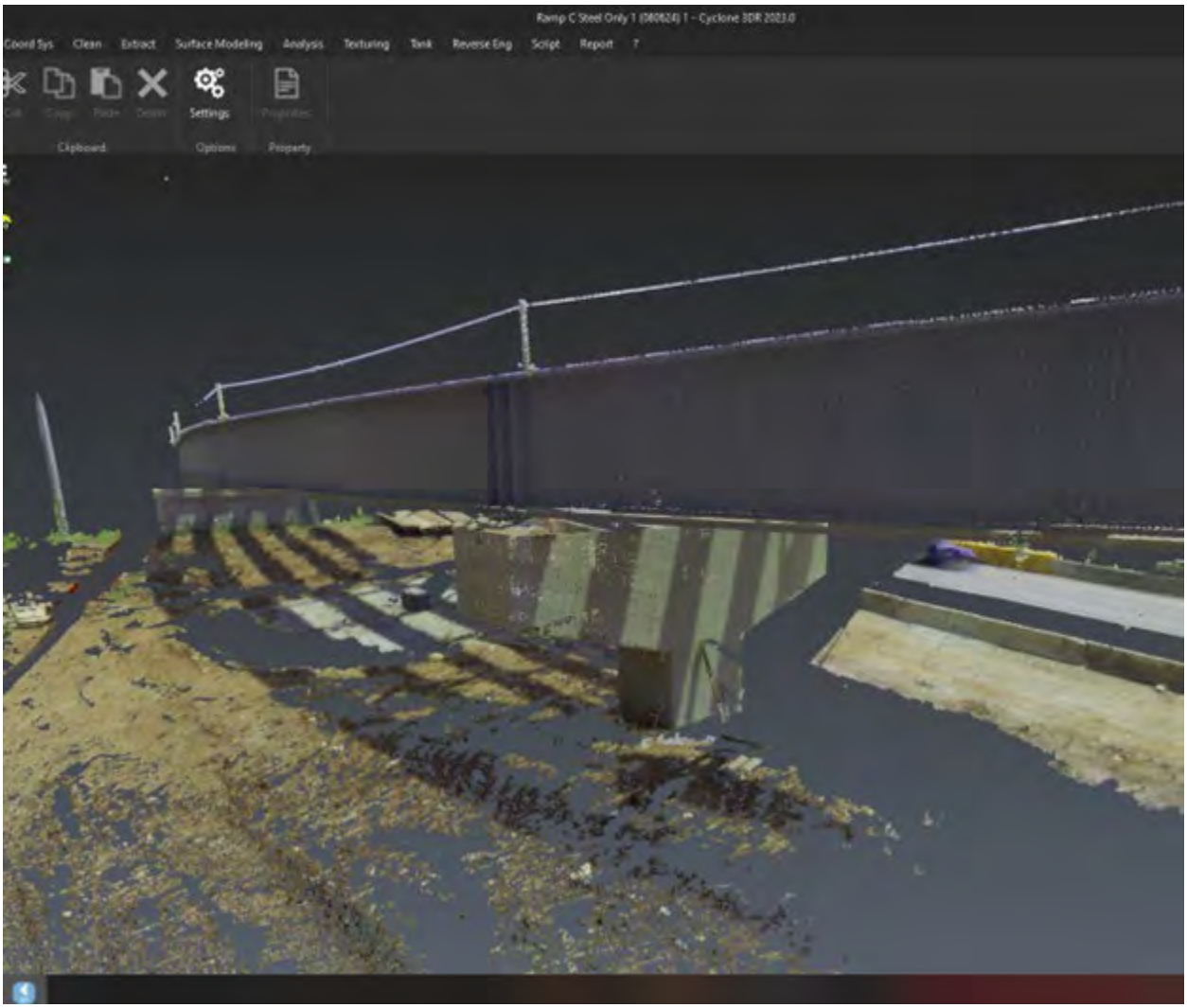

Figure 4.37: Point cloud of girder No. 1 at bent No. 6

The very large point cloud shown in the figure above contains much data that is not relevant to the goals of this project. Cyclone 3DR was therefore used to eliminate these points so that only those needed for analysis remained, with the inclusion of some additional points to help identify exactly where on the bridge these points exist. Figure 4.38 shows this reduced point cloud with the hammerhead cap at Bent No. 6. The vertical green line in the figure is a section through the plate girder that will used to export points for the LSM method. Figure 4.39 shows a graph of the point cloud data from this section.

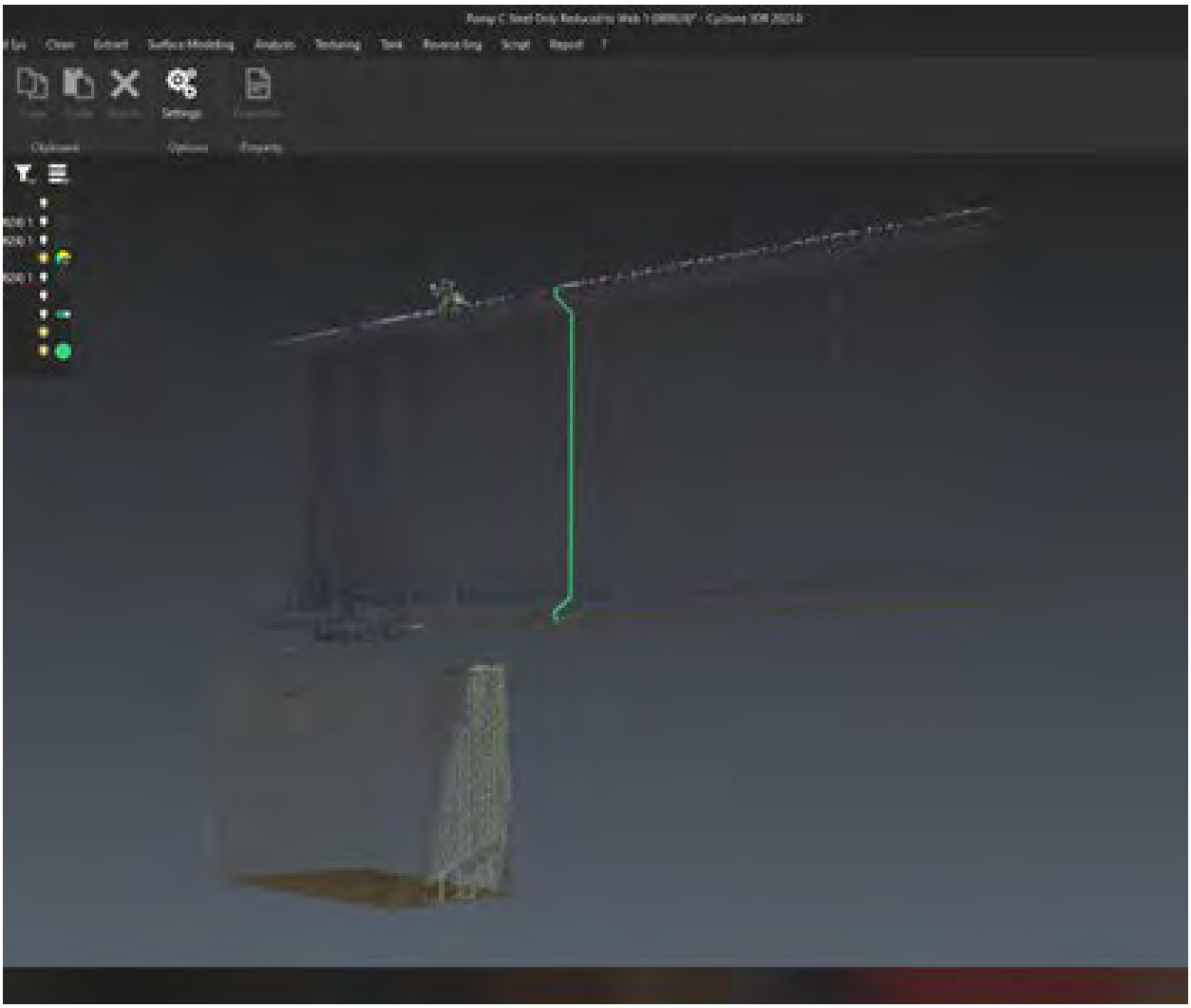

Figure 4.38: Point cloud of web on girder No. 1 just before bent No. 6

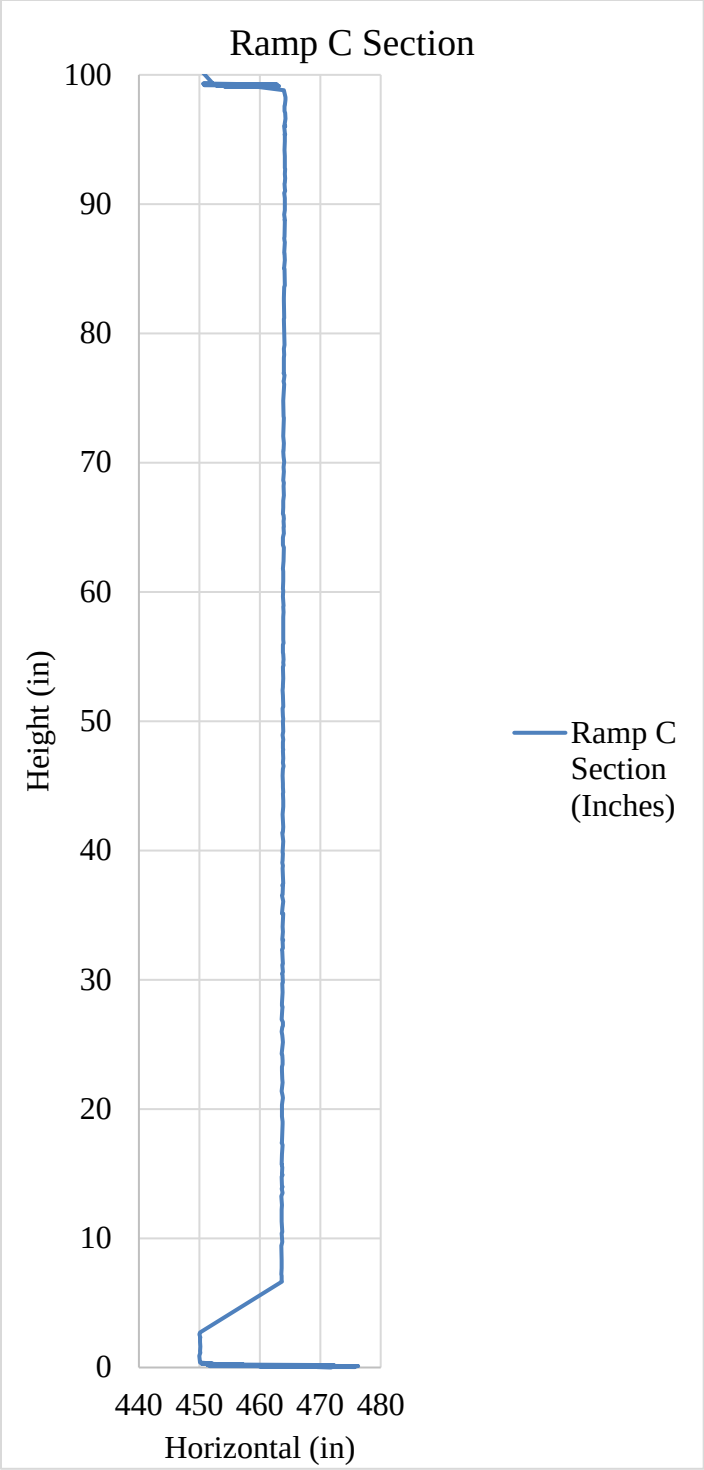

Figure 4.39: Graph of point cloud data through girder No. 1 near bent No. 6

The focal point of this cross section is the web, so it is beneficial to eliminate the points for the top and bottom flanges. Figure 4.40 shows a graph of the raw data, data after kriging, and on overlay of the two.

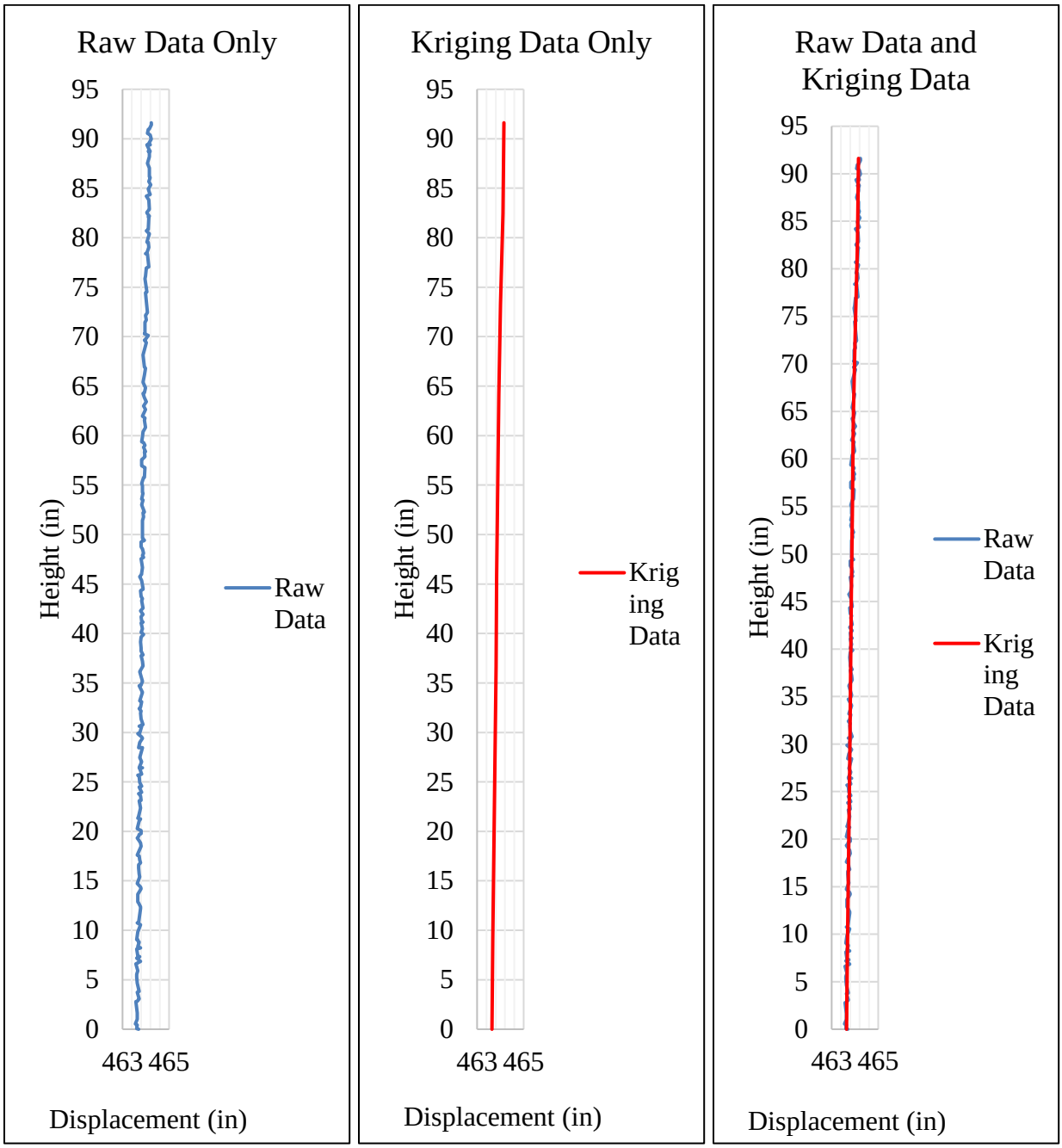

Figure 4.40: Graph comparing the raw data with the data refined by kriging

A cubic spline was constructed for the data that had been post-processed by kriging. The maximum curvature along this section of the web was determined to be approximately 0.00054 1/in. Based on the web thickness of 0.75 inches, this curvature corresponds to a moment of approximately 550 in-lbs/in and a stress of approximately 5,900 psi. This state of stress assumes that the plate was initially flat, and it is not particularly important since this project is largely concerned with fatigue issues which is related to the stress range in the AASHTO LRFD Bridge Design Specifications, 2020. Once the bridge is completed, two additional sets of LiDAR scans on the completed structure can be accomplished. One set of scans are recommended to be with the full dead load only and the other set with the ALDOT load truck (LC-3) configured to simulate the AASHTO fatigue truck. A comparison of these two scans of the web panel on girder No. 1 near bent No. 6, using the LSM method, should provide the stress range needed to evaluate web performance in accordance with the current AASHTO specifications.

CHAPTER 5
CONCLUSIONS AND RECOMMENDATIONS

When the web of straight girders is slender and susceptible to elastic buckling, the repeated out-of-plane deformation of the web, known as "web breathing," can lead to fatigue cracks under cyclic loading (Günther and Kuhlmann 2014). Web breathing related to straight girders has been comprehensively investigated through analytical and experimental studies (Mueller and Yen 1966; Toprac and Natarajan 1971; Okura et al. 1993; Spiegelhalder 2000; Crocetti 2001). Curved steel girders experience large deflection and rotations during construction and service that can intensify the web breathing effect. In addition, the curvature-induced lateral forces pushing and pulling slender curved webs develop mechanisms that can lead to critical web boundary stresses that do not typically occur in straight bridges.

There are only a few studies specifically focused on the fatigue behavior of curved steel girders; the most prominent are Daniels and Herbein (1980) at Lehigh University and Nakai et al. (1990) in Japan. The Japan study (Nakai et al. 1990) investigated the fatigue strength of fillet welds at the web boundaries of horizontally curved girders through an experimental and analytical approach. Five single simply-supported curved girders were loaded under pure bending. All test samples had the web panel aspect ratio and slenderness ratio of 0.75 and 144, respectively. Both the test and the analytical approach were based on the beam-column behavior and did not represent the actual behavior of curved bridge web panels. Fatigue cracks were detected at the location of applied concentrated loads, but no fatigue crack was detected at the web to flange or stiffener location.

As a part of the Lehigh University study (Daniels and Herbein 1980), five twin-girder, I-shaped assemblies were tested to evaluate five different fatigue detail categories. Since the test setup was not designed specifically for slender-web curved girders, only two girders that had web slenderness ratios of 192 and 186 were considered. Consequently, no fatigue cracking was observed at the web boundaries due to web out-of-plane displacements. However, fatigue cracks occurred at the web gap between the transverse stiffener and tensile flange. Although no analytical effort was made to investigate the web panel boundary stresses critical for fatigue considerations, a design limit equation was proposed. The equation was a less conservative version of a limit that was originally developed based on the stability of the curved web panels.

As a part of the present study, a parametric FEM analysis was conducted to capture the web behavior of the horizontally curved composite bridges. An advanced FEM modeling technique was developed to simulate the continuous web stress development from construction to the service state. The goal was to address the non-composite stage dead load web distortions effects on the fatigue behavior of curved web panels at the composite stage. Three fatigue prone regions were investigated: 1) web-to-flange connection at the tension flange of the high bending region; 2) web-to-bearing stiffener of the end supports at the high shear region; and 3) web-to-bearing stiffener of the mid-support at the high shear and bending region. It was observed that curved girders with slender webs experience significantly larger web stress concentrations critical for fatigue cracking compared to the equivalent straight girders.

The analytical methods corresponding to web breathing of straight and curved web panels were reviewed and evaluated by refined FEM analysis. The analytical equation developed by Japanese researchers (Nakai et al. 1990) to calculate web secondary bending stresses at the flange location was compared with refined nonlinear FEM analysis. It was observed that the Nakai et al.'s

equation is accurate for the linear response of stocky curved web panels that behave similar to beam-columns. However, it cannot be applied to curved web panels with slender webs.

In order to develop an equation to improve fatigue design methodology, isolated curved web panels under pure bending moment were analyzed by validated parametric finite element analysis. Radius of curvature, web slenderness ratio, panel aspect ratio, and in-plane stress ratio effect were studied. The following limit was derived to address the fatigue cracking at the web-to-flange connection of the compression flange:

$$\max \sigma_0 \leq \begin{cases} \dfrac{\Delta\sigma_c^{Type2}}{1-ST} \\ 1.5\sigma_{cr} \end{cases} \tag{5.1}$$

where the maximum in-plane bending stress, $\Delta\sigma_C^{Type2}$ is the fatigue resistance of crack type 2, *ST* is the stress ratio, and σ_{cr} is the linear elastic bend buckling stress of flat web. The top term is related to the fatigue crack type 2, web-to-transverse stiffener, at the tension flange. AASHTO (2020) requires the tensile in-plane stress ranges at the web-to-transverse stiffener of bending beams to be limited to the corresponding fatigue detail category strength. The top term of the proposed equation limits the in-plane bending stress range to the fatigue crack type 2 strength, and the bottom term controls the maximum in-plane bending stress in the compressive region of the web.

The fatigue crack at the web-to-stiffener (the top term of equation 5.1) controls the maximum in-plane bending stress critical for web breathing for the web slenderness up to almost 250. This means that fatigue cracks emerge first at the web-to-stiffener location for curved web panels without longitudinal stiffeners before fatigue cracks at the web-to-flange connection of the compression flange while the slenderness is less than 250.

It was also observed that curvature decreases the allowable maximum in-plane bending

stress compared to the flat web panels. However, the influence dissipates for the high web slenderness ratios, i.e. 250. In other words, the significant curvature effects on web breathing fatigue fall below the web-to-stiffener fatigue check for normal to moderately high web slenderness ratios.

There is no explicit fatigue limit state check for web breathing in the AASHTO LRFD (2020) bridge design specifications. The web bend buckling stress is conservatively limited to the theoretical elastic bend buckling stress at the service limit state, including dead and live load, to prevent fatigue issues due to web buckling. In addition, longitudinal web stiffeners are required for webs with slenderness ratios over 150.

The following recommendations are made based on the results of the analytical study. First, the current AASHTO (2020) considerations to prevent web breathing are conservative and safe to use for both straight and curved I-girder bridges. Second, both curved and straight web panels can be safely designed without fatigue cracking due to web breathing for web slenderness up to 250 provided that the web-to-stiffener fatigue detail category is checked at the fatigue limit state. Third, maximum in-plane bending stress due to fatigue loads can reach up to 1.5 times of the critical bend buckling stress for highly slender webs with no risk of web breathing.

The combined effect of in-plane shear and bending stress on web breathing of curved web panels was also studied through parametric FEM analysis. Two load combinations of $\tau_0=\sigma_0$ and $\tau_0=0.5\sigma_0$ were considered along with the following parameters: radius of curvature, web panel slenderness ratio, web panel aspect ratio, and stress ratio $\tau_0=\sigma_0$ and $\tau_0=0.5\sigma_0$. It was observed that shear stress significantly affects the fatigue performance of curved web panels. In the case of high web panel slenderness ratio, i.e. β=200, and high shear portion of combined loading, i.e. $\sigma_0=\tau_0$, web breathing critical stresses become identical for curved and straight web panels. The following

equation was developed based on the parametric finite element simulations of load combinations $\tau_0=0.5\sigma_0$ to limit the in-plane bending stress to prevent web breathing:

$$\max \sigma_0 \le \min \begin{cases} \dfrac{\Delta\sigma_c^{Type2}}{1-ST} \\ 0.7\sigma_{cr} \end{cases} \tag{5.2}$$

where *max* σ_0 is the maximum in-plane bending stress, $\Delta\sigma_c^{Type2}$ is the fatigue resistance of crack type 2, *ST* is the stress ratio, and σ_{cr} is the linear elastic bend buckling stress of a flat web.

In the case of combined loading, AASHTO (2020) limits the shear force of the interior web panels, regardless of the shear and bend load combination, to control web breathing by the following equation:

$$V_u \le V_{cr} \tag{5.3}$$

where V_u is shear in the web at the section under consideration due to the unfactored permanent load plus the factored fatigue load (kip), and V_{cr} is shear-buckling resistance. AASHTO (2020) states that "*if equation [5.3] is satisfied, significant elastic flexing of the web due to shear is not expected to occur, and the member is assumed able to sustain an infinite number of smaller loadings without fatigue cracking due to this effect*". A direct comparison between the developed equation 5.2 and the AASHTO (2020) requirement, equation 5.3, is not possible due to the nature of the parametric study. Equation 5.2 was derived based on the fatigue loads not the combined effects of dead and fatigue loads. In addition, equation 5.2 follows the approach of limiting in-plane bending stress since the curvature effects are higher compared to the straight girders, rather than limiting shear stress.

The analytical studies indicated that web breathing is more severe in the case of combined loading compared to the pure bend condition. The curvature influence on intensifying the web breathing becomes negligible for the combined loading case when the portion of shear is high such

as $\tau_0=\sigma_0$ due to dominant shear force effects. Hence, it is recommended that the fatigue design limit of curved web panels be on the basis of the fatigue design considerations related to flat web panels. In addition, it was observed that the current AASHTO (2020) limit for web panels under combined shear and bend loading is satisfactory for both curved and straight web panels.

It was demonstrated that LiDAR point cloud data can be used to capture the shape of a structural component and that the shape can be used to evaluate its structural condition. The LiDAR structural monitoring (LSM) method provided an exact match to the theoretical cantilever beam problem. The LSM method also provided good results for the plate buckling problem. The estimated curvature, moment, and bending stress at the middle of the plate column were within 5 percent of the values determined by strain gauges. Surveying the Ramp C bridge in Madison, Alabama was very challenging because of the proximity to interstate traffic, the size of the structure, and the fact that it was an active construction site. Despite these difficulties, the required LiDAR scans were made from a position of safety behind the traffic barriers. The raw point cloud data was made in less than two hours without having to contact the structure. Additional research is needed to refine the approach, but the potential benefits in speed, safety, and economy are clear.

The work thus far into the LSM method has been focused on determining the curvature of a component at an area of interest. This is very useful information for the evaluation of plate girder webs for fatigue issues since this problem is often related to bending stresses. Unfortunately, structural behavior is generally much more complex and often cannot be defined by a single, dominant behavior. Ideally, a structural assessment tool should be able to detect more than just a single component of structural performance. The results from this project indicates that the LSM method can be developed to determine much more than simply the curvature of a scanned component. Cubic splines provide an excellent tool for determining the shape of a scanned

component. Because these polynomials are accurate, it is expected that they can be used to map (geometrically define) the entire surface of a scanned component. With this refined data, a comparison of the scan taken before a deformation and the scan taken after would provide the engineer or researcher the ability to determine the surface strains in any direction and from any cause, so that the entire process does not rely on a single structural response such as bending. Additional work on the LSM method should focus on more fully describing the geometry of a scanned component and determining the best way to compare the geometry between two subsequent scans.

REFERENCES

AASHTO, LRFD. 2020. *AASHTO LRFD Bridge Design Specifications*. American Association of State Highway and Transportation Officials, 9th Ed. Washington, DC.

AASHTO, LRFD. 2017. *AASHTO LRFD Bridge Design Specifications*. American Association of State Highway and Transportation Officials, 8th Ed. Washington, DC.

AASHTO, LRFD. 2004. *AASHTO LRFD Bridge Design Specifications*. American Association of State Highway and Transportation Officials, 2nd Ed. Washington, DC.

AASHTO. 1992. *Standard Specifications for Highway Bridges*. American Association of State Highway and Transportation Officials, 15th Ed. Washington, DC.

AASHTO. 1989. *Standard Specifications for Highway Bridges*. American Association of State Highway and Transportation Officials, 14th Edition.

AASHTO. 1993. *Guide Specifications for Horizontally Curved Highway Bridges*. American Association of State Highway and Transportation Officials, 2nd Ed. Washington, DC.

ABAQUS. 2019. https://www.3ds.com. Dassault Systèmes Simulia Corp., Johnston, RI.

Ahlberg, J.H., Nilson, E.N., Walsh, J.L. 1967. *The Theory of Splines and Their Applications*. New York: Academic Press

Aribert, J. M., Remadi, A., Raoul, J.1996. "Parametric Study by FEM on Breathing of Steel Slender Webs" PD-Vol. 73, Third Biennial Joint Conference on Engineering Systems Design and Analysis, ESDA, Vol. 1, Montpellier, France.

AWS. 2010. D1.5. *Bridge Welding Code – Steel*. ANSI/AASHTO/AWS D1.5M/D1.5. American Welding Society.

ASCE. 1982. "ASCE Committee on Fatigue and Fracture Reliability." Fatigue Reliability: Journal of Structural Division, 3–23.

Barth, Karl E., and Donald W. White. 1998. "Finite Element Evaluation of Pier Moment-Rotation Characteristics in Continuous-Span Steel I Girders." *Engineering Structures*. 20 (8): 761–78. https://doi.org/10.1016/S0141-0296(97)00087-4.

Berge, S., and H. Myhre. 1977. “Fatigue Strength of Misaligned Cruciform and Butt Joints.” Norwegian Maritime Research 5 (1).

Bowman, M. D., Fu, G., Zhou, Y. E., Connor, R. J., and Godbole, A. A. 2012. *Fatigue Evaluation of Steel Bridges*. National Cooperative Highway Research Program Rep. No. 721, Transportation Research Board, National Research Council, Washington, DC.

Broujerdian, V., Mahyar, P., and Ghadami, A. 2015. Effect of curvature and aspect ratio on shear resistance of unstiffened plates. *Journal of Constructional Steel Research*. 112, 263-270.

Chacón, R., M. Serrat, and E. Real. 2012. “The Influence of Structural Imperfections on the Resistance of Plate Girders to Patch Loading.” *Thin-Walled Structures*. 53 (April): 15–25.

Consortium of University Research Teams (CURT). 1975. *Tentative Design Specifications for Horizontally Curved Highway Bridges*. Final Rep., Research Project HPR2-(111).

Clarin, M., 2004. *High Strength Steel: Local Buckling and Residual Stresses* (Doctoral dissertation, Luleå tekniska universitet).

Crocetti, R. 2001. On Some Fatigue Problems Related to Steel Bridges. Chalmers University of Technology.

Culver, C. G., Dym, C. L., and Brogan, D. K. 1972. Bending Behavior of Cylindrical Web Panels. *Journal of the Structural Division*. 98(10), 2291-2308.

Culver, C.G., Dym, C.L. and Uddin, T., 1973. Web Slenderness Requirements for Curved Girders. *Journal of the Structural Division*. 99(3), pp.417-430.

Culver, C. G., and N. Nasir. 1969. *Instability of Horizontally Curved Members, Flange Buckling Studies*. Pennsylvania Department of Highways by Department of Civil Engineering Rep. No. 68 32.

Dabrowski, R. 1968. “Gekrümte dünnwandige Träger: Theorie und Berechnung.” Springer-Verlag, Berlin.

Daniels, J. H., and W. C. Herbein. 1980. *Fatigue of Curved Steel Bridge Elements—Fatigue Tests of Curved Plate Girder Assemblies*. Rep. No. FHWA-RD-79-133, Lehigh Univ., Bethlehem, Pa., 157.

Daniels, J. H., and R. P. Batcheler. 1979. “Fatigue of Curved Steel Bridge Elements-Effect of Heat Curving on the Fatigue Strength of Plate Girders,” August. https://trid.trb.org/view/158073.

Daniels, J. H., Zettlemoyer, N., Abraham, D., and Batcheler, R. P. 1979a. ‘‘Fatigue of Curved Steel Bridge Elements—Analysis and Design of Plate Girder and Box Girder Test Assemblies.’’ DOT-FH-11-8198.1, Lehigh University, Bethlehem, PA.

Davidson, J. S., Ballance, S. R., and Yoo, C. H. 2000. Behavior of Curved I-girder Webs subjected to Combined Bending and Shear. *Journal of Bridge Engineering*. 5(2), 165-170.

Davidson, J. S., Ballance, S. R., and Yoo, C. H. 1999. Analytical Model of Curved I-girder Web Panels subjected to Bending. *Journal of Bridge Engineering*. 4(3), 204-212.

Davidson, J. S., Ballance, S. R., and Yoo, C. H. 1999. Finite Displacement Behavior of Curved I-Girder Webs subjected to Bending. *Journal of Bridge Engineering*. 4(3), 213-220.

Davies, A. W., and Roberts, T. M. (1996). Numerical Studies of Fatigue Induced by Breathing of Slender Web Plates. *Thin-walled Structures*. 25(4), 319-333. https://doi.org/10.1016/0263-8231(96)00008-0.

Dubas P. 1992. “Zum Problem der Stegatmung bei dünnwandigen Blechträgern” Publikation Nr. 92-3, Baustatik und Stahlbau, Eidgenössische Technische Hochschule Zürich.

Duchene, Y., and Maquoi, R. 1998. Fatigue Resistance to Web Breathing of Slender Plate Girders subjected to Shear. *Journal of Constructional Steel Research*. 46, 416-416.

ECCS. 1976. *Manual on Stability of Steel Structures*, 2nd Edition. European Convention for Constructional Steelwork.

EN, B. 2006. *Eurocode 3 - Design of Steel Structures - Part 2: Steel Bridges*. British Standards Institution.

Farahmand, Bahram, George Bockrath, and James Glassco. 2012. *Fatigue and Fracture Mechanics of High Risk Parts: Application of LEFM and FMDM Theory*. Springer Science and Business Media.

Fiechtl, A. L., G. L. Fenves, and K. H. Frank. 1987. *Approximate Analysis of Horizontally Curved Girder Bridges*. Final Report.

Fisher, John W., Karl Heinz Frank, Manfred A. Hirt, and Bernard M. McNamee. 1969. *Effect of Weldments on the Fatigue Strength of Steel Beams*. Final Report, (70-25).

Fisher, John W., Geoffrey L. Kulak, and Ian FC Smith. 1998. *A Fatigue Primer for Structural Engineers*. National Steel Bridge Alliance, American Institute of Steel Construction.

Forman, Royce G., V. E. Kearney, and R. M. Engle. 1967. "Numerical Analysis of Crack Propagation in Cyclic-Loaded Structures." *J. Basic Eng*. ASME. September; 89(3): 459–463.

Frankl, B. A., and Linzell, D. G. 2017. Influence of Horizontal Curvature on the Shear Resistance of Steel Plate Girders with Slender Webs. Structures Congress 2017 (pp. 292-301).

Fujii, K., and Ohmura, H.1985. Nonlinear Behavior of Curved Girder-Web Considered Flange Rigidities, *Proceedings of JSCE Structural Engineering*, No. 356, pp. 69-79.

Galambos, Theodore V. 1978. *Tentative Load Factor Design Criteria for Curved Steel Bridges*. Washington University, School of Engineering and Applied Science, Department

Ghyabi, M., Timber, L. C., Jahangiri, G., Lattanzi, D., Shenton Iii, H. W., Chajes, M. J., & Head, M. H. 2023. Vision-Based Measurements to Quantify Bridge Deformations. *Journal of Bridge Engineering*. 28(1). https://doi-org.spot.lib.auburn.edu/10.1061/(ASCE)BE.1943-5592.0001960

Griffith, Alan Arnold. 1921. "VI. The Phenomena of Rupture and Flow in Solids." Philosophical Transactions of the Royal Society of London. Series A, Containing Papers of a Mathematical or Physical Character 221 (582–593): 163–98.

Grubb, Michael A., Kenneth E. Wilson, Christopher D. White, and William N. Nickas. 2015. "Load and Resistance Factor Design (Lrfd) for Highway Bridge Superstructures-Reference Manual." National Highway Institute (US).

Grubb, M. A., and Hall, D. H. 2019. Curved Steel Bridge Research Project: I-Girder Bending Component Test–Philosophy and Design of the I-Girder Bending Component Tests (No. FHWA-HIF-19-064). Federal Highway Administration (US).

Günther, H. P., and Kuhlmann, U. 2004. Numerical Studies on Web Breathing of Unstiffened and Stiffened Plate Girders. *Journal of Constructional Steel Research*. 60(3-5), 549-559.

Hall, D. H., and Yoo, C. H. 1998. ‘‘Recommended Specifications for Steel Curved-Girder Bridges.’’ Prepared for National Cooperative Highway Research Program, Transportation Research Board, National Research Council, Washington, D.C.

Hartmann, J. L. 2005. *An Experimental Investigation of the Flexural Resistance of Horizontally Curved Steel I-Girder Systems*. PhD dissertation. University of Maryland, College Park.

Hobbacher, Adolf. 2016. *Recommendations for Fatigue Design of Welded Joints and Components*. Vol. 47. Springer.

Issa-El-Khoury, G., Linzell, D. G., and Geschwindner, L. F. 2016. Flexure–shear Interaction Influence on Curved, Plate Girder Web Longitudinal Stiffener Placement. *Journal of Constructional Steel Research*. 120, 25-32.

Issa-El-Khoury, G., Linzell, D. G., and Geschwindner, L. F. 2014. Computational Studies of Horizontally Curved, Longitudinally Stiffened, Plate Girder Webs in Flexure. *Journal of Constructional Steel Research*. 93, 97-106.

Jalali, Mehran M., Justin D. Marshall, and James S. Davidson. 2020. Buckling and Distortion Induced Fatigue of Curved Steel Plate Girders with Slender Web. *Proceedings of the Annual Stability Conference Structural Stability Research Council*. Atlanta, Georgia.

Jalali, Sayed Mohamad Moghadam. 2022. Development of Criteria for Fatigue Design of Horizontally Curved Steel Bridges. PhD dissertation, Auburn University.

Jo, H.C., Sohn, H.G., Lim, Y.M. 2020. A LiDAR Point Cloud Data-Based Method for Evaluating Strain on a Curved Steel Plate Subjected to Lateral Pressure. *Sensors*. 20(3), 721 (19 pp.). https://doi.org/10.3390/s20030721.

Jung, S. K., and White, D. W. 2006. Shear Strength of Horizontally Curved Steel I-girders—Finite Element Analysis Studies. *Journal of Constructional Steel Research*. 62(4), 329-342.

Khalil, A., Wipf, T.J., Greimann, L., Wood, D.L. and Brakke, B., 1998. Retrofit Solution for Out-of-Plane Distortion of X-type Diaphragm Bridges. Transportation Conference Proceedings, Iowa Department of Transportation (pp. 99-102).

Kim, Yoon Duk. 2010. “Behavior and Design of Metal Building Frames Using General Prismatic and Web-Tapered Steel I-Section Members,” April. https://smartech.gatech.edu/handle/1853/33965.

Kuhlmann, U., Günther, H.-P. 1999. “Zum Nachweis der Ermüdungsfestigkeit geschweißter Stahlträger mit schlanken Stegen” Research report, Institute for Construction and Design, University of Stuttgart.

Kuhlmann, U. and Spiegelhalder, U., 1999. Ermüdungsversuche an vier geschweißten Stahlträgern mit schlanken Stegen infolge Stegatmung. Universität Stuttgart, Institut für Konstruktion und Entwurf, Versuchsbericht, (1999-27X).

Kulicki, J. M., Wassef, W. G., Smith, C., and Johns, K. 2005. AASHTO-LRFD Design Example: Horizontally Curved Steel I-Girder Bridge. AASHTO.

Lee, S. C., and Yoo, C. H. 1999. Strength of Curved I-girder Web Panels under Pure Shear. *Journal of Structural Engineering*, 125(8), 847-853.

Li, H. and Schultz, A.E., 2005. *Analysis of Girder Differential Deflection and Web Gap Stress for Rapid Assessment of Distortional Fatigue in Multi-Girder Steel Bridges*. University of Minnesota, Institute of Technology, report no. MN/RC-2005-38.

Linzell, D., Hall, D., and White, D. 2004. Historical Perspective on Horizontally Curved I girder Bridge Design in the United States. *Journal of Bridge Engineering*. 9(3), 218-229.

Maeda, Y., Ishiwata, M., Kawai, Y. 1976. *Additional Tests for Type 2 Crack in Hybrid Girders*. International Association for Bridge and Structural Engineering, Tenth Congress, Final Report, Toky, S. 337-340.

Maeda, Y., Okura, I. (1984). Fatigue Strength of Plate Girder in Bending Considering Out-of-Plane Deformation of Web. *Structural Eng./Earthquake Eng*. Vol. 1, No. 2, S. 35-45.

Maeda, Y., Okura, I. (1983). Influence of Initial Deflection of Plate Girder Webs on Fatigue Crack Initiation. *Engineering Structures*. Vol. 5.

Maeda, Y., and Okura, I. 1982. Influence of Initial Deflection of Plate Girder Web on Fatigue Crack Initiation. *Proceedings of the Japan Society of Civil Engineers*. Vol. 1982, No. 319, pp. 1-11. Japan Society of Civil Engineers. https://doi.org/10.1016/0141-0296(83)90041-X.

Marshall, Peter William. 2013. *Design of Welded Tubular Connections: Basis and Use of AWS Code Provisions*. Vol. 37. Elsevier.

Marguerre, K. 1938. *Zur Theorie der gekrümmten Platte großer Formänderung*. *Proceedings of the Fifth International Congress on Applied Mechanics*. Cambridge, Mass., S. 93.

Martinsson, J. 2002. Fatigue Strength of Welded Cruciform Joint with Cold Laps. *Proceedings of Design and Analysis of Welded High Strength Steel Structures*. 163–84.

Matheron, G. 1963. *Principles of Geostatistics. Economic Geology*. 58(8), 1246–1266. https://doi-org.spot.lib.auburn.edu/10.2113/gsecongeo.58.8.1246.

MATLAB and Statistics Toolbox Release 2020a, The MathWorks, Inc., Natick, Massachusetts, United States.

Moghadam, S.M.J., Shah, A.R., and James S. Davidson. 2020. *Distortion Induced Fatigue of Horizontally Curved Steel Girders*. Research Report, Report No: IR 17-01.

Mueller, J. A., and Yen, B. T. 1966. *Fatigue Tests of Large-Size Welded Plate Girders*. June 1966, Fritz Lab Reports, Publication No. 311 (66-19).

Mueller, J. A. and Yen, B. T., 1968. *Girder Web Boundary Stresses and Fatigue*. WRC Bulletin No. 127, Reprint No. 68-2. Fritz Laboratory Reports. Paper 260.

Nakai, H., Kitada, T., Ishizaki, H., and Akehashi, K. 1990. An Experimental Study on Fatigue Strength of Web Plates for Horizontally Curved Plate Girders. Doboku Gakkai Ronbunshu, (416), 125-133. https://doi.org/10.2208/jscej.1990.416_125.

Niemi, Erkki, Wolfgang Fricke, and Stephen J. Maddox. 2018. *Structural Hot-Spot Stress Approach to Fatigue Analysis of Welded Components*. IIW Doc 13: 1819–00.

Okura, I., Yen, B. T., and Fisher, J. W. 1993. Fatigue of Thin-Walled Plate Girders. *Structural Engineering International*. 3(1), 39-44.

Paris, Paul C. 1961. A Rational Analytic Theory of Fatigue. *The Trend in Engineering*. 13: 9.

Pasternak, H., Launert, B. and Krausche, T., 2015. Welding of Girders with Thick Plates—Fabrication, Measurement and Simulation. *Journal of Constructional Steel Research*. 115, pp.407-416.

Patterson, P. J., Corrado, J. A., Huang, J. S., and Yen, B. T. 1970. Fatigue and Static Tests of Two Welded Plate Girders. *Welding Research Council Bulletin*. 155, 1-18.

Phoawanich, N. 2001. *Development of Unified Equations for Design of Curved and Straight Steel Bridge I Girders*. PhD dissertation, Georgia Institute of Technology.

Remadi, A., Aribert, J. M., and Raoul, J. 1995. Secondary Bending Stresses due to Out-of-Plane Displacement of Slender Web Panels Subject to a Bending Moment. *International Colloquium on Stability of Steel Structures*. Technical University of Budapest, Hungary (Vol. 1, pp. 277-284).

Richardson, Gordon, and Associates. 1963. Analysis and Design of Horizontally Curved Steel Bridge Girders. Structural Report ADUSS 00-6003-01. United States Steel Corporation, Pittsburgh, Pa.

Rivera, J., and Chavel, B. W. 2012. Steel Bridge Design Handbook Design Example 3: Three-Span Continuous Horizontally Curved Composite Steel I-Girder Bridge (No. FHWA-HIF-16-002). United States. Federal Highway Administration. Office of Bridge Technology.

Roberts, T. M., and Davies, A. W. 2002. Fatigue Induced by Plate Breathing. *Journal of Constructional Steel Research*. 58(12), 1495-1508.

Russo, Francesco M., Dennis R. Mertz, Karl H. Frank, and Kenneth E. Wilson. 2016. *Design and Evaluation of Steel Bridges for Fatigue and Fracture–Reference Manual*. National Highway Institute (US).

Sabato, A., Kulkarni, N. N., Fortino, G. 2023. Noncontact Sensing Techniques for AI-Aided Structural Health Monitoring: A Systematic Review. *Sensors*. 4672–4684. https://doi.org/10.1109/JSEN.2023.3240092

Sanchez, T. A., and White, D. W. 2012. Stability of Curved Steel I-girder Bridges during Construction. *Transportation Research Record*. 2268(1), 122-129.

Schijve, Jaap. 2001. *Fatigue of Structures and Materials*. Springer Science and Business Media.

Schuenzel, Peter F. 1982. *Strength of Horizontal Curved Plate Girders*. Master Thesis, Lehigh University.

Spiegelhalder, U. 2000. *Zur Materialermüdung infolge Stegatmung*. Universität Stuttgart, Mitteilungen des Instituts für Konstruktion und Entwurf, Nr. 2000-2. Doctoral dissertation, Dissertation, November.

Stegmann, T. H., and T. V. Galambos. 1976. *Load Factor Design Criteria for Curved Steel Girders of Open Section*. Research Report No 43. Washington University.

Subramanian, L., and White, D. W. 2017. Flexural Resistance of Longitudinally Stiffened I-Girders. I: Yield Limit State. *Journal of Bridge Engineering*. 22(1), 04016099.

Taras, Andreas. 2010. *Contribution to the Development of Consistent Stability Design Rules for Steel Members*. Ph.D. dissertation, Graz University of Technology.

Timoshenko, S., and Woinowsky-Krieger, S. 1959. *Theory of Plates and Shells*. McGraw-Hill, New York.125–33.

Toprac, A. A., and Natarajan, M. 1971. Fatigue Strength of Hybrid Plate Girders. *Journal of the Structural Division*. 97(4), 1203-1225.

Wachowiak, T. 1967. *Die Berechnung gekruemmter Stege duennwandigen traegern auf Grund der Shalentheorie*. PhD thesis, Politechnika Gdanska, Gdansk, Poland.

Wackernagel, H. 2003. *Multivariate Geostatistics: An Introduction with Applications*. Berlin; New York: Springer.

Washizu, K. 1975. *Variational Methods in Elasticity and Plasticity*. 2nd Ed., Pergamon Press, Tarrytown, N.Y.

Webster, G.A., and A.N. Ezeilo. 2001. Residual Stress Distributions and Their Influence on Fatigue Lifetimes. *International Journal of Fatigue*. 23: 375–83. https://doi.org/10.1016/S0142-1123(01)00133-5.

Wikipedia contributors. (2024, May 4). Kriging. In Wikipedia, The Free Encyclopedia. Retrieved 17:49, May 25, 2024, from https://en.wikipedia.org/w/index.php?title=Kriging&oldid=1222194055.

Wikipedia contributors. (2024, August 17). Lidar. In Wikipedia, The Free Encyclopedia. Retrieved 17:47, September 3, 2024, from https://en.wikipedia.org/w/index.php?title=Lidar&oldid=1240804549.

Wikipedia contributors. (2024, July 21). Spline (mathematics). In Wikipedia, The Free Encyclopedia. Retrieved 03:23, September 4, 2024, from https://en.wikipedia.org/w/index.php?title=Spline_(mathematics)&oldid=1235749524.

Wikipedia contributors. (2024, May 8). Strain gauge. In Wikipedia, The Free Encyclopedia. Retrieved 20:12, August 23, 2024, from https://en.wikipedia.org/w/index.php?title=Strain_gauge&oldid=1222938664.

Yen, B., and Mueller J.A. 1966. Fatigue Tests of Large Size Welded Steel Girders. *Welding Research Council Bulletin*. 118, pp. 1-25.

Ziemian, Ronald D. 2010. *Guide to Stability Design Criteria for Metal Structures*. John Wiley and Sons.

Zureick, A., Naqib, R., and Yadlosky, J. M. 1994. *Curved Steel Bridge Research Project*. Interim report I: Synthesis (No. FHWA-RD-93-129).